

---

# A realistic local cortical circuit model with laminar-specific connections and synaptic plasticity

## DISSERTATION

zur Erlangung des akademischen Grades  
Doktoringenieur (Dr.-Ing.)

vorgelegt der Fakultät für Biomedizinische Technik  
Institut für Biomedizinische Technik und Informatik  
der Technischen Universität Ilmenau  
von

**Dipl.-Ing. Peng Wang**

geboren am 05. Januar 1981 in Shanghai

Tag der Einreichung: 15. Oktober 2015

Gutachter:

Prof. Dr.-Ing. habil. Jens Haueisen

PD Dr. habil. Thomas R. Knöschke

Prof. Dr.rer.nat. Ingo Bojak

---

---

# Abstract

In the electroencephalography (EEG) and magnetoencephalography (MEG) studies of brain cognition functions and cortical networks, dynamic causal modeling (DCM) provides an useful tool to explore the effective coupling among brain regions. DCM is a computational method that enables the best brain models as well as parameters to be identified from the observed EEG/MEG data. One main challenge of DCM is how to construct a reasonably realistic model that can capture the important microscopic generative mechanisms of brain functions, at the same time can predict those macroscopic effects like observable oscillations or evoked responses in EEG/MEG. Such a model will allow for the integration of data from different sources, both microscopic (i.e. anatomical and physiological features of neurons) and macroscopic (i.e. measurable brain activity), as well as enabling us to test hypotheses and quantify microscopic dynamics for given macroscopic observations.

In order to achieve a more biological plausible model for DCM, this thesis contributes to the development of a biologically realistic local cortical circuit model (LCCM), based on neural masses that incorporates important aspects of the functional organization of the brain that have not been covered by previous models:

1. activity dependent plasticity of excitatory synaptic couplings via depleting and recycling of neurotransmitters and
2. realistic inter-laminar dynamics via laminar-specific distribution of and connections between neural populations.

The potential of the LCCM was demonstrated by accounting for the processes of auditory as well as somatosensory neural response adaptation of repetitive stimulation. The model parameters were specified using Bayesian inference.

In the auditory MEG study, it was found that:

1. besides the major serial excitatory information pathway (layer IV to layers II/III to layers V/VI), there existed a parallel “short-cut” pathway (layer IV to layers V/VI),
2. the inhibitory signal flow from inhibitory interneurons in layers V/VI to the pyramidal

cells seemed to be both intra- and inter-laminar,

3. the adaptation and recovery rates of the connections were different: the connection from layer IV to layers II/III was more strongly suppressed and more slowly recovered than the connection from layer IV to layers V/VI, and
4. the auditory adaptation effect seemed to last about 5 seconds.

In the somatosensory MEG study, it was found that in the excitatory pathway from Layer IV to layers V/VI:

1. Alzheimer patients showed an increased effective connection compared to healthy elderly people,
2. Alzheimer patients showed an over-activation in NMDA receptors, and
3. in comparison to both healthy young and the healthy elderly, the NMDA-receptors showed an age-related decrease in activity.

Our evaluation demonstrated that the novel features of the LCCM are of crucial importance for mechanistic explanations of brain functions. The incorporation of these features into a neural mass model makes it applicable to modeling the macroscopic data like EEG/MEG, which are usually available in human experiments. Our LCCM is therefore a valuable building block for future realistic models of human cognitive function.

---

# Zusammenfassung

Neuronale Massenmodelle sind sparsam hinsichtlich der verwendeten Parameter und biologisch plausibel in ihrer Struktur. Sie sind gut geeignet für die Modellierung der kortikalen Aktivität, die durch extrakranielle Messungen wie Elektroenzephalographie (EEG) oder Magnetoenzephalographie (MEG) erfasst werden. Die in bisherigen Studien verwendeten Modelle machen jedoch starke Annahmen und Vereinfachungen. So wird zum Beispiel die synaptische Plastizität, wichtig für Gehirnfunktionen wie Gedächtnis und Lernen, bisher nicht repräsentiert. Weiterhin wird die Vielfalt aller kortikalen Neuronen häufig nur durch drei verschiedene Populationen berücksichtigt.

Um die lokale Informationsverarbeitung besser zu verstehen ist es außerdem notwendig, die Organisation der Neuronen und ihre synaptischen Verbindungen hinsichtlich der Laminae des Kortexes detailliert darzustellen.

Das Forschungsvorhaben dieser Doktorarbeit ist es, ein solches neuronales Massenmodell mit synaptischer Plastizität und detaillierten synaptischen Verbindungen zu konstruieren und dessen Simulationen mit klinisch relevanten Messungen (Habituation von auditorisch und somatosensorisch evozierter Aktivität) zu vergleichen. Insbesondere wird gezeigt, dass das Modell eine Möglichkeit bietet, den Informationsfluss zwischen verschiedenen kortikalen Laminae und den Grad der Plastizität in verschiedenen Verbindungen zu ermitteln. Die Studie ist relevant für die Erforschung von Erkrankungen des Gehirns, die auf der Pathologie der neuronalen Konnektivität beruhen, zum Beispiel im Falle einer Alzheimererkrankung.

Da das entwickelte Modell die kognitiven Prozesse des Gehirns zur Generation von EEG/MEG-Daten erklärt, ist der wissenschaftliche Beitrag dieser Studie nicht nur für Entwickler neuronaler Massenmodelle relevant, sondern auch für ein breites Feld von Neurowissenschaftlern.



---

## Abbreviations

<b>A<math>\beta</math></b>	amyloid- $\beta$
<b>AD</b>	Alzheimer's disease
<b>AEF</b>	auditory evoked field
<b>AEP</b>	auditory evoked potential
<b>AMDA</b>	$\alpha$ -amino-3-hydroxy-5-methyl-4-isoxazolepropionic acid
<b>BEM</b>	boundary element model
<b>CCPC</b>	cortico-cortical pyramidal cell
<b>CTPC</b>	cortico-thalamic pyramidal cell
<b>DCM</b>	dynamic causal modeling
<b>diIN</b>	inhibitory interneuron in infragranular layer
<b>dPC</b>	pyramidal cell in infragranular layer
<b>eCB</b>	endocannabinoid
<b>EM</b>	Expectation-Maximization algorithm
<b>EIN</b>	excitatory interneuron
<b>EPSC</b>	excitatory postsynaptic current
<b>EPSP</b>	excitatory postsynaptic potential
<b>fMRI</b>	functional magnet resonance imaging
<b>GABA</b>	gamma-aminobutyric acid
<b>GoF</b>	goodness of fit
<b>GoP</b>	goodness of prediction
<b>IC</b>	inferior colliculus
<b>INN</b>	inhibitory interneuron
<b>IPSP</b>	inhibitory postsynaptic potential
<b>ISI</b>	inter-stimuli-interval
<b>JRM</b>	Jansen and Rit model
<b>LCCM</b>	local cortical circuit model
<b>LFP</b>	local field potentials
<b>LM</b>	Levenberg-Marquardt algorithm
<b>LTP</b>	long-term potentiation
<b>NM</b>	neural mass
<b>NMDA</b>	N-methyl-D-aspartate acid
<b>NMM</b>	neural mass model

<b>nRT</b>	nucleus reticularis thalami
<b>MCI</b>	mild cognitive impairment
<b>MRI</b>	magnet resonance imaging
<b>PC</b>	pyramidal cell
<b>PSP</b>	postsynaptic potential
<b>PT</b>	planum temporale
<b>sIIN</b>	inhibitory interneuron in supragranular layer
<b>sPC</b>	pyramidal cell in supragranular layer
<b>STG</b>	superior temporal gyrus
<b>VPm</b>	ventroposterio-medial nuclei



# Contents

Abstract .....	I
Zusammenfassung.....	III
Abbreviations .....	V
Contents .....	VII
Chapter 1 : Introduction.....	1
1.1 Motivation .....	1
1.2 Suggested solution .....	4
1.3 Structure of the thesis.....	8
Chapter 2 : Methods .....	10
2.1 Generative model.....	10
2.1.1 Neural mass model.....	10
2.1.2 Jansen and Rit model.....	16
2.1.3 Local cortical circuit model.....	20
2.1.3.1 Motivation .....	20
2.1.3.2 Brief review of some important neurons in cortical layers .....	21
2.1.3.2 Construction of the local cortical circuit model .....	28
2.1.4 Model of synaptic short-term plasticity .....	33
2.1.4.1 Motivation .....	33
2.1.4.2. Modeling short-term plasticity in local cortical circuit model.....	35
2.2 Bayesian inversion for parameter estimation .....	43
2.2.1 Motivation .....	43
2.2.2 Forward modeling .....	45

---

2.2.3 Bayesian inverse estimation.....	48
2.2.3.1 Bayesian theorem.....	48
2.2.3.2 Expectation-Maximization Algorithm.....	50
2.2.4 Bayesian model selection.....	56
2.2.5 Improved Bayesian inverse framework.....	59
2.2.5.1 Prior formulations.....	59
2.2.5.2 Implementation of Levenberg-Marquardt Algorithm.....	63
2.2.5.3 Evaluation of the Levenberg-Maquardt implementation.....	65
2.2.5.3.1 Hypothesis.....	65
2.2.5.3.2 Method specification.....	66
2.2.5.3.3 Results.....	66
2.2.5.3.4. Conclusions.....	67
Chapter 3 : Applications and Evaluations.....	69
3.1 Modeling auditory adaptation.....	69
3.1.1 Motivation.....	69
3.1.2 Tasks.....	72
3.1.3 Model specification.....	72
3.1.4 Data acquisition and processing.....	77
3.1.4.1 Experiment.....	77
3.1.4.2 MEG recording.....	78
3.1.4.3 Data preparation.....	79
3.1.5 Results.....	81
3.1.5.1 Data observation and description.....	81
3.1.5.2 Comparison of the LCCM and the JRM.....	82
3.1.5.2.1 Comparison of the goodness of fit.....	82

---

3.1.5.2.2 Comparison of the goodness of prediction .....	85
3.1.5.2.3 Comparison of the model evidence .....	88
3.1.5.3 Simulated adaptation effect with different stimulation frequencies .....	89
3.1.5.4 Laminar organization of the synaptic connections .....	92
3.1.5.4.1 Synaptic pathways .....	92
3.1.5.4.2 Synaptic dynamics .....	98
3.1.6 Discussion and conclusion .....	104
3.2 Modeling somatosensory adaptation - a pilot application in Alzheimer's disease study .....	110
3.2.1 Motivation .....	110
3.2.2 Tasks .....	115
3.2.3 Data acquisition and processing .....	116
3.2.3.1 Experiment .....	116
3.2.3.2 Data acquisition .....	117
3.2.3.3 Data preparation .....	118
3.2.3.4 Data observation and description .....	119
3.2.4 Model specification .....	122
3.2.5. Results .....	127
3.2.5.1 Comparison of LCCM and JRM in modeling somatosensory activity. ....	127
3.2.5.2 Goodness of fit of the LCCM using suppressed synaptic connections .....	128
3.2.5.3 Comparison of the LCCM using suppressed and constant inhibitory synaptic connections .....	129
3.2.5.4 Parameter comparison of different participants' groups .....	133
3.2.6. Discussion and conclusion .....	136
Chapter 4 : Summary and Future Direction .....	141
References .....	145

---

Appendix A .....	158
Appendix B.....	164
Appendix C.....	170
List of Figures.....	173
List of Tables.....	176
List of Equations .....	178
Erklärung .....	180

# Chapter 1: Introduction

*"That is the story. Do you think there is any way of making them believe it?"*

*- Plato, 428/427BC - 348/347 BC*

## 1.1 Motivation

### ***Minicolumn - column - macrocolumn***

The human cortex is perhaps the most complex thing in the world. It's a thin and folded tissue about 2-4 mm thick with a surface area of around 2600 cm<sup>2</sup> [1-2]. It contains up to 16 billion neurons and about the same number of glial cells [3-4]. These neurons are distributed in six different laminar layers vertically from the pial surface to the deep cortex [5]. The basic unit of the cortex is the minicolumn [1]. There are about 80 to 100 neurons inside a minicolumn. These neurons are grouped in a narrow chain and extend vertically across the layers II-VI of the cortex, perpendicular to the pial surface. The diameter of a minicolumn is about 50 μm. Many minicolumns, which share the similar physiological static and dynamic properties, are bounded together by short-range horizontal connections to form a cortical column [1]. For example, a cortical column in the cat somatosensory cortex, which consists of about 80 minicolumns, has a width of about 300-400 μm [6]. Even between species cortical columns vary only from 300 to 600 μm. In the evolution of the cortical expansion, only the number of the cortical columns has increased, not the individual column size [7]. Cortical columns are complex signal processing and distributing units. They receive, select and integrate the inputs from other cortical areas or subcortical areas, such as the thalamus and then provide output further to various other areas of the brain. In order to perform a given functional task, the cortical columns may cooperate with each other to form a physiological macrocolumn [8]. These physiological macrocolumns must be considered as dynamic ensembles. The number of joint columns is not fixed and may vary as a function of

time [9-10]. Research and understanding of the signal processing inside cortical columns or macrocolumns lead to understanding of the two fundamental principles of the brain organization [11]: functional integration and functional specialization. The integration within or/and among the functional specialized brain areas is through the neural connections among them.

### ***Microcircuit of a cortical column***

The neural network inside a cortical column has a specific laminar architecture. The supragranular layers (layers I-III) are the primary origin and termination of intracortical connections. Layer III receives the input from other cortical columns and layers II-III project to the other part of the cortex. The internal granular layer (layer IV) receives the input from the thalamus and sends signals to the other layers of the column, primarily up to layer II and layer III. The infragranular layers (layer V-VI) receive the signal from the supragranular layers and primarily target the subcortical regions (see [12] for review). This is an oversimplified overview of the laminar synaptic connections, which ignores numerous differences depending on cortical areas and species [13]. The laminar synaptic connection patterns across different species or different cortical areas may be fundamentally different in terms of specific functionalities [12].

### ***Current methods to study connectivity in a cortical column: a microscopic approach***

To date, there are several approaches to directly study neuronal synaptic connections *in vivo* or *in vitro* in animal studies, such as the paired neural patch-clamp recording [14], the single neuron recording with photostimulation [15-16] as well as the optical probing [17]. In brief, neurons can be dyed or labeled with biocytin to be visualizable under the microscope. Combining infrared video microscopy with patch-clamp recording makes it possible to record visually identified neurons in a defined cortical microcircuit of several hundred micrometers [14]. The paired neural recording can be applied to study the synaptic dynamics such as short and long-term synaptic plasticity between the pre- and postsynaptic neuron pair. But usually

a single neuron receives multiple inputs from different neurons in different cortical layers and also sends signals to different targets. To study connections from other layers to a specific neuron type, combining single neuron recording with photostimulation using caged glutamate [15-16] is more efficient than the paired neural recording [18]. The neurons in a small region (within 50 $\mu$ m) are selectively activated by the glutamate released by a light beam. These activated neurons are presynaptic to the recorded neuron. This technique can rapidly scan over a wide cortical surface in about 500  $\mu$ m to find the regions that contain those presynaptic neurons to the recorded neuron. However, how many neurons contribute to this postsynaptic neuron or the type of those presynaptic neurons cannot be clearly identified. The synaptic dynamics cannot be studied either. Another technique called optical probing [17] can be used to identify either input or output regions from a recorded neuron. The neurons are labeled with a calcium indicator. Regions of connected neurons can be studied by driving one recorded neuron to fire and using calcium imaging to identify the positions of other neurons activated by that cell. The inverse can also be applied [19], e.g. recording from one postsynaptic neuron and using reverse correlation to estimate the presynaptic neurons whose activity correlated with the recorded neuron. However, like the caged glutamate study, no information about the synaptic dynamics can be obtained.

These *in vivo* or *in vitro* microscopic measurements provide a direct access to neural synaptic connectivity and provide qualitative and quantitative information about the morphological and functional properties of synaptic connections in single neuron level. However, these experiments are carried out in acute brain slices, generally from animals. Stimulations are applied through microelectrodes and biocytin-fillings. Direct measurements in the healthy human cortex *in vivo* under real cognition tasks and behaviors are strictly not allowed.

### ***Research purpose***

So the purpose of this research is to develop a method for the community of computational neural science, which can be used on humans through non-invasively measured data such as electroencephalography (EEG) and magnetoencephalography (MEG) to retrieve information

about the synaptic connections among cortical layers in a local cortical area under real cognition tasks.

## 1.2 Suggested solution

In order to reach the research purpose, the author suggested: i) Composing a simple but biological plausible *local cortical circuit model* (LCCM) [20] , which is a further extended *neural mass model* (NMM) of Jansen and Rit [21-22] with laminar-specific connections and dynamic synapses. The model represents the physiological macrocolumn under specific cognition tasks. ii) Composing a framework to estimate the properties of the laminar connections from the recorded cortical neural activity through non-invasive EEG/MEG data. The estimation relies on the Bayesian inversion method and is similar to the schema of *dynamic causal modeling* (DCM) [23].

### ***The data - EEG/MEG: a macroscopic non-invasive measurement of neural activity***

In current human brain studies, non-invasive image techniques are used to obtain the anatomical and functional properties of the cortex. These techniques include EEG/MEG, magnet resonance imaging (MRI), functional MRI (fMRI) as well as diffusion-weighted MRI. They are able to record the signals while the experiment participants can perform their cognitive behaviors as usual. However, these techniques acquire the physiological data of the cortex on a different scale level: They do not measure the activity of a single neuron, but rather the activity of a large number of grouped neurons. For example, the fMRI of 3 Tesla is able to detect the changes in metabolism and blood flow with fine spatial resolution e.g. 0.5 millimeter, which are correlated with the summarized activities of neurons in this cortex volume. EEG/MEG are only capable of measuring the electric and magnetic fields, which are generated by a group of synchronized pyramidal cells (at least about fifty thousand) in a local cortical area with diameter more than 0.9 mm [24].

Although these macroscopic data are not able to discriminate the activity of a single neuron,



they still serve well to our research of the various brain functionalities because brain functions are not performed by a single particular neuron. Motivated by the anatomical theory of Franz Joseph Gall and the anatomical evidence from Korbinian Brodmann [5], the cerebral cortex is considered to be organized into spatially separated regions with different specialized functionalities. Functional MRI is able to locate the activated brain area with a high spatial accuracy. This is useful to identify which particular brain regions are involved in what particular tasks or task components. However, change in blood oxygenation is a relatively slow and delayed process in comparison to the rapid neural activation processes governed by the changes of ion fluxes and membrane potentials. Thus, fMRI has a relatively poor time resolution to provide information about the timing of the involvement of cortical areas. On the other hand, EEG/MEG measure the changes of electric and magnetic fields, which are real-time induced by intercellular currents of the pyramidal cells [25]. Because those pyramidal cells are arranged in palisades and their apical dendrites are long and well aligned perpendicularly to the cortex surface, the intercellular currents flow longitudinally along the dendrites or axons, thus generating the electric and magnetic fields, which do not cancel with each other but add together and contribute to the majority of the EEG/MEG signal. Analyzing the spatiotemporal evolution of the EEG/MEG data, for example projecting them into a single or a set of equivalent current dipoles, gives the EEG/MEG the power to provide i) locations of the centers of the activated brain areas with a reasonable spatial accuracy in millimeters, which can be superimposed onto the anatomical structure provided by the MRI, as well as ii) time courses of activations in these areas with an excellent temporal resolution in milliseconds and sub-milliseconds [24].

Decomposing the EEG/MEG sensor signal into the activity of specific neural sources enhances and clarifies stimulus and task effects. These sources could be considered to represent the functional macrocolumns in the cortex. However the source activity alone does not directly reveal any information about the laminar synaptic connectivity such as the causal effect of one cortical layer over another as well as the temporal change of the synaptic connection strength. Therefore, a suitable generative model with laminar synaptic

connections and synaptic plasticity is required in order to estimate the properties of the connections.

***The model - neural mass model: a generative model for EEG/MEG signals***

Traditionally, two main classes of models have been commonly used to explore the dynamic of neural circuits. One is based on single neuron simulation using spiking neuron models, for example, of the leaky integrate-and-fire or the more elaborate Hodgkin-Huxley types [26-27]. Such networks include multiple interconnected neurons and their short-term synaptic plasticity depends on the dynamic of the presynaptic spike trains [28-29]. These models are, for example, relevant for single cell recordings in animals, while their state variables are not captured adequately by macroscopic measurements, like EEG, MEG, local field potentials (LFP), or fMRI. In contrast, NMMs [21-22, 30-35] describe the mean activity of entire neural populations, represented by their average firing rates and average membrane potentials. Such models are, therefore, more suitable for modeling macroscopic brain signals. Despite their parsimony in parameter formulation, NMMs are still biologically realistic, that is, their parameters are related to microscopically measurable quantities, such as the receptor time constant.

In the past, brain networks and functions have been investigated using NMMs with different sets of assumptions, e.g., by Wilson and Cowan [36], Freeman [30], Wright and Liley [37], Robinson and colleagues [38], Rennie and colleagues [39], Jansen and Rit [21-22], and Lopes da Silva and colleagues [31-32]. One of the most widely used ways to account for the dynamic of a cortical circuit is the approach of Jansen and Rit [21-22], which comprises three interconnected neural populations: pyramidal cells (PCs), excitatory interneurons (EINs), and inhibitory interneurons (IINs). The average membrane potentials of the PCs are considered proportional to the observed EEG/MEG signal [25]. David and colleagues [40] added an inter-area connectivity scheme following the hierarchical rules described by Felleman and Van Essen [41], in order to assemble a network of coupled sources. Wendling and colleagues [42] separated the originally singular IIN population into a fast GABAergic and a slow

GABAergic IIN. Zavaglia and colleagues [43] added a recurrent loop to the circuit of fast GABAergic IINs. These models have been used to simulate various EEG/MEG features in both time and frequency domains, such as brain rhythms ranging from the delta to the gamma bands [22, 43-44], event-related evoked responses [40, 45-48], induced responses [35, 49], spectral responses [50-52] and epilepsy-like activities [42, 53]. Moreover these models have also been used to account for effects in other brain image modalities such as fMRI [54] and voltage sensitive dyes [55].

However, most of these approaches lack two crucial properties to serve our research purpose. First, they embody neither clear definition of the laminar distribution of the neural populations inside a column nor the laminar-specific connections among the neural populations. This severely limits their potential to study the signal pathway among the layers inside a cortical column. Second, they are based on static network structures with fixed connection strength, synaptic weights and time constants. Synaptic plasticity is another essential functional property in synaptic microcircuit and is the fundamental neural basis to high cognition abilities like memory and learning [56]. Signal transmission between different layers and neural population types can be either depressed or enhanced through the dynamic change of synaptic connections[12].

Therefore, the author proposed an extension to the Jansen and Rit model (JRM) [22] comprising 5 neural masses : one for EINs in layer IV, one for superficial pyramidal cells (sPCs) in supragranular layers II/III, one for deep pyramidal cells (dPCs) in infragranular layers V/VI as well as two for the supragranular and infragranular inhibitory interneuron populations (sIINs & dIINs). The laminar-specific connections among the populations are motivated by previous modeling attempts [12, 22, 40, 57] and animal studies [58-59]. Each synaptic connection is able to increase or decrease as a function of the dynamic change in presynaptic average firing rate. The synaptic connection strength is associated with the presynaptic neuronal release probability. Repetition of stimuli causes either an increase or decrease of the release probability of the neural vesicles, which in turn causes facilitation or adaptation in synaptic connection strength and hence EEG/MEG signal amplitude. The

resulting LCCM is more detailed and realistic with respect to the laminar organization of information processing. It is worth noting that, in this work, the "cortical column" simulated by the neural mass model indicates the physiological macrocolumn.

### ***The estimation - Bayesian inference: an inverse estimation of synaptic connection properties***

In order to link the generative model to observed data in an EEG/MEG experiment and, in particular, explore the information pathway among the cortical layers, a Bayesian inference technique is applied, which is similar to the well-known *dynamical causal modeling* approach (DCM) [45, 60]. It estimates the model parameters from measured EEG/MEG data as well as from prior information about these parameters. In previous studies, Garrido and colleagues [48] used DCM to analyze the connection among the cortical areas, which were involved in auditory processing and David and colleagues [61] used DCM to analyze the subcortical connectivity in language processing. The model evidence is approximated to account for model accuracy and model complexity [62]. It is used as an index for finding the most "optimized" connectional organization in the light of the data [63]. Here, a new technique is proposed for the formulation of priors for the connectivity parameters, which allows for accommodating larger portions of the model space within a single model that can be specified by fitting to the data.

## **1.3 Structure of the thesis**

**Chapter 2: Method** is divided into two parts in the aspect of the two key methodological issues of this presented dissertation: the modeling and the model parameter estimation. In the modeling part, the major purpose is to introduce the LCCM. It is further divided into two parts according to the two hallmarks of the LCCM in comparison of the previous neural mass models: the laminar organization of the neural population as well as the short-term synaptic plasticity. In order to theoretically support the LCCM, the mathematic background as well as

the biological evidence is described in detail. The model parameter estimation relies on the implementation of the Bayesian inverse estimation. The crucial parts such as the application of the Bayesian theorem, implementation of the Expectation-Maximization-Algorithm (EM) as well as the computation of the model evidence for the model selection are reviewed from previous literature. A novel prior formulation technique that embodies large portions of the model space within a single model is subsequently proposed. Furthermore, in order to improve the fitting accuracy of the EM-algorithm, the implementation of the Levenberg-Marquardt-Algorithm (LM) is suggested and empirically evaluated as well.

In **Chapter 3: Application and Evaluation**, two MEG experiments are chosen in order to prove and evaluate if the LCCM is advantageous for explaining and researching phenomena such as adaptation or memory effects in evoked MEG. The first MEG experiment is related to the auditory modality. The data was acquired by the author at the Max-Planck-Institute of Cognition and Brain Sciences in Leipzig. The second MEG experiment is related to the somatosensory modality. The data was provided by Dr. Akinori Nakamura from the National Center for Geriatrics and Gerontology Center for Development of Advanced Medicine for Dementia in Aichi, Japan. In each experiment section, the author focuses on three points: the model specification, the fitting validation and the parameter representation and interpretation.

The last chapter is **Chapter 4: Summary and Future Direction**.

## Chapter 2: Methods

*"The object of knowledge is what exists and its function to know about reality. "*

*- Plato, 428/427BC - 348/347 BC*

### 2.1 Generative model

#### 2.1.1 Neural mass model

Neurons consist of several components: a cell body (soma) with a nucleus, dendrites and axonal branches including an axon covered by myelin sheathes and with synapses at its terminal (Fig. 2.1). A neuron collects the information from other neurons through its dendrites. The information is integrated and processed at the soma and then sent further through the axon to the axon terminals. From there the information can move to the next neuron. A whole neuron may cross several layers of the cortex, but neurons are generally classified to a specific cortical layer depending on where their somas are located. However, their dendrites and axon terminals can pass through different layers. Therefore, two neurons may contact with each other in a layer where neither of their somas belong to.

Neurons can be characterized by four main functional properties: a) electrical excitability of the cell membrane, b) secretion of neurotransmitters, c) plasticity, and d) protein synthesis. The first three properties are closely related to information processing among neurons. The signal transmission of neurons involves changes in the resting membrane potential, which is defined as the electrical potential difference between the intra- and extracellular space of a neuron at the rest state. The transient change of the resting membrane potential caused by synaptic inputs is called postsynaptic potential. This change in the potential is mediated by the changes in the concentration of ions ( $\text{Na}^+$ ,  $\text{K}^+$ ,  $\text{Ca}^{2+}$ , etc.) in the intra- and extracellular space. The concentration of the ions is regulated by the ion channels presenting in the

cellular membrane. The opening or closing of these ion channels depends on the current membrane potential and the received neurotransmitters. These neurotransmitters bind to receptors on the membrane in order to depolarize or hyperpolarize the cell. When the postsynaptic potential exceeds a certain threshold, the neuron fires an impulse (spike). This impulse is also called action potential, and is characterized by its amplitude and duration. Information transmission at the interneuron level is considered to be encoded in terms of the frequency of the action potentials (also called spiking, firing rate) or their timing. Neurons also have the ability to strengthen or weaken the information transmission over time via varied neural mechanisms such as changing the amount of released neuronal transmitters or altering the sensitivity of the receptors.

The neural mass models (NMMs) [21-22, 30-35] are designed to describe the functional properties of a population of neurons in term of the neural signal transmission. These neurons are considered to share the similar anatomical and physiological properties and are lumped together in a limited defined volume. Together they form a neural ensemble or a neural mass (NM). The basic idea of the NMM is to describe the average input-output-behavior of a NM. The signal process is modeled by two transformation operators (Fig. 2.1).

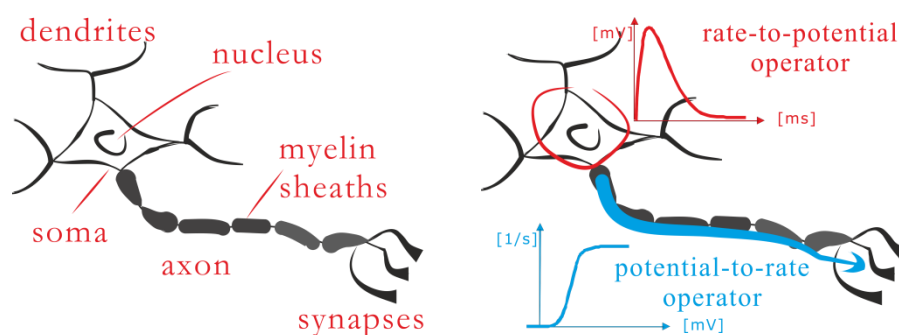


**Figure 2.1** Two operators to simulate the neuron signal transmission in the neural mass model.

The first operator, rate-to-potential operator, describes that the dendrites receive the input signal and send them to soma, on where they then cause changes in the membrane potential. The second operator, potential-to-rate operator, describes that the depolarization of membrane potential causes firing action potential, and is sent further through the axon to other neural populations.

### Rate-to-potential operator

The first operator, called rate-to-potential operator, converts the average pulse density of the action potentials coming to the population into an average postsynaptic membrane potential.

$$u(t) = Q(t) \otimes h(t)$$

$$h(t) = \begin{cases} \frac{H}{\tau} t \exp(-\frac{t}{\tau}) & t \geq 0 \\ 0 & t < 0 \end{cases} \quad (1)$$

Here, each NM receives an average firing rate,  $Q(t)$ , as an input and converts it into an average membrane potential,  $u(t)$ .  $H$  denotes the average synaptic gain and tunes the maximum amplitude of the average membrane potential. The time constant  $\tau$  describes the rise and the fall of the average membrane potential evoked by a spike, and it can be considered as a lumped representation of the activation of different receptors such as the  $\alpha$ -amino-3-hydroxy-5-methyl-4-isoxazolepropionic acid receptor (AMDA) and the N-methyl-D-aspartate receptor (NMDA). The Form of the Kernel function  $h(t)$  is inspired by the observed value of impulse response of prepyriform cortex [64-65] (Fig. 2.2). The simulated response using parameter  $H = 3.25$  mV,  $\tau = 10$  ms [22] is shown in Fig. 2.3 in blue and the impulse response using  $H = 13$  mV,  $\tau = 4$  ms is shown in red.

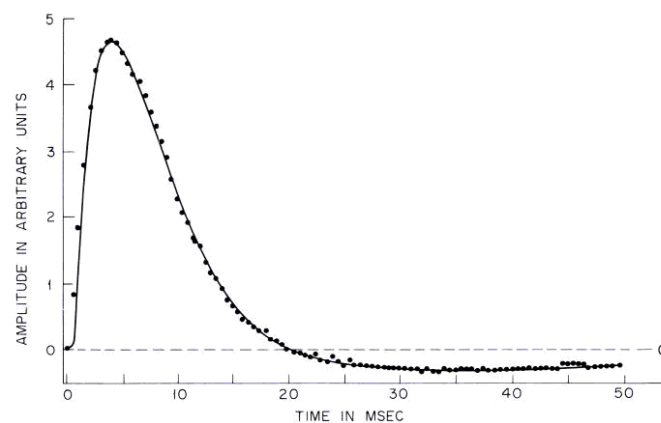


**Figure 2.2** Observed value of impulse response of prepyriform cortex (Picture from Freeman, 1975, Mass action in nervous system)



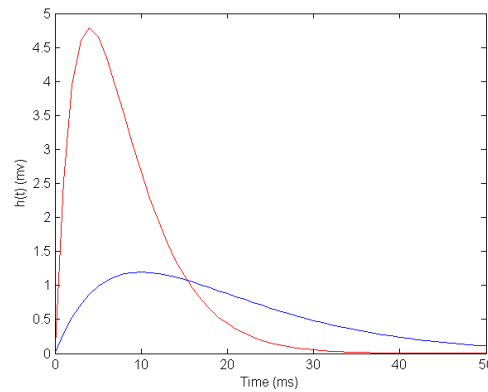


**Figure 2.3 The kernel function  $h(t)$ .** The blue curve uses parameter  $H = 3.25$  mV,  $\tau = 10$  ms [22] and the red curve uses parameter  $H = 13$  mV,  $\tau = 4$  ms. The red one is similar to that measured in the literature, see Figure 2.2.

The kernel,  $h(t)$ , can be interpreted as Green's function of a second-order ordinary differential equation, which can be further expressed as two first-order linear inhomogeneous differential equations:

$$h(t) = \frac{H}{\tau} t e^{-\frac{t}{\tau}} \quad \bullet \quad K(s) = \frac{H}{\tau(s + \frac{1}{\tau})^2}$$

$$u(t) = Q(t) \otimes h(t) \quad \bullet \quad U(s) = \frac{H}{\tau(s + \frac{1}{\tau})^2} \cdot L\{Q(t)\} \quad (2)$$

$$\frac{H}{\tau} L\{Q(t)\} = s^2 U(s) + sU(s) \frac{2}{\tau} + \frac{U(s)}{\tau^2} \quad \bullet \quad \frac{H}{\tau} Q(t) = \ddot{u}(t) + 2 \frac{\dot{u}(t)}{\tau} + \frac{1}{\tau^2} u(t)$$

$$\ddot{u}(t) = \frac{H}{\tau} Q(t) - 2 \frac{\dot{u}(t)}{\tau} - \frac{1}{\tau^2} u(t)$$

$$\dot{u}(t) = v(t) \quad (3)$$

$$\dot{v}(t) = \frac{H}{\tau} Q(t) - \frac{2}{\tau} v(t) - \frac{1}{\tau^2} u(t)$$

The kernel  $h(t)$  can also be extended with two time constant  $\tau_r$  and  $\tau_f$ . They describe the rise and the fall of the membrane potential separately [66] (Fig. 2.4).

$$h(t) = \frac{\tau_f \tau_r}{\tau_f - \tau_r} H \left( \exp\left(-\frac{t}{\tau_f}\right) - \exp\left(-\frac{t}{\tau_r}\right) \right), \quad t \geq 0 \quad (4)$$

The expression of the ordinary differential equation is changed to

$$\begin{aligned}
h(t) = h(t) &= \frac{\tau_f \tau_r}{\tau_f - \tau_r} H (e^{-\frac{t}{\tau_f}} - e^{-\frac{t}{\tau_r}}) \circ - \bullet K(s) = \frac{H}{(s + \frac{1}{\tau_f})(s + \frac{1}{\tau_r})} \\
u(t) = Q(t) \otimes h(t) \circ - \bullet U(s) &= \frac{H}{(s + \frac{1}{\tau_f})(s + \frac{1}{\tau_r})} \cdot L\{Q(t)\} \\
HL\{Q(t)\} = s^2 U(s) + sU(s) \frac{(\tau_f + \tau_r)}{\tau_f \tau_r} + \frac{U(s)}{\tau_f \tau_r} \bullet - \circ HQ(t) &= \ddot{u}(t) + \frac{(\tau_f + \tau_r)}{\tau_f \tau_r} \dot{u}(t) + \frac{1}{\tau_f \tau_r} u(t) \quad (5) \\
\ddot{u}(t) = HQ(t) - \frac{(\tau_f + \tau_r)}{\tau_f \tau_r} \dot{u}(t) - \frac{1}{\tau_f \tau_r} u(t) &
\end{aligned}$$

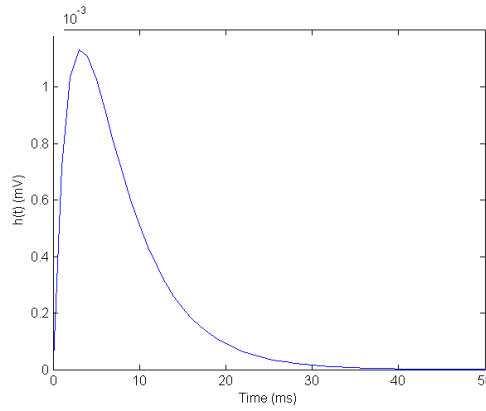


**Figure 2.4** The kernel function  $h(t)$  with two time constants. The parameters are selected from the literature [66]:  $\tau_r = 2\text{ms}$ ,  $\tau_f = 5,68\text{ms}$ ,  $H = 1\text{mV}$ .

### Potential-to-rate operator

The second operator, called potential-to-rate operator, converts the average membrane potential of the population into an average pulse density of action potentials/spikes fired by the neurons. This potential-rate transformation is obtained through a sigmoid function (Fig. 2.5):

$$Q(t) = \text{Sigm}(u) = \frac{2e_0}{1 + \exp(r(u_0 - u(t)))} - \frac{2e_0}{1 + \exp(ru_0)} \quad (6)$$

Here  $e_0$  tunes the maximal firing rate of the NM.  $u_0$  is the average membrane potential at the half of the maximal firing rate.  $r$  is the slope of the sigmoid function. The Equation (6) is a modified version of the original sigmoid function used by Jansen and Rit [21-22] with an additional term  $2e_0/1 + \exp(ru_0)$ . The motivation of this alteration is to achieve a stable

fixed-point (at  $u(t) = 0$ ,  $S(u) = 0$ ), where all the states are equal to zero. The fixed-point corresponds to the system's equilibrium or steady state meaning that state variations can be interpreted as the deviation from the steady state: i.e., positive and negative firing rate can be interpreted as higher or lower neural activity compared to steady state activity [67].

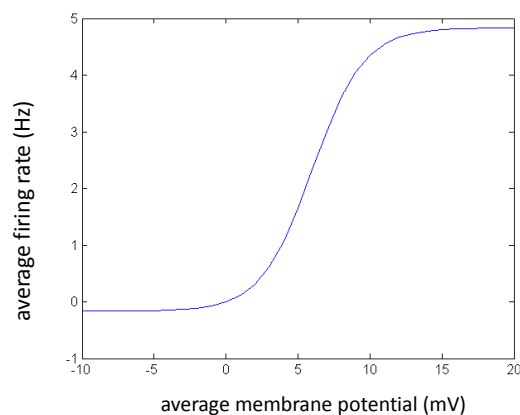


**Figure 2.5 The modified sigmoid function.** The parameters are  $e_0 = 2.5$  Hz,  $u_0 = 560$  mV<sup>-1</sup>.

The form of the sigmoid function represents the statistical distribution of the firing threshold  $u_0$  of each signal neuron in the NM. Fig. 2.6 shows a normal distribution of the firing threshold in a NM simulated with 50,000 neurons, which is a theoretically estimated necessary number for the generation of recordable signals in the human MEG [24]. Fig. 2.7 shows two courses of the summarized firing rate of the 50,000 neurons. Their firing threshold distributions are shown in Fig. 2.6. The slope of the sigmoid function is verified after the standard deviation of the firing threshold.

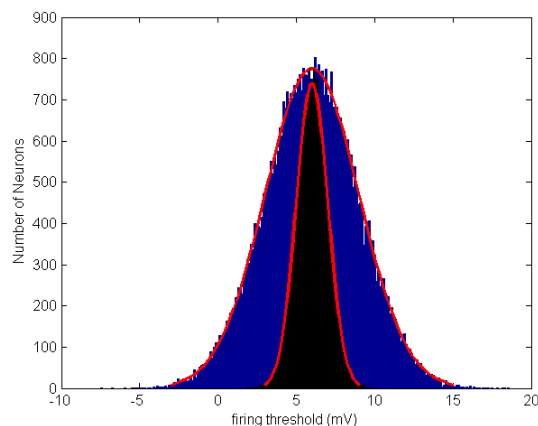


**Figure 2.6 Simulated normal distributions of 50,000 Neurons.** The mean of the firing threshold for both distributions is 6 mV and the standard deviation are 1 mV (thin) and 3 mV (broad).

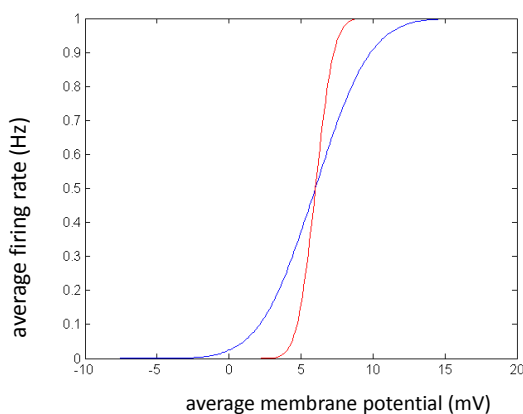


**Figure 2.7 Simulated summarized firing rate of 50,000 Neurons in a Neural mass.** Blue:  $\sim N(6 \text{ mV}, 3 \text{ mV})$ , red:  $\sim N(6 \text{ mV}, 1 \text{ mV})$ .

## 2.1.2 Jansen and Rit model

The JRM [22] comprises three different neuron types to simulate a cortical column (Fig. 2.8): excitatory interneurons (EINs), inhibitory interneurons (IINs) and pyramidal cells (PCs). The EINs represent the spiny stellate cells in cortical layer IV, and the INNs represent the GABA-ergic neural types, which are distributed throughout all the layers. EINs and PCs form an excitatory feedback loop while INNs and PCs form an inhibitory feedback loop. These two loops interactively control the rise and fall of the average membrane potential of the PCs, which is assumed to be proportional to the reordered EEG/MEG.

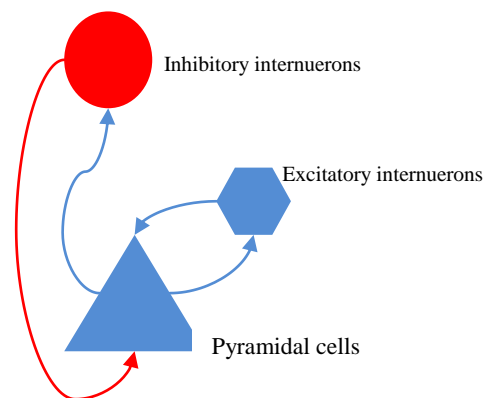


**Figure 2.8 Jansen and Rit model for a single cortical column.** The neural mass model of Jansen and Rit (1995) composed three interconnected neural masses in a cortical column: excitatory interneurons, inhibitory interneurons and pyramidal cells.

### ***External input to a cortical column***

There are different models of the external input to a NMM under different modeling aspects. In the original JRM [22], the external input targeted PCs. In the work of Haeusler and Maass [57] (although they used the Hodgkin-Huxley neuron model), the external input, which was considered as a thalamic input to a sensory cortex, targeted both pyramidal and nonpyramidal neurons throughout layers II-V. It was inspired by the biological evidence cited by White [68]. But considering that the major thalamic signals target the spiny stellate cells in the cortical layer IV in sensory cortical areas [12, 16, 59, 69-73], a simplified thalamic input pathway was used in the other research works [20, 45-47, 51-52, 60]. It assumed that the sensory evoked response was prominently driven by the thalamic input to excitatory interneuron. The external input density function is also described with different mathematic expressions. For the purpose of modeling oscillations like alpha or beta brain waves, a constant input is usually used [22, 44]. To simulate the evoked response, Equation (7) was proposed by Jansen and colleagues [21].

$$P(t) = q \left( \frac{t}{w} \right)^7 \exp\left(-\frac{t}{w}\right) \quad (7)$$

The form of the function (Fig. 2.9a) represents the signal transmission from the retina through the metathalamus to the visual cortex, where  $q$  tunes the maximal amplitude of the density function while  $w$  adjusts the latency and width (Fig. 2.9, blue one). Equation (8) was proposed by David and colleagues [45].

$$P(t) = qn_2^n t^{n-1} \exp(-n_2 t) / \text{gamma}(n_1) \quad (8)$$

In comparison to the Equation (7), which uses only one parameter to tune the form of the signal, using two parameters  $n_1$  and  $n_2$  at the same time it is much easier to control the input: The width and latency could be separately tuned.  $n_1$  and  $n_2$  both determinate the rise and fall of the impulse, the latency of the maximal peak is approximated by  $n_1/n_2$  (Fig. 2.9, red one).

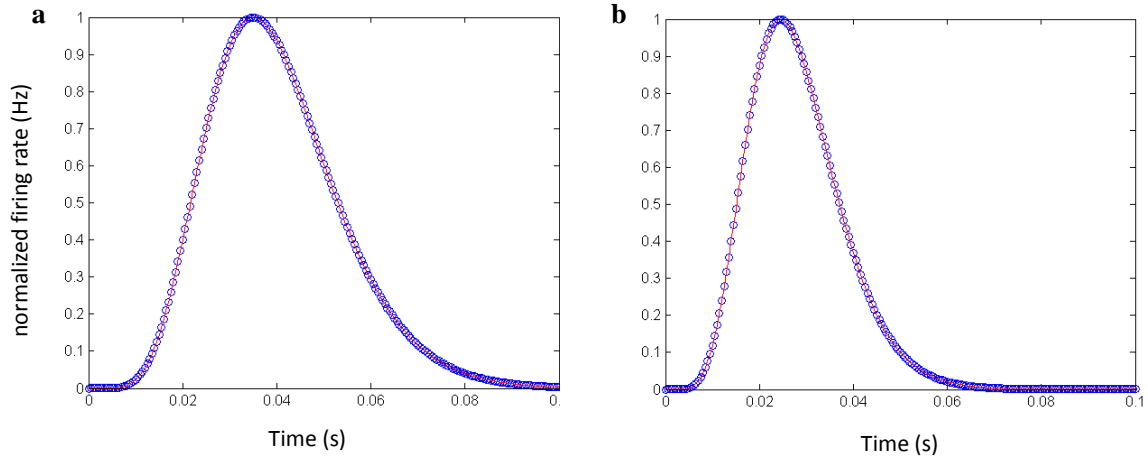


**Figure 2.9 Input density functions.** The simulated input density functions of Equation (7) (blue circle) and Equation (8). The amplitude could be considered as incoming firing rate density (Hz) and normalized of 1. a) Parameter for Equation (7):  $w = 0.005$ ; parameter for Equation (8):  $n_1 = 8$ ,  $n_2 = 200$ . b) Parameter for Equation (7):  $w = 0.0035$ ; parameter for Equation (8);  $n_1 = 8$ ,  $n_2 = 286$ .

### ***The ordinary differential equation system and parameters of Jansen and Rit model***

From Equation (3) the ordinary differential equation system of JRM [22] is composed as followed:

Connection to EINs, from PCs and external input  $P(t)$ :

$$\begin{aligned} \dot{y}_1(t) &= y_2(t) \\ \dot{y}_2(t) &= \frac{H_e}{\tau_e} P(t) - \frac{2}{\tau_e} y_2(t) - \frac{1}{\tau_e^2} y_1(t) \\ \dot{y}_3(t) &= y_4(t) \\ \dot{y}_4(t) &= \frac{H_e}{\tau_e} C_{PC,EIN} Q_{PC}(t) - \frac{2}{\tau_e} y_4(t) - \frac{1}{\tau_e^2} y_3(t) \\ Q_{PC}(t) &= \text{Sigm}(y_7(t) - y_9(t)) \end{aligned} \quad (9)$$

Connection to IINs, from PCs:

$$\begin{aligned} \dot{y}_5(t) &= y_6(t) \\ \dot{y}_6(t) &= \frac{H_e}{\tau_e} C_{PC,INN} Q_{PC}(t) - \frac{2}{\tau_e} y_6(t) - \frac{1}{\tau_e^2} y_5(t) \end{aligned} \quad (10)$$

Connection to PCs, from EINs and IINs:

$$\begin{aligned} \dot{y}_7(t) &= y_8(t) \\ \dot{y}_8(t) &= \frac{H_e}{\tau_e} C_{EIN,PC} Q_{EIN}(t) - \frac{2}{\tau_e} y_8(t) - \frac{1}{\tau_e^2} y_7(t) \\ \dot{y}_9(t) &= y_{10}(t) \\ \dot{y}_{10}(t) &= \frac{H_i}{\tau_i} C_{INN,PC} Q_{INN}(t) - \frac{2}{\tau_i} y_{10}(t) - \frac{1}{\tau_i^2} y_9(t) \\ Q_{EIN}(t) &= \text{Sigm}(y_1(t) + y_3(t)) \\ Q_{INN}(t) &= \text{Sigm}(y_5(t)) \end{aligned} \quad (11)$$

Depolarization of the PCs:

$$y_0(t) = y_7(t) - y_9(t) \quad (12)$$

The parameters are listed in Table 2.1 [22].  $y_1(t)$  and  $y_3(t)$  describe the average evoked membrane potential of EINs.  $y_5(t)$  describe the average evoked membrane potential of INNs.  $y_7(t)$  and  $y_9(t)$  describe the average evoked membrane potential of PCs. Figure 2.10 shows the output of the JRM (10Hz oscillation) with a constant input  $P(t) = 220$  and parameter values in Table 2.1.

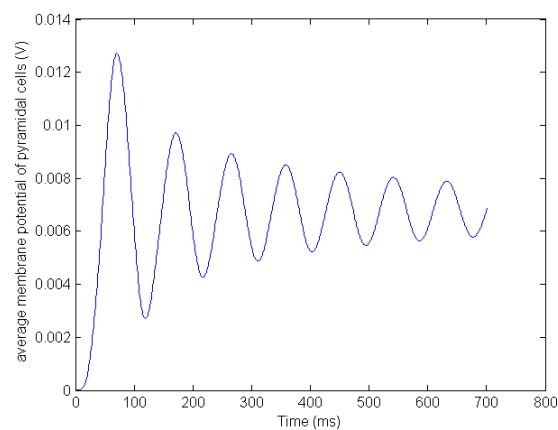


**Figure 2.10 Output of the Jansen and Rit model.** The simulated 10Hz oscillation of Jansen and Rit model using the input  $P(t) = 220$  and parameters in Table 2.1.

**Table 2.1 Parameters of the Jansen and Rit model (1995)**

Parameter	Value	Description
$H_e$	3.25 mV	synaptic gain of EPSP
$H_i$	22 mV	synaptic gain of IPSP
$\tau_e$	10 ms	time constant of EPSP
$\tau_i$	20 ms	time constant of IPSP
$v_0$	6 mV	average firing threshold of a NM
$2e_0$	5 Hz	maximal average firing rate of a NM
$r_0$	$0.56 \text{ mV}^{-1}$	slope of sigmoid function
$C_{EIN,PC}$	108	synaptic connection strength from EIN to PC
$C_{PC,EIN}$	135	synaptic connection strength from PC to EIN
$C_{PC,INN}$	33.25	synaptic connection strength from PC to INN
$C_{INN,PC}$	33.25	synaptic connection strength from INN to PC

EPSP = excitatory postsynaptic potential, IPSP = inhibitory postsynaptic potential,

NM = neural mass, EIN = excitatory interneuron, PC = pyramidal cell, INN = inhibitory interneuron

## 2.1.3 Local cortical circuit model

### 2.1.3.1 Motivation

The purpose of Local cortical circuit model (LCCM) is to refine the very parsimonious NMM of a local cortical circuit proposed by Jansen and Rit [22]. In particular, it is aimed at composing a more realistic laminar dynamics. To keep the balance between biological plausibility and model complexity, the LCCM consists of five NMs, which are distributed in three well-distinguished layers: excitatory interneurons in layer IV, pyramidal cells and inhibitory interneuron populations in supragranular layers II/III as well as in the infragranular layers IV/V.



In this chapter, at first, some important neurons in cortical layers and their prominent synaptic connections are briefly reviewed. The findings heavily rely on the data obtained by paired intracellular and paired whole-cell recordings in cortical slices in animal studies ([12, 16, 58-59, 72, 74] and their citations). These methods allow the properties of the neurons and their synaptic connections to be studied in some detail under experimenter-controlled conditions. However in any one experiment only a small number of connections can be studied. Thus, the results comprise a relatively poor representation of the ultrastructure like a certain brain tissue. At the end of the chapter, based on this evidence, the structure of LCCM is composed and discussed.

### **2.1.3.2 Brief review of some important neurons in cortical layers**

#### ***Inhibitory GABAergic interneurons in all layers***

Inhibitory Interneurons (INNs) can be divided into two major classes [72] by their axon targets: i) those that target proximal regions of pyramidal cells (PCs) (e.g., basket cells, chandelier cells); or ii) those that target pyramidal dendrites (e.g., Martionotti , bitufted, double-bouquet, bipolar and neurogliaform cells).

INNs are distributed throughout cortical layers II-VI (Fig. 2.11). For example, small and medium sized basket cells can be found in all these layers and their axons and dendrites are confined to the layer of their somas. Some large basket cells in layers III and IV have long horizontal axon branches and provide input to discrete regions at the same layer [75]. These larger cells may also have axons vertically descending two or three layers deeper, e.g. from layer III to layer V or from layer IV to layer VI [58]. Large basket cells in layer V can also target both layer V and layer III [72]. Larger bitufted inerneurons including Martionotti cells in layer II-VI have their axons course toward the pial surface and extend horizontally in layer I [76]. Double bouquet cells in layer III and layer IV have their axonal arbours near their origin [77]

and long narrow vertically descending axons that extend until deep layers V/VI [78]. Evidence also shows that, in thalamo-cortical slices, electrical stimulation of the thalamus causes depressed PSPs in layer 4 INNs [79]. On the other hand, in contrast to the synaptic connections of INNs to PCs, very little evidence has been documented for synaptic connections among the INNs.

*Summary for the modeling aspect:* Throughout layers II-IV, each layer contains INNs that intralaminar connect (within the same layer) with the pyramidal cells. Interlaminar (between different layers) inhibition is also possible due to the large basket cells and bitufted cells (Fig. 2.11) .

#### ***Pyramidal cells and spiny stellate cells in layer IV***

It's very difficult to distinguish between spiny stellate cells and PCs in layer IV. The spiny neurons in this layer receive thalamic afferents from thalamus "core" regions and then project to layers III and V [80-86], where they innervate PCs and may, in very rare case, innervate INNs in layer III [58]. They may also receive excitatory inputs from cortico-thalamic PCs in layer VI [87]. Synaptic input from the thalamus seems to be via depressing synapses [88-89]. Synaptic connection from layer IV to layer III is also via depressing synapses [90].

*Summary for the modeling aspect:* One NM could be used to represent both spiny stellate cells and PCs in layer IV, and it should receive excitatory input from thalamic "core" regions (probably depressing) and from PCs in layer VI. It sends excitatory output to PCs in layer III (probably depressing) and layer V (Fig. 2.12) and INNs in the same layer and layer III (Fig. 2.13).

#### ***Pyramidal cells in layer VI***

There are three broad classes of PCs in cortical layer VI [91]: cortico-thalamic pyramidal cells (CTPCs) , cortico-cortical pyramidal cells (CCPCs) as well as claustrum projecting pyramidal cells.

***CTPCs in layer VI.*** There are two kinds of CTPCs in layer VI: the "longer" ones as well as the

"shorter" ones. Both types of CTPCs have a narrow apical dendritic tree and a vertically projecting axonal arbour. However, the axonal arbour and the dendritic tree of the "longer" CTPC extend to layers IV-V, while the apical dendrites and axons of the "shorter" ones end at layer V. Moreover, they have different cortico-thalamic projections. The "longer" CTPCs project to the nucleus reticularis thalami (nRT) and/or to "specific" or "core" thalamic nuclei such as the ventroposterio-medial nuclei (VPM), while the "shorter" ones project to both VPM and "non-specific" thalamic regions, but not the nRT. The CTPCs of primary sensory regions receive input from thalamic "core" areas, while other PCs in layer VI receive much smaller proportions of their input from thalamo-cortical afferents [92-95]. The CTPCs innervate and deliver facilitating input to IINs in layer VI [96] as well as the nuclei in thalamus (e.g.: VPM, nRT, posterior nuclei) [97]. They are also reported to target interneurons in layer IV [79, 98-99].

**CCPCs in layer VI.** There are three kinds of CCPCs in layer VI: short upright PCs, modified and inverted PCs as well as spiny bipolar cells. All CCPCs appear to have similar long and horizontally oriented axonal arbours and their dendritic trees can be found in deep layers VI-V. Their apical dendrites do not project beyond layer V. The dendrites of modified and inverted PCs and spiny bipolar cells may occasionally project into the underlying white matter. The CCPCs innervate the other PCs in layers VI-V and deliver strongly depressing excitatory postsynaptic potentials (EPSPs) [100].

**Clastrum projecting cells.** These pyramidal cells project output to claustrum. They have a very long apical dendrites that may reach layer I but without well-developed dendritic trees in layer IV [101]. They have long and horizontally extended axonal arbours similar to CCPCs in layers VI-V and end there. The claustrum projecting cells, similar to CCPCs, innervate the other PCs in layers VI-V and deliver strongly depressing excitatory postsynaptic potentials (EPSPs) [100].

*Summary for modeling aspect:* In a simplified case, one may assume only one PC population representing all types of PCs in layer VI, which are interconnected with each other. In that case, this PC NM should be considered to receive excitatory input from thalamus ("core" as

well as "non-specific" areas), cortico-cortical connections and PCs in layer V. It sends excitatory output to PCs in layer V (probably depressing), spiny cells in layer IV (Fig. 2.12), INNs in layer IV-VI (probably facilitation) (Fig. 2.13), thalamus (probably facilitation in EPSP) and other cortical areas.

### ***Pyramidal cells in layer V***

There are two major subclasses of PCs in layer V: CTPCs and CCPCs. The large CTPCs extend their long apical dendritic trees to layer II and layer I and project to several subcortical regions, including non-specific thalamus regions, the spinal cord, pons as well as superior colliculus. But the smaller and shorter CCPCs rarely extend beyond layers II/III [102]. PCs in layer V receive short and long range CC projections, but CTPCs receive no inputs from the thalamus [103]. They also receive the descending excitation from PCs in layer III via depressing synapses [58, 104] and may also receive a weak projection from layer IV, too [74]. In contrast, PCs in layer III receive only extremely weak inputs from ascending layer V pyramidal axons [104]. The target of PCs in layer V may be PCs in layer V-VI [74] and INNs in layer V [58] and layer 2/3 [72].

*Summary for modeling aspect:* If it is assumed that only one PC NM is used to represent the PCs in layer V, this PC NM should be considered to receive excitatory input from cortico-cortical connection, PCs in layer VI and PCs in layer III. It sends excitatory output to PCs in layer V (Fig. 2.12), INNs in layer V and layer II/III (Fig. 2.13) and other cortical and subcortical areas.

### ***Pyramidal cells in layer II/III***

PCs in layer III are trans-callosal neurons and are heavily interconnected. They receive inputs from the opposite hemisphere [105]. In contrast with the other callosal CCPCs in layer VI, which target the layers IV and VI, the CCPCs in layer III target all layers [106], both in the same or in the opposite hemisphere [107]. The PCs in layer III also receive input from spiny stellate cells in layer IV. They may also receive thalamo-cortical inputs from primary sensory

thalamus through their basal dendrites in layer IV [92]. The axons of layer III PCs arborize primarily into layers II/III and V. The vertical descending axons may pass through layer IV with little or no ramification there [108]. Both PCs in layers II/III provide outputs to association brain regions. INNs in layer IV [74] and layer V [109] are found to be innervated by layer III pyramidal axons. PCs in layers II/III send descending projection to layer V PCs via depressing synapses [104].

*Summary for modeling aspect:* When it is assumed that only one NM is used to present the PCs in layer II/III, this PC NM should be considered to receive excitatory input from cortico-cortical connections, spiny stellate cells in layer IV. It sends excitatory output to PCs in layer V (Fig. 2.12), INNs in layers II-V (Fig. 2.13) and other cortical areas.

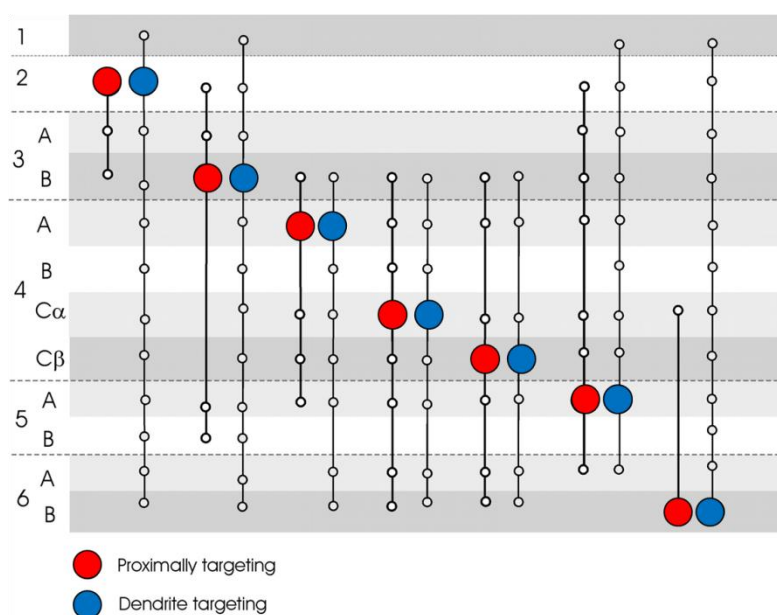


**Figure 2.11 The major interlaminar inhibitory projections.** The major interlaminar inhibitory projections that have been documented in primarily anatomical studies. The numbers on the left indicate the cortical layers. The larger circles indicate the positions of the soma and the smaller ones the positions of the axon terminals. All the inhibitory interneurons also provide intra-laminar and sometimes long horizontal collaterals, e.g. large basket cells in layer III and layer IV, which are not shown here. (Picture from Thomson and Bannister, 2003 [74])

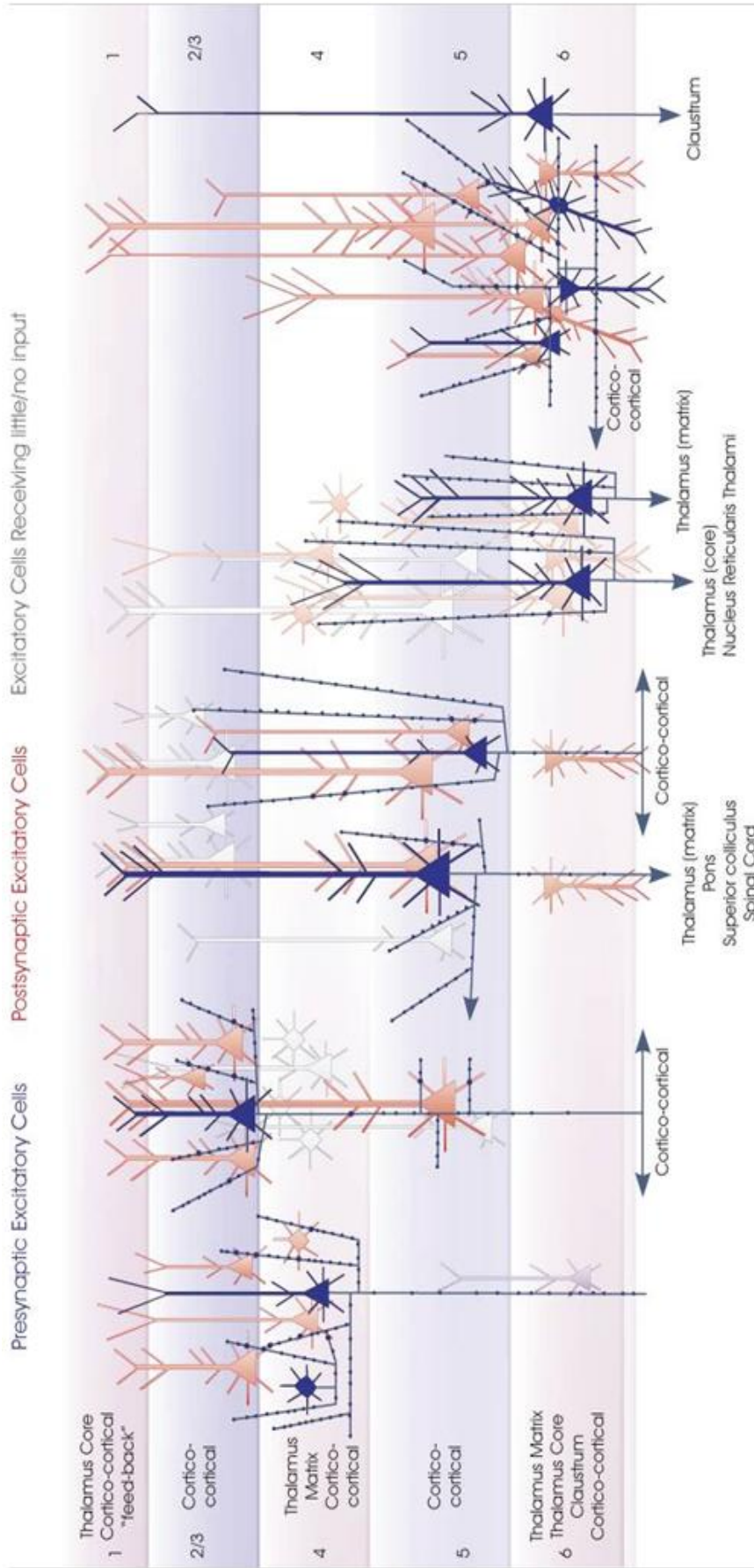


**Figure 2.12 Local circuit excitatory spiny cell targets of pyramidal and spiny stellate cells.** The major longer distance inputs to each cortical layer are indicated to the left. The excitatory postsynaptic targets have been reported with paired intracellular recordings in animal studies. Presynaptic excitatory cells are shown in blue and postsynaptic excitatory cells are shown in red. Purple cells indicate that such an input has been recorded but has not been very well researched. The white cells indicate cells that appear not to be significant targets. (Picture from Thomson and Lamy, 2007 [72]).

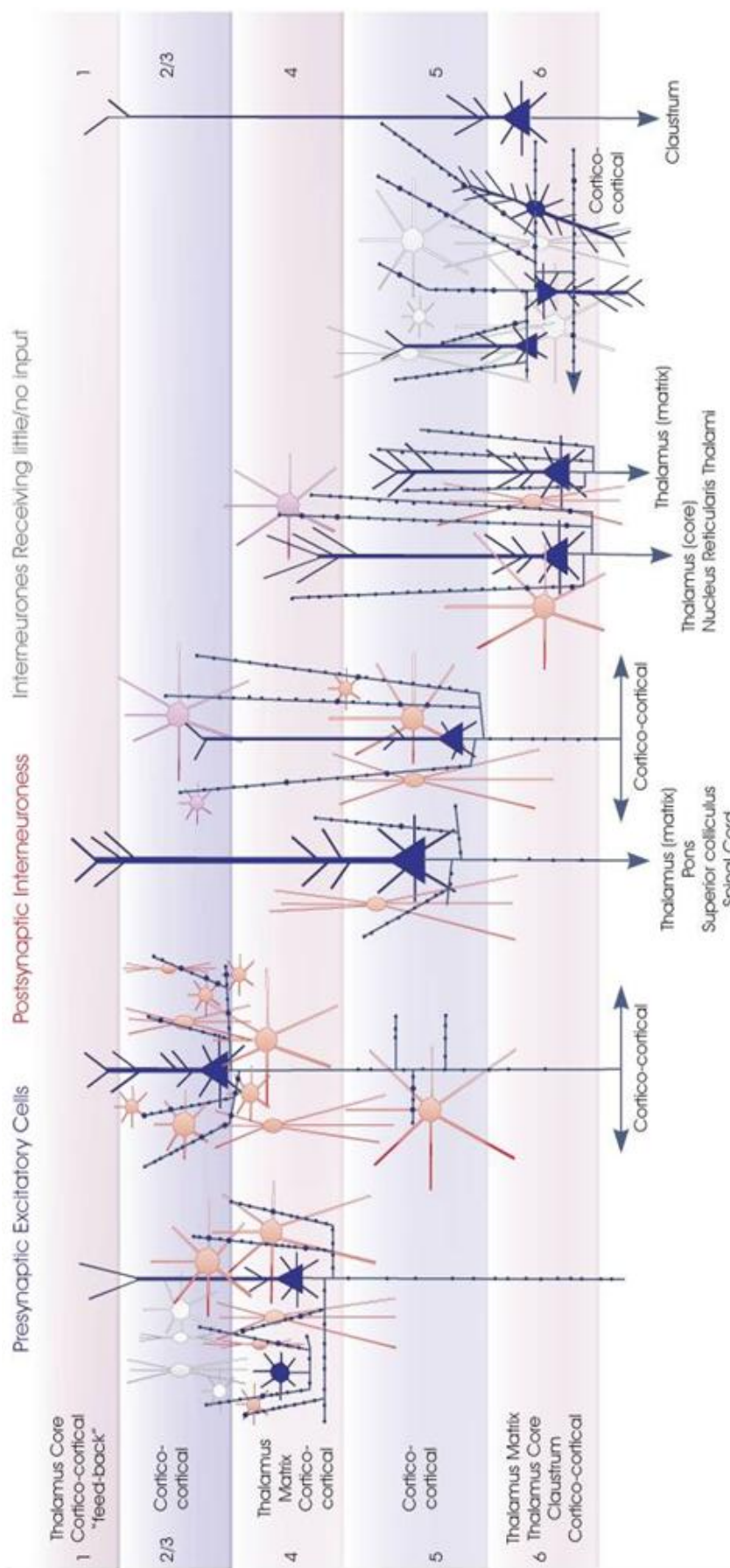


**Figure 2.13 Local circuit excitatory spiny cell targets of inhibitory interneurons.** The major longer distance inputs to each cortical layer are indicated to the left. The excitatory postsynaptic targets have been reported with paired intracellular recording in animal studies. Presynaptic excitatory cells are shown in blue and postsynaptic inhibitory cells are shown in red. The purple cell indicates that such an input has been recorded but has not been very well researched. The white cells indicate cells that appear not to be significant targets. (Picture from Thomson and Lamy, 2007 [72]).

**Table 2.2 Excitatory and inhibitory inputs and targets from each cortical layer [72].**

	The major external input	Spiny cells send excitatory input to	INNs send inhibitory input to	External output
Layers II/III	Cortico-cortical	PCs in layer V; INNs in layer II/III, INNs in layer IV, INNs in layer V	PCs in layer II/III, (spiny cells in layer IV), PCs in layer V, (PCs in layer VI)	Higher cortical areas
layer IV	Thalamus core, Cortico-cortical	PCs in layer II/III, (PCs in layer V); IINs in layer IV, (IINs in layer III)	Spiny cells in layer IV, PCs in layer III, (PCs in layer V), PCs in layer VI	
layer V	Cortico-cortical	PCs in layer VI, (PCs in layer III); IINs in layer V, (IINs in layer II/III)	PCs in layer V, PCs in layer II/ III, (Spiny cells in layer IV), (PCs in layer IV)	Thalamus non-specific, Subcortical areas, Cortico-cortical
layer VI	Thalamus core, Thalamus non-specific, Cortico-cortical	PCs in layer V, spiny cells in layer IV; IINs in layer VI, (IINs in layer IV)	PCs in layer VI, (PCs in layer V), (Spiny cells in layer IV), (PCs in layer II/III)	Thalamus core Thalamus non-specific Cortico-cortical Claustrum

*Note.* PCs = pyramidal cells, IINs = inhibitory interneurons.

### 2.1.3.2 Construction of the local cortical circuit model

One of the functional interpretations of a simple cortical local circuit diagram was provided by Gilbert and Wiesel in 1983 [82, 108], which was based on their intracellular recordings and reconstructions of individual neurons in the cat visual cortex. In its simplest form, the specific thalamic input first arrives at layer IV, which is considered as the first station of the sensory/columnar processing [12]. There, the excitatory spiny stellate cells project to superficial layers, from layer IV to layer III and thence to layer II. The layer III is considered as



the second station of the columnar processing. PCs in layers II/III project vertically further deeper into layer V, the third columnar processing station, and then from layer V to layer VI. The loop is closed by a projection from layer VI back to the input layer IV. The processed information leaves layer III to other cortical regions and/or from deep layers to other cortical and subcortical regions.

Inspired by this description, the local cortical circuit model (LCCM) [20] (Fig. 2.14) comprises 5 NMs in 3 different sublayers: one for EINs in input layer IV, one for sPCs in supragranular layers II/III, one for dPCs in infragranular layers V/VI, as well as two for the supragranular sIINs and infragranular dIINs. The layers II and III are lumped together as the PCs in these layers are interconnected and share large similarities in terms of output connections (Fig. 2.12 & Fig. 2.13). They were usually not separately discussed in previous animal studies [58-59]. Layers V and VI are also lumped together to form the NM of infragranular dPCs in consideration of their interconnection as well as the large similarity of their projections (to the thalamus and other cortical areas, Table 2.3). The IINs in layer IV are lumped into sIINs, while they share the same inputs (EINs/PCs in layer IV as well as PCs in layer III) and outputs (PCs in layer II/III, EINs/PCs in layer IV as well as PCs in layer V/VI) (Table 2.3).

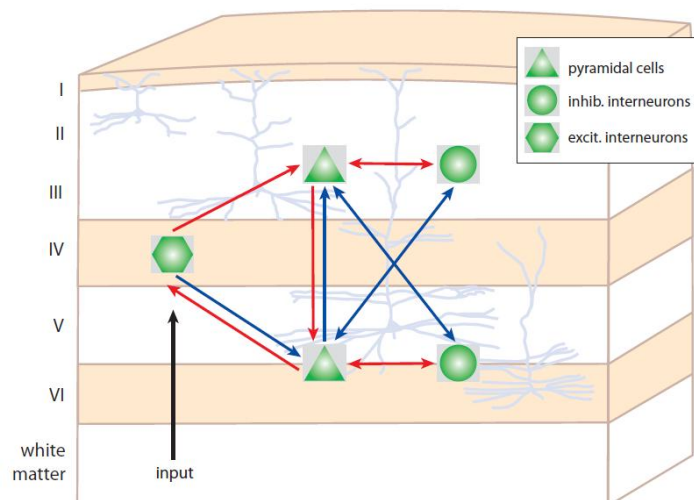


**Figure 2.14 Local cortical circuit model.** The local cortical circuit model is composed of 5 neural masses. Thirteen intrinsic connections are classified into two groups: "certain" connections in red and "uncertain" ones in blue (see text for further explanation). The sensory input from the thalamus is assumed to target excitatory interneurons. The measured evoked EEG/MEG data is simulated by the superposition of the average membrane potentials of both pyramidal cell populations.

The excitatory connections between EINs and PCs were motivated by previous modeling studies [12, 22, 57, 70] as well as animal studies [58-59]. In particular,  $EIN \rightarrow sPC$  was considered as the most prominent connection in a cortical column of the sensory cortex (for reviews, see [110] and references cited therein). However, the interlaminar connectivity between the EINs in layer IV and the sPCs in layers 2/3 has been suggested to be uni-directional in the sensory cortex [58-59]. In terms of information flow, the anatomical existence of the connection  $sPC \rightarrow dPC$  [59, 104, 108] inspired the proposition of a serial signal pathway from layer IV up to layers II/III and then down to layers V/VI [12, 57, 70]. The reciprocal connection  $dPC \rightarrow sPC$  has also been confirmed in animal studies [58, 111-114], but has been found to be much weaker than  $sPC \rightarrow dPC$  [58]. The feedback connection  $dPC \rightarrow EIN$  has been reported as a projection from PCs in layer VI to the input layer IV in visual cortex [108] and an interaction between layer IV spiny stellate cells and layer V PCs in the somatosensory cortex [85]. This connection was not mentioned in animal study [58]. The direct connection from layer IV to infragranular layers ( $EIN \rightarrow dPC$ ) was motivated by reports of a synaptic connection between layer IV spiny stellate neurons and layer 5A PCs in rat barrel cortex [85-86]. As a consequence, in addition to the serial path way ( $EIN \rightarrow sPC \rightarrow dPC$ ), a parallel pathway from layer IV to layers II/III and to layers V/VI [111-112] is proposed here. The connections between IINs and PCs are motivated by previous studies of Thomson and colleagues on rat and cat cortexes [58, 74].

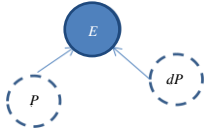
In summary, the LCCM structure could be simply considered as one input layer (EIN) with two output layers (sPC & dPC). The sPC targets of other cortical areas. The dPC targets of cortical and subcortical areas.

Based on our *a priori* knowledge, these 13 intrinsic synaptic connections of LCCM are classified into two groups. The first group of “certain” connections included  $EIN \rightarrow sPC$ ,  $sPC \rightarrow dPC$ , and  $dPC \rightarrow EIN$ . They form the basic laminar circuit of a column with forward ( $EIN \rightarrow sPC$  &  $sPC \rightarrow dPC$ ) and backward ( $dPC \rightarrow EIN$ ) connections, as well as intra-laminar connections between PCs and IINs ( $sPC \rightarrow sIIN$ ,  $sIIN \rightarrow sPC$ ,  $dPC \rightarrow dIIN$  as well as  $dIIN \rightarrow dPC$ ). The second group of “uncertain” connections, in relation to our study perspective,

comprised the key connection for the parallel signal processing  $EIN \rightarrow dPC$  as well as additional cross-laminar connections ( $sPC \rightarrow dIIN$ ,  $dIIN \rightarrow sPC$ ,  $dPC \rightarrow sIIN$  as well as  $sIIN \rightarrow dPC$ ). These "uncertain" connections are given zero prior expectation (see chapter 2.2.5.1).

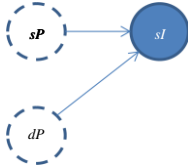
From Equation (3) the ordinary differential equation system of LCCM could be composed as followed:

Connection to EIN ( $E$ ), from dPC ( $dP$ ) and external thalamo-cortical input  $P(t)$  ( $P$ ):



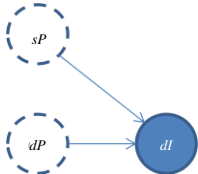
$$\begin{aligned}
 \dot{y}_1(t) &= y_2(t) \\
 \dot{y}_2(t) &= \frac{H_e}{\tau_{e,PE}} W_{PE}(t) C_{PE} P(t) - \frac{2}{\tau_{e,PE}} y_2(t) - \frac{1}{\tau_{e,PE}^2} y_1(t) \\
 \dot{y}_3(t) &= y_4(t) \\
 \dot{y}_4(t) &= \frac{H_e}{\tau_{e,dPE}} W_{dPE}(t) C_{dPE} Q_{dP}(t) - \frac{2}{\tau_{e,dPE}} y_4(t) - \frac{1}{\tau_{e,dPE}^2} y_3(t) \\
 Q_{dP}(t) &= \text{Sigm}(y_{21}(t) + y_{23}(t) - y_{25}(t) - y_{27}(t))
 \end{aligned} \tag{13}$$

Connection to sIIN ( $sI$ ), from sPC ( $sP$ ) and dPC ( $dP$ ):



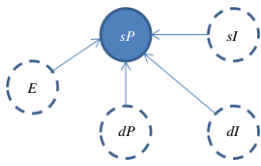
$$\begin{aligned}
 \dot{y}_5(t) &= y_6(t) \\
 \dot{y}_6(t) &= \frac{H_e}{\tau_{e,sPsl}} W_{sPsl}(t) C_{sPsl} Q_{sP}(t) - \frac{2}{\tau_{e,sPsl}} y_6(t) - \frac{1}{\tau_{e,sPsl}^2} y_5(t) \\
 \dot{y}_7(t) &= y_8(t) \\
 \dot{y}_8(t) &= \frac{H_e}{\tau_{e,dPsl}} W_{dPsl}(t) C_{dPsl} Q_{dP}(t) - \frac{2}{\tau_{e,dPsl}} y_8(t) - \frac{1}{\tau_{e,dPsl}^2} y_7(t) \\
 Q_{sP}(t) &= \text{Sigm}(y_{13}(t) + y_{15}(t) - y_{17}(t) - y_{19}(t))
 \end{aligned} \tag{14}$$

Connection to dIIN ( $dI$ ), from dPC ( $dP$ ) and sPC ( $sP$ ):



$$\begin{aligned}
 \dot{y}_9(t) &= y_{10}(t) \\
 \dot{y}_{10}(t) &= \frac{H_e}{\tau_{e,dPdl}} W_{dPdl}(t) C_{dPdl} Q_{dP}(t) - \frac{2}{\tau_{e,dPdl}} y_{10}(t) - \frac{1}{\tau_{e,dPdl}^2} y_9(t) \\
 \dot{y}_{11}(t) &= y_{12}(t) \\
 \dot{y}_{12}(t) &= \frac{H_e}{\tau_{e,sPdl}} W_{sPdl}(t) C_{sPdl} Q_{sP}(t) - \frac{2}{\tau_{e,sPdl}} y_{12}(t) - \frac{1}{\tau_{e,sPdl}^2} y_{11}(t)
 \end{aligned} \tag{15}$$

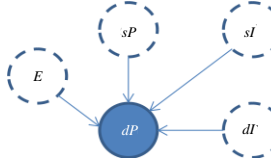
Connection to sPC ( $sP$ ), from EIN ( $E$ ), dPC ( $dP$ ), sIIN ( $sI$ ) and dIIN ( $dI$ ):



$$\begin{aligned}
 \dot{y}_{17}(t) &= y_{18}(t) \\
 \dot{y}_{18}(t) &= \frac{H_i}{\tau_{i,slSP}} W_{slSP}(t) C_{slSP} Q_{sl}(t) - \frac{2}{\tau_{i,slSP}} y_{18}(t) - \frac{1}{\tau_{i,slSP}^2} y_{17}(t) \\
 \dot{y}_{19}(t) &= y_{20}(t) \\
 \dot{y}_{20}(t) &= \frac{H_i}{\tau_{i,dlsP}} W_{dlsP} C_{dlsP} Q_{dl}(t) - \frac{2}{\tau_{i,dlsP}} y_{20}(t) - \frac{1}{\tau_{i,dlsP}^2} y_{19}(t)
 \end{aligned}$$

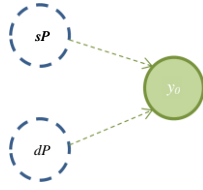
$$\begin{aligned}
Q_E(t) &= \text{Sigm}(y_1(t) + y_3(t)) \\
Q_{sI}(t) &= \text{Sigm}(y_5(t) + y_7(t)) \\
Q_{dI}(t) &= \text{Sigm}(y_9(t) + y_{11}(t))
\end{aligned} \tag{16}$$

Connection to dPC (*dP*), from EIN (*E*), sPC (*sP*), dIIN (*dI*) and sIIN (*sI*):



$$\begin{aligned}
\dot{y}_{21}(t) &= y_{22}(t) \\
\dot{y}_{22}(t) &= \frac{H_e}{\tau_{e,EdP}} W_{EdP}(t) C_{EdP} Q_E(t) - \frac{2}{\tau_{e,EdP}} y_{22}(t) - \frac{1}{\tau_{e,EdP}^2} y_{21}(t) \\
\dot{y}_{23}(t) &= y_{24}(t) \\
\dot{y}_{24}(t) &= \frac{H_e}{\tau_{e,sPdP}} W_{sPdP}(t) C_{sPdP} Q_{sP}(t) - \frac{2}{\tau_{e,sPdP}} y_{24}(t) - \frac{1}{\tau_{e,sPdP}^2} y_{23}(t) \\
\dot{y}_{25}(t) &= y_{26}(t) \\
\dot{y}_{26}(t) &= \frac{H_i}{\tau_{i,dIdP}} W_{dIdP}(t) C_{dIdP} Q_{dI}(t) - \frac{2}{\tau_{i,dIdP}} y_{26}(t) - \frac{1}{\tau_{i,dIdP}^2} y_{25}(t) \\
\dot{y}_{27}(t) &= y_{28}(t) \\
\dot{y}_{28}(t) &= \frac{H_i}{\tau_{i,sIdP}} W_{sIdP}(t) C_{sIdP} Q_{sI}(t) - \frac{2}{\tau_{i,sIdP}} y_{28}(t) - \frac{1}{\tau_{i,sIdP}^2} y_{27}(t)
\end{aligned} \tag{17}$$

Depolarization of pyramid cells:



$$y_0(t) = \alpha_0 \left( \beta_0 (y_{13}(t) + y_{15}(t) - y_{17}(t) - y_{19}(t)) + (y_{21}(t) + y_{23}(t) - y_{25}(t) - y_{27}(t)) \right)$$

(18)

The lowercase indices *e* and *i* indicate the connection types: *excitatory* or *inhibitory*; *E*, *sP*, *dP*, *sI* and *dI* indicates the neural populations EIN, sPC, dPC, sIIN and dIIN, respectively. The uniform synaptic gain parameters  $H_e$  and  $H_i$  are used for the excitatory and inhibitory connections, but the connection time constants  $\tau_{e,xy}$  and  $\tau_{i,xy}$  are individually specific. The pair of indices *xy* indicates the connection from neural population *x* to neural population *y* (EIN, sPC, dPC, sIIN or dIIN). This means that each connection will be uniquely characterized by three parameters: the static coupling strength  $C$ , the dynamic coupling strength  $W$  (see **Chapter 2.1.4**) and the time constant  $\tau$ . The EEG/MEG signal is assumed to be proportional to the superposition of the average membrane potential of neural population sPCs and dPCs. The linear relationship between the measurable dipole moment  $y_0$  [nAm] and the depolarization of the pyramidal cell populations [mV] is described by the parameter  $\alpha_0$

[nAm/mV]. Considering the fact that the dendrites of the pyramidal cells in layer V are much larger than the those in layer II/III, the parameter  $\beta_0$  describes the different contribution of sPCs and dPCs to the measurement. This value is suggested to be about from 1/6 to 1/3 by the simulation study of Murakami and Okada [115].

## 2.1.4 Model of synaptic short-term plasticity

### 2.1.4.1 Motivation

Short-term plasticity [116-119] including short-term habituation and short-term facilitation. It is one of the important and necessary processes for all brain functions. The words "short-term" indicate that the induced change of the synaptic efficacy is rapid and temporary on very short time scales from milliseconds to minutes [117-119]. The modulation of the synaptic efficacy is use-dependent. Without continued presynaptic activity, the synaptic efficacy will quickly return back to its resting state level. In this chapter, first, the short-term adaptation is focused. A phenomenological model of short-term adaptation is composed to describe the depleting and recycling of neurotransmitters depending on average presynaptic firing rates. Then, this model is extended to fit short-term facilitation according to the Abbott model [29, 120].

#### ***Short-term adaptation***

The words "adaptation" or "habituation" refer to the suppression of neural and behavioral responses as a result of repeated stimulation. In this dissertation the term "adaptation" is used to describe the decay of neural responses to repetitive sensory stimuli. It usually follows an exponential decay function and it is reversible if the stimulation changes [121]. This neural mechanism helps us to use our limited brain resources to interact with our environment in an efficient way: repeated irrelevant information will be ignored. Short-term adaptation could be observed through auditory event-related responses using EEG/MEG

[122-123]. The *N100* and *N100m* are the most reliable and prominent peaks observed in the auditory evoked potential (AEP) and auditory evoked field (AEF), respectively, and appear about 100 ms after stimulus onset [124]. Repeated stimulation causes attenuation of the *N100/N100m* amplitude, if the stimuli (e.g. short tones) are presented in rapid succession (e.g. with 500 ms spacing) [123, 125-126]. This amplitude suppression recovers after about 6 to 10 seconds of stimuli free time [127]. This effect is of great interest in clinical neuroscience because impaired adaptation has been observed in patients suffering from schizophrenia [128], Alzheimer's disease [129] and migraines [130]. In cognitive neuroscience, the neuronal adaptation in the auditory cortex is associated with the *mismatch negativity*. This is a negative EEG deflection in response to deviant stimuli and has been explained in terms of short-term adaptation [131-132]. Its MEG counterpart is called the *mismatch field* [126].

The underlying neural mechanisms of short-term adaptation, however, are still not fully understood. On a microscopic level, considerable insight has been gained from animal studies. In the 1970s, based on series of experiments of the aplysia gill-withdrawal reflex, Castellucci and Kandel [133-134] showed that synaptic modification might be a possible basis for adaptation. They found that after adaptation there were fewer synaptic vesicles released per action potential. Furthermore, studies of frog neuromuscular junctions as well as hippocampal synapses in rats suggested that a decrease in transmitter release can be caused by a depletion of the readily releasable pool of vesicles, or a decrease in the release probability of each docked vesicle, or both [118, 135-138].

On a very different level of detail, there are a number of EEG and MEG studies that have shed light on the mechanisms of the adaptation. Garrido and colleagues [48] used human EEG and computational modeling techniques to suggest that the reduction of evoked responses is associated with a reduction in the connectivity within or between the involved cortical areas. In their MEG study, Rosburg and colleagues [125] found that only the first repetition of auditory stimuli resulted in a decrease of the amplitude of the AEF. There was no evidence for any further reduction in responses after the second stimulus. The results

suggested that the suppression of the AEF was probably due to the refractoriness of cell populations involved in the generation of AEF components. Todorovic and colleagues [139] demonstrated in their MEG auditory experiment that the reduction of the AEF was larger for expected repetitions than for unexpected ones and, thereby, provided evidence for a top-down prior expectation modulation of the adaptation.

The question is: How can these different scales of description be linked together? That is, how to construct a comprehensive model of neural circuits that can capture important aspects of the microscopic generative mechanism of short-term adaptation and, at the same time, predict macroscopic effects like N100 or N100m amplitude reduction? Such a comprehensive model would allow for data from different sources, both macroscopic and microscopic, to be integrated and enable testing of hypotheses and quantification of microscopic dynamics for given macroscopic observations [51].

In this approach, the neural adaptation is modeled as a function of the dynamic change in average firing rate. The synaptic connection strength is associated with the neuronal vesicles' release probability. Repetition of stimuli causes insufficient availability of vesicles in releasing pools and reduces the release probability that in turn causes a reduction in synaptic connection strength and hence EEG/MEG signal amplitude. The recovery from adaptation is linked to the process of recycling these vesicles back to the releasing pools, which occurs spontaneously.

## **2.1.4.2. Modeling short-term plasticity in local cortical circuit model**

### ***Principal synaptic transmission mechanisms for the short-term adaptation***

The neurons connect with each other primarily through chemical synapses. A synapse consists of presynaptic and postsynaptic sides [140]. The presynaptic side is located at an axon terminal of the signal origin neuron and the postsynaptic side may be located at

different parts of the target neuron's membrane, depending on the different pre- and post synaptic neuron types such as: dendrites, soma or axon internal segment [141]. A morphologically specialized area at the presynaptic side is called the *active zone*, where the neural vesicles [142], which are containers for neuronal transmitters, are clustered and prepared for release. A presynaptic action potential travels through the axon and arrives at the terminal side. The change of the membrane potential there opens the voltage-gated  $\text{Ca}^{2+}$  channels, thus causing a brief elevation in the intercellular calcium-ions concentration at the active zone, which increases probability of vesicle fusion with the cell membrane and subsequent release of the neuron transmitters into the synaptic cleft between the pre- and postsynaptic sides [143-144]. The neural transmitters bind to the receptors at the postsynaptic side and evoke the postsynaptic potential at the target neuron. The released neural vesicles are recycled rapidly through transporter proteins in neurons or glial cells [145].

There are two anatomically distinguishable neural vesicle populations inside the active zone [118] (Fig. 2.15): docked vesicles form the *releasable pool* and those in waiting form the *reserve pool*. At most, only a very small fraction of the neural vesicles are attached directly to the release sites. They are close to the  $\text{Ca}^{2+}$  channels and are immediately releasable due to high concentration of the local  $\text{Ca}^{2+}$  after the opening of the channel. These vesicles are rapidly replaced by other docked vesicles in the readily releasable pool. However, most vesicles are stored more distant in a large cluster behind the cell plasma membrane and are unable to respond rapidly. These are referred to as the reserve pool and they refill the readily releasable pool after it is depleted. The vesicle release process is called *exocytosis*. The retrieval process of the empty vesicles is called *endocytosis*. The refill process of vesicles from the reserve pool to the releasable pool is called *replenishment*.



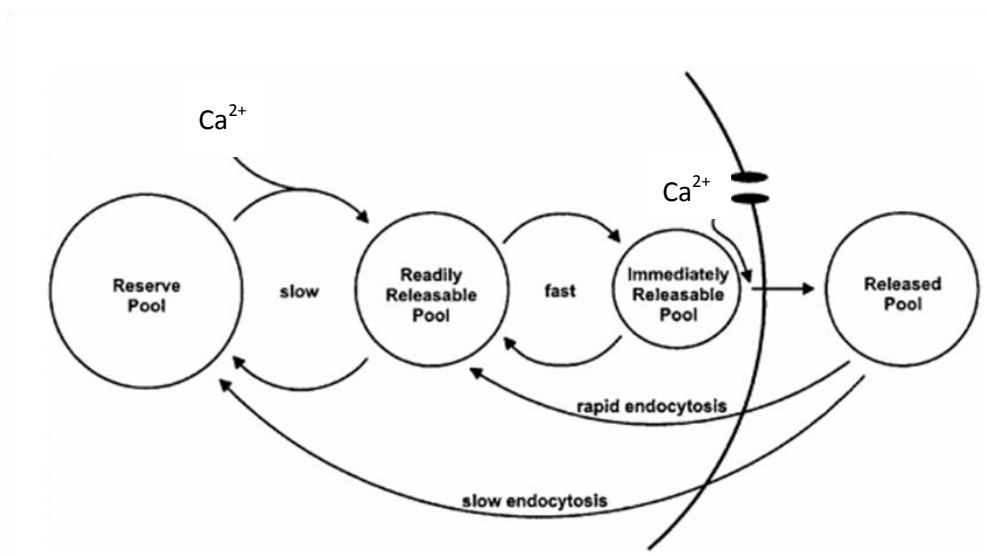


**Figure 2.15 Functional anatomy of an active zone.**

Each active zone contains very a few vesicles attached to release sites docked at the plasma membrane and these vesicles are releasable by the local high concentration of the  $\text{Ca}^{2+}$ . These vesicles are rapidly replaced by other docked vesicles in the readily releasable pool. Most vesicles are stored in a large reserve pool behind the plasma membrane. They refill the readily releasable pool after it is depleted. Released vesicles are recovered by fast and slow endocytic processes into readily releasable and reserve pools. (Picture from Zucker and Regehr, 2002 [118])

A key characteristic of depression in many synapses is use-dependence [133-134]. The releasable neural vesicles under presynaptic action potentials are limited. Thus, their depletion during ongoing activity can lead to suppression of the postsynaptic response. A simple form of a vesicle depletion model was postulated in the studies of neuromuscular junction of rats by Liley and North [135] as well as of frogs by Betz [136]. According to this model, a synaptic connection is assumed to contain a store of releasable vesicles,  $R(t)$  is the occupancy of the release pool and bounded between 0 and 1. Each presynaptic action potential  $\delta(t-t_i)$  releases a fraction of the vesicles  $F$  and this fraction is assumed to be constant. So if each vesicle evokes a synaptic current  $A$ , the evoked postsynaptic response  $AFR(t)$  is related to the occupancy of the current releasable pool. The refill of the readily releasable store is followed by a mono-exponential function with the time constant  $\tau_r$ . A simple first order differential equation can be used to describe this process:

$$\begin{aligned}\frac{dR(t)}{dt} &= -FR(t)\delta(t-t_j) + \frac{1-R(t)}{\tau_r} \\ \frac{dI(t)}{dt} &= AFR(t)\delta(t-t_j) - \frac{I(t)}{\tau_i}\end{aligned}\tag{19}$$

$I(t)$  indicates the evoked postsynaptic current by the total amount of released neurotransmitter  $FR(t)$  in the synaptic cleft,  $\tau_i$  is the time constant of the evoked postsynaptic current  $I(t)$ , which is related to the dynamics of the neural processes at the postsynaptic sides, such as the time constant for the fast AMPA receptor or the slow NMDA receptor. With a global firing rate  $G(t)$ , the time evolution for the postsynaptic current  $I(t)$  can be obtained by averaging Equation (19) over different realizations of the Poisson processes according to different spikes [146]:

$$\begin{aligned}\frac{dR(t)}{dt} &= -FR(t)G(t) + \frac{1-R(t)}{\tau_r} \\ I(t) &= \tau_i AFR(t)G(t)\end{aligned}\tag{20}$$

This model predicts an exponential decay of the postsynaptic response during the stimulation and can fit *in vitro* recordings from some depressing synapses very well at the microscopic level [135, 147].

In spite of its success, the form of the depletion model is inadequate on several points such as the assumption of a constant release fraction, which is actually modulated by the concentration of the calcium-ions [143, 148-149]. The study of the hippocampal synapses by Murthy and colleagues [150] also suggested that different release sides have different initial release probabilities. The increase in release fraction, which is produced by increasing the  $\text{Ca}^{2+}$  concentration, also depends on the initial value.

Some improved depletion models have taken these considerations into account. For example, the model proposed by Tsodyks and Markram [147] extended Equation (20) with an additional first-order differential equation to describe the dynamic of the vesicle release probability. The depression of the postsynaptic response was a resultant effect of both the current amount of readily releasable vesicles  $R(t)$  and the release probability  $F(t)$ :

$$\begin{aligned}
\frac{dR(t)}{dt} &= -F(t)R(t)G(t) + \frac{1-R(t)}{\tau_r} \\
\frac{dF(t)}{dt} &= U(1-F(t))G(t) - \frac{F(t)}{\tau_f} \\
I(t) &= \tau_i AF(t)R(t)G(t)
\end{aligned} \tag{21}$$

where  $U$  is the fraction of release probability incremented by increased  $\text{Ca}^{2+}$  concentration evoked by incoming presynaptic action potentials and  $\tau_r$  is the time constant for the recovery of the release probability.

It is also worth considering the anatomy of synapses, such as in the models composed by Zucker and Regehr [118] as well as Sara and colleagues [138]. Instead of using only two state of the vesicles: in a readily releasable pool or in a reserve pool, a more realistic and biological motivated structure of vesicles pools was used:

$$\begin{aligned}
\frac{dC_0}{dt} &= -\alpha C_0 + \gamma C_2 \\
\frac{dC_1}{dt} &= \alpha C_0 - \beta C_1 \\
\frac{dC_2}{dt} &= \beta C_1 - \gamma C_2
\end{aligned} \tag{22}$$

Equation (22) [138] shows the dynamic mobilization of neural vesicles in three different states: in a readily releasable pool  $C_0$ , mobilizing to the fused state  $C_1$  with rate  $\alpha$  as well as being taken back into the reserve pool  $C_2$  by endocytosis with rate  $\beta$ .  $\gamma$  indicates the rate that the reserve pool refills the readily release pool.

### ***Short-term adaptation model for LCCM***

The adaptation model of the LCCM embodies the simple form of the depletion model of a single neuron in the microscopical level. This kind of model captures the central biophysical processes in synaptic transmission and keeps a relatively simple mathematical form. In the NMM, parameter  $C$  (see Equation (9)-(11)) describes the connection strength between two neural populations. It highlights the anatomical and physiological features such as: the amount of the synaptic connections, the amount of neural transmitter released by presynaptic activity as well as the amount of neural receptors opened at the postsynaptic side. In a very parsimonious view, parameter  $C$  could be considered as a coefficient of the signal transmission between two neural populations, which determinates how effectively

one neural population will be driven by another. According to the preceding outline, it is impossible for connection strength  $C$  to remain a static value over the time, while it is affected by at least one or both pre- and post synaptic neural transmitter transmission processes, which results depression or enhancement of the connection.

Accordingly, the synaptic connection strength in LCCM is assumed to be a dynamic process:

$$C(t) = W_{pre}(t)W_{post}(t)C_0 \quad (23)$$

where  $C_0$  is the initial base value of the connection strength, which could be determined by biological features (e.g., the total amount of synapse connections, the size of the neural vesicle pools, the vesicle initial release probability, the amount of postsynaptic receptors, etc.) that cannot be suddenly changed in millisecond to minutes (the time scale of the short-term plasticity). Therefore, it can be considered as a constant.  $W_{pre}(t)$  as well as  $W_{post}(t)$  indicate the change rates of the  $C_0$  and they are determined by presynaptic neural processes (i.e. releasing neurotransmitter) as well as postsynaptic neural processes (i.e. opening postsynaptic channels). Since the short-term plasticity is only involved at the presynaptic side and will not affect the receptors at the postsynaptic side [133-134, 140],  $W_{post}(t)$  is irrelevant here and is considered to have a constant value of 1 and, for the short-term adaptation,  $W_{pre}(t)$  is bound between 0 and 1.  $W_{pre}(t)$  here is equal to  $W_i$  in Equation (14)–(17) of the LCCM.

It is assumed that the dynamic synaptic efficacy  $W_i$  is proportional to the averaged neural transmitter release probability of the whole presynaptic neural population. It is considered as a result of a series of involved neural processes, such as the increase of the neural vesicle release induced by the changing of the  $Ca^{2+}$  concentration as well as the depletion of the readily releasable pool. While the short-term adaptation is a consequence dominated by the insufficient supply of neural vesicles in the readily releasable pool during the release processes heavily overloaded by the presynaptic activities, in order to keep the balance between the biological plausibility and the model complexity, the dynamic synaptic efficacy  $W_i$  in the LCCM is assumed to take the most parsimonious form of the depletion model (see Equation (20)) :

$$\begin{aligned}\dot{W}(t) &= -n_1 \frac{Q(t)}{Q_{\max}} W(t) + n_2 (1 - W(t)), \text{ for } Q(t) \geq 0 \\ \dot{W}(t) &= n_2 (1 - W(t)), \text{ for } Q(t) < 0\end{aligned}\quad (24)$$

It is assumed that the dynamic synaptic efficacy  $W$  ( $0 < W \leq 1$ ) is determined by the averaged activity of the presynaptic NM (in the NMM the relevant parameter is the averaged firing rate  $Q(t)$ , see Equation (6)), which has the maximal adaptation ratio at  $Q(t) = Q_{\max}$ . The term  $Q(t)/Q_{\max}$  indicates a semi-linear relationship before  $Q(t)$  reach its maximum (Fig. 2.5), which is somehow in agreement with the increment of neural vesicle releasable probability caused by the elevation of the  $\text{Ca}^{2+}$  concentration, which per se is caused by the incoming presynaptic action potentials. However, some evidence points out that the relationship between  $\text{Ca}^{2+}$  concentration and vesicles release probability is not linear but follow a steep power function with an exponent between three or four [148-149, 151]. The parameters  $n_1$  and  $n_2$  indicate the adaptation and recovery rates of the averaged synaptic connection strength between two neural populations. Although  $W$  takes a form similar to the depletion model (Equation (20)),  $n_1$  and  $n_2$  do not directly describe parameters at the microscopical level, such as the time constant of depletion of the readily releasable pool or the time constant of its refill. They describe average activities of a neural population. They may have totally different time scales.  $n_1$  and  $n_2$  should be considered as the indicators for how easily the synaptic connection strength will be suppressed ( $n_1$ ) by presynaptic activity or how strongly it will resist the suppression ( $n_2$ ).

Wehr and Zador [152] reported in their *in vivo* studies that the forward masking of auditory cortex cells was due to synaptic depression rather than inhibitory postsynaptic potentials (IPSPs), and Galarreta and Hestrin [153] showed that excitatory synapses were depressed much more strongly than inhibitory ones. Motivated by these studies, in the LCCM, the adaptation was assumed to only affect the excitatory pathways. Moreover, because the same presynaptic neuron may have different short-term plasticity for connections to different types of target neurons [154], different depression and recovery rates are allowed for each excitatory connection.

### ***Extension of short-term adaptation model to short-term facilitation model***

A previous paired-pulse facilitation study of the synapses from granule to Purkinje cells (in the cerebellum) by Atluri and Regehr [155] as well as the study of the synapses from interneurons to pyramidal cells by Batow and colleges [156] suggested that a potential underlying neural mechanism for facilitation is an increment of residual calcium ions in the presynaptic sides. Increased concentration of the residual  $\text{Ca}^{2+}$  causes rapid facilitation of the voltage-gated calcium channels [144, 157]. As a result, it increases the release probability of the neural vesicles. A simple phenomenological model was developed by Abbott and colleagues [29, 120]:

$$\frac{dP_{rel}(t)}{dt} = \frac{P_0 - P_{rel}(t)}{\tau_p} + f_F(1 - P_{rel}(t))\delta(t - t_j) \quad (25)$$

where the parameter  $P_{rel}$  indicates the fraction of the released neural transmitters on the presynaptic side, which is assumed to be proportional to the synaptic connection strength.  $P_0$  indicates the resting state level. Without the presence of a presynaptic action potential  $\delta(t - t_j)$ , the release fraction  $P_{rel}$  will drop exponentially with time constant  $\tau_p$  back to  $P_0$ . The parameter  $f_F$  controls the degree of the facilitation. The term  $(1 - P_{rel}(t))$  assumes that the maximal release probability is 1.

The model of Tsodyks and Markram [147] (see Equation (21)) is also able to explain the facilitation by assuming that the release probability facilitation counteracts the readily releasable pool depletion [136]. The joint effect of readily releasable vesicles and release probability  $F(t)R(t)$  determines whether facilitation or depression of the postsynaptic current. With a small change rate  $U$  of the release probability  $F(t)$  and a very small recovery time constant  $\tau_r$  of the readily releasable pool  $R(t)$  ( $\tau_r$  should be much smaller than the recovery time constant  $\tau_f$  of the release probability  $F(t)$ ), the dominant effect will be facilitation. In the opposite case, the dominant effect will be adaptation.

The Abbott model [29, 120] (Equation (25)) is adapted to the LCCM to mimic short-term facilitation. It is assumed that there is only one kind of dominant short-term plasticity: adaptation or facilitation during the time period of one hundred milliseconds to about one second of an evoked potential/field of EEG/MEG. According to Equation (25) and Equation

(24), the synaptic short-term facilitation model in LCCM is composed as:

$$\begin{aligned} \dot{W}(t) &= n_1 \frac{Q(t)}{Q_{\max}} (2 - W(t)) + n_2 (1 - W(t)), \text{ for } Q(t) \geq 0 \\ \dot{W}(t) &= n_2 (1 - W(t)), \text{ for } Q(t) < 0 \end{aligned} \quad (26)$$

where the synaptic efficacy  $W$  ( $1 \leq W < 2$ ) of facilitation is symmetric to the adaptation  $W$  ( $0 < W \leq 1$ ). Parameter  $n_1$  indicates the rate of the increase of the synaptic connection under the averaged presynaptic firing rate  $Q(t)/Q_{\max}$ , Parameter  $n_2$  indicates the recovery rate.

## 2.2 Bayesian inversion for parameter estimation

### 2.2.1 Motivation

In spite of its parsimony, the local cortical circuits model (LCCM) still embodies some important properties of the neural dynamics such as detailed distribution of neural populations among cortical layers, rich available signal transmission pathways among the populations as well as short-term plasticity of the signal transmission. These properties should ensure enough space for the researchers to compose their hypotheses and test them against the experiment's observations, e.g., the EEG/MEG data. Transferring biophysical theories into detailed model parameter sets for predicting observations is called solving the "*forward modeling problem*". The reciprocal situation, where observations are used to estimate the values of model parameters corresponds to the "*inverse modeling problem*".

In this dissertation, the MEG data were used to inference the parameters of those neural mass models, i.e. the LCCM and the JRM. It is an inverse problem. However, the forward modeling has an unique solution, because of the causality principle, the inverse modeling may have many solutions: when different models predict similar observations. This problem then turns out to be: which model best "fits" the observations. A specific mathematical method is introduced here to solve this problem.

The term *dynamic causal modeling* (DCM) was first proposed by Friston [23, 158] in his work studying the effective connectivity between different brain areas using fMRI data. Later this

framework was adapted by David and colleagues [45] as well as Kiebel and colleagues [67] to EEG/MEG data.

In principle, the DCM for EEG / MEG consists of three parts:

- *Forward modeling*, using a generative model to predict the EEG/MEG observations.
- *Inverse modeling*, updating the model parameters via finding the maximum of the Bayesian *a-posteriori* distribution.
- *Model comparison*, if more than two generative models are used, the "best" model to explain the experimental observation is chosen via highest model evidence.

In the forward modeling, a predicted EEG/MEG signal is generated by the selected neural mass model, which is composed under some hypotheses. In the inverse modeling, the generated data is then compared with the collected EEG/MEG measurements. The difference between them is described by the likelihood-function. According to the Bayesian theory (see **chapter 2.2.3.1**), the *a-posteriori* distribution of the model parameters is proportional to the product of the *likelihood* function and the *a-priori* distribution (Fig. 2.16). The *a-priori* distribution of the parameters reflects prior knowledge and confidence about the hypotheses. The maximum of the *a-posteriori* distribution (i.e. in this work, it is assumed that the *a-posteriori* distribution is a normal distribution) is the optimized parameter set and can be obtained via the Expectation-Maximization-Algorithm iteratively (see **chapter 2.2.3.2**). In the model comparison, different models are compared with each other via their model evidences [62-63] in order to determine the "best" model that can explain the observed data.

In this chapter, first the basic framework of the DCM will be introduced in the following order: (1) forward modeling, (2) inverse modeling using Bayesian inversion and (3) model selection. They include the introduction of the Bayesian theorem, computation of the *a-posteriori* distribution (based on the generative model, the EEG/MEG measurement and the prior), the EM-algorithm for optimization and the calculation of the model comparison. The introduction of Bayesian inversion (computation of the *a-posteriori* distribution and the EM-algorithm) is cited from the previous works of Friston and colleagues [23, 158]. The



introduction of model selection is cited from previous work of Penny and colleagues [62]. After that, the author suggests some new methods to improve the current DCM framework including an improved optimization algorithm using the Levenberg - Marquardt algorithm [159-160] and a new technique for the formulation of the priors, which allows for accommodating larger portions of the model space within a single model that can be specified by fitting to the data.

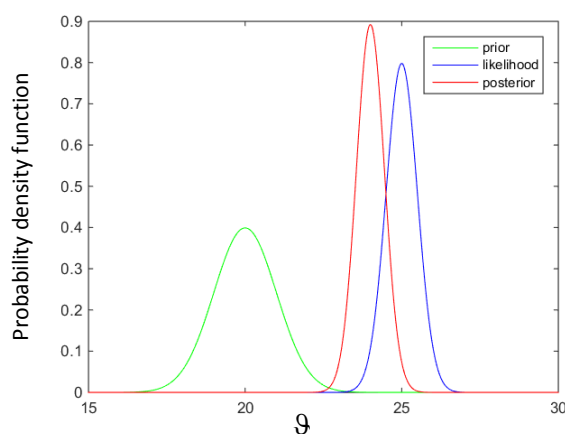


**Figure 2.16 Illustration of probability density functions of normal distributed prior, likelihood as well as posterior.** The assumed mean and variance of the prior distribution are 20 and 1. The assumed mean and variance of the likelihood function are 25 and 0.25. Thus, the estimated mean and variance of the posterior distribution are 24 and 0.2.

## 2.2.2 Forward modeling

Depending on different research purposes as well as different detail levels of the models, the forward modeling is usually composed of several concatenated blocks. For example, first, a measurable neural activity can be modeled by a dynamic model, e.g., in this study, the post synaptic potential (PSP) of the pyramidal cells is simulated by the NMM. The NMM describes the average PSP of the pyramidal cells population for each generator or source. Based on the postsynaptic transmembrane currents as well as the geometric (e.g., dendrite length as well as radius) and physical properties of the dendrites (e.g., membrane conductivity, membrane resistance, intracellular resistance), the PSP can be converted into a dipole model that regards the dendrite as a coaxial cable and uses the cable equation to determine the primary

strom for the current dipole. The dipole model is applied to describe the cause of the electromagnetic field, which is detectable by the EEG/MEG. In this dissertation, the output of the neural mass model is simply assumed to be proportional to the source activity generated by the dipole model. The source activity is obtained by the inverse source estimation method such as equivalent dipole approach or source image approach [24] (Fig. 2.17) via appropriate software solutions, i.e. Brainstorm [161]. Finally, the propagation of the electromagnetic field through the head is described by a volume conductivity model/head model (lead field) [162], which describes the geometry and the tissue conductivity of the head.

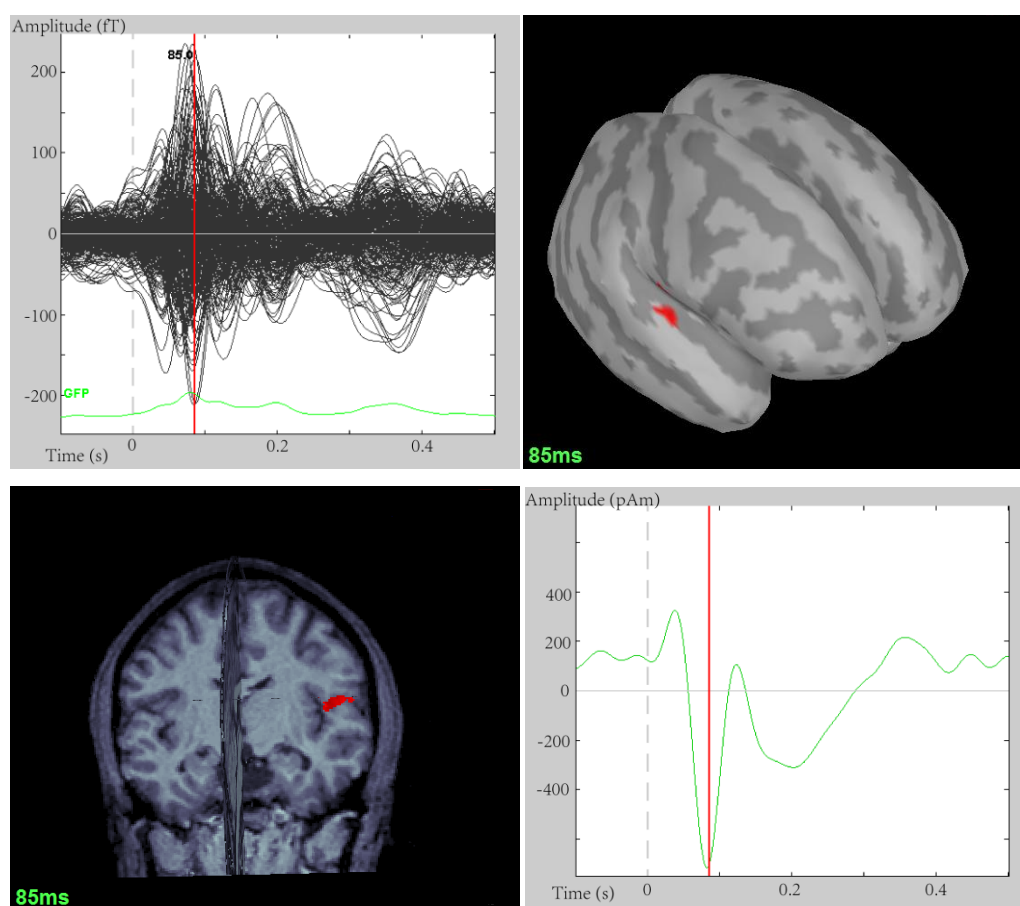


**Figure 2.17 Estimation of source location and activity via image approach.** The figure on the top left shows the recorded MEG signal in sensor space. The figure on the top right and bottom left show the estimated (sLORETA [163-164]) most active area of the cortex 85ms (N100m) later after a tone stimulation in both ears. As expected, it was localized in the right hemisphere Heschl's gyrus (on the top of the superior temporal gyrus). The figure on the bottom right shows the average average (over about  $5.73 \text{ cm}^2$ ) source activity of Heschl's gyrus and it is assumed to be proportional proportional to the output of the neural mass model.

The mathematical description of the simplified forward modeling (the relationship between the observation and the simulation) is:

$$\mathbf{Y}_{N \times T} = \mathbf{H}(\boldsymbol{\theta}) + \mathbf{E} \quad (27)$$

where  $\mathbf{Y}$  is the estimated source activity with  $N$  sources (or  $N$  experimental conditions for the same source) and  $T$  is the number of time samples.  $\mathbf{H}(\boldsymbol{\theta})$  is the  $N \times T$  output of the NMM.  $\boldsymbol{\theta}$  is the  $P \times 1$  parameter vector for the NMM.  $\mathbf{E}$  is the noise/error matrix with the dimension  $N \times T$ .

In order to compute the *likelihood* function later (see **chapter 2.2.3.1**), the estimated source activity  $\mathbf{Y}$  is further converted from a  $N \times T$  matrix into a  $NT \times 1$  vector  $\mathbf{y}$ . Each column of the matrix  $\mathbf{Y}$  is successively written into the vector  $\mathbf{y}$ . The other terms in Equation (27) are also treated accordingly.

$$\begin{aligned} \mathbf{y}_{NT \times 1} &= \text{vec}(\mathbf{Y}^T) = \text{vec}(\mathbf{H}(\boldsymbol{\theta})^T) + \text{vec}(\mathbf{E}^T) \\ \mathbf{y} &= \mathbf{h}(\boldsymbol{\theta}) + \boldsymbol{\varepsilon} \end{aligned} \quad (28)$$

It is assumed that the noise  $\boldsymbol{\varepsilon}$  follows the zero mean normal distribution and the  $NT \times NT$  covariance matrix  $\mathbf{C}_{\boldsymbol{\varepsilon}}$  is assumed to be given the following form:

$$\mathbf{C}_{\boldsymbol{\varepsilon}} = \text{diag}(\exp(\boldsymbol{\lambda}_{N \times 1})) \otimes \mathbf{V}_{T \times T} = \begin{bmatrix} \exp(\lambda_1) \mathbf{V} & 0 & 0 & 0 \\ 0 & \exp(\lambda_2) \mathbf{V} & \cdots & 0 \\ \vdots & \vdots & \ddots & \vdots \\ 0 & 0 & \cdots & \exp(\lambda_N) \mathbf{V} \end{bmatrix} \quad (29)$$

The noise covariance matrix  $\mathbf{C}_{\boldsymbol{\varepsilon}}$  is computed with the Kronecker product  $\otimes$  between hyperparameter vector  $\boldsymbol{\lambda}$  and temporal autocorrelation matrix  $\mathbf{V}$  [60, 165].  $\boldsymbol{\lambda}$  is an unknown  $N \times 1$  vector of the source specific variables, which represent the noise/error level between the estimated sources and the NMM outputs. This vector is estimated iteratively in the M-step in the EM algorithm (see **chapter 2.2.3.2**) and can be used to represent the goodness of the fit (GoF). The exponential operator  $\exp(\cdot)$  ensures the positive value of the covariance matrix. The matrix  $\mathbf{V}$  represents the  $T \times T$  autocorrelation of the noise processes between the  $N$  sources. Under the assumption that the noise process of each source is independent,  $\mathbf{V}$  is simply assumed to be an identity matrix.

Assuming that  $\mathbf{Q}_i$  is the derivative of  $\mathbf{C}_{\boldsymbol{\varepsilon}}$  at  $\lambda_i$ , the noise covariance matrix  $\mathbf{C}_{\boldsymbol{\varepsilon}}$  is reformulated as:

$$\begin{aligned}
Q_i &= \frac{\partial C_\varepsilon}{\partial \lambda_i} \\
C_\varepsilon &= \sum_{i=1}^N \exp(\lambda_i) Q_i
\end{aligned} \tag{30}$$

## 2.2.3 Bayesian inverse estimation

### 2.2.3.1 Bayesian theorem

In Bayesian inverse estimation, the optimal parameters of the dynamic model will be inferred using both observations and *a-priori* knowledge on the model (i.e., the expectation of the model structure and the model parameters). Under the Bayesian aspect, the *a-posteriori* information can be described by a probability  $P(\boldsymbol{\theta} | \mathbf{y})$ , which means a parameter set with the maximal occurring probability regarding to the observed data  $y$ .

According to the Bayesian Theorem (Equation (31)), the *a-posterior* probability is proportional to the product of the *Likelihood*  $P(\mathbf{y}|\boldsymbol{\theta})$  and the *a-priori* probability  $P(\boldsymbol{\theta})$  of the parameter  $\boldsymbol{\theta}$  :

$$P(\boldsymbol{\theta} | \mathbf{y}) = \frac{P(\mathbf{y} | \boldsymbol{\theta}) P(\boldsymbol{\theta})}{P(\mathbf{y})} \tag{31}$$

The *Likelihood*  $P(\mathbf{y}|\boldsymbol{\theta})$  describes the probability of the observation  $y$  generated through parameter  $\boldsymbol{\theta}$ . It can also be regarded as the similarity between the model output and the measurement. The *a-priori* probability  $P(\boldsymbol{\theta})$  represents the previous expectation of the model parameter  $\boldsymbol{\theta}$  according to prior knowledge.  $P(\mathbf{y})$  is the occurring probability of the measured data  $y$ .

The product rules of probability, as well as Bayesian theorem, applies equally to the case of probability densities (Equation (32)). Its validity can be seen by dividing each real variable into intervals of width  $\Delta$ , taking the limit  $\Delta \rightarrow 0$  and considering the discrete probability distribution over these intervals [166].

$$p(\boldsymbol{\theta} | \mathbf{y}) = \frac{p(\mathbf{y} | \boldsymbol{\theta}) p(\boldsymbol{\theta})}{p(\mathbf{y})} \tag{32}$$

Under the assumption that  $p(\mathbf{y})$  is a constant, then the *a-posteriori* distribution  $p(\boldsymbol{\theta}|\mathbf{y})$  is

proportional to the product of the *Likelihood* function  $p(\mathbf{y}|\boldsymbol{\theta})$  and the *a-priori* distribution  $p(\boldsymbol{\theta})$  of the model parameter:

$$p(\boldsymbol{\theta} | \mathbf{y}) \propto p(\mathbf{y} | \boldsymbol{\theta}) p(\boldsymbol{\theta}) \quad (33)$$

Now the search of the optimal parameter set for the maximum of the *a-posteriori* probability  $P(\boldsymbol{\theta}|\mathbf{y})$  is equivalent to the search of a parameter set for the maximum of the *a-posteriori* distribution  $p(\boldsymbol{\theta}|\mathbf{y})$ :

$$\boldsymbol{\theta} = \arg_{\boldsymbol{\theta}}(\max(p(\boldsymbol{\theta} | \mathbf{y}))) \quad (34)$$

In this dissertation, both the *likelihood* function and the *a-priori* distribution of the parameter are assumed to be Gaussian. According to the definition of the multi variable normal distribution:  $p(\mathbf{x}) \sim N(\boldsymbol{\mu}, \mathbf{C})$ , the  $n$  dimension vector  $\mathbf{x}$  with the expectation vector  $\boldsymbol{\mu}$  as well as the covariance  $\mathbf{C}$  can be expressed as:

$$p(\mathbf{x}) = (2\pi)^{-\frac{n}{2}} |\mathbf{C}|^{-\frac{1}{2}} \exp\left\{-\frac{1}{2}(\mathbf{x}-\boldsymbol{\mu})^T \mathbf{C}^{-1}(\mathbf{x}-\boldsymbol{\mu})\right\} \quad (35)$$

The *a-priori* distribution of the parameters is defined as:  $p(\boldsymbol{\theta}) \sim N(\boldsymbol{\eta}_{\boldsymbol{\theta}}, \mathbf{C}_{\boldsymbol{\theta}})$  with the expectation vector  $\boldsymbol{\eta}_{\boldsymbol{\theta}}$  as well as the covariance  $\mathbf{C}_{\boldsymbol{\theta}}$ :

$$p(\boldsymbol{\theta}) \propto \exp\left\{-\frac{1}{2}(\boldsymbol{\theta}-\boldsymbol{\eta}_{\boldsymbol{\theta}})^T \mathbf{C}_{\boldsymbol{\theta}}^{-1}(\boldsymbol{\theta}-\boldsymbol{\eta}_{\boldsymbol{\theta}})\right\} \quad (36)$$

According to Equation (28), the *likelihood* function  $p(\mathbf{y}|\boldsymbol{\theta}) \sim N(h(\boldsymbol{\theta}), \mathbf{C}_{\boldsymbol{\varepsilon}})$  can be obtained through a Taylor series approximation of the non-linear system  $h(\boldsymbol{\theta})$ :

$$\begin{aligned} h(\boldsymbol{\theta}) &\approx h(\boldsymbol{\eta}_{\boldsymbol{\theta}|\mathbf{y}}) + \mathbf{J} \cdot (\boldsymbol{\theta} - \boldsymbol{\eta}_{\boldsymbol{\theta}|\mathbf{y}}) \\ \mathbf{J} &= \left. \frac{\partial h(\boldsymbol{\theta})}{\partial \boldsymbol{\theta}} \right|_{\boldsymbol{\theta}=\boldsymbol{\eta}_{\boldsymbol{\theta}|\mathbf{y}}} \end{aligned} \quad (37)$$

$$\mathbf{r} = \mathbf{y} - h(\boldsymbol{\eta}_{\boldsymbol{\theta}|\mathbf{y}}) \approx \mathbf{J} \cdot (\boldsymbol{\theta} - \boldsymbol{\eta}_{\boldsymbol{\theta}|\mathbf{y}}) + \boldsymbol{\varepsilon} \quad (38)$$

$$p(\mathbf{y} | \boldsymbol{\theta}) \propto \exp\left\{-\frac{1}{2}(\mathbf{r} - \mathbf{J} \cdot (\boldsymbol{\theta} - \boldsymbol{\eta}_{\boldsymbol{\theta}|\mathbf{y}}))^T \mathbf{C}_{\boldsymbol{\varepsilon}}^{-1}(\mathbf{r} - \mathbf{J} \cdot (\boldsymbol{\theta} - \boldsymbol{\eta}_{\boldsymbol{\theta}|\mathbf{y}}))\right\} \quad (39)$$

So according to Equation (33), Equation (35) and Equation (37), the *a-posteriori* distribution  $p(\boldsymbol{\theta}|\mathbf{y}) \sim N(\boldsymbol{\eta}_{\boldsymbol{\theta}|\mathbf{y}}, \mathbf{C}_{\boldsymbol{\theta}|\mathbf{y}})$  can be expressed as:

$$\begin{aligned} p(\boldsymbol{\theta} | \mathbf{y}) &\propto \exp\left\{-\frac{1}{2}(\mathbf{r} - \mathbf{J} \cdot (\boldsymbol{\theta} - \boldsymbol{\eta}_{\boldsymbol{\theta}|\mathbf{y}}))^T \mathbf{C}_{\boldsymbol{\varepsilon}}^{-1}(\mathbf{r} - \mathbf{J} \cdot (\boldsymbol{\theta} - \boldsymbol{\eta}_{\boldsymbol{\theta}|\mathbf{y}}))\right\} \\ &\quad \cdot \exp\left\{-\frac{1}{2}(\boldsymbol{\theta} - \boldsymbol{\eta}_{\boldsymbol{\theta}})^T \mathbf{C}_{\boldsymbol{\theta}}^{-1}(\boldsymbol{\theta} - \boldsymbol{\eta}_{\boldsymbol{\theta}})\right\} \end{aligned} \quad (40)$$

### 2.2.3.2 Expectation-Maximization algorithm

The Expectation-Maximization algorithm (EM) [167] is an iterative parameter estimation method. This method was used by Fristion [23] in his work on *dynamic causal modeling* (DCM) to solve the *maximum a-posteriori problem* (MAP) of the Bayesian *a-posteriori* distribution (Equation (40)).

Generally, there are two estimation steps in the EM-algorithm: The expectation step (E-step) and the maximization step (M-step). In the E-step, the conditional mean  $\boldsymbol{\eta}_{\boldsymbol{\theta}|\mathbf{y}}$  as well as the conditional covariance  $\mathbf{C}_{\boldsymbol{\theta}|\mathbf{y}}$  of the *a-posteriori* distribution  $p(\boldsymbol{\theta}|\mathbf{y})$  will be estimated. These two parameters will be then be considered as a constant and will be further used in the following M-step. In the M-step, the hyperparameter  $\boldsymbol{\lambda}$  (see Equation (29)) will be estimated through the maximization of the *likelihood* function  $p(\mathbf{y}|\boldsymbol{\lambda})$  to acquire the noise/error covariance  $\mathbf{C}_{\boldsymbol{\varepsilon}}$ , which will be used in the next E-step to estimate the new conditional mean

$\boldsymbol{\eta}_{\boldsymbol{\theta}|\mathbf{y}}$  :

$$\text{E-step: } \arg_{\boldsymbol{\theta}}(\max(p(\boldsymbol{\theta}|\mathbf{y}))) \rightarrow \boldsymbol{\eta}_{\boldsymbol{\theta}|\mathbf{y}}$$

$$\text{M-step: } \arg_{\boldsymbol{\lambda}}(\max(p(\mathbf{y}|\boldsymbol{\lambda}))) \rightarrow \boldsymbol{\lambda}$$

According to the previous work of Fristion [23], the EM-algorithm in the Bayesian inversion framework can be computed as followed:

#### **The E-step**

As the *a-posteriori* distribution  $p(\boldsymbol{\theta}|\mathbf{y})$  is defined to be normal distributed here, so in the E-step, estimation of the conditional mean  $\boldsymbol{\eta}_{\boldsymbol{\theta}|\mathbf{y}}$  is equal to searching for the maximum of the *a-posteriori* distribution. To solve this optimization problem, a simple Newton's Method is applied.

It is assumed that there is a function  $f(x)$ . It is differentiable with  $x$  and has a maximum. Then the maximum can be found at  $x$  where  $f'(x) = 0$ . Newton's Method can find the solution for  $f'(x) = 0$  iteratively with the first and second derivative at  $x^i$  :

$$x^{i+1} = x^i - \frac{f'(x^i)}{f''(x^i)} \quad (41)$$

$x^i$  is the  $i$ -th step estimated value.

According to the Newton's Method (Equation 41), the first and second derivatives of the  $a$ -posteriori distribution  $p(\boldsymbol{\theta}|\mathbf{y})$  should be calculated. In order to simplify the calculation, the  $a$ -posteriori distribution in Equation (39) is converted to a *Log a-posteriori* distribution through the natural logarithm operator  $\ln(\cdot)$ . This way the multiplication of the *likelihood* function and the  $a$ -priori distribution can be replaced by the addition of the *log likelihood* function and the *log a-priori* distribution:

$$l = \ln(p(\boldsymbol{\theta}|\mathbf{y})) \propto \left( -\frac{1}{2}(\mathbf{r} - \mathbf{J} \cdot (\boldsymbol{\theta} - \boldsymbol{\eta}_{\theta|\mathbf{y}}))^T \mathbf{C}_\varepsilon^{-1} (\mathbf{r} - \mathbf{J} \cdot (\boldsymbol{\theta} - \boldsymbol{\eta}_{\theta|\mathbf{y}})) \right) + \left( -\frac{1}{2}(\boldsymbol{\theta} - \boldsymbol{\eta}_\theta)^T \mathbf{C}_\theta^{-1} (\boldsymbol{\theta} - \boldsymbol{\eta}_\theta) \right) \quad (42)$$

While the natural logarithm is a monotonic function, the parameter vector  $\boldsymbol{\eta}_{\theta|\mathbf{y}}$  for the maximum of the  $a$ -posteriori distribution  $p(\boldsymbol{\theta}|\mathbf{y})$  is the same as the one for the maximum of the *Log a-posteriori* distribution  $\ln(p(\boldsymbol{\theta}|\mathbf{y}))$ .

If  $\boldsymbol{\eta}_{\theta|\mathbf{y}}^i$  is the  $i$ -th estimated parameter of the maximum of the *log a-posteriori* distribution  $l = \ln(p(\boldsymbol{\theta}|\mathbf{y}))$ , Newton's Method (Equation (41)), gives:

$$\boldsymbol{\eta}_{\theta|\mathbf{y}}^{i+1} = \boldsymbol{\eta}_{\theta|\mathbf{y}}^i + \left( -\frac{\partial^2 l(\boldsymbol{\eta}_{\theta|\mathbf{y}}^i)}{\partial \boldsymbol{\theta} \partial \boldsymbol{\theta}^T} \right)^{-1} \frac{\partial l(\boldsymbol{\eta}_{\theta|\mathbf{y}}^i)}{\partial \boldsymbol{\theta}} \quad (43)$$

According to Equation (42), the first derivative at  $\boldsymbol{\eta}_{\theta|\mathbf{y}}^i$  is given by:

$$\begin{aligned} \frac{\partial l}{\partial \boldsymbol{\theta}} &= \mathbf{J}^T \mathbf{C}_\varepsilon^{-1} (\mathbf{r} - \mathbf{J} \cdot (\boldsymbol{\theta} - \boldsymbol{\eta}_{\theta|\mathbf{y}}^i)) + \mathbf{C}_\theta^{-1} (\boldsymbol{\eta}_\theta - \boldsymbol{\theta}) \\ \frac{\partial l(\boldsymbol{\eta}_{\theta|\mathbf{y}}^i)}{\partial \boldsymbol{\theta}} &= \mathbf{J}^T \mathbf{C}_\varepsilon^{-1} \mathbf{r} + \mathbf{C}_\theta^{-1} (\boldsymbol{\eta}_\theta - \boldsymbol{\eta}_{\theta|\mathbf{y}}^i) \end{aligned} \quad (44)$$

and the second derivative at  $\boldsymbol{\eta}_{\theta|\mathbf{y}}^i$  is:

$$-\frac{\partial^2 l(\boldsymbol{\eta}_{\theta|\mathbf{y}}^i)}{\partial \boldsymbol{\theta} \partial \boldsymbol{\theta}^T} = \mathbf{J}^T \mathbf{C}_\varepsilon^{-1} \mathbf{J} + \mathbf{C}_\theta^{-1} \quad (45)$$

Substituting Equation (44) and Equation (45) into Equation (43), the iterative search schema for the conditional mean  $\boldsymbol{\eta}_{\theta|\mathbf{y}}$  is given by:

$$\boldsymbol{\eta}_{\theta|\mathbf{y}}^{i+1} = \boldsymbol{\eta}_{\theta|\mathbf{y}}^i + \left( \mathbf{J}^T \mathbf{C}_\varepsilon^{-1} \mathbf{J} + \mathbf{C}_\theta^{-1} \right)^{-1} \left( \mathbf{J}^T \mathbf{C}_\varepsilon^{-1} \mathbf{r} + \mathbf{C}_\theta^{-1} (\boldsymbol{\eta}_\theta - \boldsymbol{\eta}_{\theta|\mathbf{y}}^i) \right) \quad (46)$$

The term  $\mathbf{J}^T \mathbf{C}_\varepsilon^{-1} \mathbf{r}$  ensures a minimization of the residuals  $\boldsymbol{\varepsilon}$ . The term  $\mathbf{C}_\theta^{-1} (\boldsymbol{\eta}_\theta - \boldsymbol{\eta}_{\theta|\mathbf{y}}^i)$

ensures a minimization of the difference between the *a-priori* expectation  $\boldsymbol{\eta}_0$  and the *a-posteriori* estimation. The relative strength of these two terms is moderated by the precisions of the measurements as well as the *a-priori* information. If the error covariance matrix is smaller than the variability of the prior, more weight is given to minimizing the residuals and vice versa [23].

The conditional covariance  $\mathbf{C}_{\theta|y}$  for the normal distributed *a-posteriori* distribution  $p(\boldsymbol{\theta}|y)$  can be estimated with the help of the second derivative of  $l$ . It is assumed that for the normal distributed functions  $g(\mathbf{a})$  and  $\ln(g(\mathbf{a}))$  exists a maximum at  $\hat{\mathbf{a}}$ . The first order Taylor series expansion of  $\ln(g(\mathbf{a}))$  at  $\hat{\mathbf{a}}$  is:

$$\ln(g(\mathbf{a})) = \ln(g(\hat{\mathbf{a}})) + \frac{1}{2}(\mathbf{a} - \hat{\mathbf{a}})^T \frac{\partial^2 \ln(g(\hat{\mathbf{a}}))}{\partial \mathbf{a}^2} (\mathbf{a} - \hat{\mathbf{a}}) \quad (47)$$

Then follows the estimation of the covariance  $\mathbf{V}$  for  $g(\mathbf{a})$

$$\begin{aligned} g(\mathbf{a}) &= \text{constant} \cdot \exp\left\{-\frac{1}{2}(\mathbf{a} - \hat{\mathbf{a}})^T \frac{\partial^2 (-g(\hat{\mathbf{a}}))}{\partial \mathbf{a}^2} (\mathbf{a} - \hat{\mathbf{a}})\right\} \\ &= \text{constant} \cdot \exp\left\{-\frac{1}{2}(\mathbf{a} - \hat{\mathbf{a}})^T \mathbf{V}^{-1} (\mathbf{a} - \hat{\mathbf{a}})\right\} \\ \mathbf{V}^{-1} &= -\frac{\partial^2 g(\hat{\mathbf{a}})}{\partial \mathbf{a}^2} \end{aligned} \quad (48)$$

According to Equation (45) and Equation (48), the conditional covariance  $\mathbf{C}_{\theta|y}$  is computed by:

$$\mathbf{C}_{\theta|y}^{-1} = \mathbf{J}^T \mathbf{C}_\varepsilon^{-1} \mathbf{J} + \mathbf{C}_0^{-1} \quad (49)$$

### **The M-step**

In the M-step, the conditional mean  $\boldsymbol{\eta}_{\theta|y}$  as well as the conditional covariance  $\mathbf{C}_{\theta|y}$ , which is estimated from the previous E-step, will be regarded as a constant to update the hyperparameter  $\boldsymbol{\lambda}$  for the unknown error covariance  $\mathbf{C}_\varepsilon$ .

According to the rules of probability calculation:

$$p(A) = \int_{-\infty}^{+\infty} p(A, B) dB \quad (50)$$

The *log likelihood* function  $\ln(p(y|\boldsymbol{\lambda}))$  can be written as:



$$\begin{aligned}\ln(p(\mathbf{y}|\boldsymbol{\lambda})) &= \ln\left(\int_{-\infty}^{+\infty} p(\mathbf{y}, \boldsymbol{\theta}|\boldsymbol{\lambda})d\boldsymbol{\theta}\right) \\ &= \ln\left(\int_{-\infty}^{+\infty} p(\mathbf{y}, \boldsymbol{\theta}|\boldsymbol{\lambda})\frac{q(\boldsymbol{\theta})}{q(\boldsymbol{\theta})}d\boldsymbol{\theta}\right)\end{aligned}\quad (51)$$

As the logarithm is a concave function, according to the Jensen's inequality [168]:

$$\begin{aligned}f(x) \geq 0, \int_{-\infty}^{+\infty} f(x)dx = 1, \quad \varphi \text{ is concave} \\ \varphi\left(\int_{-\infty}^{+\infty} g(x)f(x)dx\right) \geq \int_{-\infty}^{+\infty} \varphi(g(x))f(x)dx\end{aligned}\quad (52)$$

further gives:

$$\ln(p(\mathbf{y}|\boldsymbol{\lambda})) = \ln\left(\int_{-\infty}^{+\infty} q(\boldsymbol{\theta})\frac{p(\mathbf{y}, \boldsymbol{\theta}|\boldsymbol{\lambda})}{q(\boldsymbol{\theta})}d\boldsymbol{\theta}\right) \geq \int_{-\infty}^{+\infty} q(\boldsymbol{\theta})\ln\left(\frac{p(\mathbf{y}, \boldsymbol{\theta}|\boldsymbol{\lambda})}{q(\boldsymbol{\theta})}\right)d\boldsymbol{\theta}\quad (53)$$

with substitution  $\ln(\cdot) = \varphi(\cdot)$ ,  $f(x) = q(\boldsymbol{\theta})$ ,  $g(x) = \frac{p(\mathbf{y}, \boldsymbol{\theta}|\boldsymbol{\lambda})}{q(\boldsymbol{\theta})}$ .

Assuming the goal function  $F = \int_{-\infty}^{+\infty} q(\boldsymbol{\theta})\ln\left(\frac{p(\mathbf{y}, \boldsymbol{\theta}|\boldsymbol{\lambda})}{q(\boldsymbol{\theta})}\right)d\boldsymbol{\theta}$ , with  $p(\mathbf{y}, \boldsymbol{\theta}|\boldsymbol{\lambda}) = p(\mathbf{y}|\boldsymbol{\theta}, \boldsymbol{\lambda})d\boldsymbol{\theta}$ , then

gives:

$$\begin{aligned}F &= \int_{-\infty}^{+\infty} q(\boldsymbol{\theta})\ln\left(\frac{p(\mathbf{y}|\boldsymbol{\theta}, \boldsymbol{\lambda})p(\boldsymbol{\theta})}{q(\boldsymbol{\theta})}\right)d\boldsymbol{\theta} \\ &= \int_{-\infty}^{+\infty} q(\boldsymbol{\theta})\ln(p(\mathbf{y}|\boldsymbol{\theta}, \boldsymbol{\lambda}))d\boldsymbol{\theta} - \int_{-\infty}^{+\infty} q(\boldsymbol{\theta})\ln\left(\frac{q(\boldsymbol{\theta})}{p(\boldsymbol{\theta})}\right)d\boldsymbol{\theta}\end{aligned}\quad (54)$$

$q(\boldsymbol{\theta})$  here is the estimated *a-posteriori* distribution  $p(\boldsymbol{\theta}|\mathbf{y})$ , which is computed from the previous E-step.  $p(\boldsymbol{\theta})$  is the *a-priori* distribution of the parameter. The first term  $\int_{-\infty}^{+\infty} q(\boldsymbol{\theta})\ln(p(\mathbf{y}|\boldsymbol{\theta}, \boldsymbol{\lambda}))d\boldsymbol{\theta}$  in Equation (54) represents the expectation of the *log likelihood* function  $\ln(p(\mathbf{y}|\boldsymbol{\theta}, \boldsymbol{\lambda}))$  under the *a-posteriori* distribution  $q(\boldsymbol{\theta})$ . It describes the similarity between the model's simulated data and the observation. The second term  $\int_{-\infty}^{+\infty} q(\boldsymbol{\theta})\ln\left(\frac{q(\boldsymbol{\theta})}{p(\boldsymbol{\theta})}\right)d\boldsymbol{\theta}$  represents the Kullback-Leibler-divergence [169]. It describes the difference between the *a-posteriori* distribution and the *a-priori* distribution and it is always positive. The goal function  $F$  can be maximized, if the expectation term is maximized and the difference between the *a-posteriori* distribution and the *a-priori* distribution is minimized. As the divergence term is independent of the hyperparameter  $\boldsymbol{\lambda}$ , the maximization of the *log likelihood* function  $\ln(p(\mathbf{y}|\boldsymbol{\lambda}))$  is equivalent to the search for the maximum of the expectation

term  $f = E\{\ln(p(\mathbf{y} | \boldsymbol{\theta}, \boldsymbol{\lambda}))\}_q$  with respect to  $\boldsymbol{\lambda}$ .

According to the formula of multivariable normal distribution (Equation (35)) as well as the *log likelihood* function (Equation (39)), the formula of  $\ln(p(\mathbf{y} | \boldsymbol{\theta}, \boldsymbol{\lambda}))$  can be expressed as :

$$\begin{aligned} \ln(p(\mathbf{y} | \boldsymbol{\theta}, \boldsymbol{\lambda})) &= -\frac{1}{2} \ln |\mathbf{C}_\varepsilon| - \frac{1}{2} (\mathbf{r} - \mathbf{J} \cdot (\boldsymbol{\theta} - \boldsymbol{\eta}_{\theta|y}))^T \mathbf{C}_\varepsilon^{-1} (\mathbf{r} - \mathbf{J} \cdot (\boldsymbol{\theta} - \boldsymbol{\eta}_{\theta|y})) + \text{const.} \\ &= -\frac{1}{2} \ln |\mathbf{C}_\varepsilon| - \frac{1}{2} \left( \mathbf{r}^T \mathbf{C}_\varepsilon^{-1} \mathbf{r} - (\mathbf{J} \cdot (\boldsymbol{\theta} - \boldsymbol{\eta}_{\theta|y}))^T \mathbf{C}_\varepsilon^{-1} (\mathbf{J} \cdot (\boldsymbol{\theta} - \boldsymbol{\eta}_{\theta|y})) \right) + \text{const.} \quad (55) \\ &= -\frac{1}{2} \ln |\mathbf{C}_\varepsilon| - \frac{1}{2} \left( \mathbf{r}^T \mathbf{C}_\varepsilon^{-1} \mathbf{r} - (\boldsymbol{\theta} - \boldsymbol{\eta}_{\theta|y})^T \mathbf{J}^T \mathbf{C}_\varepsilon^{-1} \mathbf{J} \cdot (\boldsymbol{\theta} - \boldsymbol{\eta}_{\theta|y}) \right) + \text{const.} \end{aligned}$$

Substituting  $\mathbf{J}^T \mathbf{C}_\varepsilon^{-1} \mathbf{J} = \mathbf{C}_{\theta|y}^{-1} - \mathbf{C}_\theta^{-1}$  (Equation (49)) in Equation (55), gives:

$$\ln(p(\mathbf{y} | \boldsymbol{\theta}, \boldsymbol{\lambda})) = -\frac{1}{2} \ln |\mathbf{C}_\varepsilon| - \frac{1}{2} \left( \mathbf{r}^T \mathbf{C}_\varepsilon^{-1} \mathbf{r} - (\boldsymbol{\theta} - \boldsymbol{\eta}_{\theta|y})^T (\mathbf{C}_{\theta|y}^{-1} - \mathbf{C}_\theta^{-1}) \cdot (\boldsymbol{\theta} - \boldsymbol{\eta}_{\theta|y}) \right) + \text{const.} \quad (56)$$

The term  $-\frac{1}{2} \ln |\mathbf{C}_\varepsilon|$  and the term  $-\frac{1}{2} \mathbf{r}^T \mathbf{C}_\varepsilon^{-1} \mathbf{r}$  are independent of  $\boldsymbol{\theta}$ . According to Equation (54), Equation (56) multiplies with  $q(\boldsymbol{\theta})$  and then integrates over  $\boldsymbol{\theta}$ , which gives the expectation term  $f = E\{\ln(p(\mathbf{y} | \boldsymbol{\theta}, \boldsymbol{\lambda}))\}_q$ :

$$\begin{aligned} f &= \int_{-\infty}^{+\infty} q(\boldsymbol{\theta}) \ln(p(\mathbf{y} | \boldsymbol{\theta}, \boldsymbol{\lambda})) d\boldsymbol{\theta} \\ &= -\frac{1}{2} \ln |\mathbf{C}_\varepsilon| - \frac{1}{2} \mathbf{r}^T \mathbf{C}_\varepsilon^{-1} \mathbf{r} - \frac{1}{2} \int_{-\infty}^{+\infty} q(\boldsymbol{\theta}) (\boldsymbol{\theta} - \boldsymbol{\eta}_{\theta|y})^T (\mathbf{C}_{\theta|y}^{-1} - \mathbf{C}_\theta^{-1}) \cdot (\boldsymbol{\theta} - \boldsymbol{\eta}_{\theta|y}) d\boldsymbol{\theta} + \text{const.} \quad (57) \end{aligned}$$

Because the distribution of term  $(\boldsymbol{\theta} - \boldsymbol{\eta}_{\theta|y})$  is Gaussian:  $(\boldsymbol{\theta} - \boldsymbol{\eta}_{\theta|y}) \sim N(0, \mathbf{C}_{\theta|y})$ , according to the lemma for every normal distribution  $p(\mathbf{x}) \sim N(\boldsymbol{\mu}, \mathbf{C})$ :

$$E\{\mathbf{x}^T \mathbf{A} \mathbf{x}\} = \boldsymbol{\mu}^T \mathbf{C} \boldsymbol{\mu} + \text{tr}\{\mathbf{A} \mathbf{C}\} \quad (58)$$

this gives the second term of Equation (57):

$$\begin{aligned} &-\frac{1}{2} \int_{-\infty}^{+\infty} q(\boldsymbol{\theta}) (\boldsymbol{\theta} - \boldsymbol{\eta}_{\theta|y})^T (\mathbf{C}_{\theta|y}^{-1} - \mathbf{C}_\theta^{-1}) \cdot (\boldsymbol{\theta} - \boldsymbol{\eta}_{\theta|y}) d\boldsymbol{\theta} \\ &= -\frac{1}{2} \text{tr}\{(\mathbf{C}_{\theta|y}^{-1} - \mathbf{C}_\theta^{-1}) \mathbf{C}_{\theta|y}\} \quad (59) \end{aligned}$$

Substituting Equation (59) in Equation (57) then gives the expectation term  $f$ :

$$f = -\frac{1}{2} \ln |\mathbf{C}_\varepsilon| - \frac{1}{2} \mathbf{r}^T \mathbf{C}_\varepsilon^{-1} \mathbf{r} - \frac{1}{2} \text{tr}\{(\mathbf{C}_{\theta|y}^{-1} - \mathbf{C}_\theta^{-1}) \mathbf{C}_{\theta|y}\} + \text{const} \quad (60)$$

where  $\mathbf{C}_{\theta|y}$  is estimated from the previous E-step and is regarded as a constant here. Now

only the term  $-\frac{1}{2}\ln|\mathbf{C}_\varepsilon|$  and the term  $-\frac{1}{2}\mathbf{r}^T\mathbf{C}_\varepsilon^{-1}\mathbf{r}$  depend on the  $\lambda$ .<sup>1</sup> The first and second derivatives of  $f$  are necessary for Newton's method. It is difficult to calculate the second derivative of  $f$  directly. Instead, a modification of Newton's method involving the Fisher-Scoring-Method has been suggested by a previous study of Fristion [23]. The second derivative can be approximated by the Fisher information matrix.

The updating procedure for the  $\lambda$  is then formulated as [23]:

$$\begin{aligned} \lambda^{i+1} &= \lambda^i + \mathfrak{F}^{-1}\mathbf{g} \\ g_i &= \frac{\partial f}{\partial \lambda_i} = -\frac{1}{2}\text{tr}\{\mathbf{PQ}_i\} + \frac{1}{2}\mathbf{r}^T\mathbf{PQ}_i\mathbf{r} \\ \mathfrak{F}_{ij} &= \text{E}\left\{-\frac{\partial^2 f}{\partial \lambda_i \partial \lambda_j}\right\} = \frac{1}{2}\text{tr}\{\mathbf{PQ}_i\mathbf{PQ}_j\} \\ \mathbf{P} &= \mathbf{C}_\varepsilon^{-1} - \mathbf{C}_\varepsilon^{-1}\mathbf{J}\mathbf{C}_{\theta|y}\mathbf{J}^T\mathbf{C}_\varepsilon^{-1} \end{aligned} \tag{61}$$

$\lambda^{i+1}$  is the updated new hyperparameter for the new error covariance matrix  $\mathbf{C}_\varepsilon$  (Equation (30) ) and will be use in the next E-step.

### Summary

In the EM-algorithm, the conditional mean  $\eta_{\theta|y}$  for the *a-posteriori* distribution in E-step and the hyperparameter  $\lambda$  for the error covariance  $\mathbf{C}_\varepsilon$  in M-step will be iteratively estimated. The initial value for  $\eta_{\theta|y}^1$  is generally the expectation of the *a-priori* distribution of the parameter (the prior). The initial value for  $\lambda^1$  depends on the noise level of the measurement. With the consideration to the exponential operator in Equation (29), a large positive value reflects noisy data and a small negative value represents "clean" data.

The complete EM-algorithm procedure is presented as following:

#### I. initialization

$$\begin{aligned} \eta_{\theta|y}^1 &= \eta_0 \\ \lambda^1 &= \lambda_0 \\ \mathbf{C}_\varepsilon &= \sum_{i=1}^N \exp(\lambda_i) \mathbf{Q}_i \end{aligned}$$

---

<sup>1</sup>  $\frac{\partial}{\partial \lambda_i} \ln(\mathbf{C}_\varepsilon) = \text{Spur}\left\{\mathbf{C}_\varepsilon^{-1} \frac{\partial \mathbf{C}_\varepsilon}{\partial \lambda_i}\right\}$ ,  $\frac{\partial}{\partial \lambda_i} \mathbf{C}_\varepsilon^{-1} = -\mathbf{C}_\varepsilon^{-1} \frac{\partial \mathbf{C}_\varepsilon}{\partial \lambda_i} \mathbf{C}_\varepsilon^{-1}$

until convergence {

$$\mathbf{J} = \left. \frac{\partial \mathbf{h}(\boldsymbol{\theta})}{\partial \boldsymbol{\theta}} \right|_{\boldsymbol{\theta} = \boldsymbol{\eta}_{0\mathbf{y}}^s}$$

$$\mathbf{r} = \mathbf{y} - \mathbf{h}(\boldsymbol{\eta}_{0\mathbf{y}}^s)$$

II. M-step

$$\mathbf{P} = \mathbf{C}_\varepsilon^{-1} - \mathbf{C}_\varepsilon^{-1} \mathbf{J} (\mathbf{J}^T \mathbf{C}_\varepsilon^{-1} \mathbf{J} + \mathbf{C}_\theta^{-1})^{-1} \mathbf{J}^T \mathbf{C}_\varepsilon^{-1}$$

$$g_i = \frac{\partial f}{\partial \lambda_i} = -\frac{1}{2} \text{tr}\{\mathbf{PQ}_i\} + \frac{1}{2} \mathbf{r}^T \mathbf{PQ}_i \mathbf{r}$$

$$\mathfrak{S}_{ij} = \mathbb{E}\left\{-\frac{\partial^2 f}{\partial \lambda_i \partial \lambda_j}\right\} = \frac{1}{2} \text{tr}\{\mathbf{PQ}_i \mathbf{PQ}_j\}$$

$$\boldsymbol{\lambda}^{s+1} = \boldsymbol{\lambda}^s + \mathfrak{S}^{-1} \mathbf{g}$$

III. E-step

$$\mathbf{C}_\varepsilon^{s+1} = \sum_{i=1}^N \exp(\lambda_i^{s+1}) \mathbf{Q}_i$$

$$\frac{\partial l}{\partial \boldsymbol{\theta}} = \mathbf{J}^T (\mathbf{C}_\varepsilon^{s+1})^{-1} \mathbf{r} + \mathbf{C}_\theta^{-1} (\boldsymbol{\eta}_0 - \boldsymbol{\eta}_{0\mathbf{y}}^{s+1})$$

$$-\frac{\partial^2 l}{\partial \boldsymbol{\theta} \partial \boldsymbol{\theta}^T} = (\mathbf{J}^T (\mathbf{C}_\varepsilon^{s+1})^{-1} \mathbf{J} + \mathbf{C}_\theta^{-1})^{-1}$$

$$\boldsymbol{\eta}_{0\mathbf{y}}^{s+1} = \boldsymbol{\eta}_{0\mathbf{y}}^s + (\mathbf{J}^T (\mathbf{C}_\varepsilon^{s+1})^{-1} \mathbf{J} + \mathbf{C}_\theta^{-1})^{-1} (\mathbf{J}^T (\mathbf{C}_\varepsilon^{s+1})^{-1} \mathbf{r} + \mathbf{C}_\theta^{-1} (\boldsymbol{\eta}_0 - \boldsymbol{\eta}_{0\mathbf{y}}^s))$$

check the convergence criterion

}

The convergence criterion by the simplest case used in this dissertation is that the sum of squared change in conditional means falls below  $10^{-5}$ .

## 2.2.4 Bayesian model selection

In order to find out which kind of model  $m$  ( $m = 1, 2, \dots, k$ ) is more favored by the observed data  $\mathbf{y}$  according to the Bayesian theorem, a probability distribution of models is considered to be a posterior distribution of the prior belief of the model  $p(m)$  and the model evidence  $p(\mathbf{y} | m)$ :

$$p(m | \mathbf{y}) = \frac{p(\mathbf{y} | m) p(m)}{p(\mathbf{y})} \quad (62)$$

It is assumed that the distribution of *a-priori* information on the model  $p(m)$  is an uniform distribution:  $p(m) = 1/k$ , due to the absence of any specific prior information here. Moreover,

the model evidence  $p(y|m)$  is given by:

$$p(y|m) = \int p(y|\theta, m)p(\theta|m)d\theta \quad (63)$$

In Bayesian model selection, a model will be selected, which can maximize the posterior:

$$\arg_m (\max (p(m|y))) \rightarrow M_{m|y} \quad (64)$$

Under the assumption of a uniform prior, this is equal to selecting the model with the highest model evidence:

$$\arg_m (\max (p(y|m))) \rightarrow M_{y|m} \quad (65)$$

The Bayesian model selection is then implemented through the comparison of the Bayes factors [170].

### **Bayes factor**

To compare model  $m = i$  and model  $m = j$ , the Bayes factor is defined by the model evidence as [170]:

$$B_{ij} = \frac{p(y|m=i)}{p(y|m=j)} \quad (66)$$

which is also equal to using logarithms of the model evidence:

$$\ln B_{ij} = \ln(p(y|m=i)) - \ln(p(y|m=j)) \quad (67)$$

when  $B_{ij} > 1$ , the measured data is more in favor of model  $m = i$ , when  $B_{ij} < 1$ , the data is more in favor of model  $m = j$ . If there are more than two models to compare, then a reference model will be chosen and the Bayesian factors will be calculated relative to the reference.

The Bayesi factor is the summary of the evidence provided by the data in favor of one scientific hypothesis against another. An interpretation of the Bayesi factor was presented by Raftery [171] and is summarized in Table 2.3. Considering the two given models  $m = i$  and  $m = j$ , a Bayesian factor  $B_{ij}$  of 20 corresponds to a belief of 95% in the statement "the data is in favor of the model  $m = i$ ". This is a strong evidence in favor of the model  $m = i$ . While a

Bayesian factor  $B_{ij}$  of 3 corresponds to positive evidence in favor of the model  $m = i$ .

**Table 2.3 Interpretation of Bayes factor**

$B_{ij}$	$p(m=i y)$ (%)	Evidence in favor of model $m=i$
1 to 3	50-75	weak
3 to 20	75-95	positive
20 to 150	95-99	strong
$\geq 150$	$\geq 99$	very strong

### Computing log model evidence

The log model evidence can be computed according to the previous work of Penny and colleagues [62] as follows:

Assuming the *a-priori* distribution and the *likelihood* function for a given model  $m$  are:  $p(\boldsymbol{\theta}|m) \sim N(\boldsymbol{\eta}_0, \mathbf{C}_0)$  and  $p(\mathbf{y}|\boldsymbol{\theta}, m) \sim N(\mathbf{h}(\boldsymbol{\theta}), \mathbf{C}_\varepsilon)$ , then according to Equation (35), they can be expanded as:

$$p(y|m) = -\frac{Ns}{2} \ln(2\pi) - \frac{1}{2} \ln |\mathbf{C}_\varepsilon| - \frac{p}{2} \ln(2\pi) - \frac{1}{2} \ln |\mathbf{C}_0| - \frac{p}{2} \ln(2\pi) - \frac{1}{2} |\mathbf{C}_{0|y}| - \frac{1}{2} (\mathbf{y} - \mathbf{h}(\boldsymbol{\eta}_{0|y}))^T \mathbf{C}_\varepsilon^{-1} (\mathbf{y} - \mathbf{h}(\boldsymbol{\eta}_{0|y})) - \frac{1}{2} (\boldsymbol{\eta}_{0|y} - \boldsymbol{\eta}_0)^T \mathbf{C}_0^{-1} (\boldsymbol{\eta}_{0|y} - \boldsymbol{\eta}_0) \quad (68)$$

The model evidence is then given by:

$$p(\mathbf{y}|m) = \int p(\mathbf{y}|\boldsymbol{\theta}, m) p(\boldsymbol{\theta}|m) d\boldsymbol{\theta} = (2\pi)^{-\frac{Ns}{2}} |\mathbf{C}_\varepsilon|^{-\frac{1}{2}} (2\pi)^{-\frac{p}{2}} |\mathbf{C}_0|^{-\frac{1}{2}} I(\boldsymbol{\theta}) \quad (69)$$

where,

$$I(\boldsymbol{\theta}) = \int \exp\left\{-\frac{1}{2} (\mathbf{y} - \mathbf{h}(\boldsymbol{\theta}))^T \mathbf{C}_\varepsilon^{-1} (\mathbf{y} - \mathbf{h}(\boldsymbol{\theta})) - \frac{1}{2} (\boldsymbol{\theta} - \boldsymbol{\eta}_0)^T \mathbf{C}_0^{-1} (\boldsymbol{\theta} - \boldsymbol{\eta}_0)\right\} d\boldsymbol{\theta} \quad (70)$$

Assuming that the estimated *a-posterior* distribution is  $p(\boldsymbol{\theta}|\mathbf{y}, m) \sim N(\boldsymbol{\eta}_{0|y}, \mathbf{C}_{0|y})$ , then

substituting  $\mathbf{y} - \mathbf{h}(\boldsymbol{\theta}) = (\mathbf{y} - \mathbf{h}(\boldsymbol{\eta}_{0|y})) + (\mathbf{h}(\boldsymbol{\eta}_{0|y}) - \mathbf{h}(\boldsymbol{\theta}))$  and  $\boldsymbol{\theta} - \boldsymbol{\eta}_0 = (\boldsymbol{\theta} - \boldsymbol{\eta}_{0|y}) + (\boldsymbol{\eta}_{0|y} - \boldsymbol{\eta}_0)$  in

Equation (70) and removing the terms, which do not depend on  $\boldsymbol{\theta}$ , from the integral gives:

$$I(\boldsymbol{\theta}) = \int \exp\left\{-\frac{1}{2}(\boldsymbol{\theta} - \boldsymbol{\eta}_{\theta|y})^T \mathbf{C}_{\theta|y}^{-1}(\boldsymbol{\theta} - \boldsymbol{\eta}_{\theta|y})\right\} d\boldsymbol{\theta} \quad (71)$$

$$\cdot \exp\left\{-\frac{1}{2}(\mathbf{y} - \mathbf{h}(\boldsymbol{\eta}_{\theta|y}))^T \mathbf{C}_{\varepsilon}^{-1}(\mathbf{y} - \mathbf{h}(\boldsymbol{\eta}_{\theta|y})) - \frac{1}{2}(\boldsymbol{\eta}_{\theta|y} - \boldsymbol{\eta}_{\theta})^T \mathbf{C}_{\theta}^{-1}(\boldsymbol{\eta}_{\theta|y} - \boldsymbol{\eta}_{\theta})\right\}$$

where the first term is the normalizing term of the multivariable normal distribution, hence:

$$I(\boldsymbol{\theta}) = (2\pi)^{\frac{p}{2}} |\mathbf{C}_{\theta|y}|^{-\frac{1}{2}} \exp\left\{-\frac{1}{2}(\mathbf{y} - \mathbf{h}(\boldsymbol{\eta}_{\theta|y}))^T \mathbf{C}_{\varepsilon}^{-1}(\mathbf{y} - \mathbf{h}(\boldsymbol{\eta}_{\theta|y})) - \frac{1}{2}(\boldsymbol{\eta}_{\theta|y} - \boldsymbol{\eta}_{\theta})^T \mathbf{C}_{\theta}^{-1}(\boldsymbol{\eta}_{\theta|y} - \boldsymbol{\eta}_{\theta})\right\} \quad (72)$$

Substituting Equation( 66) into Equation (65), and taking the  $\ln()$  operator gives:

$$\ln p(y|m) = \left( -\frac{1}{2} \ln |\mathbf{C}_{\varepsilon}| - \frac{1}{2}(\mathbf{y} - \mathbf{h}(\boldsymbol{\eta}_{\theta|y}))^T \mathbf{C}_{\varepsilon}^{-1}(\mathbf{y} - \mathbf{h}(\boldsymbol{\eta}_{\theta|y})) - \frac{N_S}{2} \ln(2\pi) \right) \quad (73)$$

$$- \left( \frac{1}{2} \ln |\mathbf{C}_{\theta}| - \frac{1}{2} |\mathbf{C}_{\theta|y}| + \frac{1}{2}(\boldsymbol{\eta}_{\theta|y} - \boldsymbol{\eta}_{\theta})^T \mathbf{C}_{\theta}^{-1}(\boldsymbol{\eta}_{\theta|y} - \boldsymbol{\eta}_{\theta}) \right)$$

where, the first term is expressed as the accuracy term of the log model evidence and the second term is expressed as the complexity term [62].

The complex term depends on the prior covariance  $\mathbf{C}_{\theta}$  and the prior expectation  $\boldsymbol{\eta}_{\theta}$ . This means that the model comparison could be biased by the fixed prior (mean and covariance) [62]. When a large covariance is present, for example when the *prior* is uninformative, the model comparison will consistently favor the models that are less complex (i.e. the parameters are estimated near to the prior expectation) over the true model.

## 2.2.5 Improved Bayesian inverse framework

### 2.2.5.1 Prior formulations

The prior distribution reflects our *a-priori* knowledge about the model structure and the parameters that is based on anatomical and physiological studies. In the previously introduced Bayesian framework (see **Chapter 2.2.3**), the prior distributions are defined as Gaussian. The *a-priori* knowledge about the parameters is specified in terms of their means and variances. The mean corresponds to the expectation on a particular parameter value and the variance reflects the beliefs in this expectation. The assumption of Gaussian priors is useful in order to simplify the problem of computing the posterior distribution as well as the

model evidence. However, in the neural mass model, some parameter classes, such as synaptic receptor time constants (see **Chapter 2.1.1**) can only be positive. To ensure non-negativity during the parameter estimation, a reformulation of the original model parameters is necessary.

### ***Exponential formulation***

David and colleagues [45] suggested a re-parameterization method using the exponential formulation:

$$\theta = \eta_{\theta} \exp(\varphi) \quad (74)$$

The original model parameter  $\theta$  is expressed through its original expectation  $\eta_{\theta}$  as well as a new normal distributed parameter  $\varphi \sim N(0, \sigma^2)$ . The expectation of this new parameter  $\varphi = 0$  corresponds to the *a-priori* expectation of the original model parameter  $\theta = \eta_{\theta}$ . The variance  $\sigma^2$  of the new parameter  $\varphi$  corresponds to the amount of prior information about the model parameter. A loose distribution (large variance) reflects uninformative *a-priori* information and a tight distribution (small variance) reflects informative *a-priori* information. The variance  $\sigma^2$  is suggested to be 1/2 for an uninformative prior and 1/16 for an informative one [45, 60]. This re-parameterization with a zero mean normally distributed new parameter yields a shrinkage prior behavior, i.e. the new parameter is assumed to be zero (*a-priori* expectation) unless the data provides sufficient evidence to the contrary.

After the re-parameterization, the model parameters  $\theta$  as well as  $\theta / \eta_{\theta}$  follow the log-normal distribution (Fig. 2.18) and 95% of the possible values of  $\theta$  are found between  $[\eta_{\theta} \exp(-2\sigma), \eta_{\theta} \exp(2\sigma)]$ , i.e. by an uninformative prior ( $\sigma^2 = 1/2$ ) from  $0.24 \eta_{\theta}$  to  $4.11 \eta_{\theta}$  and by an informative prior ( $\sigma^2 = 1/16$ ) from  $0.61 \eta_{\theta}$  to  $1.65 \eta_{\theta}$ .



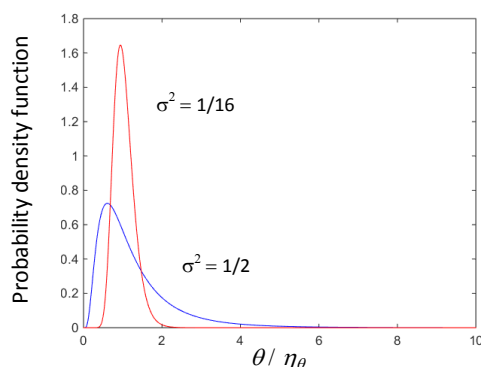


**Figure 2.18 Illustration of the log normal distribution.**  $\theta/\eta_\theta = \exp(\varphi)$ ,  $\varphi \sim \mathcal{N}(0, 1/16)$  is used for the informative prior and  $\varphi \sim \mathcal{N}(0, 1/2)$  is used for the uninformative prior.

### Quadratic formulation

Wang and Knösche [20] further extended this re-parameterization method with a quadratic formulation:

$$\begin{aligned}
 \theta &= \theta_0 \varphi^2 \\
 \varphi &= \sqrt{\frac{\theta}{\theta_0}} \quad \text{for } \varphi \geq 0 \\
 \varphi &= -\sqrt{\frac{\theta}{\theta_0}} \quad \text{for } \varphi < 0 \\
 \varphi &\sim \mathcal{N}(0, \sigma^2)
 \end{aligned} \tag{75}$$

This new formulation enables the model parameter to keep positive while also including the value zero. For the LCCM with six ( $N = 6$ ) uncertain connections, there are total  $n = \sum_{i=1}^N C_N^i = 63$  possible combination of connections. If the exponential formulation is used for each connection parameter, there are total of 63 different models that need to be compared to find the most "optimized" one in light of the data using the Bayesian model selection (see **Chapter 2.2.4**). By contrast, the quadrate formulation allows a single model to embody the whole possible connection variants, in that, assuming the connection strength to be zero and let the data to provide the sufficient evidence to contrast it.

After the re-parameterization, the model parameter  $\theta/\theta_0$  follows an exponential distribution (Fig. 2.19):

$$p\left(\frac{\theta}{\theta_0}\right) = \frac{1}{\sqrt{2\pi}} \exp\left(-\frac{\theta}{\theta_0 \sigma^2}\right) \tag{76}$$

where the expectation value of the prior is zero (corresponding to an uninformative connection) and 95% of all possible value are found in  $[0, \theta_0(2\sigma)^2]$ .  $\theta_0$  is a scaling factor to avoid using too large value of variance  $\sigma$  for the large prior range. When  $\sigma=1$ , the prior range is from 0 to  $4\theta_0$ . It is similar to the uninformative prior  $0.24\eta_\theta$  to  $4.11\eta_\theta$  using the exponential formulation.

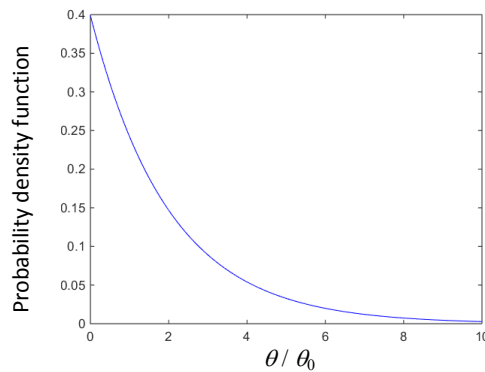


**Figure 2.19 Illustration of the exponential distribution.**  $\theta/\theta_0 = \varphi^2$ ,  $\varphi \sim N(0,1)$ , the model parameter  $\theta/\theta_0$  follows an exponential distribution.

### Summary

Table 2.4 is the summary of the prior formulation of the synaptic connections among the neural populations in the LCCM. In the LCCM, each synaptic connection between two neural populations can be described by four parameters: the synaptic connection strength  $C$ , the synaptic receptor constant  $\tau$  (see **Chapter 2.1.1**), the habituation/facilitation rate  $n_1$ , and the recovery rate  $n_2$  (see **Chapter 2.1.4.2**). The synaptic gains, as well as the parameters of the sigmoid function (see **Chapter 2.1.1**) are kept constant. There are in total 14 connections (including the input to EINs) among the five neural populations in the LCCM. These connections are classified into two groups: "certain" connections and "uncertain" connections (see **Chapter 2.1.3.2**).

It is assumed under the conditions of the experiment that the synaptic connection could only experience either adaptation or facilitation. Under these circumstances, the synaptic dynamic  $W(t)$  (adaptation/facilitation) can be formulated in respect of Equation (25) as well as Equation (26):

$$\begin{aligned}
\dot{W}(t) &= -n_1 \frac{Q(t)}{Q_{\max}} W(t) + n_2(1 - W(t)), & \text{for } Q(t) \geq 0, n_1 >= 0 \\
\dot{W}(t) &= -n_1 \frac{Q(t)}{Q_{\max}} (2 - W(t)) + n_2(1 - W(t)), & \text{for } Q(t) \geq 0, n_1 < 0 \\
\dot{W}(t) &= n_2(1 - W(t)), & \text{for } Q(t) < 0
\end{aligned} \tag{77}$$

The parameter  $n_1 \sim \mathcal{N}(0, \sigma^2)$  has a zero mean normal distribution prior. The property of the synaptic dynamics, adaptation (positive  $n_1$ ) or facilitation (negative  $n_1$ ), should be determined by the observed data.

**Table 2.4** Prior formulations of the synaptic connections in the LCCM

parameter definition	re-parameterization	original parameter	parameter classes	suggested $\sigma^2$	95% parameter interval
positive	$\varphi = \ln(\theta/\eta_\theta)$ $\varphi \sim \mathcal{N}(0, \sigma^2)$	$\theta = \eta_\theta \exp(\varphi)$ expectaton $\eta_\theta$	C of "certain" connections, $\tau, n_2$	1/2 1/16	$[0.24 \eta_\theta, 4.11 \eta_\theta]$ $[0.61 \eta_\theta, 1.65 \eta_\theta]$
positive, including zero	$\varphi = \pm \sqrt{\theta/\theta_0}$ $\varphi \sim \mathcal{N}(0, \sigma^2)$	$\theta = \theta_0 \varphi^2$ expectaton 0	C of "certain" connections	1	$[0, 4\theta_0]$
no specific	$\varphi = \theta/\theta_0$ $\varphi \sim \mathcal{N}(0, \sigma^2)$	$\theta = \theta_0 \varphi$ expectaton 0	$n_1$	10	$[-6\theta_0, 6\theta_0]$

C: synaptic connection strength,  $\tau$ : synaptic time constant,  $n_1$ : habituation or facilitation rate,  $n_2$ : recovery rate.

## 2.2.5.2 Implementation of Levenberg-Marquardt algorithm

### **Motivation**

The EM-algorithm (see **Chapter 2.2.3.2**) is an iterative parameter estimation method that searches for the maximum of the *a-posterior* distribution in the E-step as well as the maximum of the *likelihood* function in the M-step. Both *a-posterior* distribution and the

*likelihood* function are expressed through the non-linear functions of the NMM. This search algorithm is based on Newton's Method (Equation (41)). In practice, by using a larger parameter space, such as in the LCCM, this search algorithm performs relatively poorly. Figure 2.20 shows the goodness of fits of 28 time courses using the original EM algorithm [23]. The GoFs were calculated through:

$$\text{GoF}=1-(\text{var}(\mathbf{y}_{\text{mess}}-\mathbf{h}_{\text{model}})/\text{var}(\mathbf{y}_{\text{mess}})) \quad (78)$$

The GoF describes the proportion of variance in the observed data  $\mathbf{y}_{\text{mess}}$  explained by the simulated data  $\mathbf{h}_{\text{model}}$ . When the model output is identical to the observed data, the GoF has the maximum value of 1. The observed data here are the 1x301 time series of the estimated somatosensory evoked brain activity (for details about the data and the priors, see **Chapter 3.2.3** and **Chapter 3.2.4**). There are a total of 59 free parameters and the maximal number of iterative steps is 512.

A high goodness of fit plays an essential role in studies based on the Bayesian framework. A model that is unable to explain the measured data may be seen as a "bad" model, but it may only have failed in the optimization. To improve the performance of the optimization/fit, the Newton method (Equation (41)) in the E-step of EM algorithm is modified by the Levenberg-Marquardt-algorithm [159-160].

#### ***The Levenberg-Marquardt algorithm***

Equation (79) shows a modified E-step in the EM-algorithm using the LM-algorithm in respect of Equation (43):

$$\boldsymbol{\eta}_{0\mathbf{y}}^{i+1} = \boldsymbol{\eta}_{0\mathbf{y}}^i + \left( -\frac{\partial^2 l(\boldsymbol{\eta}_{0\mathbf{y}}^i)}{\partial \boldsymbol{\theta} \partial \boldsymbol{\theta}^T} + \kappa \mathbf{I} \right)^{-1} \frac{\partial l(\boldsymbol{\eta}_{0\mathbf{y}}^i)}{\partial \boldsymbol{\theta}} \quad (79)$$

where  $\kappa$  is a damping factor,  $\mathbf{I}$  is an identity matrix with the dimension  $p \times p$ , and  $p$  is equal to the number of free parameters in the model. If the damping factor  $\kappa$  is set to a small value, the searching algorithm approximates to the original Newton's Method. If the damping factor  $\kappa$  is set to a large value, the searching algorithm approximates to a steepest descent algorithm. The damping factor is reduced when the iterative step can improve the fit,

otherwise it is increased. In this way, the LM algorithm is adaptive; it can alternate between a slow descent approach (when far away from the minimum) and a fast convergence (when brought closer to the minimum) [160]. However, like Newton's Method, it could be trapped into the local minimum if the search landscape is complex and there are a lot of local extremes.

The iterative steps of the LM-algorithm implementation are summarized as:

(1) initializing  $\kappa = \kappa_0$  ( $\kappa_0 = 1$ ,  $\kappa_s = 10$ ,  $\kappa_{min} = 0.001$ ,  $\kappa_{max} = 1000$ );

**begin of the E-step**

(2) updating the estimated parameters through Equation 79 in E-step and calculate the log model evidence (Equation (73)) as well as the GoF (Equation (78)).

(3a) *if* the log model evidence is increased by  $\rho$  ( *if*  $\text{GoF} \leq 0.9$ ,  $\rho = 0.5$ ; otherwise  $\rho = 0.1$ ),  $\kappa = \max(\kappa / \kappa_s, \kappa_{min})$ ;

(3b) *otherwise*  $\kappa = \min(\kappa \kappa_s, \kappa_{max})$  and back to step 2);

(3c) *if*  $\kappa = \kappa_{max}$  and the log model evidence is still not improved by  $\rho$ , keep the result from  $\kappa = \kappa_0$

**end the of E-step**

(4) *if*  $\kappa > \kappa_0$ ,  $\kappa = \kappa_0$ , waiting for the next E-step.

## 2.2.5.3 Evaluation of the Levenberg-Maquardt implementation

### 2.2.5.3.1 Hypothesis

Null-Hypothesis  $H_0$ : There is no improvement in the GoF by implementation of the LM-algorithm to fit the data.

Alternative-Hypothesis  $H_A$ : The GoF is increased through implementation of LM-algorithm.

### 2.2.5.3.2 Method specification

Test data:	The estimated somatosensory evoked brain activity time courses of 26 participants (for details, see <b>Chapter 3.2.3</b> ). The dimension of the time series (300ms) is 1 x 301.
Test model:	The LCCM (for priors and initial values see Table 3.8)
Estimation setup:	The maximal number of iterative steps is set to 512. The LM-group is implemented with the LM-algorithm in the E-step (Equation (79)) of the Bayesian inverse estimation framework. The No-LM-group uses the original E-step (Equation (43)).
Statistics:	one way ANOVA

### 2.2.5.3.3 Results

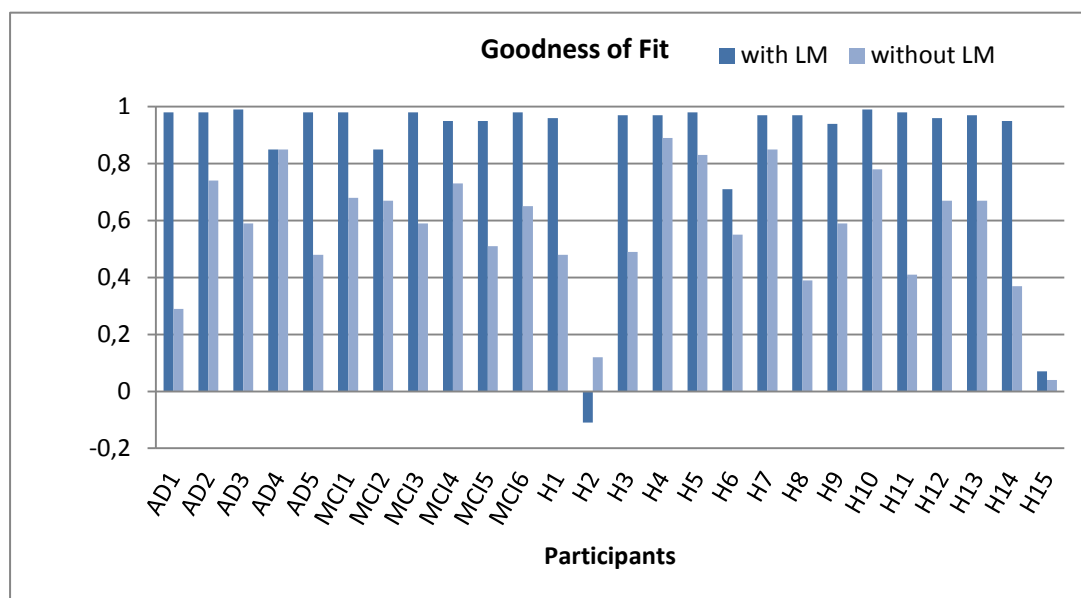
The fit results (GoFs) are shown in Figure 2.20. The value table is listed in Appendix B Table B.4. The GoF for the LM-group range from 0.71 to 0.99 (except two extreme low value: -0.11 as well as 0.07). The mean is 0.88, variance is 0.07, median is 0.97. The GoF for No-LM-group are range from 0.29 to 0.89 (except one extremely low value 0.04). The mean is 0.57, the variance is 0.04, the median is 0.59. The p-value of the ANOVA test is  $1e^{-5}$ , far below the significance level  $p = 0.05$ . The GoF of LM-group is significantly better than No-LM-group.

Figure 2.21 shows the GoF of each iterative step by data AD4, which has the same GoF by using LM-algorithm as well as not using LM-algorithm. With the LM-algorithm the fit converged much earlier.

By using the LM-algorithm, the two extremely low fit results (-0.11 of data H2 as well as 0.04 of data H15) were improved to be 0.98 and 0.97, when initialized with the estimated parameter of data H10 (GoF = 0.99).

### 2.2.5.3.4. Conclusions

Modifying the EM-algorithm with the LM-algorithm in E-step can improve the GoF of the Bayesian inverse estimation framework. The fit result can also be influenced by the "suitability" of the initial value.



Note. LM = Levenberg-Maquardt algorithm, AD = Alzheimer Disease, MCI = mild cognitive impairment, H = Healthy elderly

**Figure 2.20 Goodness of Fits of using as well as not using Levenberg-Maquardt algorithm in the E-step of the Bayesian inverse estimation.**

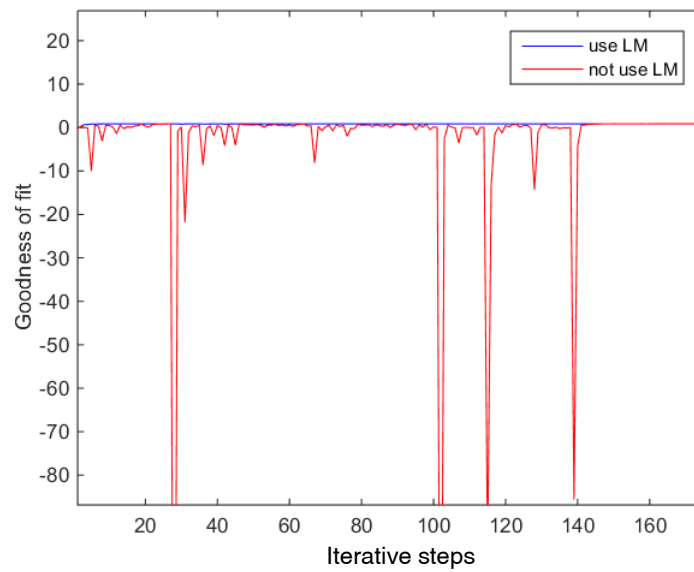


**Figure 2.21** The Goodness of fit of each iterative steps of using as well as not using **levenberg-Maquardt algorithm**. The blue line shows the iterative GoFs of fitting the data A4 using LM-algorithm. In contrast, the iterative GoFs of not using LM-algorithm are shown in red. Although both estimation procedures were convergent at value 0.85, using LM-algorithm helped to accelerate the convergence.



## Chapter 3: Applications and Evaluations

*Essentially, all models are wrong, but some are useful.*

*- George E. P. Box 1919-2013*

### 3.1 Modeling auditory adaptation

#### 3.1.1 Motivation

A simple, repetitive pure tone evokes reduced brain activity in the auditory cortex (auditory adaptation). This phenomenon can be observed through non-invasive brain image techniques such as EEG/MEG with excellent temporal resolution. The repetitive auditory stimuli evoke auditory evoked fields (AEFs) and auditory evoked potentials (AEPs), which are generated by mass synchronized neurons in superior temporal gyrus (STG), Heschl's gyrus and planum temporale (PT) [124, 126, 131, 172-174]. The most prominent AEF/AEP deflection is referred to as N100/N100m, which occurs around 100ms after the stimulus onset [124]. The N100/N100m peak is sensitive to the repeated stimulations in a short inter-stimuli-interval (ISI), i.e. 500ms ISI can strongly suppress the N100/N100m amplitude [123, 125-126, 175]. This amplitude suppression recovers after about 6 to 10 seconds of stimuli free time [127].

Different approaches have been used in previous studies to account for the generators of the auditory N100/N100m response in EEG/MEG observations. Zouridakis and colleagues [173] found that using a single moving dipole within the primary auditory cortex could account for the entire duration of the N100m (from about 70 ms to 150 ms after stimulus) and that, during the evolution of the component, it followed a bilateral posterior-anterior, medial-lateral, superior-inferior trajectory extending about 2 cm into the superior surface of the temporal lobes. This finding was confirmed by several other MEG studies [126, 172]. Lu

and colleagues [176] postulated that it might be possible for one neural source in the primary auditory cortex to account for a short ISI response but an additional one would be needed in the auditory association cortex for the long ISI response. Näätänen and Picton [124] reviewed the previous literature on the N100 (50–150 ms after stimulus) and postulated three neural generators. The first one tangentially oriented to the head surface and bilaterally located in the auditory cortices and makes the largest contribution to the N100 recording [177]. Due to its radial orientation, the second generator in auditory association cortex in STG is insensitive to MEG. Finally, the third generator was found only with intracranial recordings [178-179]. Its location remains unclear but is supposedly located somewhat posterior to the first generator. Another multi-generator approach was reported by Jääskeläinen and colleagues [131]. They found two separate sources in the anterior STG and posterior STG/PT contributing to the N100 by combining MEG, EEG and fMRI recordings. The posterior source activated at around 85 ms and is considered related to the “where” information. The anterior source activated at around 150 ms and is related to the “what” information [174].

In summary, the generation of the major component of the N100m for a series of identical (location and pitch) stimuli with short ISI might be explained by a single dipole at each time step. All dipoles are located near the primary auditory cortex and their orientations seem to be very similar [126]. Hence, they have very similar leadfields and their dynamics cannot be separated easily. Consequently, in this study these sources are decided to be lumped together and described by a single LCCM in Heschl's gyrus in order to count the N100m (70-130ms) component in contrast to the previous EEG study of the auditory adaptation done by Garrido and colleagues[46], where two different neural mass models were used to account for different source areas (primary auditory cortex and STG) in each hemisphere while modeling the whole 400ms response duration.

Furthermore, MEG was chosen to be the measurement modality despite its high cost in comparison to an EEG, because the MEG can more accurately localize the superficial and tangential sources in the somatosensory or auditory cortex. The MEG is less affected by

other possible "unexpected" sources because it is particularly insensible to radial sources [24, 180] perpendicular to the scalp surface as well as deep source in the center of the head. The most prominent sensor of EEG to capture the auditory N100 is the Cz, which is placed at the middle of the scalp surface [124]. The observed data are a result of the superposition of the sources in both left and right hemisphere. In contrast, the MEG can capture the activity of the right and left auditory cortex separately with the sensor sets that are closely above them.

In this LCCM approach, the adaptation of the AEF is assumed to be associated with the decrease of the excitatory connections, i.e. the synaptic connections originate from neural populations of EINs and PCs. This can be modeled by the synaptic dynamic model (see **Chapter 2.1.4.2**) with respect to depletion and refill of the neurotransmitters at the presynaptic sides of the neurons. The repetitive stimuli cause an insufficient availability of vesicles in the releasing pool, thus the release probability of the vesicles is reduced and that, in turn, causes a reduction in the synaptic connection strength and hence the EEG/MEG signal amplitude. The recovery from the adaptation is linked to the process of refilling these vesicles back to the releasing pool, all of which occurs spontaneously.

In the modeling process, the goal was not only to test the hypothesis for the short-term adaptation on the basis of current knowledge from cellular research, but also to prove the necessity to refine the very parsimonious NMM of a local cortical circuit proposed by Jansen and Rit [22]. In particular, the expectation is that a more realistic laminar organization of information processing can better explain the measured EEG/MEG data.

The specific aim of this modeling was also to study the effect of stimulus repetition on the inter-/intra-columnar connections among the different sub-populations. The research asked the following questions: How was the information processing organized with respect to the different cortical layers, and how were these connections affected by the stimuli repetition? There were two different hypotheses concerning the information pathways following the arrival of the bottom-up input at EINs in layer IV: (1) information follows a serial pathway where it first ascends from layer IV to the sPC in layers II/III and then goes down to the dPC

in layers V/VI; (2) information follows parallel pathways where it flows simultaneously from layer IV to both layers II/III and layers V/VI and then integrates at the dPC. The excitatory and the inhibitory cross-layer connection probability between the superficial layers and the deep layers were also investigated.

### 3.1.2 Tasks

- i. To evaluate if the synaptic dynamic model is able to mimic the adaptation as well as the recovery of the AEF.
- ii. To evaluate if the LCCM has an advantage against the JRM with respect to explaining the observed AEFs.
- iii. To explore the relationship between the adaptation and the ISIs.
- iv. To explore the laminar organization of the synaptic connections and to test the parallel signal pathway hypothesis.
- v. To explore the temporal changes of the synaptic connections.

### 3.1.3 Model specification

The specification of the priors was crucially important for the performance of the Bayesian inversion. The priors reflect the *a-priori* information about the model structure and the parameters, which are based on previous anatomical and physiological knowledge. They are coded in terms of Gaussian priors in the Bayesian inversion framework (see **Chapter 2.2.5.1**).

The mean corresponds to the expectation on a particular parameter value and the variance reflects the beliefs in these expectation. The author prefers to divide the parameters of the LCCM (see **Chapter 2.1.3.2**) into four groups:

- (i) Parameters for connection dynamics that reflect prior knowledge on the connections between the NMs within a cortical area such as: the connection strength  $C$ , which describes

how strong is the connection from one NM to another one; the synaptic time constant  $\tau$ , which is a lumped representation of the conduction time delays and synaptic receptor time constants of the target NM; the adaptation rate  $n_1$  as well as the recovery rate  $n_2$ . These are the key parameters for this research and explain the laminar organization of the signal processing inside a cortical column.

(ii) Parameters for the NM dynamics per se such as: the synaptic gate  $H$ , which tunes the maximum amplitude of the average membrane potential of a NM as well as parameters for the sigmoid functions  $(e_0, u_0, r)$  (Equation (6)), which control the convolution from the averaged membrane potential to the averaged firing rate of a NM. Considering the mathematic description of the LCCM (Equation (13)-(17)), there is redundancy between these parameters and the parameters of the connection dynamics ( $C$  and  $W$ ) in the Bayesian inversion. These parameters are assumed to be constant (prior variance equal to zero) and they take their values from the literature [22].

(iii) Parameters for the inputs  $(q, w)$  (Equation (7)), which control the maximum amplitude as well as the width of the input. It is assumed that the thalamic input going into the LCCM has a Gaussian-like form (Fig. 2.9), which is inspired by the previous modeling work of Jansen and colleagues [21] and mimics the signal transmission from the retina through the metathalamus to the visual cortex. In this study, only the parameter  $w$ , which tunes the latency as well as the width of the input, is taken into account. The maximum amplitude of the input is normalized to 5 Hz, the same as the maximum averaged firing rate of a NM, which is according to the previous work of the JRM [22].

(iv) Parameters  $(\alpha_0, \beta_0)$  (Equation (18)) describe the linear proportionality from simulated neural activity, i.e. the average membrane potential of PCs, to experimental observations, i.e. the measurable evoked magnetic field in MEG. In this study, it is simply assumed that the sPCs and the dPCs have the same contribution to the sensors ( $\beta_0 = 1$ ) and the maximum amplitude of the source (N100m) is normalized to 1.

The prior expectations of the synaptic time constants as well as the synaptic connection strength values are chosen according to the study by Jansen and Rit [22].

Wehr and Zador [152] reported in their *in vivo* studies that the forward masking of auditory cortex cells was due to synaptic depression rather than inhibitory postsynaptic potentials (IPSPs) and Galarreta and Hestrin [153] showed that excitatory synapses depressed much more strongly than inhibitory ones. Motivated by these studies, it was assumed that the adaptation would only affect the excitatory pathways. It was also assumed that there was no adaptation on the input signal. According to the animal study of the spike-frequency adaptation of inferior colliculus (IC) by Ingham and McAlpine [181], the IC's recovery could be approximated with an exponential function with a time constant  $225.5 \pm 210.2$  ms. Therefore, in this study, using an ISI larger than 500ms, the observed adaptation of AEFs were assumed to depend primarily on adaptation processes inside the auditory cortex and not on the input from the thalamus. Moreover, because the same presynaptic neuron may have different short-term plasticity for connections to different types of target neurons [154], different depression and recovery rates for each excitatory connection were used.

It was assumed that the expectation of the recovery rate was  $2s^{-1}$ . This value ensures that in the absence of concurrent adaptation, the connection efficiency could rise from 0 to 1 within 3 seconds ( $5\tau = 3s$ , time constant  $\tau = 600$  ms). It was similar to the time constants of recovery from depression observed in the animal studies that were fitted with an exponential function:  $476 \pm 104$  ms (least-squares fit  $\pm$  estimated fitting error) for synapses between excitatory layer IV neurons [182],  $634 \pm 96$  ms [183] and  $480 \pm 40$  ms [184] reported for EPSPs in layers II/III pyramidal cells evoked by extracellular field stimulation,  $813 \pm 240$  ms for connected neighboring layer V pyramidal cells and  $399 \pm 295$ ms for layer V pyramidal to interneuron synapses [154]. The adaptation should be far faster than the recovery, so this parameter was assumed to be  $20s^{-1}$ . By using this pair of adaptation-recovery parameters, simulated N100m data decreased in amplitude at a similar rate as observed in other experiments.

The prior setup of the LCCM are summarized in Table 3.1. The prior setup of the JRM are summarized in Table 3.2

**Table 3.1 Prior setup of the LCCM for the auditory adaptation experiment**

	Expectation	Prior Type (U/I/C)
<i>Intrinsic connection parameters</i>		
<i>Certain intrinsic connections</i>		
EIN→sPC	108	U
sPC→sIIN	33.75	U
sIIN→sPC	33.75	U
sPC→dPC	135	U
dPC→EIN	135	U
dPC→dIIN	33.75	U
dIIN→dPC	33.75	U
Thalamic input →EIN	50	I
<i>Uncertain intrinsic connections</i>		
dPC→sPC	0	U
EIN→dPC	0	U
sIIN→dPC	0	U
dPC→sIIN	0	U
dIIN→sPC	0	U
sPC→dIIN	0	U
<i>Synaptic gain parameters</i>		
$H_e$	$3.25 \times 10^{-3} [\text{V}]$	C
$H_i$	$22 \times 10^{-3} [\text{V}]$	C
<i>Synaptic time constants (from NM x to NM y)</i>		
$\tau_{e,xy}$	$10 \times 10^{-3} [\text{s}]$	U
$\tau_{i,xy}$	$20 \times 10^{-3} [\text{s}]$	U
<i>Sigmoid parameter</i>		
$e_0$	$2.5 [\text{s}^{-1}]$	C
$r$	$560 [\text{V}^{-1}]$	C

$u_0$	$6 \times 10^{-3} [\text{V}]$	C
<i>Input parameter</i>		
$w$	$0.005 [\text{s}]$	I
<i>Depression and recovery rate (from NM <math>i</math> to NM <math>j</math>)</i>		
Depression rate $n_{1,ij}$	$20 [\text{s}^{-1}]$	U
Recovery rate $n_{2,ij}$	$2 [\text{s}^{-1}]$	U

Note. Re-parameterization for uncertain intrinsic connections used:  $\theta = \theta_0 \varphi^2$ ,  $p(\varphi) \sim \text{N}(0,1)$  for uninformative prior.

Re-parameterization for other parameters use:  $\theta = 108 \exp(\varphi)$ , is the expectation. The un-informative priors are  $p(\varphi) \sim \text{N}(0, 1/2)$ , the informative priors are  $p(\varphi) \sim \text{N}(0, 1/16)$ . EIN = excitatory interneurons, sPC = superficial pyramidal cells, sIIN = superficial inhibitory interneurons, dPC = deep pyramidal cells, dIIN = deep inhibitory interneurons. U = uninformative prior, I = informative prior, C = constant.

**Table 3.2 Prior setup of the JRM for the auditory adaptation experiment**

	Expectation	Prior Type (U/I/C)
<i>Intrinsic connection parameters</i>		
<i>Certain intrinsic connections</i>		
EIN $\rightarrow$ PC	108	U
PC $\rightarrow$ EIN	135	U
PC $\rightarrow$ IIN	33.75	U
IIN $\rightarrow$ PC	33.75	U
Thlamic input $\rightarrow$ EIN	100	I
<i>Synaptic gain parameters</i>		
$H_e$	$3.25 \times 10^{-3} [\text{V}]$	C
$H_i$	$22 \times 10^{-3} [\text{V}]$	C
<i>Dendritic time constants (from NM <math>x</math> to NM <math>y</math>)</i>		
$\tau_{e,xy}$	$10 \times 10^{-3} [\text{s}]$	U
$\tau_{i,xy}$	$20 \times 10^{-3} [\text{s}]$	U



*Sigmoid parameter*

$e_0$	2.5 [s <sup>-1</sup> ]	C
$r$	560 [V <sup>-1</sup> ]	C
$u_0$	6x10 <sup>-3</sup> [V]	C

*Input parameter*

$w$	0.005[s]	I
-----	----------	---

*Depression and recovery rate (from NM i to NM j)*

Depression rate $n_{1,ij}$	20[s <sup>-1</sup> ]	U
Recovery rate $n_{2,ij}$	2[s <sup>-1</sup> ]	U

Note. Re-parameterization for parameters use:  $\phi=108\exp(\theta)$ ,  $u$  is the expectation. The un-informative priors are  $p(\theta)\sim N(0, 1/2)$ , the informative priors are  $p(\theta)\sim N(0, 1/16)$ . EIN = excitatory interneurons, PC = pyramidal cells, IIN = inhibitory interneurons. U = uninformative prior, I = informative prior, C = constant.

### 3.1.4 Data acquisition and processing

#### 3.1.4.1 Experiment

##### **Ethic statement**

The study follows the guidelines of the declaration of Helsinki and has the ethical approval of the ethics commission of the University of Leipzig, Germany.

##### **Description**

Thirteen right-handed and normal-hearing participants participated in the experiment. Written informed consent was obtained from all subjects prior to the experiment. The stimulation paradigm was based on previous auditory short-term adaptation studies [123, 125-126]. The subjects were binaurally stimulated via earphones with a total of 160 sequences (divided into two equal blocks of ca. 20 min duration) of ten identical tones each. The tones were 900 Hz sine waves 15 ms long (including 1.5 ms fade-in and 1.5 ms fade-out time). Within one sequence, the tones were separated by 500 ms (from onset to onset).

Sequences were separated by 10 s of silence (Fig. 3.1). The participants were instructed to recline on a comfortable bed and watch a silent movie with subtitles of their own choice during the MEG recordings.

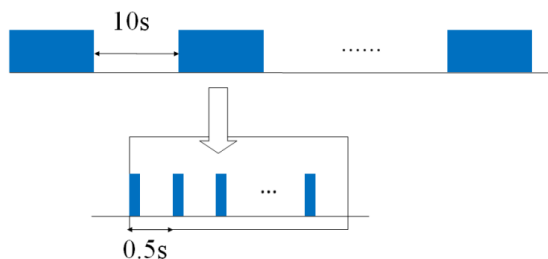


**Figure 3.1 Stimulation design of the experiment of auditory adaptation.** Ten identical tones were separated by 0.5s (from onset to onset). Sequences were separated by 10s of silence.

### 3.1.4.2 MEG recording

MEG was recorded with a NEUROMAG-306 system (Elekta Oy, Helsinki) with 204 planar gradiometers and 102 magnetometers. Two EOG channels (vertical, horizontal) were used to detect eye blink and eye movement artifacts. The head position relative to the sensors was monitored online with 5 Head Position Indicator (HPI) coils. The signal was digitized with a bandwidth from DC to 330 Hz and a sampling rate of 1000 Hz. The raw data were corrected using MaxFilter™ for noise contamination. MaxFilter™ is based on the Signal Space Separation (SSS) method [185], which separates the biomagnetic and external interference signals. The raw MEG data were filtered offline with a 1–20 Hz band-pass filter (4096 points, FIR). The AEF of each stimulus (1-10) was separately averaged: from 0 ms (presentation time of each stimulus 1-10) to 499 ms (1 ms before next stimulus presenting time). The time range from -100 ms to 0 ms of the first stimulus was used for base-line correction. The averaging and base line correction was performed by software MNE [186].

### 3.1.4.3 Data preparation

A volume conductor model was prepared for each participant for the source estimation. It was a realistically shaped *boundary element model* (BEM), which was constructed from individual anatomical MRI data. The segmentation of the MRI-data was performed in software *FreeSurfer* [187]. The BEM surfaces were created in software *OpenMEEG* [188]. The BEM surfaces included three layers (scalp, inner skull, outer skull) as well as the source space (cortex space). The scalp layer used 1082 vertices, the outer skull used 642 vertices, the inner skull used 642 vertices, and the cortex surface used 15002 vertices. The source activity was computed using software *Brainstorm* [161] with the sLORETA Algorithm [163-164]. It was considered that each vertex of the cortex surface contained only one dipole, which was perpendicular to the cortex surface. A region of interest (ROI) was chosen by each participant individually to represent their Heschel's gyrus (Fig. 3.2). It is worth noting that, in this study, the ROI was not required to have a high anatomical accuracy, but it should functionally represent the source generator of the N100m on the upper side of the STG. The vertex, which was located on the right STG and had the highest activity at the N100m peak time of the first stimulus response, was marked as the centre of the ROI. The ROI covered about 3-5 cm<sup>2</sup> (Fig. 3.3). The activity of the ROI is calculated through the average of the activities of all dipoles inside the ROI. This time course would be used as the observed source activity of the N100m generator in the Bayesian inversion. For each participant, the first five responses to the repetitive stimuli were used to estimate the model parameters, while the last five responses were used to check the prediction ability of the model.

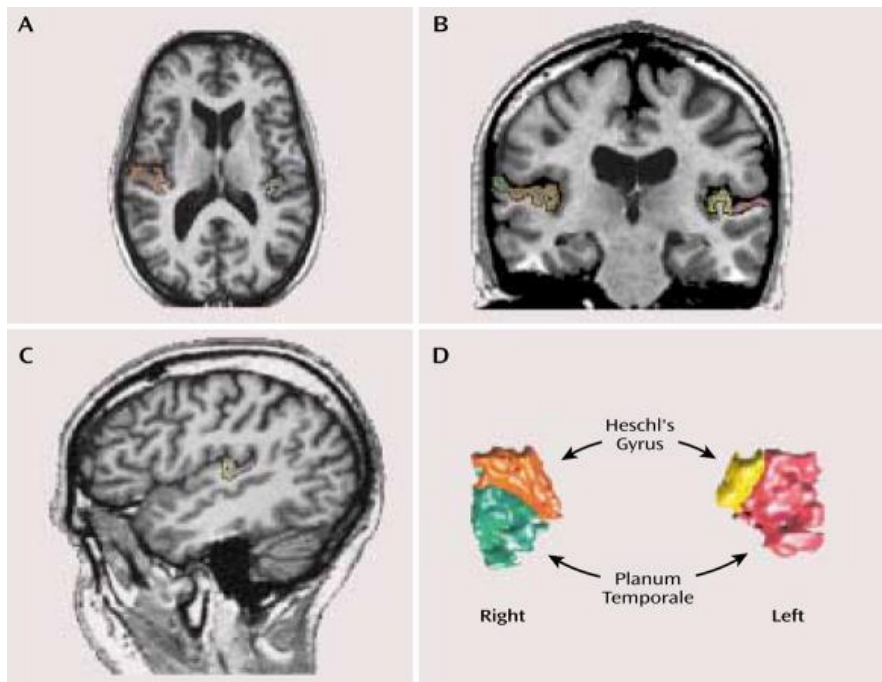


**Figure 3.2 Anatomical view of the Heschl's gyrus as well as Planum temporale.**

(Picture from Dickey, 2002 [189]. Reprinted with permission from The American Journal of Psychiatry, (Copyright ©2002). American Psychiatric Association.)

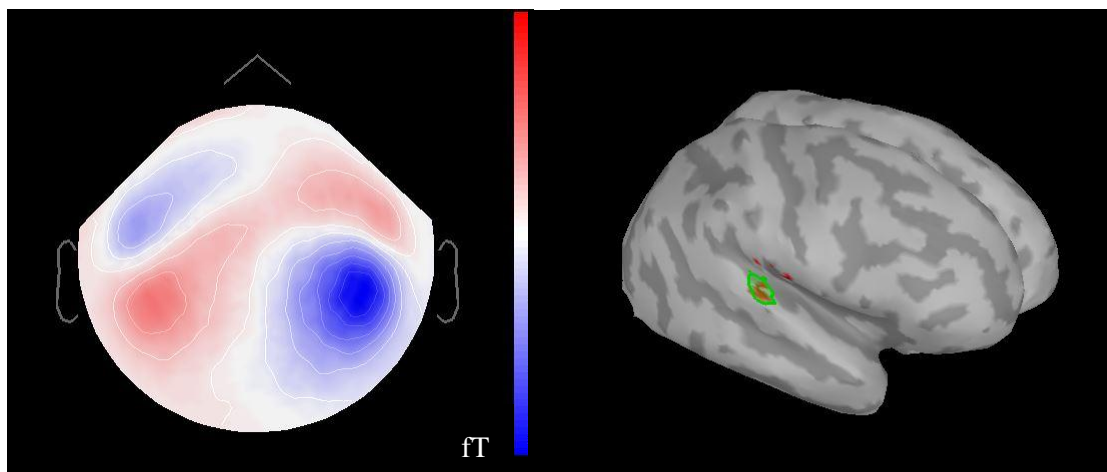


**Figure 3.3 ROI of the N100m.** A region of interest (ROI) (right panel) was selected to represent the source generator of the N100m peak. The centre of the ROI was determined by the vertex with the highest activity on the upper side of the right STG. Each vertex included a dipole perpendicular to the cortex surface.

## 3.1.5 Results

### 3.1.5.1 Data observation and description

The source activations of the 13 participants at the time point of N100m peak (see Appendix A, Table A.1.) were averaged to examine the adaptation effect. The source activity dropped off about 50% off for the second repetition of the tone (Fig. 3.4). Further presentation of the stimuli evoked less additional depression and seemed to reach a boundary value at approximately 30% of the strength of the first response after 6 stimuli with the ISI 500ms.

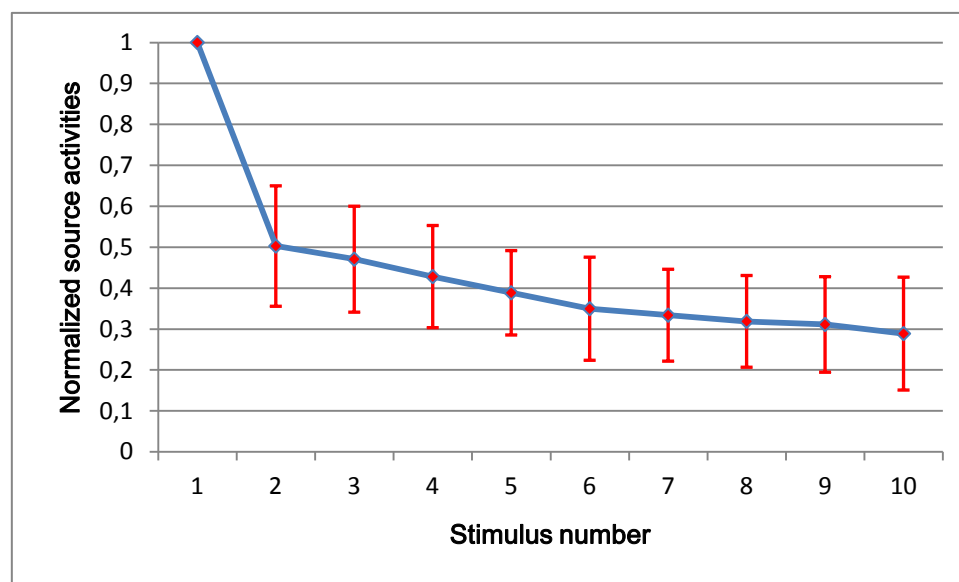


**Figure 3.4 Adaptation of the source activities at N100m peak time.** A repetitive stimulus in short ISI (500ms) evoked the adaptation of the N100m component of the auditory evoked field. For each participant, the source activities at the N100m peak time of each stimulus were normalized to the first one. The mean value and the standard error are shown in the figure in red. The adaptation effect seems to have been converged after 6 stimuli.

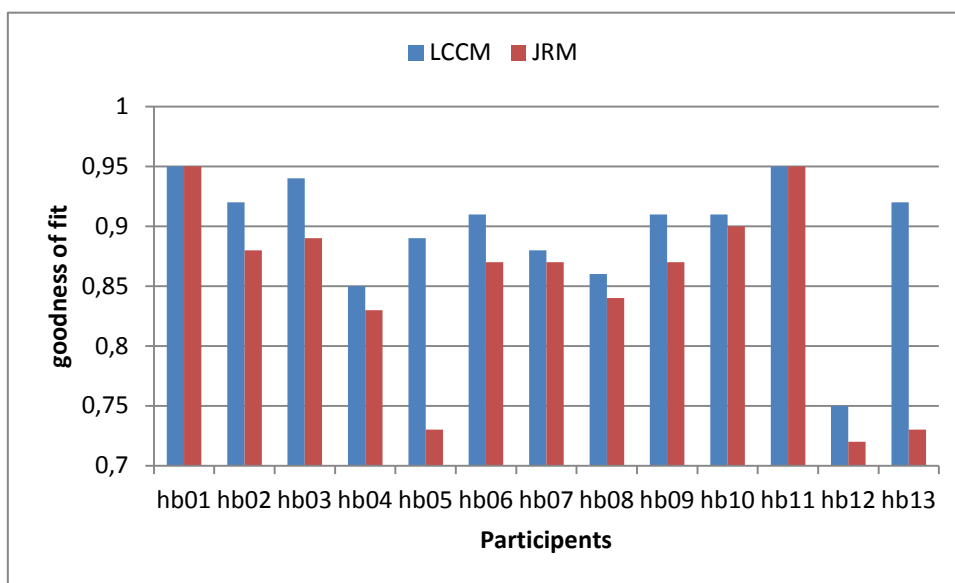
### 3.1.5.2 Comparison of the LCCM and the JRM

#### 3.1.5.2.1 Comparison of the goodness of fit

The GoFs (of the first 5 responses) of both the LCCM as well as the JRM are shown in Figure 3.5. The value table is documented in Appendix A, Table A.2.

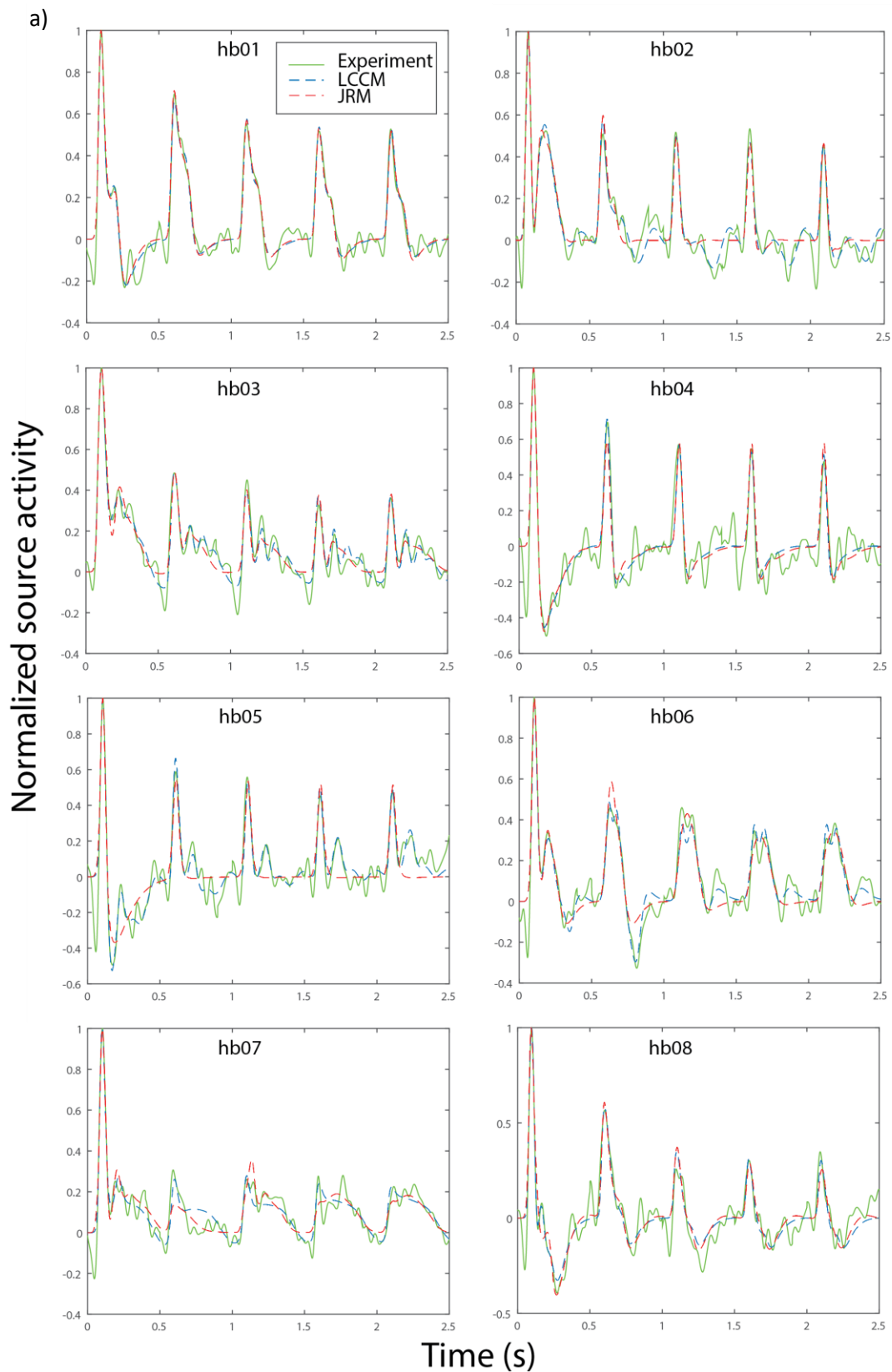
The mean GoF of the LCCM was 0.89, and the mean GoF of the JRM was 0.85. The p value of the one way ANOVA test was 0.10. There was no significant benefit in respect to fitting the observed data by using the LCCM.

Both the LCCM and the JRM were able to fit the main peak as well as its adaptation at the N100m peak time. The individual fitting results are shown in Figure 3.6.

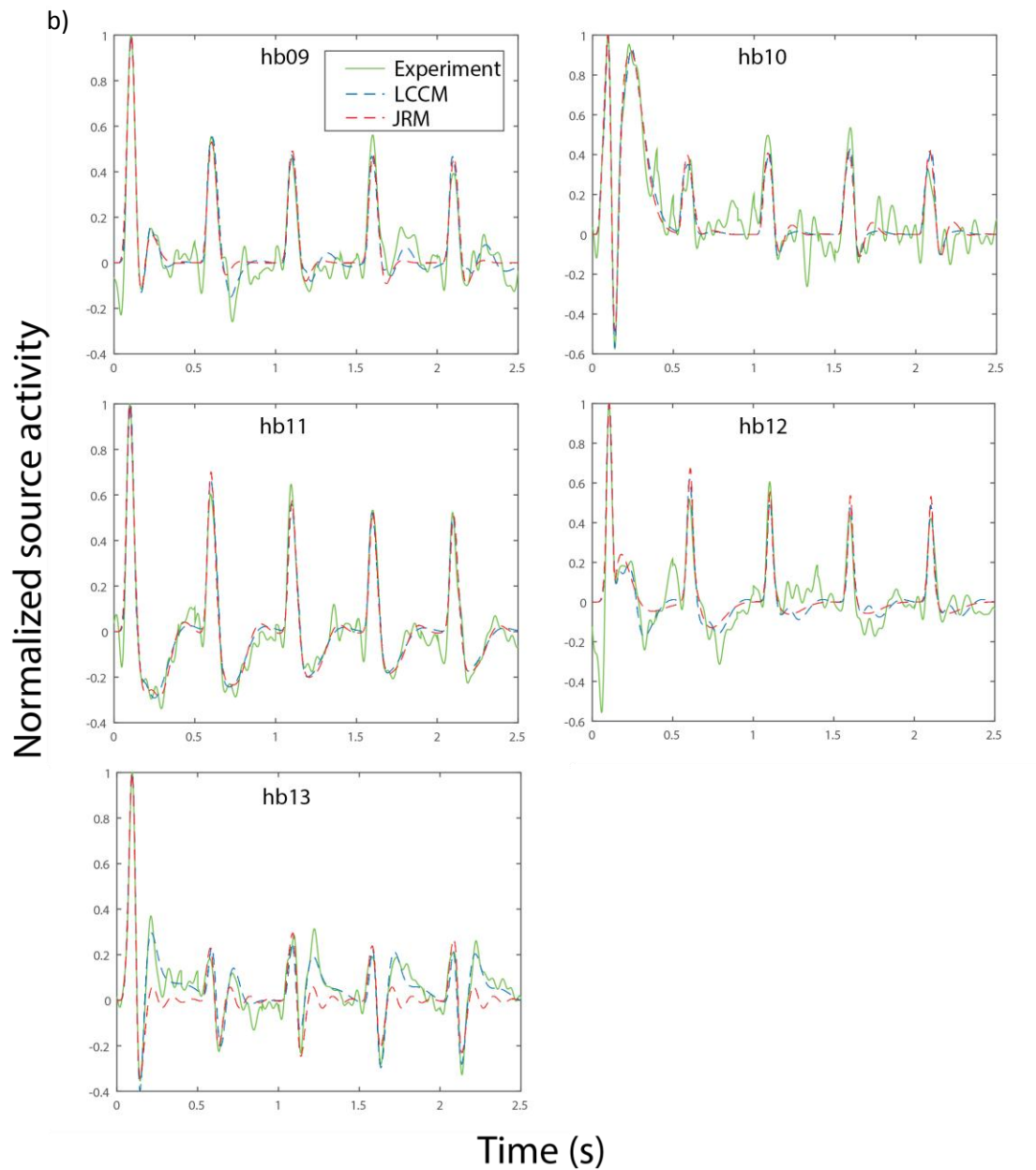


*Note.* LCCM = local cortical circuit model, JRM = Jansen and Rit model.

**Figure 3.5 Goodness of fits for the first five responses.**



*Note.* LCCM = local cortical circuit model, JRM = Jansen and Rit model.



*Note.* LCCM = local cortical circuit model, JRM = Jansen and Rit model.

**Figure 3.6 Individual fitting results.** The figures a) and b) show the individual fitting results of the estimated source activity of the N100m source generator by using LCCM as well as JRM. Five identical auditory stimuli were presented at 0s, 0.5s, 1s, 1.5s as well as 2s.

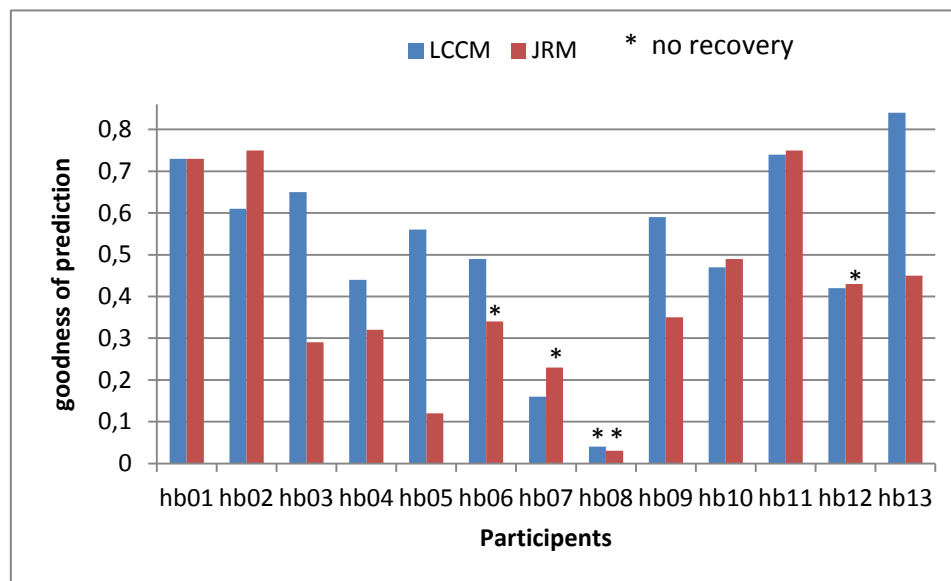


### 3.1.5.2.2 Comparison of the goodness of prediction

The goodness of prediction for the last 5 responses of both the LCCM as well as the JRM are shown in Figure 3.7. The value table is documented in Appendix A, Table A.2.

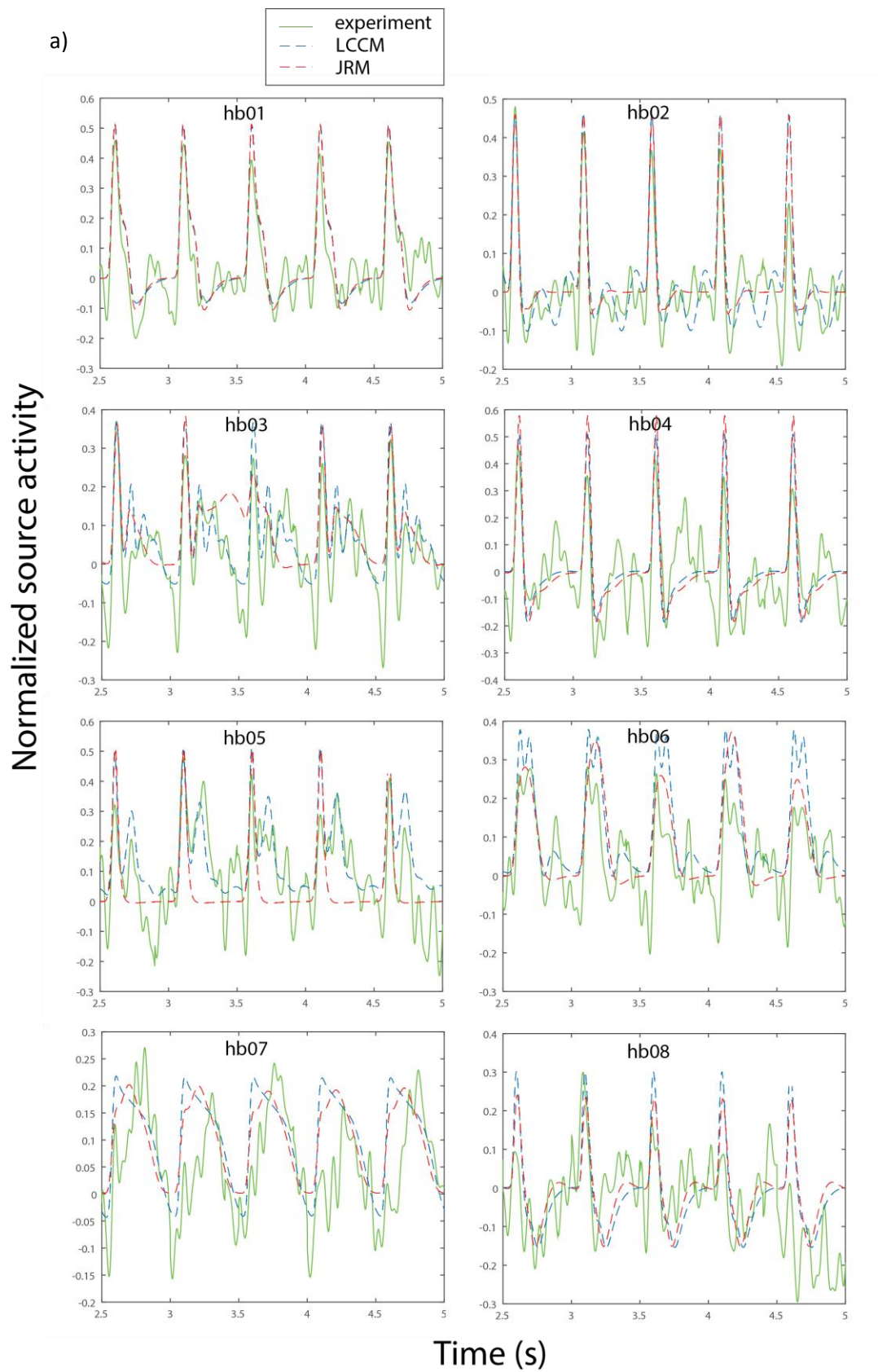
The goodness of predictions (GoPs) describe how well the model can be used to predict future data. The mean GoP of the LCCM was 0.52, the mean GoP of the JRM was 0.41. The p value of the one way ANOVA-test was 0.13. There is no significant benefit in respect to predicting future data by the LCCM.

Both the LCCM and the JRM were able to qualitatively simulate the preservation of the n100m amplitude at the presentation of the 6th-10th. The individual prediction results are shown in Figure 3.8.

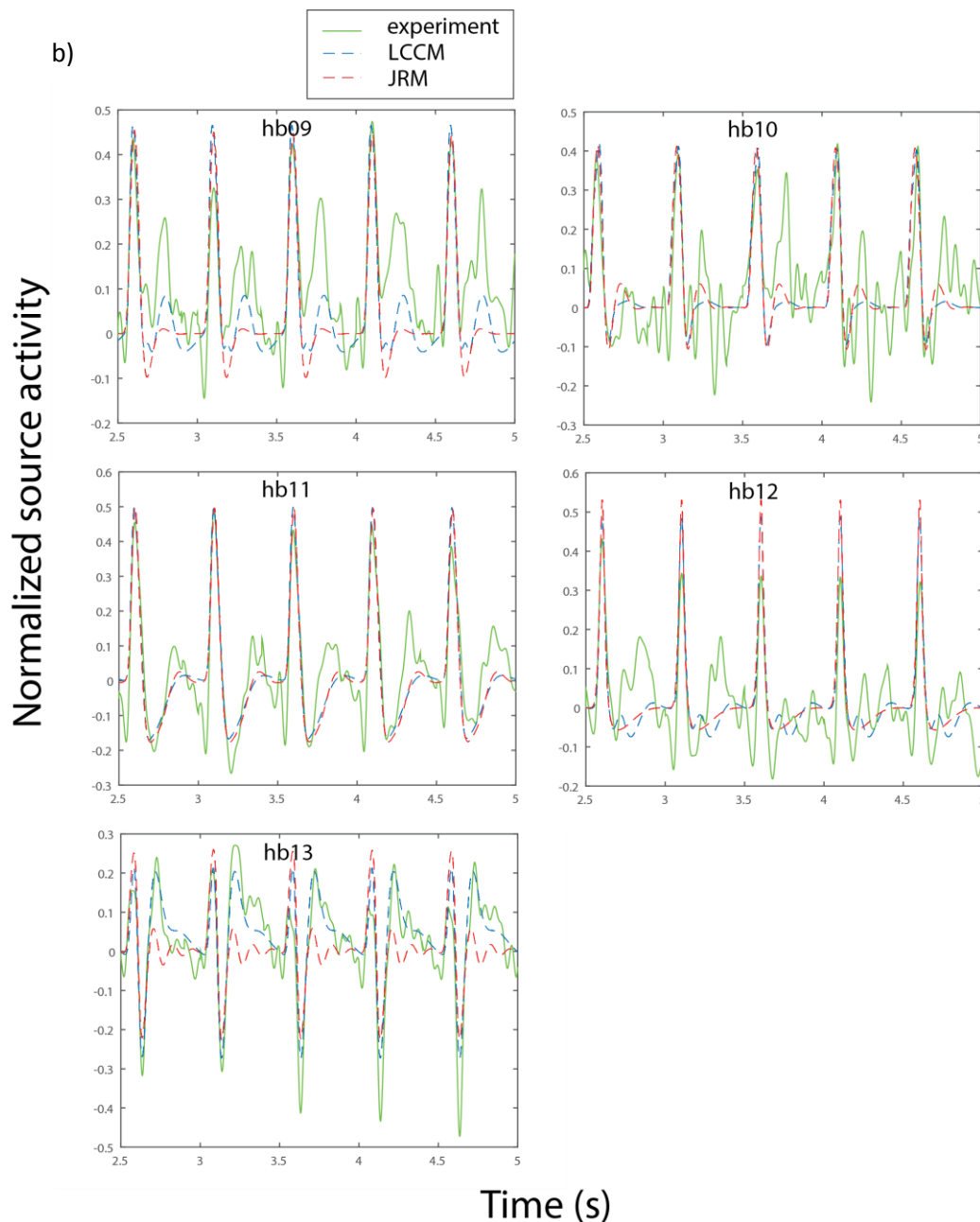


*Note.* LCCM = local cortical circuit model, JRM = Jansen and Rit model. no recovery = after 10s stimulus free time, the simulated source activity is not able to fully recovered from the habituation.

**Figure 3.7 Goodness of predictions for the last five responses**



Note. LCCM = local cortical circuit model, JRM = Jansen and Rit model.



Note. LCCM = local cortical circuit model, JRM = Jansen and Rit model.

**Figure 3.8 Individual prediction results.** The figures a) and b) show the individual prediction results of the estimated source activity of the N100m source generator by using LCCM as well as JRM. Five identical auditory stimuli were presented at 2.5s, 3.5s, 3.5s, 4s as well as 4.5s, directly after the adaptation of five stimuli (ISI = 500ms).

Furthermore, the adaptation (using 10 stimuli) - recovery (10s stimuli free time) - adaptation (using 10 stimuli again - circle (Fig. 3.9) was simulated for each estimated model. Four JRMs (hb06, hb07, hb08, hb12) as well as one LCCM (hb08) failed to simulate the recovery process.

Note that the LCCM of hb08 as well as of hb07 were discarded and removed from further analysis in consideration of their bad GoP.

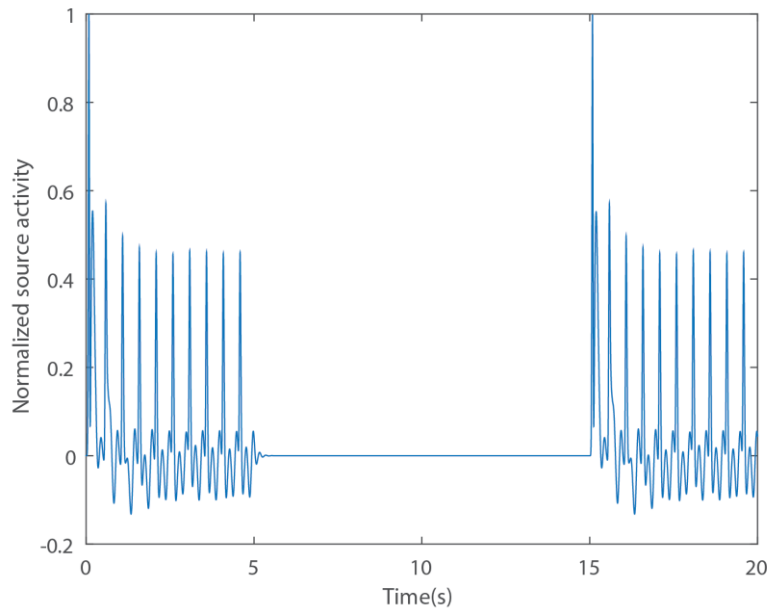


**Figure 3.9 Simulation of a 10 stimuli - 10 second pause - 10 stimuli - circle.** The estimated local cortical circuit models as well as the Jansen and Rit models were used to stimulation the adaptation-recovery-adaptation circle. It was expected that after 10s stimulus free time the amplitude of the first response should able to recover. The models were estimated from subject hb02.

### 3.1.5.2.3 Comparison of the model evidence

The Bayesian factor (see **Chapter 2.2.4**) describes how one model is "more" favored than another in respect to the observed data. According to Equation (67), the log Bayesian factor was computed as:

$$\ln B = \ln(p(y|m=LCCM)) - \ln(p(y|m=JRM)) \quad (80)$$

By a value  $B > 20$ , equivalent to  $\ln(B) > 3$ , means that the data favors the LCCM more than the JRM.

Twelve of the thirteen participants' data favored the LCCM (Fig. 3.10). The value table is documented in Appendix A, Table A.2.

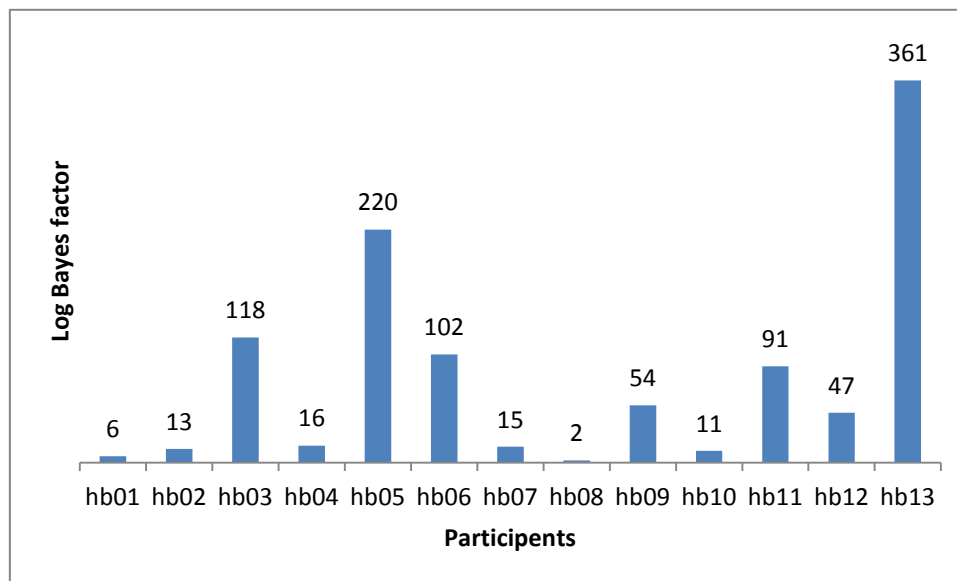


**Figure 3.10 Log Bayesian factors.** The Bayesian factors described the differences of the log model evidence between LCCM and JRM (LCCM minus JRM). By a value bigger as three mean that the observed data strongly favor the LCCM.

### 3.1.5.3 Simulated adaptation effect with different stimulation frequencies

To study the relationship between the adaptation level and the ISIs, the estimated LCCMs were used to simulate the evoked source activity in source space with different stimulation frequencies.

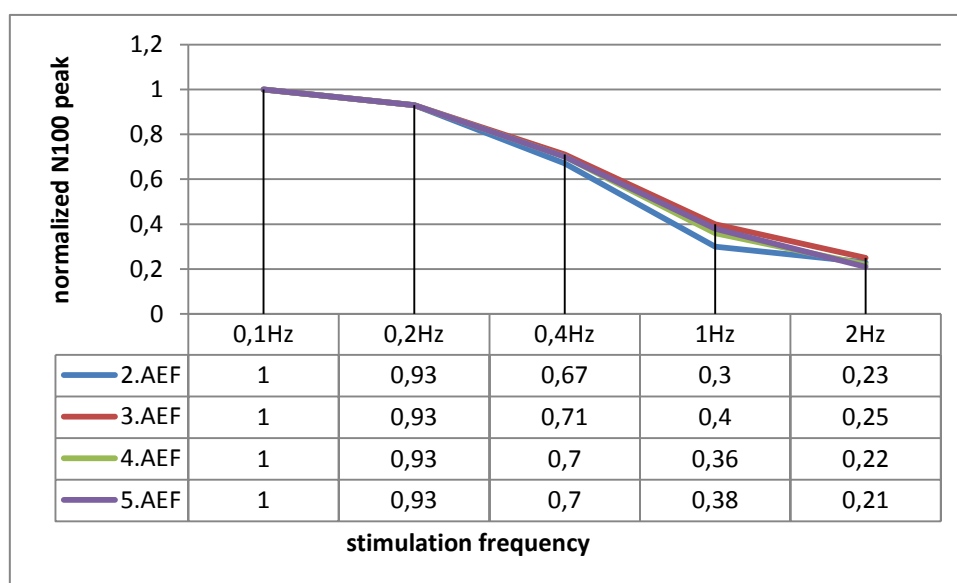
Each model was stimulated with 5 stimuli with followed ISIs:

stimulation frequency	0.1 Hz	0.2 Hz	0.4 Hz	1Hz	2Hz
ISI	10 s	5 s	2.5 s	1 s	500 ms

The N100m peak amplitudes of each corresponding response (1.AEF, 2.AEF, 3.AEF, 4.AEF and 5.AEF) evoked by different stimulation frequencies were recorded and normalized of the first evoked N100m peak (1.AEF) (Fig. 3.11). The mean values of 11 participants (having removed

hb07 and hb8) are listed in Table 3.3. The value table for each estimated LCCM is documented in Appendix A, Table A.2.

No adaptation was observed in the simulation when the stimulation frequency dropped lower than 0.2Hz (ISI longer than 5s) (Fig. 3.12). With higher stimulation frequency such as 2Hz (ISI = 500ms), the second AEF already decreased by about 50% (Fig.3.12).



*Note.* AEF = auditory evoked field

### Figure 3.11 Simulation of auditory adaptation with different inter-stimuli-intervals

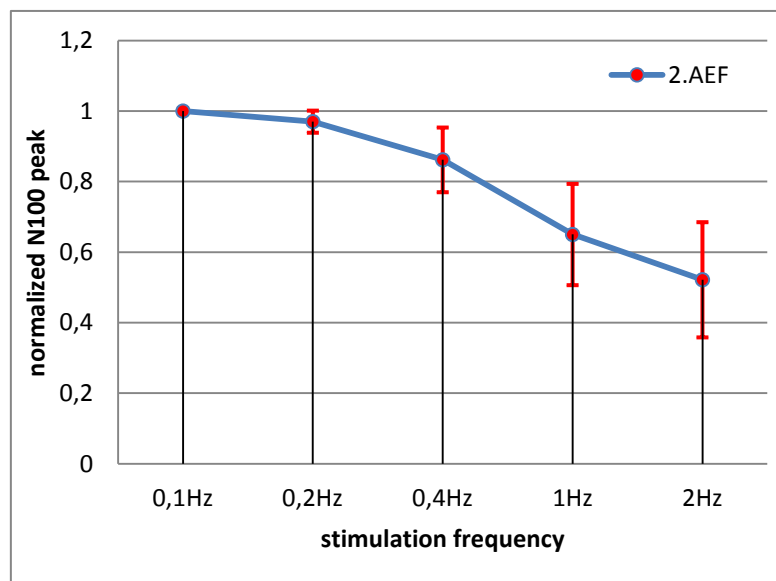
The estimated LCCM (of hb13) was used to simulate the adaptation effect with different ISIs (10s, 5s, 2.5s as well as 500ms). The N100m peak amplitudes of five evoked responses (in source space): 1.AEF, 2.AEF, 3.AEF, 4.AEF and 5.AEF were recorded and normalized of the first evoked N100m peak (1.AEF). This figure shows that the strength of the evoked N100m is dependent on the stimulation frequency. Higher stimulation frequencies evoke stronger adaptation. With 0.1 Hz stimulation frequency (ISI = 10s), there was no adaptation to be observed. With stimulation frequency 1 Hz, strong adaptation was already observable at the second response (2.AEF).

**Table 3.3 Adaptation in respect of the stimulation frequency**

mean $\pm$ std	0,1Hz	0,2Hz	0,4Hz	1Hz	2Hz
<b>2. AEF</b>	1 $\pm$ 0,009	0,97 $\pm$ 0,03	0,86 $\pm$ 0,09	0,65 $\pm$ 0,14	0,52 $\pm$ 0,16
<b>3. AEF</b>	1 $\pm$ 0,009	0,97 $\pm$ 0,03	0,86 $\pm$ 0,08	0,62 $\pm$ 0,1	0,45 $\pm$ 0,11
<b>4. AEF</b>	1 $\pm$ 0,009	0,97 $\pm$ 0,03	0,86 $\pm$ 0,09	0,61 $\pm$ 0,11	0,43 $\pm$ 0,11
<b>5. AEF</b>	1 $\pm$ 0,009	0,97 $\pm$ 0,03	0,86 $\pm$ 0,09	0,61 $\pm$ 0,11	0,42 $\pm$ 0,11

Note. AEF = auditory evoked field, std = standard deviation.

The LCCM simulated source activities at the N100m peak time. The amplitudes were normalized to the first AEF and averaged over 11 participants. No adaptation was observed when the stimulation frequency dropped lower than 0.2 Hz. With higher stimulation frequency such as 2 Hz, the second AEF already decreased about 50%.



	0,1 Hz	0,2 Hz	0,4 Hz	1 Hz	2 Hz
<b>mean</b>	1	0,97	0,86	0,65	0,52
<b>std</b>	±0,01	±0,03	±0,10	±0,14	±0,16

Note. AEF = auditory evoked field, std = standard deviation.

### Figure 3.12 Simulation of adaptation of paired stimuli with different stimulation frequencies

The estimated LCCM of each participant was used to simulate the adaptation level of different ISIs (10s, 5s, 2.5s as well as 500ms). The amplitudes were normalized of the N100m of the first evoked response and averaged over 11 participants.

### 3.1.5.4 Laminar organization of the synaptic connections

#### 3.1.5.4.1 Synaptic pathways

##### *Estimated "uncertain" connections*

In the LCCM, there were six connections (EIN->dPC, dPC->EIN, dPC->sPC, sPC->dIIN, dPC->siIN) assumed to be zero at the beginning. The estimated results are listed in Table 3.4.

**Table 3.4** Estimated "uncertain" connections. Non-zero connections are marked with "X".

	Parallel	Inter-laminar		Inter-laminar		Backwards
	pathway	excitatory		inhibitory		
	EIN->dPC	sPC->dIIN	dPC->siIN	siIN->dPC	dIIN->sPC	dPC->sPC
<b>hb01</b>	x	x		x	x	
<b>hb02</b>	x	x	x		x	
<b>hb03</b>	x				x	
<b>hb04</b>	x				x	x
<b>hb05</b>	x	x	x	x		
<b>hb06</b>		x	x	x		
<b>hb09</b>	x			x	x	
<b>hb10</b>		x			x	x
<b>hb11</b>	x	x			x	x
<b>hb12</b>	x					
<b>hb13</b>	x		x	x		
<b>counter</b>	81%	54%	36%	45%	63%	27%

*Note.* EIN = excitatory interneurons, sPC = superficial pyramidal cells, siIN = superficial inhibitory interneurons, dPC = deep pyramidal cells, dIIN = deep inhibitory interneurons. "x" = the connection is estimated away from zero.

The posterior distribution of the estimated parameter is Gaussian. The criterion for a



non-zero estimation was defined as: the value zero should be inside the 0-5% quantile of the posterior distribution (Fig. 3.13):

$$\varphi_{\varphi|y} - 1.6\sigma_{\varphi|y} - 0 > 0 \quad (81)$$

where  $\varphi_{\varphi|y}$  is the estimated mean of the posterior,  $\sigma_{\varphi|y}$  is the estimated standard deviation.

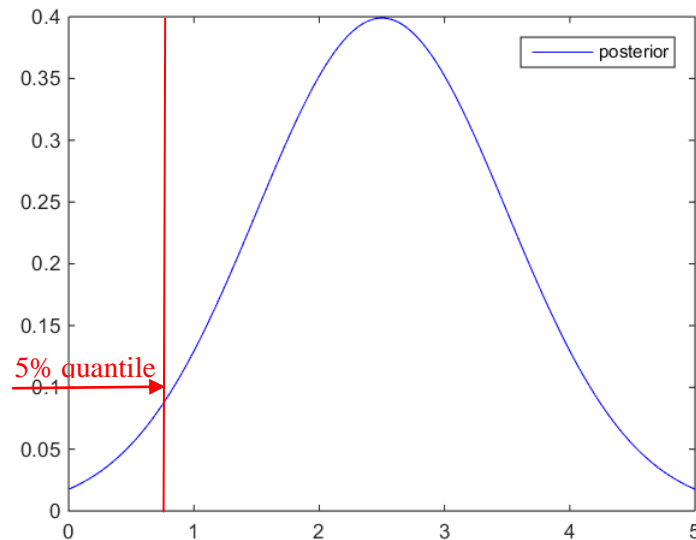


**Figure 3.13 The 5% quantile of a normal distribution.** The figure shows a Gaussian distribution  $N\sim(2.5,1)$ . The upper boundary of the 5% quantile is 0.9. The value zero is inside the 5% quantile.

In this study, the connection probabilities of the "uncertain" connections were counted on the occurring frequency (the number of subjects with a non-zero estimate). The "uncertain" connections over 60% probability are illustrated in red in Figure 3.14.

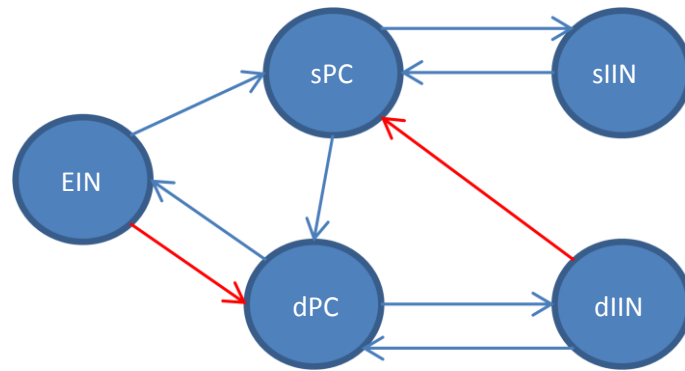


**Figure 3.14 Estimated laminar connection pattern of the N100m source generator.** "Certain connections" are shown in blue, "uncertain" connections over 60% probability are shown in red. EIN = excitatory interneurons, sPC = superficial pyramidal cells, dPC = deep pyramidal cells, sIIN = superior inhibitory interneurons, dIIN = deep inhibitory interneurons.

**Pathway/Connection patterns analysis**

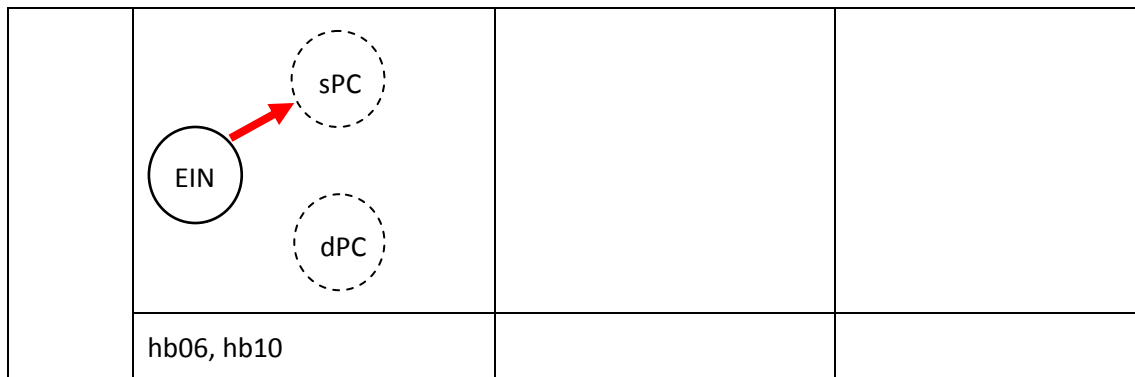
In this section, the laminar connection patterns in respect of having the same NM origin were analyzed. The connection strengths were normalized to the  $C_{esp}$  (EIN->sPC). All available connections that originated from the same NM were compared. The most prominent connections were marked in red. The value table is documented in the Appendix, Table A.4

**Table 3.5 Estimated most prominent connections in auditory N100m source generator**

from	Connection Pattern	
sPC:		
	hb01, hb02, hb06, hb10, hb11	hb05

	hb03, hb04, hb09, hb12, hb13		
<b>dPC:</b>			
	hb01, hb09, hb12	hb03	
	hb02, hb05	hb06	hb13
hb04, hb11	hb10		
<b>sIIN:</b>			

	hb01, hb09, hb13	hb05, hb06	
	hb02, hb03, hb04, hb10, hb11, hb12		
<b>dIIN:</b>			
	hb01, hb03	hb02, hb04, hb09, hb10, hb11	
	hb05, hb06, hb12, hb13		
<b>EIN:</b>			
	hb01, hb11, hb12, hb13	hb02, hb03, hb04, hb05, hb09	



*Note.* sPC = superficial pyramidal cells, dPC = deep pyramidal cells, EIN = excitatory interneurons, sIIN = superficial inhibitory interneurons, dIIN = deep inhibitory interneurons,

Those connections that have the same original NM were compared in their connection strength.

The most prominent one was marked in red.

According to Table 3.5:

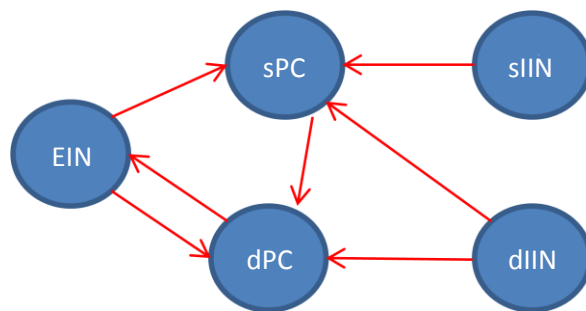
(1) Six of the eleven models favored the serial pathway (EIN->sPC) and two of them suggested there was no parallel pathway (EIN->dPC). Additionally, five of the eleven models favored the parallel pathway. The simulation results did not show which signal pathway was more prominent after the thalamic input arrived at layer IV.

(2) Suggested by ten of the eleven models, the most prominent connection from sPC is the connection from sPC to dPC.

(3) The most prominent connection from dPC is the feed forward connection from dPC to EIN.

(4) The sIIN (9 of 11) seemed to send the most prominent inhibitory connection to the pyramidal cells of the same layer. In contrast, it is hard to ascertain which kind of inhibitory connection from deep layers V/VI (dIIN) is more prominent, the intra-inhibitory (6 of 11) or the inter-inhibitory (5 of 11).

The estimated most prominent signal pathways of the auditory N100m source generator are illustrated in Figure 3.15.



*Note.* sPC = superficial pyramidal cells, dPC = deep pyramidal cells, EIN = excitatory interneurons, sIIN = superficial inhibitory interneurons, dIIN = deep inhibitory interneurons,

**Figure 3.15 The estimated prominent laminar signal pathways of the auditory N100m source generator.** After the thalamic input reaches the layer IV excitatory interneurons, the signal may proceed following a serial pathway (EIN->sPC) as well as a parallel pathway (EIN->dPC). The prominent synaptic connection from superficial pyramidal cells is sPC-> dPC. The prominent synaptic connection from deep pyramidal cells is dPC->EIN. The prominent inhibitory connection from superficial inhibitory interneurons is sIIN->sPC. The deep inhibitory interneurons inhibited both superficial as well as deep pyramidal cells.

### 3.1.5.4.2 Synaptic dynamics

#### *Adaptation patterns*

The estimated LCCMs were stimulated with ten identical stimuli (ISI = 500ms). Among the synaptic connections, the adaptation-recovery patterns can be categorized into three types according to when they reach the maximal adaptation level ( = lowest connection efficacy, the maximal value of connection efficacy is 1 ) as well as how they preserve it (Fig. 3.16).

Type A: The synaptic connection already reaches its maximal adaptation level during the first stimulus.

Type B: The synaptic connection reaches its maximal adaptation level during the stimulus occurring after the first one.

Type C: The synaptic connection has a maximal adaptation level during the first stimulus, but it decreased with each additional stimulus and converged at a much lower adaptation level (= higher connection efficacy).

The details of each connection type for each estimated LCCM are listed in Table 3.6. Figure 3.17 illustrated a histogram of the connection types.

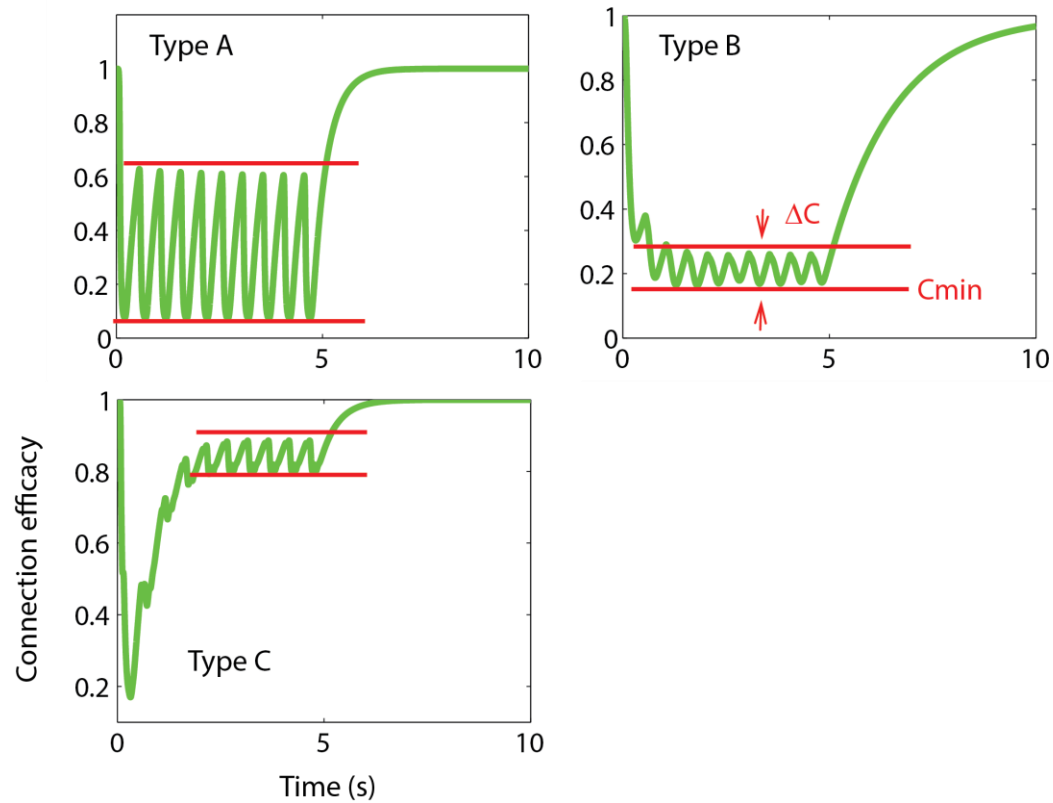
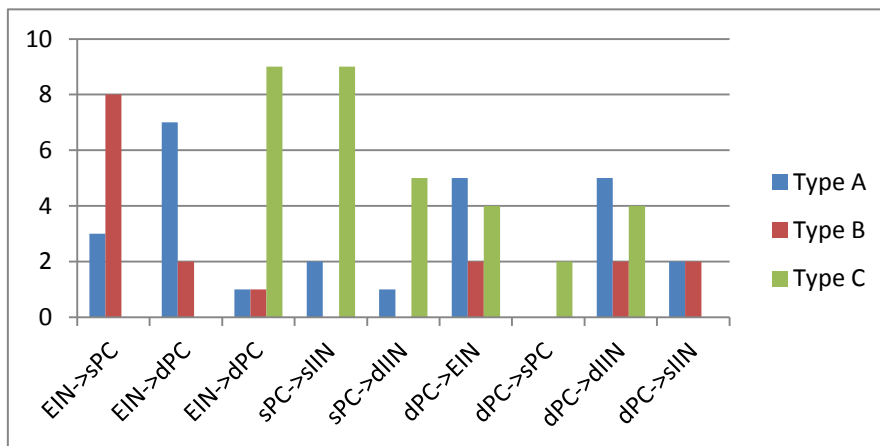


**Figure 3.16 Adaptation-recovery patterns of laminar synaptic connections.** Estimated LCCMs were stimulated with a simulation train of ten identical tones with ISI 500ms. Adaptation-recovery patterns of the synaptic connections can be categorized into three types (A, B and C, see text for details) according to how they reach their maximal adaptation level as well as how they preserve it. The line  $C_{min}$  marked the boundary of the lowest connection efficacy after adaptation (converged). The interval  $\Delta C$  illustrated the amount of the recovered connection efficacy inside the 500ms inter stimuli interval.



note. EIN = excitatory interneurons, sPC = superficial pyramidal cells, dPC = deep pyramidal cells, sIIN = superficial inhibitory interneurons, dIIN = deep inhibitory interneurons

Figure 3.17 Histogram of the adaptation-recovery patterns

Table 3.6 Adaptation-recovery pattern of each laminar synaptic connection

	e->sp	e->dp	sp->dp	sp->si	sp->di	dp->e	dp->sp	dp->di	dp->si
hb01	B	A	A	A	A	C	-	C	-
hb02	B	B	C	C	C	A	-	A	A
hb03	B	A	C	C	-	A	-	A	-
hb04	B	A	C	C	-	A	-	A	-
hb05	A	B	C	C	C	B	-	B	B
hb06	B	-	C	C	C	B	-	B	B
hb09	B	A	C	C	-	A	-	A	-
hb10	B	-	C	C	C	C	C	C	-
hb11	B	A	C	C	C	C	C	C	-
hb12	A	A	B	A	-	C	-	C	-
hb13	A	A	C	C	-	A	-	A	A

note. e = excitatory interneurons, sp = superficial pyramidal cells, dp = deep pyramidal cells, si = superficial inhibitory interneurons, di = deep inhibitory interneurons.

The Adaptation-recovery patterns of laminar synaptic connections are categorized into three types (A, B and C, see text for details). "-" means that the estimated connection strength is zero.



The simulated results suggested that those synaptic connections originating from sPC mostly have the adaptation pattern type C. The serial pathway (EIN->sPC) mostly have the pattern type B, the parallel pathway (EIN->dPC) mostly have the pattern type A.

### **Adaptation recovery dynamics**

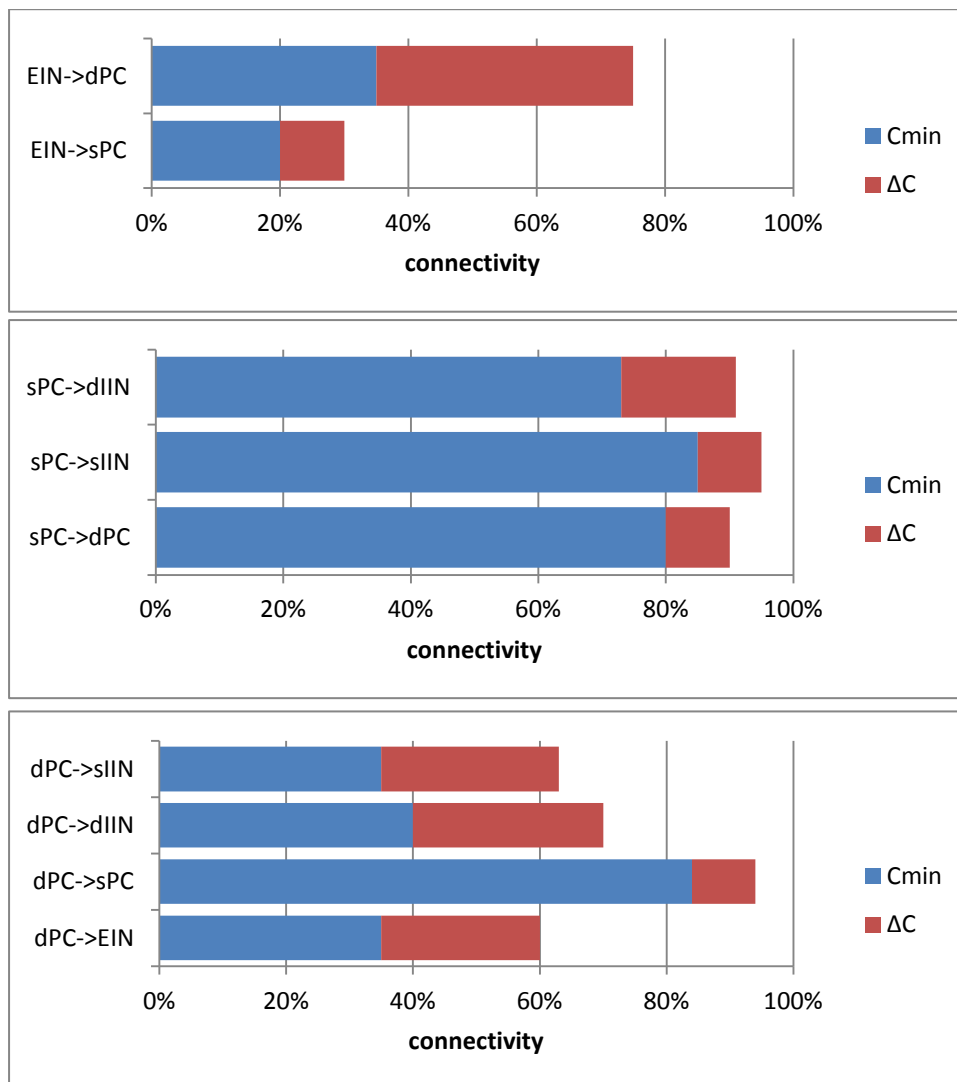
For each estimated LCCM, the maximal adaptation level  $C_{min}$  (converged after 4-6 stimuli) as well as the recovered amount innerhalb 500ms  $\Delta C$  (Fig. 3.16) are documented in Appendix A, Table A.5. The median values are illustrated in Table 3.7 as well as in Figure 3.18. Note that the synaptic connections dPC->sPC, dPC->siIN as well as sPC->diIN had less than five candidates for statistic analysis. The histograms of  $C_{min}$  and  $\Delta C$  for all excitatory connections are illustrated in Figure 3.19.

The simulation result showed that those connections originating from EIN as well as deep dPC were strongly suppressed by the repetition of the stimulus. In contrast, the connections originating from superficial pyramidal cells were less affected. The serial connection pathway (e->sp) was strongly suppressed but recovered less in comparison to the parallel connection pathway (e->dp) (Fig. 3.18)

**Table 3.7 The median values of the connection efficiency after adaptation as well as the median values of the amount of recovery inside 500ms.**

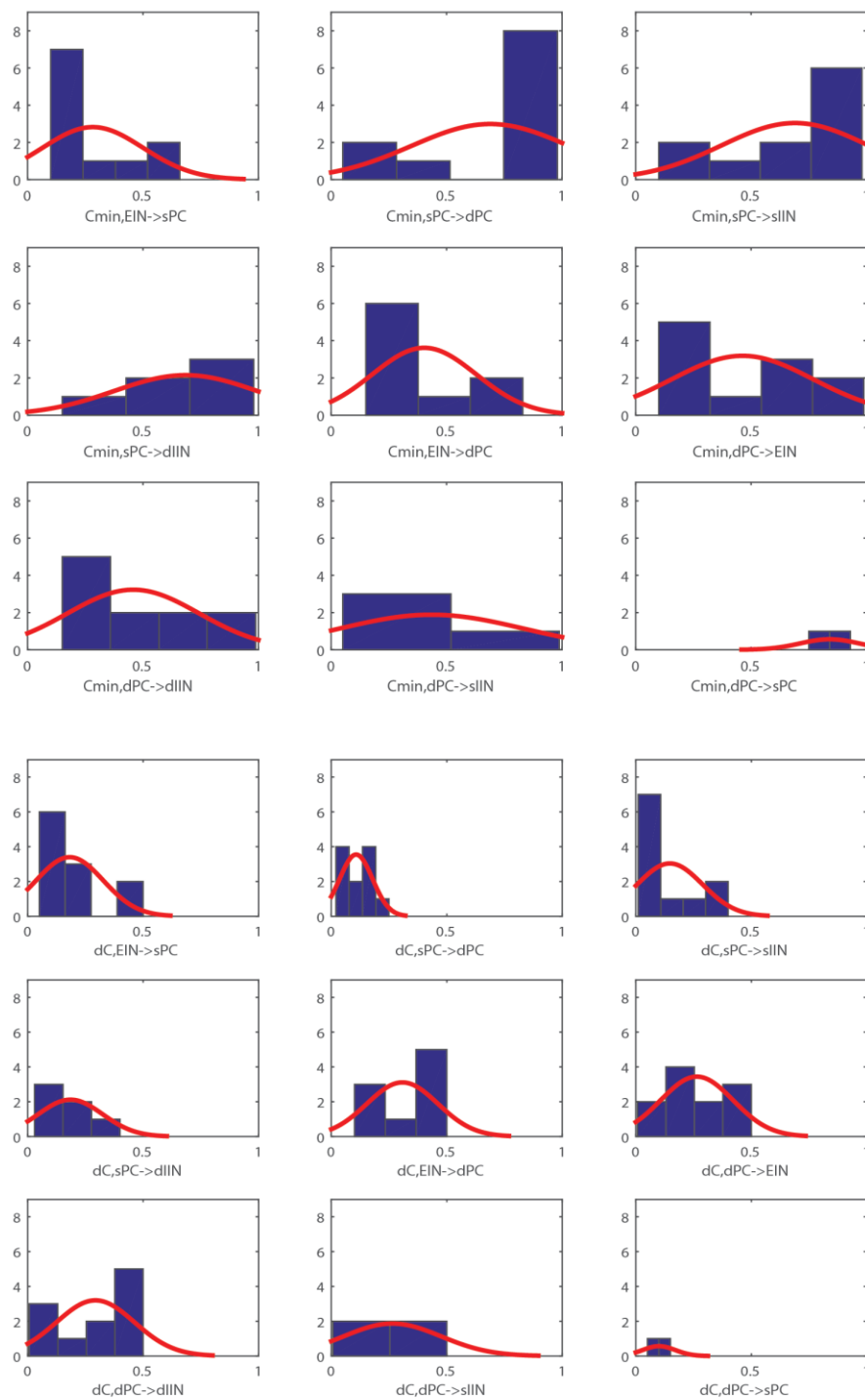
	$C_{min}$	$\Delta C$		$C_{min}$	$\Delta C$
<b>EIN-&gt;sPC</b>	0,2	0,1	<b>dPC-&gt;EIN</b>	0,35	0,25
<b>EIN-&gt;dPC</b>	0,35	0,4	<b>dPC-&gt;sPC</b>	0,84	0,1
<b>sPC-&gt;dPC</b>	0,8	0,1	<b>dPC-&gt;diIN</b>	0,4	0,3
<b>sPC-&gt;siIN</b>	0,85	0,1	<b>dPC-&gt;siIN</b>	0,35	0,28
<b>sPC-&gt;diIN</b>	0,73	0,18			

*Note.* EIN = excitatory interneurons, sPC = superficial pyramidal cells, dPC = deep pyramidal cells, siIN = superficial inhibitory interneurons, diIN = deep inhibitory interneurons.  $C_{min}$  = lowest connection efficacy after 6 stimuli.  $\Delta C$  = amount of recovered connection efficiency in 500ms.



*note.* EIN = excitatory interneurons, sPC = superficial pyramidal cells, dPC = deep pyramidal cells, sIIN = superficial inhibitory interneurons, dIIN = deep inhibitory interneurons.

**Figure 3.18 Estimated adaptation - recovery dynamics of the synaptic connections.** Eleven estimated LCCMs were stimulated with a simulated train of ten identical tones with ISI=500ms. The blue bar illustrates the median value of each connection efficiency after the adaptation (converged after 6 stimuli ). The red bar illustrates the median value of the amount of recovery for each connection inside the 500ms inter stimuli interval. The maximum connection efficiency is 1 (before the stimuli presentation).



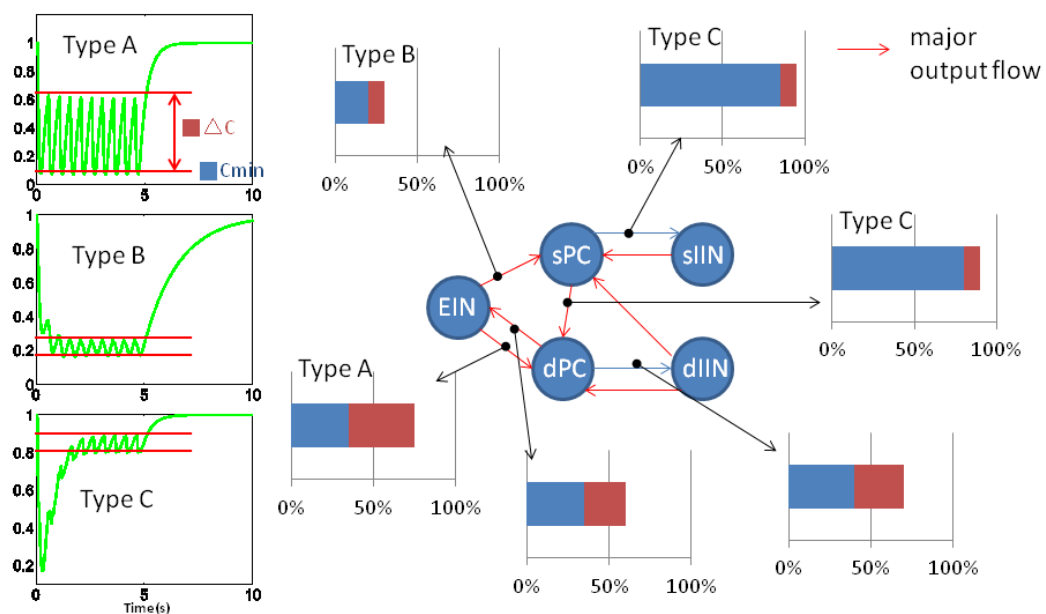
*note.* EIN = excitatory interneurons, sPC = superficial pyramidal cells, dPC = deep pyramidal cells, sIIN = superficial inhibitory interneurons, dIIN = deep inhibitory interneurons, Cmin = lowest connection efficiency after 6 stimuli, dC = amount of recovered connection efficiency within 500ms.

**Figure 3.19 Histograms of synaptic adaptation - recovery dynamics**

### 3.1.6 Discussion and conclusion

The LCCM extends the NMM proposed by Jansen and Rit [6] by distinguishing populations in three different cortical layers (input layer IV, superficial layers II/III and deep layers V/VI) with anatomically motivated intra- as well as inter-layer connections. The excitatory connections among the neural populations were endowed with dynamic synapses. These synapses decreased their efficacy in response to the input and recovered spontaneously. The rate of this adaptation was related to the processes of exhaustion and recycling of neurotransmitters, in this case glutamate. The modeling results show that these assumptions are sufficient to reproduce the adaptation as well as the recovery effects in the observed experiment. Furthermore, the employed Bayesian inference technique allowed us to examine both model structure and model parameters. It enabled the observed data to identify the most probable signal flow circuits inside a defined cortical area as well. The results suggest that beside the main signal flow, which first ascended from input layer IV to superficial layers and then ran down to the deep layers, there possibly exists a “short-cut” parallel input flow running directly from layer IV into deep layers. The results also show that the excitatory signal flow from the pyramidal cells to the inhibitory interneurons seemed to be preferably intra-laminar, in contrast, the signal flow from the deep inhibitory interneurons to the pyramidal cells seems to be both intra- and interlaminar. The most prominent excitatory signal circuit is suggested to be EIN->sPC->dPC->EIN as well as EIN->dPC. The most prominent inhibitory connections might be sIIN->sPC, dIIN->dPC as well as dIIN->sPC. Further interesting findings were acquired through the examination of the estimated temporal dynamics of the connection strengths. Three different adaptation patterns were observed in the simulation: Type A, which arrived the maximal adaptation during the first stimulus and preserved it by the further presentations of the stimulus; Type B, which reached the maximal adaptation during the stimulus occurring later than the first one; Type C, which has the maximal adaptation during the first stimulus, but it decreased with each additional presentation of stimulus and converged after 4-6 stimuli. It is found

that the connections originating from sPC prefer Type C. The serial pathway (layer IV -> layers II/III ) as well as the parallel pathway (layer IV -> layers V/VI) seem to have different adaptation patterns: respectively Type B and Type A. Finally, the serial pathway is also far more suppressed by the adaptation process than the parallel pathway, and the serial pathway is also recovered slower. The synaptic connections from sPC seem to be less affected by the stimuli repetition in comparison to those originating from dPC as well as from EIN. These computational findings are summarized and illustrated in Figure 3.20.



*Note.* EIN = excitatory interneurons, sPC = superficial pyramidal cells, dPC = deep pyramidal cells, sIIN = superficial inhibitory interneurons, dIIN = deep inhibitory interneurons,  $C_{min}$  = lowest connection efficiency after 6 stimuli.  $\Delta C$  = amount of recovered connection efficiency within 500ms.

**Figure 3.20 Summarized computational findings for the N100m source generator in right Heschl's gyrus.**

The most challenging part of the interpretation of the computational findings (in fact, the most challenging part of the modeling in general) was to show that our model is reasonable in terms of the reflected level of detail and physical realism. Concerning detail, the model should be adapted to the quality and the quantity of the available data as well as to the

questions the model is supposed to answer. Physical realism concerns the interpretability of structure, state variables, and parameters of the model in terms of physically observable quantities. The LCCM is a suitable candidate for modeling cortex as will be discussed, with respect to the aforementioned aspects, in the following sections.

### ***LCCM versus JRM***

According to the GoF (Fig. 3.5) as well as GoP (Fig. 3.7), there was no significant statistic difference supporting the claim that the LCCM yielded a better fitting than the JRM in respect to the main N100m peak. However, the LCCM might have a small advantage in mimicking the later component (after 130ms) of the source activity (fitting details, see Fig. 3.6) as well as the recovery from the adaptation (Fig. 3.7). Why and in what respect is the LCCM proposed in this work more biologically realistic than the classical model of Jansen and Rit?

The cortex has a clear laminar structure and neural populations in different layers are structurally and functionally different. In particular, the cortical connections are layer-dependent: forward and backward connections target different neural populations in different layers [41]: the sPC projects to the input layers and superficial layers of other cortical areas, while the dPC sends its axons through the white matter to more distant cortical and subcortical areas. The JRM features only one neural mass of pyramidal cells and is, therefore, not capable of separating the different types of long-range connectivity. Using separate supra- and infragranular populations also allows a distinction to be made between different local information processing schemes (serial vs. parallel pathway) that might relate to different cognitive functions. It is also worth noting that in the original JRM the synaptic connections are constant, therefore without the short-term synaptic plasticity model, it alone can not explain the observed adaptation of the AEF. In these respects, the LCCM constitutes an improvement in biological realism as compared to the JRM. This improvement appears relevant in light of the available MEG data as shown by our model comparison results (Fig. 3.10). It is expected that the LCCM will be useful in building more extended

models in the future, endowing them with the above-described advantages.

### ***Laminar connections and signal flow***

In this study, MEG recordings were combined with the LCCM in order to infer the laminar connections in the auditory cortex. It was postulated that there are thirteen connections within and between cortical layers divided into “certain” and “uncertain” (with logarithmic and quadratic prior, respectively connections. The results show that, in some subjects, beside the main serial excitatory signal flow circuit (layer IV → layers II/III → layers V/VI), a “short-cut” parallel pathway allows the sensory input directly from EINs access to the pyramid cells in deep layers V/VI. The functional meaning of this finding is not entirely clear. The serial and parallel pathway could be related to “specific” and “unspecific” input; in this case, the “unspecific” input might be able to bypass the superficial layer through the connection EIN→dPC [86]. Clearly, the question remains as to whether this phenomenon is universal but not visible in some subjects due to unfortunate anatomical circumstances or other peculiarities of measurement, or if there are variable processing modes across subjects.

Another interesting finding was that most of the models (10 of 11) needed a cross-layer inhibition in order to achieve reasonable fitting results. Seven of them suggested an inter-layer inhibitory connection from deep inhibitory interneurons (dIIN→sPC) (Table 3.5). Among the seven, five suggested that this inter-layer inhibition was even stronger than intra-layer inhibition (dIIN→dPC) (Table 3.5). This result might suggest that the hierarchical signal flow descending from superficial to deep layers is excitatory dominate but the signal flow ascending from deep layers to superficial layers is inhibitory dominate.

From the computational evidence of the laminar signal flows, the author postulates a hypothesis of the information processing schema in the sensory cortex. For the important sensory input, the input information will be send to the superficial layers II/III for the processing and from there it will be further sent to higher cortical areas. For the unimportant sensory input, this signal will "bypass" layers II/III and be sent directly to the

deep layers V/VI. The signal processing in sPCs will be strongly suppressed through the adaption on input (EIN->sPC) as well as the inhibition from deep layers (dIIN->sPC), therefore the information flows to the higher cortical area for the further processing will be suppressed. The Author hopes that this hypothesis will interest neuroscientists to test it in animal models and it may inspire the future animal studies to look into the functional laminar connectivity associatively with the special feature of the stimulations.

### ***Modeling adaptation***

In this study, the short-term adaptation of the N100m and its recovery was successfully reproduced via a dynamic modification of the synaptic strength. The simulations of the different ISIs (Table. 3.3) were qualitatively in agreement with the previous experiment observations [125, 175] and suggests that the auditory adaptation effect last around 5s. This may give a hint to the auditory short-term memory time. The suppression and recovery of the synaptic connections were related to the exhaustion and refilling of the neural vesicles at the readily releasable pool. The key notion is that the brain is not a static machine nor does it have unlimited resources. The brain will change its reaction to the incoming information depending on strategies of how to assign these resources. It is worth noting that we did not directly modify our model output with an adaptation rule based on phenomenological observation as was the case in previous work by Laxminarayan and colleagues [190] developing an NMM for rat EEG or by Petersen [182] modeling the excitatory postsynaptic potentials on single neuron level. Instead, a physiologically motivated process was implemented to generate dynamic synapses in the NMM, which increased the biological plausibility. The observed stimuli repetition related short-term adaptation is only the final result of a series of dynamic processes. In other words, the main purpose here was not to just to mimic the phenomenon of adaptation (like parameterized curve fitting), but to develop a simple yet biological plausible model, which contains sufficient detail to reproduce this aspect of real brain activity and makes testable predictions on the underlying mechanisms. These mechanisms may concern, for example, the recycling



rate of neurotransmitters, the effect of ISIs, the different suppression patterns of the connection, and the existence of a parallel bypass pathway.

## **3.2 Modeling somatosensory adaptation - a pilot application in Alzheimer's disease study**

### **3.2.1 Motivation**

#### ***Alzheimer's disease***

According to the fact report [191] of the World Health Organization in 2015, Alzheimer's disease (AD) is the most common cause of dementia in individuals over 65 years of age. The total number of people with dementia worldwide in 2010 is estimated at 35.6 million and is projected to nearly double every 20 years (i.e. to 65.7 million in 2030) and 60%-70% of the cases are AD related [192]. AD is a chronic neurodegenerative disease that progressively decreases the patients' cognitive abilities including memory, thinking, language and learning and disables their behaviours and abilities that allow them to carry out normal everyday activities. It often starts with mild symptoms, such as impaired memory, apathy and depression, and ends up with neuron death and severe brain damage [193]. People with AD lose their abilities at different rates [194-197] and right now there are no available treatments to reverse or stop the progression of AD. The etiology of AD remains unclear, however, the risk factors include age, genetics and environment [192]. There are currently no specific biomarkers that can confirm an AD diagnosis with a 100% certainty. A combination of brain imaging, such as MRI, fMRI and PET [198-200], and clinical assessment checking for signs of memory impairment are used to identify patients with AD [201]. Definitive diagnosis can only be only obtained after an autopsy of patient's brain tissues [202-203]. Therefore, there is a clear need for tangible advances in the area of biomarkers for assessment of risk, diagnosis and monitoring disease progression.

#### ***Hypothesis of Amyloid- $\beta$ and impaired glutamatergic system***

Recent AD Studies from animal models suggest that amyloid- $\beta$  peptide (A $\beta$ ) plays a crucial role in the pathological genesis of AD (for review, see [204-205] and their citations).

Glutamate is the most abundant excitatory neurotransmitter in the central nervous system and the glutamatergic system (e.g., the neurotransmitter, receptors and glial cells) is known to be involved in a variety of functions such as neural signal transmission, synaptic plasticity, learning and memory [206-207]. A $\beta$  causes the deregulation of the glutamate neurotransmission, which is implicated as the primary mechanism of synapse failures in AD (Fig. 3.21).

In the pathological synaptic signal transmission, A $\beta$  increases the release of glutamate at the presynaptic terminal [208-209] and inhibits recycling the rest of the glutamate from the synaptic cleft through the glial cells [210-213]. These abnormal neural mechanisms lead to the accumulation of glutamate in the synaptic cleft, which is highly toxic to neurons and triggers a cell death cascade [214]. This phenomenon comprises a self-propagating cycle. First, the high concentration level of the glutamate at the synaptic cleft overstimulates glutamate receptors, which causes abnormal increases in intracellular calcium by directly opening ion channels and secondarily affecting calcium homeostatic mechanisms [215]. The accumulation of high intracellular calcium levels triggers a cascade of membrane, cytoplasmic, and nuclear events leading to cell death [216-217]. Second, the dead neurons leak additional glutamate to the extracellular space, which in turns kills more neurons [218-219].

A $\beta$  also increases the release of the D-serine into the synaptic cleft. D-serine is the co-agonist to NMDA-receptors [220-221]. The NMDA-receptor is the glutamate receptor known to be extremely important for the synaptic plasticity mechanisms, such as long-term potentiation (LTP) of the synaptic connection strength [222-223]. This synaptic modification is widely accepted to be an underlying mechanism for learning and memory [223-224]. In comparison to other glutamate receptors such as AMPA, the NMDA receptor has some crucial biophysical properties that are responsible for its important role in mediating postsynaptic responses to the input signal, which are important for the learning function: high permeability to Ca<sup>2+</sup> ions, voltage dependent blocking by Mg<sup>2+</sup> ions and relatively slow ligand gated kinetics [224-225]. Under normal resting membrane potential or even normal fast

transient depolarization (by activation of the AMPA receptors), NMDA receptors are blocked by  $Mg^{2+}$  and the intracellular  $Ca^{2+}$  levels remain low. This means that the neural background activity or irrelevant incoming information are associated with low activation of NMDA and low intracellular  $Ca^{2+}$  level. Only during strong and long lasting excitation caused by important neural events that are required for the learning process, the  $Mg^{2+}$  block is lifted due to the sufficiently high membrane potential. Then  $Ca^{2+}$  can freely move into the neurons through the NMDA receptor channel and trigger a cascade of second messenger processes that are involved in the fixation or enhancement of synaptic connections. The slow dynamics of the EPSP mediated by the NMDA also facilitates the temporal summation of the output signal that strengthens the further signal transmission [225].

The excessive D-serine in the synaptic cleft abnormally enhances the NMDA to bind with the glutamate and leads to a hyperactivation of the NMDA [204]. This triggers the pathological influx of  $Ca^{2+}$  into neurons. The prolonged  $Ca^{2+}$  overload leads first to impaired synaptic function and energy metabolism, then is followed by excitotoxicity and ultimately cell death [216-217], which correlates with the loss of memory function and learning ability in AD patients.

Taken together, in AD brains the  $A\beta$  promotes an accumulation of glutamate and D-serine in the synaptic cleft and this leads to an overactivation of glutamate receptors, especially the NMDA-receptors. This triggers abnormally high levels of intracellular  $Ca^{2+}$  with noxious impacts and causes the loss of neurons, which correlates with the loss of the NMDA function, memory and learning ability.

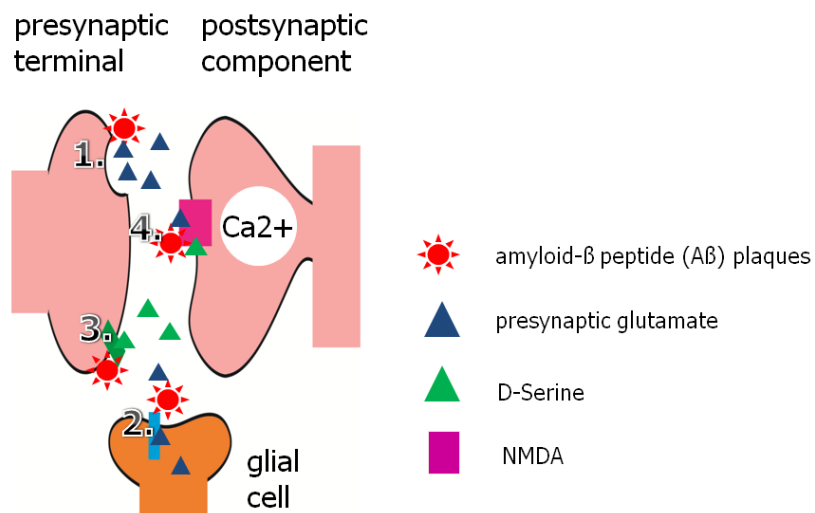


**Figure 3.21 Pathological synaptic signal transmission in Alzheimer Disease.**

1) The A $\beta$  plaques increase the glutamate release at the presynaptic terminal and 2) inhibit the glutamate recycling through the glial cells. Both promote accumulation of concentration of the glutamate in the synaptic cleft and leads to overactivation of the glutamate receptors and it abnormally enhances the excitatory signal pathway in the brain network.

3) The A $\beta$  plaques also increase the release of the D-serine into the synaptic cleft and 4) D-serine is a co-agonist to the NMDA-receptor and enhances the NMDA to bind with the glutamate leading to a hyperactivation of the NMDA. The NMDA is also known for its high permeability to calcium. Opening the channel of the NMDA leads to an influx of calcium into the neurons, which increases the intercellular calcium level. This will trigger a series of neural toxic processes and leads to cell death.

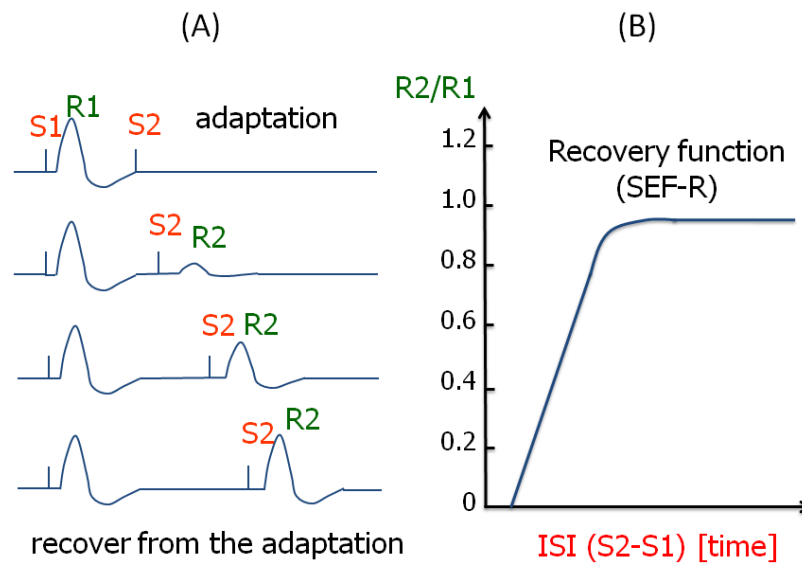
### ***Recovery function of paired somatosensory stimulation***

A pilot study using non-invasive EEG/MEG to measure the pathological hyper-activation of the glutamatergic excitatory neurotransmission in AD patients was composed here. The cortical responses to paired identical somatosensory stimulation can be used to evaluate the cortical excitability [226]. The measured ratios of two corresponding paired responses in relationship to different inter-stimuli-intervals are known as the recovery-function of the somatosensory evoked fields/potentials (SEF-R) (Fig. 3.22B) [226]. Two identical stimuli, which are close to each other, result in an attenuated second cortical response. By increasing

the inter-stimuli-interval, a recovered second response can be observed (Fig. 3.22A). This phenomenon is considered to reflect the synaptic plasticity such as the adaptation and the recovery of the connection strength, which is associated with the dynamic of the neural transmission like depletion and recycling of neurotransmitters (see **Chapter 2.4.1.1**). The cortical responses were measured with MEG using a 1000Hz sampling rate. The excellent temporal resolution of 1ms is capable of capturing the rapid changes in membrane potentials (averaged membrane potentials of the pyramidal cell populations) governed by the activations of the neural receptors. The time constant  $\tau$  (estimated with an exponential model:  $I=I_0 \cdot \exp(-t/\tau)$ ) of the AMPA-mediated excitatory postsynaptic current (EPSC) of the synaptic connection from pyramidal cell to inhibitory interneuron in rats was reported at about 2ms, the NMDA-mediated one was reported at about 52 ms in rat neocortex [227]. In comparison to the measurement at single neuron level, the time dynamic for the grouped neural populations were considered to be much slower [21, 66].

#### ***Computational model for analyzing of the neural circuit in the somatosensory cortex***

The neuronal mass models have been proposed as realistic, yet parsimonious, mesoscopic model of cortical activity (see **Chapter 2.1**). They are especially suited to accounting for extracranial measurements like EEG/MEG. In particular, the local cortical circuit model [20], which embodies the use-dependent dynamic synapses, is especially suitable to those EEG/MEG researches involved short-term synaptic plasticity like adaptation or facilitation. Moreover, the LCCM provides detailed inter- as well as intra-excitatory-inhibitory circuits, which allows to draw specific conclusions on the information of the neurotransmission among different cortical layers such as the effective connection strength, the receptor time constant and the degree of the synaptic plasticity. Therefore, in this pilot study, the measured MEG-data were analyzed with the LCCM to explore pathological changes in the somatosensory cortex and to see if the same impaired glutamatergic neurotransmission result could be obtained from computational evidence.



*Note.* S = stimulus, R = cortical response, SEF-R = somatosensory recovery, ISI = inter-stimuli-interval,

**Figure 3.22 Recovery function of Somatosensory evoked fields.** (A) Two identical stimuli that are close to each other evoked an attenuated second cortical response. The amplitude of the second response recovers with increasing inter-stimuli-interval. (B) The recovery function of somatosensory evoked fields describes the relationship of the ratios of two cortical responses to the inter-stimuli-intervals.

### 3.2.2 Tasks

- i. Modeling the SEF-R process using the LCCM.
- ii. Evaluating if the LCCM has an advantage against the JRM with respect to explaining the observed SEF.
- iii. Exploring the model parameters to find the group differences among patients, healthy elderly and the young people and interpreting the findings.

## 3.2.3 Data acquisition and processing

### 3.2.3.1 Experiment

#### *Ethic statement*

This experiment was approved by the Ethic Committee of National Center for Geriatrics and Gerontology, Aichi, Japan. A written informed consent was obtained from all participants or their proxies.

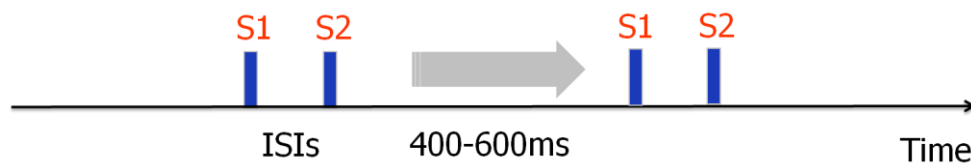
#### *Declaration*

The experiment as well as the data acquisition and pre-processing were done by Dr. Akinori Nakamura from the National Center for Geriatrics and Gerontology Center for Development of Advanced Medicine for Dementia in Aichi, Japan.

#### *Description*

The left median nerves (wrist) of the participants were electrically stimulated. Stimulus intensity was 1.3 times above the motor threshold. One single and five pairs of stimuli utilizing different inter-stimuli-intervals (ISI = 30, 60, 90, 120, 150 ms) were randomly administered with 150 repetitions each. The stimulus onset asynchrony (SOA) is randomly jittered from 400ms to 600ms (Fig. 3.23). 40 participants' data were available for this pilot study. Among them were 10 healthy young people ranging from 20 to 33 years of age (median: 24, 4 females), 18 healthy elderly people ranging from 61 to 77 years of age (median: 69, 10 females), which were amyloid-negative ( $A\beta^-/PiB^-$ , PiB-PET amyloid imaging see **Chapter 3.2.3.2**) and 12 patients ranging from 66 to 82 years of age (median: 78, 9 females), which were amyloid-positive ( $A\beta^+/PiB^+$ ). The patient group consisted of 6 people with a clinical diagnosis of AD and 6 others diagnosed with mild cognitive impairment (MCI).





*Note.* S = stimulus, ISI = inter-stimuli-interval

**Figure 3.23 Stimulation design of the somatosensory adaptation.** 5 pairs of stimuli utilizing different ISIs (30, 60, 90, 120, 150 ms) were randomly administered with 150 repetitions each. The stimulus onset asynchrony (SOA) is randomly jittered between 400ms and 600ms (Fig. 3.23)

### 3.2.3.2 Data acquisition

#### *PiB-PET amyloid imaging*

The positron emission tomography (PET) imaging data were recorded using PET-CT camera (Biograph True V, Siemens). The participants were scanned 50-70min after the intravenous injection of  $555 \pm 185$  MBq  $^{11}\text{C}$ - Pittsburgh compound B (PiB) [198-200]. The PiB retention was visually determined by a trained neuroradiologist.

#### *MEG*

MEG data was recorded using a Neuromag Vectorview MEG device (306 channels). The signal was digitized with a bandwidth from 0.1 to 120 Hz and a sampling rate of 1000 Hz. The raw data were first offline corrected using Signal Space Separation (SSS) [185], which separates the biomagnetic and external interference signals. The setup for the SSS correction were: 4s epoch length and 0.99 correlation value. Before averaging, the MEG data were epoched from -100ms to 300ms. The first stimulation pulse was registered at 0ms. The thresholds for automatic artifact rejection were: 6 pT for magnetometers and 3 pT/cm for gradiometers.

### 3.2.3.3 Data preparation

Considering the anatomical structure as well as the somatotopic arrangement of the primary somatosensory cortex [228], the source of SEFs is expected to be locally restricted and located superficially under the scalp [229]. The gradiometers are sensitive to superficial and tangential sources and relatively insensitive to distant disturbing sources. It was expected that a single gradiometer pair, which is nearest to the source generator of the SEFs, can record the source activation with little contamination. Therefore, the somatosensory cortex activity was modeled by the first PCA (principal component analysis [230]) component of the pair of gradiometers with the largest amplitude at about 20ms (Figure 3.24). Activity strength was estimated for each participant: It was expected that the estimated signal should be able to explain over 80% of the original SEFs.

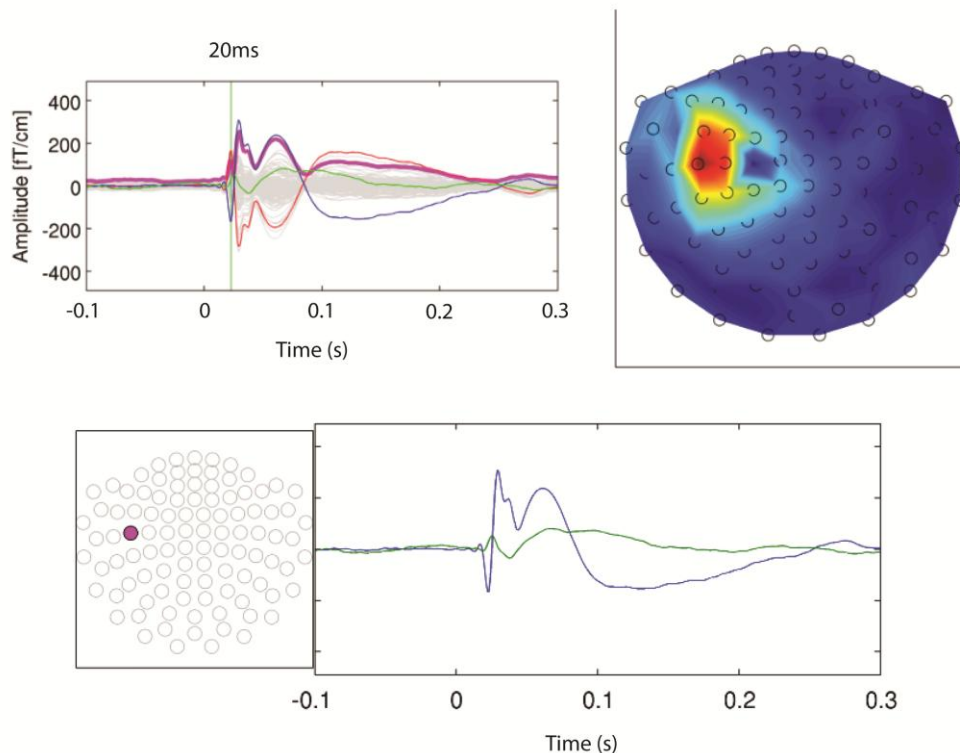
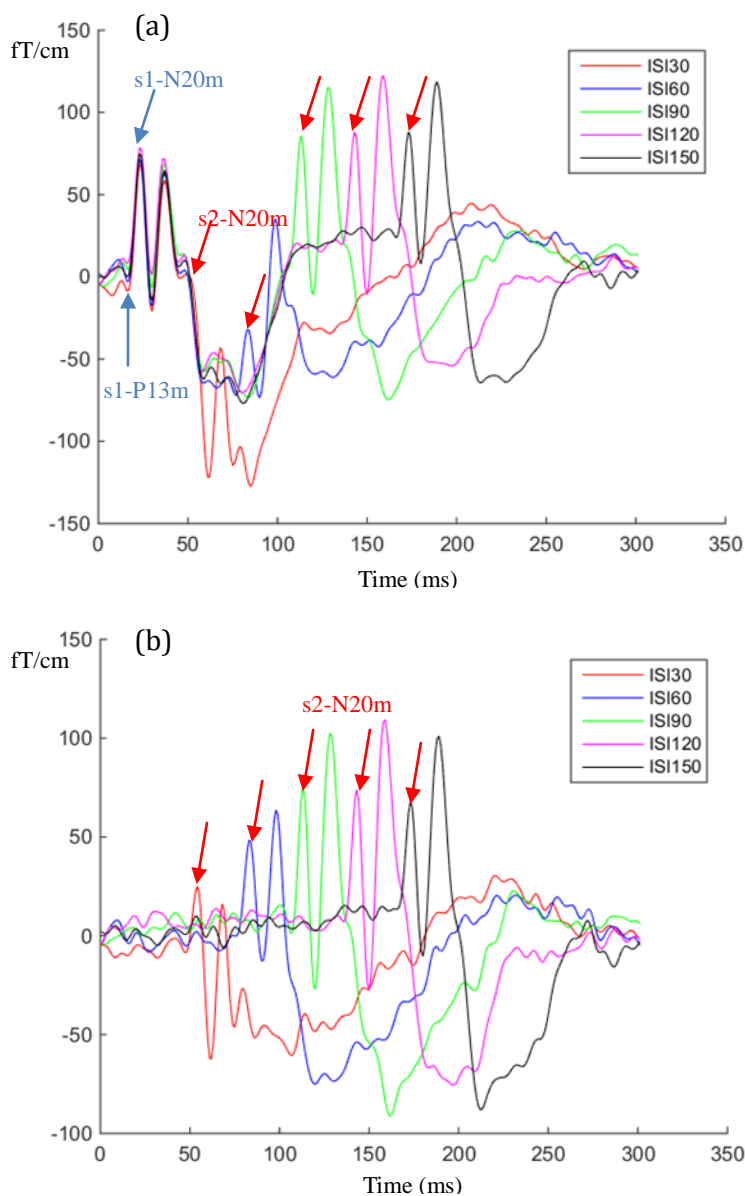


**Figure 3.24** The gradiometer pair chosen according to having the largest amplitude at about 20ms

### 3.2.3.4 Data observation and description

Figure 3.25a illustrates the estimated SEFs, which were assumed to represent the somatosensory activity. The ISIs between the paired stimuli were: 30ms, 60ms, 90ms, 120ms and 150ms. The relevant SEF component is called N20m, which occurs about 20-25ms after the stimulus presentation. The N20m peak values were measured through the peak-to-peak values of P10m-N20m. For short ISIs, such as ISI = 30ms as well as ISI = 60ms, the N20m peaks of the second SEFs (s2) were in most cases overlapped by the late component of the first SEFs (s1). To obtain a clear structure of the s2-N20m, the paired stimuli data (s1&s2) were subtracted from the recording of the single stimulus condition(s1) (Fig. 3.25b).

The amplitudes of the N20m for the single stimulation condition as well as the paired stimulations are documented in Appendix B, Table B.1. The SEF-R functions [226] of patients, healthy elderly and young people are illustrated in the Fig. 3.26. The N20m peaks of the second responses showed the most prominent adaptation effect at the shorter ISIs such as 30ms and 60ms. However, no group differences among the three groups were observed. In contrast, with the longer ISIs such as 90ms to 150ms, it was found that the young people still kept the adaptation, the healthy elderly showed less adaptation, but the patients showed an enhancement of the second response, especially by 120ms.



Note. ISI = inter-stimuli-interval

**Figure 3.25 The first PCA component of the somatosensory evoked fields.** The somatosensory cortex activities were modeled by the first PCA component of a paired gradiometer that showed largest amplitude at about 20ms. The inter stimulus interval (ISI) was varied from 30ms to 150ms, at steps of 30ms. The first stimulus was presented at 0ms. (a) The components s1-N20m (response to the first stimulus) as well as s2-N20m (response to the second stimulus). (b) The paired SEFs after subtraction of the single SEF recordings.

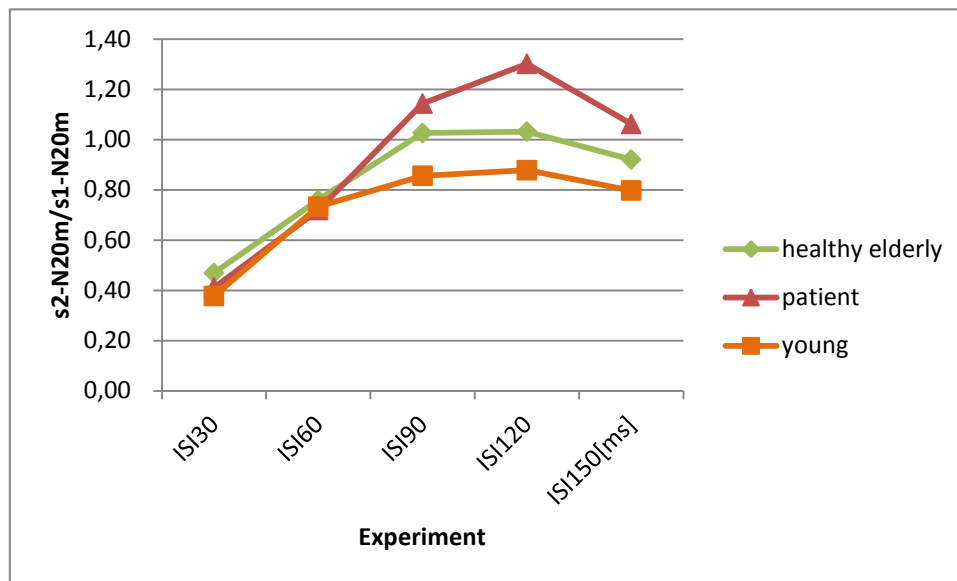


**Figure 3.26 Recovery function of Somatosensory evoked fields for patients, healthy elderly and young people.** The recovery function represents the mean ratio of N20m of the second response (s2-N20m) to the first one (s1-N20m) in paired stimuli conditions with different inter-stimuli-intervals (ISI = 30, 60, 90, 120, 150ms).

The significant differences (tested by one-way ANOVA) in the amplitude ratio s2-N20m/s1-N20m among the healthy elderly, the young and the patient group are listed below:

<i>o Healthy elderly v.s. patient</i>		
ISI120:	p < 0.05,	larger for patient
<i>o Young v.s. patient</i>		
ISI90:	p < 0.05,	larger for patient
ISI120:	p < 0.01,	larger for patient
ISI150:	p < 0.01,	larger for patient
<i>o Young v.s. healthy elderly</i>		
ISI90:	p < 0.05,	larger for healthy elderly
ISI120:	p < 0.01,	larger for healthy elderly
ISI150:	p < 0.05,	larger for healthy elderly

The second responses of ISI = 120ms were significantly different among all three groups (Fig. 3.27). In general, with longer ISIs (i.e. from 90ms to 150ms) the patients showed larger s2-N20m than the healthy elderly and the young people.

It is worth noting that the observed s1-N20m amplitude in single and other paired conditions were not the same (they were expected to be identical) (Fig. 3.25A). The small differences were considered as the noise and the data were normalized to the mean value of the s1-N20m over single and paired conditions. These mean values are documented in Appendix B, Table B.2.

### 3.2.4 Model specification

The prior specifications were similar to the previous modeling study of auditory adaptation (see **Chapter 3.1.3**). Considering the differences between the AEFs and the SEFs, some prior expectations were adjusted.

First the excitatory synaptic time constant is change to 2.5 ms, which is similar to the time constant of the AMPA-mediated EPSC of about 2ms reported in the previous animal study [227]. This prior expectation could be considered as that it was assumed that the dominantly activated receptors were AMPA-receptors. In comparison to the NMDA-receptors, the AMPA-receptors were reported to be less affected by the aging process (see review [231] and its citations) and the major contribution to the EPSP shifted from NMDA mediated neurotransmission to AMPA mediated over the lifespan [232]. This assumption on the parameter prior is suitable for the healthy elderly group. However, for the patient group as well as the young group, NMDA-receptor mediated neurotransmission, which is much slower than the AMPA-mediate one [227], is expected to be more dominant. It means that the estimated parameter value is expected to be much larger than the prior expectation.

Second, the adaptation and the recovery rate were changed in order to fit the much faster adaptation-recovery cycle of the SEFs. It seems that the N20m has already recovered from the adaptation after 90 ms stimulus free time (Fig. 3.26), while the N100m needs more than

5 s (Fig. 3.12) for the recovery. The adaptation as well as the recovery rate were set to be 33 ( $3\tau = 0.09$ ,  $1/\tau = 33$ ).

Third, considering that the inter stimulus interval is short, that is 30ms, the adaptation of the input signal cannot be neglected [181].

Furthermore, in this study, it was assumed that the sPC and dPC had different signal contributions to the sensors (Equation (18)) with consideration to their anatomical and geometrical differences. The expectation of the ratio was set to 1/3 according to the previous modeling study of Murakami and Okada [115].

The prior specification of the LCCM as well as the JRM for this pilot study are listed in Table 3.8 as well as Table 3.9.

**Table 3.8 Prior setup for LCCM in the somatosensory adaptation experiment**

	Expectation	Prior Type (U/I/C)
<i>Intrinsic connection parameters</i>		
<i>"Certain" intrinsic connections</i>		
EIN→sPC	108*4	U
sPC→sIIN	33.75*4	U
sIIN→sPC	33.75*4	U
sPC→dPC	135*4	U
dPC→EIN	135*4	U
dPC→dIIN	33.75*4	U
dIIN→dPC	33.75*4	U
Thalamic input →EIN	500	U
<i>"Uncertain" intrinsic connections</i>		
dPC→sPC	0	U
EIN→dPC	0	U
sIIN→dPC	0	U
dPC→sIIN	0	U

dIIN→sPC	0	U
sPC→dIIN	0	U
<i>Synaptic gain parameters</i>		
$H_e$	$3.25 \times 10^{-3} [\text{V}]$	C
$H_i$	$22 \times 10^{-3} [\text{V}]$	C
<i>Synaptic time constants (from NM x to NM y)</i>		
$\tau_{e,xy}$	$2.5 \times 10^{-3} [\text{s}]$	U
$\tau_{i,xy}$	$5 \times 10^{-3} [\text{s}]$	U
<i>Sigmoid parameter</i>		
$e_0$	$2.5 [\text{s}^{-1}]$	C
$r$	$560 [\text{V}^{-1}]$	C
$u_0$	$6 \times 10^{-3} [\text{V}]$	C
<i>Input parameter</i>		
$w$	$0.0035 [\text{s}]$	I
<i>Depression and recovery rate (from NM i to NM j)</i>		
Depression rate $n_{1,ij}$	$33 [\text{s}^{-1}]$	U
Recovery rate $n_{2,ij}$	$33 [\text{s}^{-1}]$	U
<i>Linear scaling factor</i>		
Linear fitting factor $\alpha$	100	U
Contribution ratio $\beta$	1/3	I

*Note.* Re-parameterization for "uncertain" intrinsic connections used:  $\theta = \theta_0 \varphi^2$ ,  $p(\varphi) \sim \text{N}(0,1)$  for uninformative priors. Re-parameterization for other parameters use:  $\theta = \theta_0 \times p(\varphi)$ ,  $p(\varphi) \sim \text{N}(0, 1/2)$  for uninformative priors and  $\theta = \theta_0 \times p(\varphi)$ ,  $p(\varphi) \sim \text{N}(0, 1/16)$  for informative priors.  $\theta_0$  is the prior expectation. EIN = excitatory interneurons, sPC = superficial pyramidal cells, sIIN = superficial inhibitory interneurons, dPC = deep pyramidal cells, dIIN = deep inhibitory interneurons. U = uninformative prior, I = informative prior, C = constant.



**Table 3.9 Prior setup for JRM in the somatosensory adaptation experiment**

	Expectation	Prior Type (U/I/C)
<i>Intrinsic connection parameters</i>		
<i>Certain intrinsic connections</i>		
EIN→PC	108*4	U
PC→EIN	135*4	U
PC→IIN	33.75*4	U
IIN→PC	33.75*4	U
Thlamic input → EIN	500	U
<i>Synaptic gain parameters</i>		
$H_e$	$3.25 \times 10^{-3} [\text{V}]$	C
$H_i$	$22 \times 10^{-3} [\text{V}]$	C
<i>Dendritic time constants (from NM x to NM y)</i>		
$\tau_{e,xy}$	$2.5 \times 10^{-3} [\text{s}]$	U
$\tau_{i,xy}$	$5 \times 10^{-3} [\text{s}]$	U
<i>Sigmoid parameter</i>		
$e_0$	$2.5 [\text{s}^{-1}]$	C
$r$	$560 [\text{V}^{-1}]$	C
$u_0$	$6 \times 10^{-3} [\text{V}]$	C
<i>Input parameter</i>		
$w$	$0.0035 [\text{s}]$	I
<i>Depression and recovery rate (from NM i to NM j)</i>		
Depression rate $n_{1,ij}$	$20 [\text{s}^{-1}]$	U
Recovery rate $n_{2,ij}$	$2 [\text{s}^{-1}]$	U
<i>Linear scaling factor</i>		
Linear fitting facto $\alpha$	100	U

Note. Re-parameterization for uninformative parameters use:  $\phi = \theta_0 \exp(\theta)$ ,  $p(\theta) \sim N(0, 1/2)$ . Re-parameterization for informative parameters use:  $\phi = \theta_0 \exp(\theta)$ ,  $p(\theta) \sim N(0, 1/16)$ .  $\theta_0$  is the prior expectation. EIN = excitatory interneurons, PC = pyramidal cells, IIN = inhibitory interneurons. U = uninformative prior, I = informative prior, C = constant.

In this study, two model pairs were proposed and compared to fulfill the followed research purpose:

(i) *Comparison of the LCCM and the JRM in fitting SEF:*

Using LCCM as well as JRM to fit the SEF of single stimulus conditions.

(ii) *Comparision of the LCCM with adapted and constant inhibitory synaptic connections:*

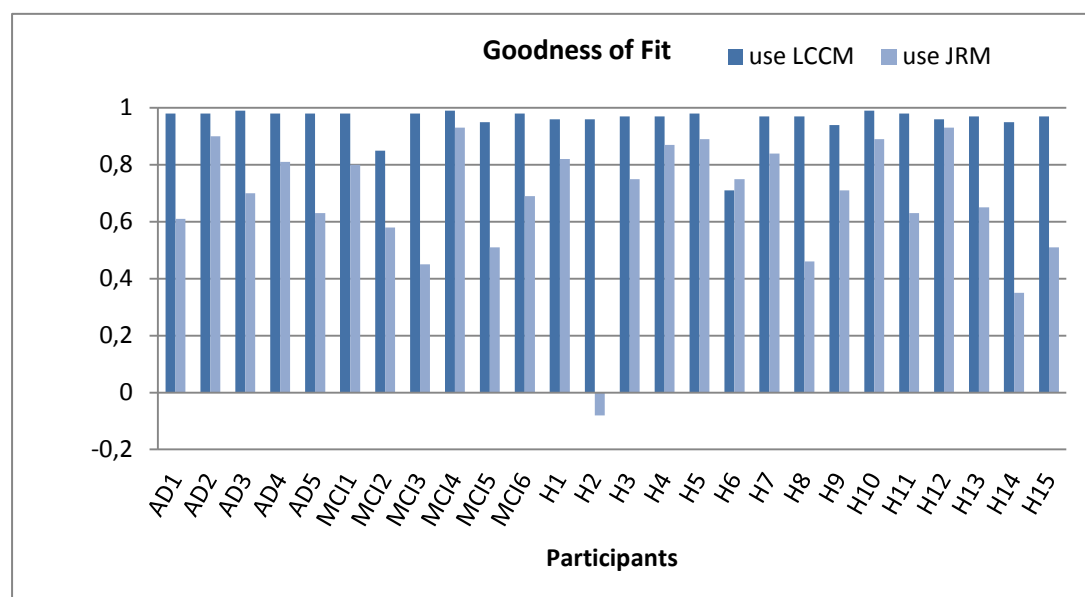
Two LCCMs were compared. One was composed of suppressed inhibitory synaptic connections (sIIN->sPC, sIIN->dPC, dIIN->sPC,dIIN->dPC). The other one was composed of constant inhibitory connections. The excitatory pathway of both models was assumed to have suppressed synaptic connections.

## 3.2.5. Results

### 3.2.5.1 Comparison of LCCM and JRM in modeling somatosensory activity.

The LCCM fitted the somatosensory cortex activity better than the JRM. In both models, all synaptic connections were assumed to have the property of use-dependent adaptation.

Figure 3.27 illustrates the GoFs of the SEFs of a single stimulus (time course: 300ms) using the LCCM as well as the JRM. The average GoF of the JRM was lower than the average GoF of the LCCM ( $\text{GoF}_{\text{JRM}} < \text{GoF}_{\text{LCCM}}$ ,  $p < 0.01$ , ANOVA). The median GoF of the LCCM is 0.97. The median GoF of the JRM is 0.71. The values are documented in Appendix B.4.



Note. LCCM = local cortical circuit model, JRM = Jansen and Rit model, AD = Alzheimer Disease, MCI = mild cognitive impairment, H = healthy elderly.

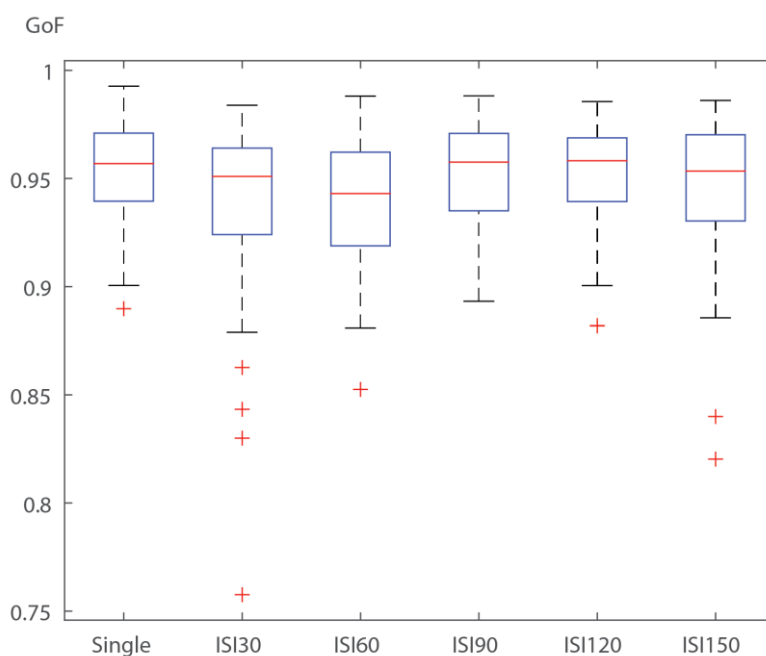
**Figure 3.27 Goodness of Fits of using LCCM and JRM to fit the somatosensory evoked field of the single stimulus condition.**

### 3.2.5.2 Goodness of fit of the LCCM using suppressed synaptic connections

The LCCM was used to fit all experimental conditions: single, ISI = 30,60,90,120 and 150ms.

Use-dependent short-term adaptation was modeled at all synaptic connections.

Figure 3.28 illustrates the GoFs. The value table is given in Appendix B, Table B.5. In Appendix C, Figure C.1 illustrated an example of the fitting results. The median GoF over all participants and all conditions is 0.95. All GoF values were larger than 0.75.



*Note.* GoF = goodness of fit, ISI = inter-stimulus-interval

**Figure 3.28** Box-plot of goodness of fit (GOF) of LCCM. It is over 40 subjects and 6 different experimental conditions: single stimulus as well as paired stimuli with different inter-stimuli-intervals (ISI = 30, 90, 120, 150 ms).

### 3.2.5.3 Comparison of the LCCM using suppressed and constant inhibitory synaptic connections

The data sets of the observed somatosensory cortex activity were grouped into three subclasses:

- (a) *all conditions* = SEF of single stimulus condition plus all paired stimulus conditions. (b) *short ISIs* = SEF of single stimulus condition plus 2 paired stimuli conditions with short ISI: 30 & 60ms. (c) *long ISIs* = SEF of single stimulus condition plus 3 paired stimuli conditions with long ISI: 90, 120 & 150ms.

The LCCMs with suppressed synaptic connections for both excitatory and inhibitory synapses were able to fit the data sets of all experimental conditions at the same time. The GoFs are documented in Table 3.10. The median value was  $GoF_{\text{supp. inhib.}} = 0.94$ , the worst fit result was 0.87. In contrast, the LCCM with constant inhibitory connections yielded a worse fit result (mean value  $GoF_{\text{const. inhib.}} < GoF_{\text{supp. inhib.}}$ ,  $p < 0.01$ , ANOVA) (Table 3.10). The median was  $GoF_{\text{const. inhib.}} = 0.85$ .

The LCCM with constant inhibitory connections was further tested with the data of short ISIs as well as long ISIs separately (Table 3.11). The median value of the GoFs for long ISIs was  $GoF_{\text{const. inhib., long ISIs}} = 0.91$ . The median value of the GoFs for short ISIs was 0.89. It seemed that the best fit result was obtained by fitting long ISIs. ( $GoF_{\text{const. inhib.}} < GoF_{\text{const. inhib., long ISIs}}$ ,  $p < 0.01$ ;  $GoF_{\text{const. inhib.}} < GoF_{\text{const. inhib., short ISIs}}$ ,  $p = 0.36$ ,  $GoF_{\text{const. inhib., short ISIs}} < GoF_{\text{const. inhib., long ISIs}}$ ,  $p < 0.05$ , ANOVA). There was no statistically significant difference between the fitting of all conditions and fitting of the short ISIs.

The log model evidence of the LCCM using suppressed inhibitory connections and the LCCM using constant inhibitory connections are shown in Table 3.12. The natural logarithm Bayesian factor was calculated as the difference between the two log model evidences:  $\log(p(y|m = \text{suppressed inhibitory connections})) - \log(p(y|m = \text{constant inhibitory$

connections)). A value larger than 3 indicates there is strong evidence to support the LCCM with suppressed inhibitory connections (Table 2.3).

The data (fitting all six experimental conditions) suggests that the adaptation of the inhibitory connections may play a key role in the observed SEFs of the paired stimuli.

**Table 3.10 Fitting somatosensory cortex activity (single as well as paired conditions) using suppressed as well as constant inhibitory connections.**

Participants/GoF	supp.	const.	Participants/GoF	supp.	const.
AD1	0,95	0,85	H3	0,94	0,93
AD2	0,94	0,93	H4	0,9	0,84
AD3	0,97	0,93	H5	0,92	0,71
AD4	0,96	0,92	H6	0,92	0,44
AD5	0,96	0,91	H7	0,92	0,89
MCI1	0,96	0,88	H8	0,91	0,76
MCI2	0,9	0,62	H9	0,87	0,78
MCI3	0,93	0,85	H10	0,96	0,93
MCI4	0,95	0,84	H11	0,96	0,89
MCI5	0,9	0,82	H12	0,93	0,89
MCI6	0,92	0,72	H13	0,93	0,82
H1	0,94	0,84	H14	0,93	0,37
H2	0,96	0,95	H15	0,95	0,47

*Note.* GoF = goodness of fit, supp. = LCCM using suppressed inhibitory connections, const. = LCCM using constant inhibitory connections. AD = Alzheimer disease, MCI = mild cognitive impairment, H = healthy elderly.

**Table 3.11 GoFs of LCCM using constant inhibitory synaptic connections**

Participants/ GoF	all conditions	single + ISI30 + ISI60	single + ISI90 + ISI120 + ISI150 [ms]	Participants/ GoF	all conditions	single + ISI30 + ISI60	single + ISI90 + ISI120 + ISI150 [ms]
<b>AD1</b>	0,85	0,95	0,92	<b>H3</b>	0,93	0,89	0,91
<b>AD2</b>	0,93	0,95	0,9	<b>H4</b>	0,84	0,85	0,88
<b>AD3</b>	0,93	0,97	0,94	<b>H5</b>	0,71	0,91	0,9
<b>AD4</b>	0,92	0,82	0,96	<b>H6</b>	0,44	0,42	0,87
<b>AD5</b>	0,91	0,89	0,87	<b>H7</b>	0,89	0,94	0,9
<b>MCI1</b>	0,88	0,96	0,94	<b>H8</b>	0,76	0,94	0,88
<b>MCI2</b>	0,62	0,83	0,79	<b>H9</b>	0,78	0,67	0,84
<b>MCI3</b>	0,85	0,44	0,87	<b>H10</b>	0,93	0,95	0,94
<b>MCI4</b>	0,84	0,86	0,92	<b>H11</b>	0,89	0,57	0,94
<b>MCI5</b>	0,82	0,86	0,9	<b>H12</b>	0,89	0,95	0,91
<b>MCI6</b>	0,72	0,86	0,9	<b>H13</b>	0,82	0,94	0,92
<b>H1</b>	0,84	0,94	0,91	<b>H14</b>	0,37	0,75	0,91
<b>H2</b>	0,95	0,95	0,94	<b>H15</b>	0,47	0,71	0,92

*Note.* GoF = goodness of fit, ISI = inter stimulus interval, AD = Alzheimer disease, MCI = mild cognitive impairment, H = healthy elderly.

The LCCM using constant inhibitory synaptic connections were tested by three data sets: using observed data of all experimental conditions, using only short ISIs (single, ISI = 30ms, ISI = 90ms) as well as using only long ISIs (single, ISI = 90ms, ISI = 120ms and ISI = 150ms).

**Table 3.12 Log model evidence of models using suppressed and constant inhibitory connections.**

Participants/ Log model evidence	supp.	const.	Log Bayesian factor	Participants/ Log model evidence	supp.	const.	Log Bayesian factor
<b>AD1</b>	1215	187	1028	<b>H4</b>	1376	1152	224
<b>AD2</b>	1907	1814	93	<b>H5</b>	1288	1050	238
<b>AD3</b>	-350	-1017	667	<b>H6</b>	1745	1419	326
<b>AD4</b>	2222	1792	430	<b>H7</b>	1159	205	954
<b>AD5</b>	1033	461	572	<b>H8</b>	975	-573	1548
<b>MCI1</b>	1848	1046	802	<b>H9</b>	2031	1789	242
<b>MCI2</b>	360	8	352	<b>H10</b>	856	347	509
<b>MCI3</b>	1183	561	622	<b>H11</b>	1559	1102	457
<b>MCI4</b>	765	-140	905	<b>H12</b>	1678	1271	407
<b>MCI5</b>	1475	1022	453	<b>H13</b>	1031	301	730
<b>MCI6</b>	1341	287	1054	<b>H14</b>	910	655	255
<b>H1</b>	1956	1357	599	<b>H15</b>	1790	117	1673
<b>H2</b>	2364	1782	582	<b>H16</b>	592	-1153	1745
<b>H3</b>	1082	229	853	<b>H17</b>	1958	1166	792

*Note.* supp. = LCCM using suppressed inhibitory connections, const. = LCCM using constant inhibitory connections.

The Log Bayesian factors were calculated by the difference between the two log model evidence:  
 $\log(p(y|m = \text{suppressed inhibitory connections})) - \log(p(y|m = \text{constant inhibitory connections}))$



### 3.2.5.4 Parameter comparison of different participants' groups

For the LCCM in this study, there were a total of 14 synaptic connections (Table 3.8). Each connection was described through 4 parameters: (i) synaptic connection strength  $C$ , (ii) synaptic time constant  $\tau$ , (iii) adaptation rate  $n_1$ , (iv) recovery rate  $n_2$ . Furthermore, there were three additional parameters to describe the input as well as the output: (v) input parameter  $w$  as well as (vi) scaling parameter  $\alpha$  and  $\beta$ . Therefore, there were 59 free parameters. The comparison of the parameter group differences was according to the estimated parameters from **Chapter 3.2.5.2**. Forty participants from three different groups were included.

A series of 59 one-way AONVAs were conducted to compare the estimated parameters between groups (patients vs. healthy elderly, patients vs. young and healthy elderly vs. young). The significant  $p$  values after the Bonferroni correction (factor 59) are listed below:

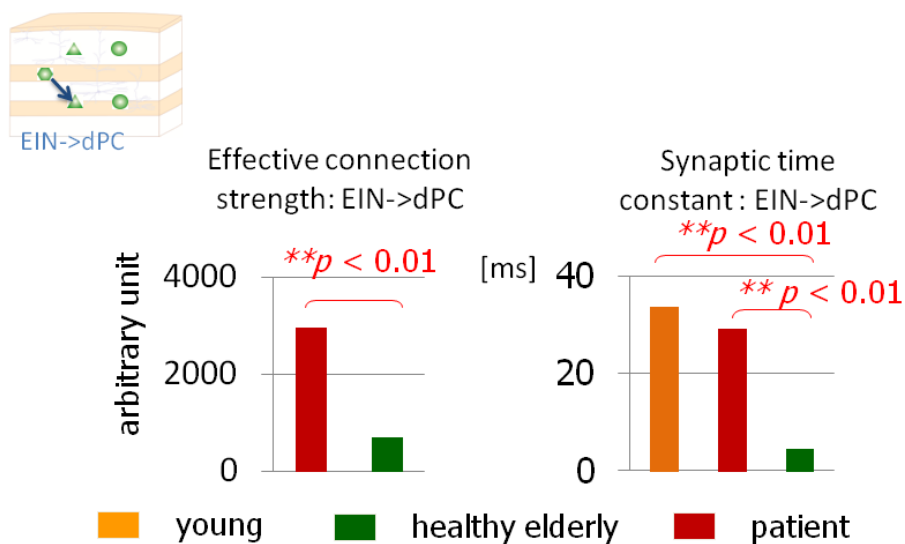
Significantly different model parameters between groups:

<i>o Healthy elder vs. patient</i>		
effective connection strength $C_{\text{EIN} \rightarrow \text{dPC}}$ ,	$p < 0.01$ ,	larger for patient
synaptic receptor time constant $\tau_{\text{EIN} \rightarrow \text{dPC}}$ ,	$p < 0.01$ ,	larger for patient
<i>o Healthy young vs. healthy elderly</i>		
synaptic time constant $\tau_{\text{EIN} \rightarrow \text{dPC}}$ ,	$p < 0.01$ ,	larger for young

The ANOVA-test suggests two significantly different model parameters among the groups: the effective connection strength  $C_{\text{EIN} \rightarrow \text{dPC}}$  as well as the synaptic time constant  $\tau_{\text{EIN} \rightarrow \text{dPC}}$ . Both parameters are related to the excitatory connection from EIN in layer IV to dPC in layers V/VI. The patients show strong excitatory neurotransmission as well as larger time constants than the healthy elderly (Fig. 3.29). The young people also showed larger time constants than the healthy elderly (Fig 3.29).

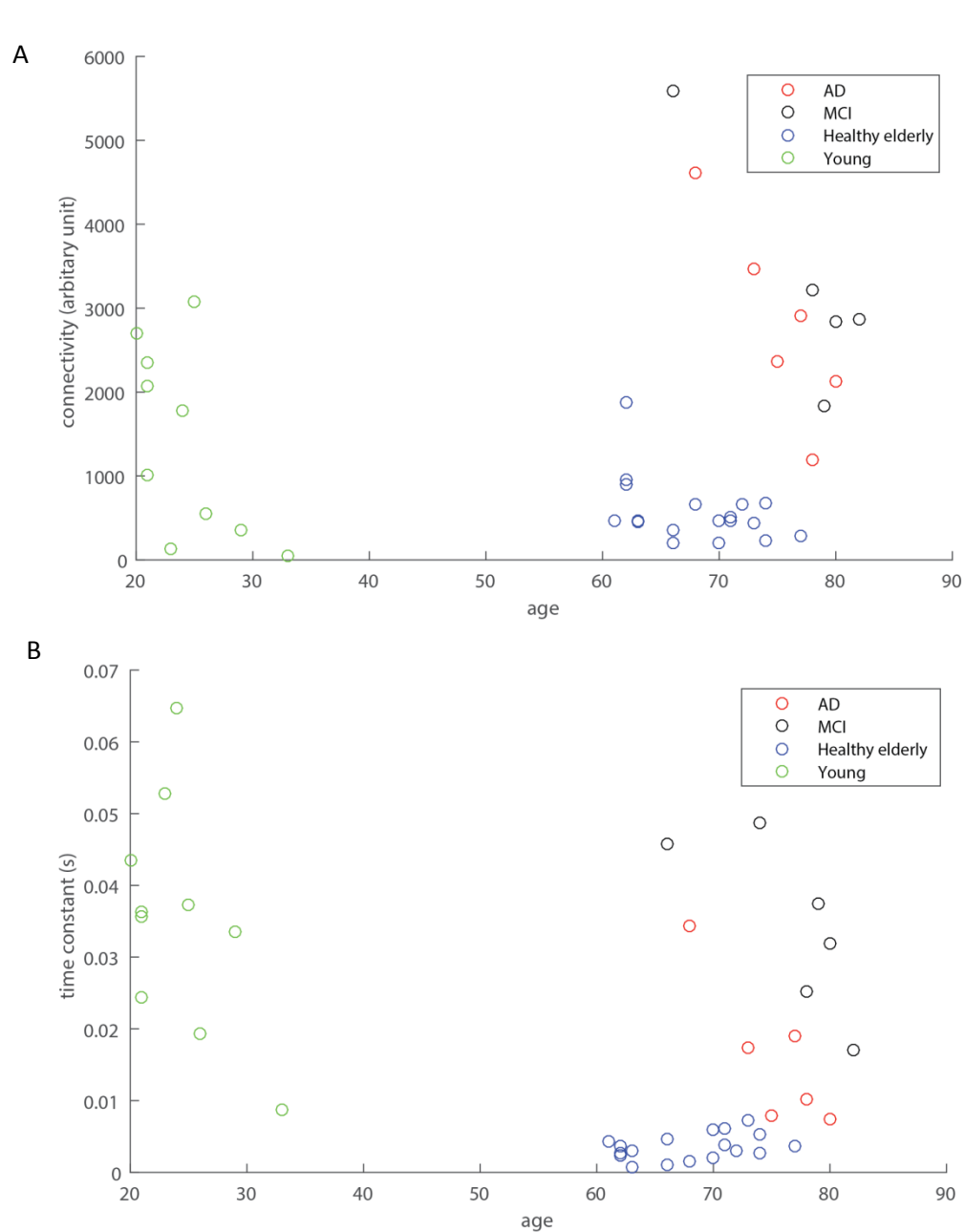
The effective synaptic connection strength  $C_{\text{EIN} \rightarrow \text{dPC}}$  represents the glutamate-mediated neurotransmission. The increase in the connection strength may implicate an increase in glutamate neurotransmission. The time constant  $\tau_{\text{EIN} \rightarrow \text{dPC}}$  can be interpreted as superposition effect of two synaptic receptors having different time scales: the faster AMPA and slower NMDA. A slower time constant may implicate a change in relevance between NMDA and AMPA, such that NMDA gains more importance.

The estimated connection strength as well as time constants are further analysed in their relationship to the participants' age in Figure 3.30. An age-related decrease of the synaptic time constant is observed in Figure 3.30B, but the effective connection strength didn't show such clear tendency (Fig. 3.30A). However, an AD-related increase in the synaptic connection as well as time constant can be clearly observed (Fig. 3.30).



Note. EIN = excitatory interneurons, dPC = deep pyramidal cells

**Figure 3.29** Significantly different model parameters between young, healthy elderly and patient group.



Note. AD = Alzheimer disease, MCI = mild cognitive impairment.

**Figure 3.30** Scatter plots of estimated LCCM model parameters "effective connectivity " (A) and (A) and "synaptic time constant " (B) of excitatory connection from excitatory interneurons in layer IV to deep pyramidal cells in layers V/VI over age for all subjects. Data of young participants is shown in green, of healthy elderly in blue, Alzheimer patients in red and mild cognitive impairment patients in black.

### 3.2.6. Discussion and conclusion

In this pilot study, the LCCM was used to simulate the somatosensory cortex activity of paired stimuli, in particular using the same model to account for all different ISIs. Suggested by previous AD research [204], the glutamatergic system in an AD brain appears to be dysregulated by the A $\beta$ . It promotes the accumulation of glutamate and D-serine at the synaptic clefts and this leads to overactivation of glutamate receptors and later neuron death. The NMDA-receptors seem to be centrally involved in this pathological neurotransmission process. The consequences of the dysfunction of the NMDA-receptors may be associated with the dysfunction of the synaptic plasticity and the loss of the memory function in AD patients. This abnormally increased glutamate neurotransmission as well as increased receptors activation was expected to be observable through the non-invasive imaging techniques such as EEG/MEG. The excitability of the somatosensory cortex was calculated through the ratio of the SEFs to paired stimuli [226]. The patient group showed an enhancement of the second cortical response to the paired stimulation with long ISIs, such as 90ms and 120ms (Fig. 3.26). This finding was further analyzed through the LCCM. The LCCM was featured with intra-/inter laminar organization of the excitatory and inhibitory signal flows as well as use-dependent dynamic synapses. This modeling approach mapped the differences in SEFs captured by macroscopic extracranial measurements into mesoscopic biological plausible model parameters such as the synaptic connections among different neural populations inside the somatosensory cortex and the synaptic time constant governing the rise and fall of the EPSPs through the Bayesian inversion method. The Bayesian inversion estimated the model parameters with a compromise of satisfying both prior assumption as well as the observed data at the same time. An uninformative prior was applied in this study, and the specific weight was given more to the data. Interesting findings were obtained by comparing the model parameters between patient, healthy elderly and healthy young groups: (i) patients seemed to have a stronger excitatory connection from EIN to dPC than the healthy elderly, (ii) patients seemed to have a larger synaptic time constant

of the excitatory connection from EIN to dPC than the healthy elderly, and (iii) the young people showed a larger synaptic time constant of the excitatory connection from EIN to dPC than the healthy elderly.

### ***Modeling approaches***

The most challenging part of this pilot study is the interpretation of these computational findings. First, it is important to show that the model is reliable in explaining the observed data. In contrast to the previous modeling study using the LCCM in the auditory modality (see **Chapter 3.1.5.2**), the LCCM outperformed the JRM in fitting the SEFs (Fig. 3.27). Moreover, in this study, the LCCM was not restricted on a single prominent component of the evoked field with short duration, such as AEF-N100m (70ms-130ms), but it was used to simulate the whole duration of the SEF as well as its rich dynamics implicated by stimulation with different ISIs. The LCCM yielded reasonable GoFs (Fig. 3.28) of all available observed data in the different experimental conditions. This fit result may suggest that the cortical activity with short latency and fast dynamics relies more on complicated information exchange between the inter- and intra-laminar, excitatory and inhibitory neurons. Therefore, the previous neural mass models, which summarized all cells into three neural populations, seem to have oversimplified the aspect of the laminar organization of the local cortical area. Our modeling also indicates that in addition to the laminar organization of the excitatory/inhibitory signal flow, the short-term synaptic plasticity (adaptation) of inhibitory interneurons is another crucial aspect in the modeling of cortical activity (see **Chapter 3.2.5.3**). Inhibitory interneurons use GABA as neurotransmitter and shape the neural network activity in cortex by filtering incoming information and dictating the activity of postsynaptic neurons. Recent studies show that similar to the excitatory (glutamatergic) synapses, also inhibitory synapses can undergo use-dependent plasticity (for review: [233-234] and their citations). Among the vast different types of the inhibitory interneurons, retrograde signaling has been shown to play a prominent role in the modulation of GABAergic synaptic plasticity. In simple words, *endocannabinoids* (eCBs) [235] are

synthesized by postsynaptic neurons in response to increased  $\text{Ca}^{+2}$  concentrations, action potential trains and metabotropic glutamate [236]. After their synthesis, eCbs travel backwards from the postsynaptic cells to presynaptic terminals and generate a short-term suppression of GABA release in seconds to minutes and/or long-term depression in minutes to hours [237-238]. However, in this pilot study, the observed data suggests a much faster short-term plasticity of the inhibitory synapses, which recovered in about 150ms (Fig. 3.26). A phenomenological model, similar to the short-term plasticity of excitatory synapses that describes the change of the inhibitory synapses in dependence of the presynaptic firing rate is proposed in the LCCM. This assumption is sufficient to explain the observed data. And the observed enhancement of the second response in the long ISI stimulation conditions (ISI = 90ms, ISI = 120ms) by patients may relate to the insufficient inhibition, which is caused by the short-term synaptic adaptation, to compensate the abnormally strong excitation in the neural networks [239].

#### ***Estimated model parameters***

A series of 59 one-way AONVA-tests were composed to compare the estimated parameters between participant groups (patients vs. healthy elderly, patients vs. young, young vs. healthy elderly). Fifty-six estimated model parameters characterized the 14 different inter-/intra laminar excitatory as well as inhibitory synaptic connections in their connection strength, time constant and short-term plasticity (adaptation and recovery rates). Three additional parameters controlled the input signal timing as well as the output contribution to the extracranial sensors. Significant differences were confirmed through the Bonferroni-corrected results (multiple factor 59). Two model parameters that related to the excitatory connection from EINs in layer IV to dPCs in layers V/VI were found different among the three groups (Fig. 3.29).

The first of the two parameters is the synaptic connection strength, which represents the strength of the glutamate-mediated excitatory neurotransmission. The fact that the synaptic connection was stronger in the patient group than in the healthy elderly group may implicate

an increase of glutamate neurotransmission in AD brains, which is caused by the A $\beta$  induced accumulation of glutamate in the synaptic clefts and overactivation of the glutamate receptors [204].

The second parameter that was found to be different between the patients and healthy elderly is the synaptic time constant. The time constant reflects the rise and fall of the EPSP and is a lumped effect of the activation of the faster AMPA and slower NMDA-receptors. A slower time constant in the patients compared to the healthy elderly may implicate a change in relevance between NMDA and AMPA so that NMDA gains more importance. The finding is alignment with those in animal models indicating that A $\beta$  induces a hyper-activation of the NMDA-receptors due to high concentration of glutamate and D-serine at synaptic clefts [204]. Overactivation of the NMDA triggers a cascade of excitotoxic processes [216-217] that lead to cell death and reduce the number of the NMDA-receptors and decrease NMDA function, which contributes to the loss of memory. A two-stage hypothesis [240] postulated that in the early stage of the AD, the NMDA receptors increase in sensitivity to the glutamate, which leads to hyper-activation. However, in the late stage, death and deletion of the NMDA-receptor bearing neurons causes hypo-function of the NMDA-receptors and disrupts the normal mental functions. So it will be interesting not only to show an increase in NMDA-activation of the AD patients (Fig. 3.30B) but also to demonstrate the AD-stage-related change of the NMDA. Indeed, in this pilot study, the MCI patients, who are considered as to be in the early stage of the AD, show a tendency to have even stronger NMDA activity (larger time constant) than the AD patients (Fig. 3.30B).

Another interesting finding in this study is that there is an age-related decrease in the NMDA-activation (reduced time constant) (Fig. 3.30B). This computational evidence is also in alignment with previous studies of aging [231-232]: the AMPA-receptors are less affected by the aging process than the NMDA-receptors. In contrast to the NMDA-receptors, which are related to synaptic plasticity and memory function, the synaptic connection strength (EIN->dPC) seemed also less affected by age. Similar computational evidence was also reported by a recent study on mismatch negativity in the auditory cortex [241]. It was

reported that it was synaptic plasticity, and not the synaptic connectivity strength baseline, that was affected by age.

Taken together, an age-related decrease and AD-related increase in synaptic time constant are suggested by this modeling study according to the MEG data. These findings are interpreted in terms of changes in NMDA-receptor activity, which is important to memory function. This parameter may be a suitable candidate for a biomarker in future AD research.



## Chapter 4: Summary and Future Direction

*"One cannot know more than one knows"*

*- Karl Popper 1902-1994*

NMM is proposed as a biologically plausible, yet parsimonious, mesoscopic model of cortical activity. It is especially suited to accounting for extracranial measurements like EEG or MEG. However, previous models seem to be oversimplified in several aspects that are crucial for the mechanistic understanding of a wide range of brain processes. In particular, synaptic plasticity is a necessary feature for models targeting brain functions involving adaptation, learning and memory. Moreover, in the classical neural mass model, i.e., JRM, all cells in the cortex are summarized in just three populations. In order to understand better the local information processing mechanisms it would be necessary to account for the local circuitry in more detail. Therefore, in this thesis the local cortical circuit model is proposed for extending the NMM with (1) realistic inter-/intra-laminar connections in cortical layers, and (2) use-dependent synaptic plasticity via depleting and recycling of neurotransmitters. Hence, it can better link the observed EEG/MEG with the potential underlying neural mechanisms.

In order to validate the LCCM and demonstrate its usefulness, two experiments of evoked responses in MEG are used, and both of them are related to the phenomenon of short-term adaptation that describes the fact that brain resources are taken away from the processing of repetitive information and measurable responses diminish accordingly. The models were fitted to the MEG-data using Bayesian inversion estimation.

In the first auditory adaptation experiment, the LCCM shows the potential that it is able to account for the process of adaptation and recovery, which were observed in MEG. The simulated recovery time with different ISIs was qualitatively in agreement with the literature and it suggests that the auditory adaptation effect can last about 5s. In particular, the LCCM allows drawing specific conclusions on the information flow between different cortical layers and

the extent of plasticity in different connections caused by the adaptation. The computational evidence suggests that besides the major serial excitatory information pathway (layer IV to layers II/III to layers V/VI), there exists a parallel “short-cut” pathway (layer IV to layers V/VI). In case of the irrelevant repetitive information, the excitatory connection from layer IV to layers II/III is more strongly suppressed and more slowly recovered than the one from layer IV to layers V/VI, and the pyramidal cells in layers II/III are inhibited by the inhibitory interneurons from both layers II/III and layers V/VI. This laminar circuit may allow the unimportant input flow “bypassing” the layers II/III, hence not be sent from there to higher cortical areas for further processing.

In the second somatosensory adaptation experiment, the LCCM demonstrates that it is useful for estimating the differences in the cortex amongst the young people, healthy elderly and Alzheimer's patients, which are related to the observable effect in MEG. More important, its biologically plausible parameters have the potential to give meaningful interpretations of the results and linking MEG data to specific biomarkers. The findings can be validated with those in animal models. In this experiment, it was found that the parameter values of effective connection strength (EIN->dPC) and the synaptic receptor time constant (EIN->dPC) in Alzheimer's patients were high. The young people also showed higher values in synaptic receptor time constant (EIN->dPC) than the healthy elderly. The estimated results were well in agreement with the evidence from animal models. In patient group, the strong connection strength indicates the abnormal enhancement of the glutamate-mediated excitatory neurotransmission in patients and the long synaptic constant time indicates the overactivation of the NMDA-receptors. The difference of the synaptic time constant between the young people and the healthy elderly indicates an aging process of the NMDA. The modeling results suggest that, in the normal aging process, the decrease of the activation of NMDA receptor is expected. An abnormally increase of the NMDA-activation in elderly may indicate a potential development of Alzheimer's disease.

In both experiment, the LCCM outperforms the classic NMM, i.e., the JRM, in fitting the MEG data. But it's worth noting that the main purpose of LCCM is not just to mimic the EEG/MEG

data better in such a way as parameterized curve fitting. Instead, the motivation of extension of the parsimonious JRM into a more complex LCCM comes from the necessity for accounting for fundamental neural mechanisms to explain the brain function, which are observable in EEG/MEG experiment.

The author hopes that the presented LCCM will interest other developers of neural mass model and, most importantly, to a broad range of neuroscientists who are, or might get, interested in using generative models to gain insight into cognitive processes via EEG/MEG data. Certainly these EEG/MEG data analyses should not be restricted to the evoked potentials/fields in future works. One interesting future development of LCCM may be using the LCCM-based nodes to simulate the whole brain network, therefore it can available for those experiment using the resting state data. Some other important aspects for modeling the brain function in such a model of whole brain should be investigated and included, i.e., the signal traveling time delay among the cortical areas, which is related to the neural myelination.



# References

- [1] V. B. Mountcastle, "The columnar organization of the neocortex," *Brain*, vol. 120, pp. 701-722, 1997.
- [2] E. R. Kandel, *et al.*, *Principles of neural science* vol. 4: McGraw-Hill New York, 2000.
- [3] F. A. Azevedo, *et al.*, "Equal numbers of neuronal and nonneuronal cells make the human brain an isometrically scaled - up primate brain," *Journal of Comparative Neurology*, vol. 513, pp. 532-541, 2009.
- [4] S. Herculano-Houzel, "The human brain in numbers: a linearly scaled-up primate brain," *Frontiers in human neuroscience*, vol. 3, 2009.
- [5] K. Brodmann, *Vergleichende Lokalisationslehre der Grosshirnrinde in ihren Prinzipien dargestellt auf Grund des Zellenbaues*: Barth, 1909.
- [6] O. V. Favorov and M. E. Diamond, "Demonstration of discrete place - defined columns—segregates—in the cat SI," *Journal of Comparative Neurology*, vol. 298, pp. 97-112, 1990.
- [7] P. Rakic, "Radial versus tangential migration of neuronal clones in the developing cerebral cortex," *PROCEEDINGS-NATIONAL ACADEMY OF SCIENCES USA*, vol. 92, pp. 11323-11327, 1995.
- [8] D. P. Buxhoeveden and M. F. Casanova, "The minicolumn hypothesis in neuroscience," *Brain*, vol. 125, pp. 935-951, 2002.
- [9] C. Von Der Malsburg, *The correlation theory of brain function*: Springer, 1994.
- [10] C. Von der Malsburg, "The what and why of binding: the modeler's perspective," *Neuron*, vol. 24, pp. 95-104, 1999.
- [11] G. Deco, *et al.*, "The dynamic brain: from spiking neurons to neural masses and cortical fields," *PLoS Computational Biology*, vol. 4, p. e1000092, 2008.
- [12] G. Silberberg, *et al.*, "Synaptic pathways in neural microcircuits," *Trends in neurosciences*, vol. 28, pp. 541-551, 2005.
- [13] J. F. Linden and C. E. Schreiner, "Columnar transformations in auditory cortex? A comparison to visual and somatosensory cortices," *Cerebral cortex*, vol. 13, pp. 83-89, 2003.
- [14] H.-U. Dodt and W. Zieglgänsberger, "Visualizing unstained neurons in living brain slices by infrared DIC-videomicroscopy," *Brain Research*, vol. 537, pp. 333-336, 1990.
- [15] E. M. Callaway and L. C. Katz, "Photostimulation using caged glutamate reveals functional circuitry in living brain slices," *Proceedings of the National Academy of Sciences*, vol. 90, pp. 7661-7665, 1993.
- [16] D. Schubert, *et al.*, "Mapping functional connectivity in barrel-related columns reveals layer-and cell type-specific microcircuits," *Brain Structure and Function*, vol. 212, pp. 107-119, 2007.
- [17] Z. A. Peterlin, *et al.*, "Optical probing of neuronal circuits with calcium indicators," *Proceedings of the National Academy of Sciences*, vol. 97, pp. 3619-3624, 2000.

- 
- [18] D. Schubert, *et al.*, "Layer-specific intracolumnar and transcolumnar functional connectivity of layer V pyramidal cells in rat barrel cortex," *The Journal of neuroscience*, vol. 21, pp. 3580-3592, 2001.
- [19] G. Aaron and R. Yuste, "Reverse optical probing (ROPING) of neocortical circuits," *Synapse*, vol. 60, pp. 437-440, 2006.
- [20] P. Wang and T. R. Knösche, "A Realistic Neural Mass Model of the Cortex with Lamina-Specific Connections and Synaptic Plasticity—Evaluation with Auditory Habituation," *PLoS one*, vol. 8, p. e77876, 2013.
- [21] B. H. Jansen, *et al.*, "A neurophysiologically-based mathematical model of flash visual evoked potentials," *Biological Cybernetics*, vol. 68, pp. 275-283, 1993.
- [22] B. H. Jansen and V. G. Rit, "Electroencephalogram and visual evoked potential generation in a mathematical model of coupled cortical columns," *Biological Cybernetics*, vol. 73, pp. 357-366, 1995.
- [23] K. Friston, "Bayesian estimation of dynamical systems: an application to fMRI," *NeuroImage*, vol. 16, pp. 513-530, 2002.
- [24] P. Hansen, *et al.*, *MEG: An introduction to methods*: Oxford university press, 2010.
- [25] F. H. Lopes da Silva and A. Rotterdam, "Biophysical aspects of EEG and magnetoencephalogram generation," *Electroencephalography: Basic Principles, Clinical Applications and Related Fields, 4th edition*, pp. 93-109, 1998.
- [26] A. L. Hodgkin and A. F. Huxley, "A quantitative description of membrane current and its application to conduction and excitation in nerve," *The Journal of physiology*, vol. 117, p. 500, 1952.
- [27] R. FitzHugh, "Mathematical models of threshold phenomena in the nerve membrane," *Bulletin of Mathematical Biology*, vol. 17, pp. 257-278, 1955.
- [28] M. Tsodyks, *et al.*, "Synchrony generation in recurrent networks with frequency-dependent synapses," *J Neurosci*, vol. 20, pp. 825-835, 2000.
- [29] L. Abbott, *et al.*, "Synaptic depression and cortical gain control," *Science*, vol. 275, p. 221, 1997.
- [30] W. Freeman, "Models of the dynamics of neural populations," *Electroencephalography and clinical neurophysiology. Supplement*, p. 9, 1978.
- [31] F. Lopes da Silva, *et al.*, "Model of brain rhythmic activity," *Biological Cybernetics*, vol. 15, pp. 27-37, 1974.
- [32] F. Lopes da Silva, *et al.*, "Models of neuronal populations: the basic mechanisms of rhythmicity," *Progress in brain research*, vol. 45, pp. 281-308, 1976.
- [33] P. L. Nunez, "The brain wave equation: A model for the EEG," *Mathematical Biosciences*, vol. 21, pp. 279-297, 1974.
- [34] A. Spiegler, *et al.*, "Bifurcation analysis of neural mass models: Impact of extrinsic inputs and dendritic time constants," *NeuroImage*, vol. 52, pp. 1041-1058, 2010.
- [35] A. Spiegler, *et al.*, "Modeling Brain Resonance Phenomena Using a Neural Mass Model," *PLoS Computational Biology*, vol. 7, p. e1002298, 2011.
- [36] H. R. Wilson and J. D. Cowan, "A mathematical theory of the functional dynamics of cortical and thalamic nervous tissue," *Biological Cybernetics*, vol. 13, pp. 55-80, 1973.

- 
- [37] J. J. Wright and D. T. J. Liley, "Dynamics of the brain at global and microscopic scales: Neural networks and the EEG," *Behavioral and Brain Sciences*, vol. 19, pp. 285-294, 1996.
- [38] P. A. Robinson, *et al.*, "Propagation and stability of waves of electrical activity in the cerebral cortex," *Physical Review E*, vol. 56, p. 826, 1997.
- [39] C. Rennie, *et al.*, "Unified neurophysical model of EEG spectra and evoked potentials," *Biological Cybernetics*, vol. 86, pp. 457-471, 2002.
- [40] O. David, *et al.*, "Modelling event-related responses in the brain," *NeuroImage*, vol. 25, pp. 756-770, 2005.
- [41] D. J. Felleman and D. C. Van Essen, "Distributed hierarchical processing in the primate cerebral cortex," *Cerebral cortex*, vol. 1, p. 1, 1991.
- [42] F. Wendling, *et al.*, "Epileptic fast activity can be explained by a model of impaired GABAergic dendritic inhibition," *European Journal of Neuroscience*, vol. 15, pp. 1499-1508, 2002.
- [43] M. Zavaglia, *et al.*, "A neural mass model to simulate different rhythms in a cortical region," *Computational Intelligence and Neuroscience*, vol. 2010, p. 5, 2010.
- [44] O. David and K. J. Friston, "A neural mass model for MEG/EEG:: coupling and neuronal dynamics," *NeuroImage*, vol. 20, pp. 1743-1755, 2003.
- [45] O. David, *et al.*, "Dynamic causal modeling of evoked responses in EEG and MEG," *NeuroImage*, vol. 30, pp. 1255-1272, 2006.
- [46] M. I. Garrido, *et al.*, "Dynamic causal modelling of evoked potentials: a reproducibility study," *NeuroImage*, vol. 36, pp. 571-580, 2007.
- [47] S. J. Kiebel, *et al.*, "Dynamic causal modelling of evoked responses: the role of intrinsic connections," *NeuroImage*, vol. 36, pp. 332-345, 2007.
- [48] M. I. Garrido, *et al.*, "Repetition suppression and plasticity in the human brain," *NeuroImage*, vol. 48, pp. 269-279, 2009.
- [49] C. Chen, *et al.*, "Dynamic causal modelling of induced responses," *NeuroImage*, vol. 41, pp. 1293-1312, 2008.
- [50] M. Zavaglia, *et al.*, "A neural mass model for the simulation of cortical activity estimated from high resolution EEG during cognitive or motor tasks," *Journal of neuroscience methods*, vol. 157, pp. 317-329, 2006.
- [51] R. Moran, *et al.*, "Bayesian estimation of synaptic physiology from the spectral responses of neural masses," *NeuroImage*, vol. 42, pp. 272-284, 2008.
- [52] R. Moran, *et al.*, "A neural mass model of spectral responses in electrophysiology," *NeuroImage*, vol. 37, pp. 706-720, 2007.
- [53] F. Wendling, *et al.*, "Relevance of nonlinear lumped-parameter models in the analysis of depth-EEG epileptic signals," *Biological Cybernetics*, vol. 83, pp. 367-378, 2000.
- [54] I. Bojak, *et al.*, "Connecting mean field models of neural activity to EEG and fMRI data," *Brain topography*, vol. 23, pp. 139-149, 2010.
- [55] M. N. Trong, *et al.*, "Associating spontaneous with evoked activity in a neural mass model of visual cortex," *NeuroImage*, 2012.
- [56] S. Martin, *et al.*, "Synaptic plasticity and memory: an evaluation of the hypothesis," *Annual review of neuroscience*, vol. 23, pp. 649-711, 2000.
- [57] S. Haeusler and W. Maass, "A statistical analysis of information-processing properties of

- lamina-specific cortical microcircuit models," *Cerebral cortex*, vol. 17, pp. 149-162, 2007.
- [58] A. M. Thomson, *et al.*, "Synaptic connections and small circuits involving excitatory and inhibitory neurons in layers 2–5 of adult rat and cat neocortex: triple intracellular recordings and biocytin labelling in vitro," *Cerebral cortex*, vol. 12, p. 936, 2002.
- [59] J. Lübke and D. Feldmeyer, "Excitatory signal flow and connectivity in a cortical column: focus on barrel cortex," *Brain Structure and Function*, vol. 212, pp. 3-17, 2007.
- [60] S. J. Kiebel, *et al.*, "Dynamic causal modelling for EEG and MEG," *Cognitive Neurodynamics*, vol. 2, pp. 121-136, 2008.
- [61] O. David, *et al.*, "Dynamic causal modeling of subcortical connectivity of language," *The Journal of neuroscience*, vol. 31, pp. 2712-2717, 2011.
- [62] W. Penny, *et al.*, "Comparing dynamic causal models," *NeuroImage*, vol. 22, pp. 1157-1172, 2004.
- [63] W. D. Penny, *et al.*, "Comparing families of dynamic causal models," *PLoS Computational Biology*, vol. 6, p. e1000709, 2010.
- [64] W. J. Freeman, "A linear distributed feedback model for prepyriform cortex," *Experimental Neurology*, vol. 10, pp. 525-547, 1964.
- [65] W. J. Freeman, "Mass action in the nervous system," ed: Academic Press, New York, 1975.
- [66] J. Wright, *et al.*, "Simulated electrocortical activity at microscopic, mesoscopic, and global scales," *Neuropsychopharmacology*, vol. 28, p. S80, 2003.
- [67] S. J. Kiebel, *et al.*, "Dynamic causal modelling of evoked responses in EEG/MEG with lead field parameterization," *NeuroImage*, vol. 30, pp. 1273-1284, 2006.
- [68] E. L. White and A. Keller, "Cortical circuits," 1989.
- [69] E. M. Callaway, "Local circuits in primary visual cortex of the macaque monkey," *Annual review of neuroscience*, vol. 21, pp. 47-74, 1998.
- [70] R. J. Douglas and K. A. C. Martin, "Neuronal circuits of the neocortex," *Annu. Rev. Neurosci.*, vol. 27, pp. 419-451, 2004.
- [71] K. D. Alloway, "Information processing streams in rodent barrel cortex: the differential functions of barrel and septal circuits," *Cerebral cortex*, vol. 18, pp. 979-989, 2008.
- [72] A. M. Thomson and C. Lamy, "Functional maps of neocortical local circuitry," *Frontiers in neuroscience*, vol. 1, p. 19, 2007.
- [73] C. C. Petersen, "The functional organization of the barrel cortex," *Neuron*, vol. 56, pp. 339-355, 2007.
- [74] A. M. Thomson and A. P. Bannister, "Interlaminar connections in the neocortex," *Cerebral cortex*, vol. 13, pp. 5-14, 2003.
- [75] Z. F. Kisvárdy and U. T. Eysel, "Functional and structural topography of horizontal inhibitory connections in cat visual cortex," *European Journal of Neuroscience*, vol. 5, pp. 1558-1572, 1993.
- [76] Y. Kawaguchi and Y. Kubota, "GABAergic cell subtypes and their synaptic connections in rat frontal cortex," *Cerebral cortex*, vol. 7, pp. 476-486, 1997.
- [77] G. Tamás, *et al.*, "Differentially interconnected networks of GABAergic interneurons in the visual cortex of the cat," *The Journal of neuroscience*, vol. 18, pp. 4255-4270, 1998.
- [78] T. Freund, *et al.*, "Synaptic connections, axonal and dendritic patterns of neurons



- immunoreactive for cholecystokinin in the visual cortex of the cat," *Neuroscience*, vol. 19, pp. 1133-1159, 1986.
- [79] M. Beierlein, *et al.*, "Two dynamically distinct inhibitory networks in layer 4 of the neocortex," *Journal of neurophysiology*, vol. 90, pp. 2987-3000, 2003.
- [80] A. Burkhalter, "Intrinsic connections of rat primary visual cortex: laminar organization of axonal projections," *Journal of Comparative Neurology*, vol. 279, pp. 171-186, 1989.
- [81] M. L. Feldman and A. Peters, "The forms of non - pyramidal neurons in the visual cortex of the rat," *Journal of Comparative Neurology*, vol. 179, pp. 761-793, 1978.
- [82] C. D. Gilbert, "Microcircuitry of the visual cortex," *Annual review of neuroscience*, vol. 6, pp. 217-247, 1983.
- [83] J. Parnavelas, *et al.*, "Organization of neurons in the visual cortex, area 17, of the rat," *Journal of anatomy*, vol. 124, p. 305, 1977.
- [84] F. Valverde, "Aspects of cortical organization related to the geometry of neurons with intra-cortical axons," *Journal of neurocytology*, vol. 5, pp. 509-529, 1976.
- [85] D. Schubert, *et al.*, "Morphology, electrophysiology and functional input connectivity of pyramidal neurons characterizes a genuine layer Va in the primary somatosensory cortex," *Cerebral cortex*, vol. 16, pp. 223-236, 2006.
- [86] D. Feldmeyer, *et al.*, "Monosynaptic connections between pairs of spiny stellate cells in layer 4 and pyramidal cells in layer 5A indicate that lemniscal and paralemniscal afferent pathways converge in the infragranular somatosensory cortex," *The Journal of neuroscience*, vol. 25, p. 3423, 2005.
- [87] C. D. Gilbert and T. N. Wiesel, "Morphology and intracortical projections of functionally characterised neurones in the cat visual cortex," *Nature*, vol. 280, pp. 120-125, 1979.
- [88] M. A. Castro-Alamancos and B. W. Connors, "Spatiotemporal properties of short-term plasticity sensorimotor thalamocortical pathways of the rat," *The Journal of neuroscience*, vol. 16, pp. 2767-2779, 1996.
- [89] S. Chung, *et al.*, "Short-term depression at thalamocortical synapses contributes to rapid adaptation of cortical sensory responses in vivo," *Neuron*, vol. 34, pp. 437-446, 2002.
- [90] D. Feldmeyer, *et al.*, "Synaptic connections between layer 4 spiny neurone-layer 2/3 pyramidal cell pairs in juvenile rat barrel cortex: physiology and anatomy of interlaminar signalling within a cortical column," *The Journal of physiology*, vol. 538, pp. 803-822, 2002.
- [91] Z. Zhang and M. Deschenes, "Projections to layer VI of the posteromedial barrel field in the rat: a reappraisal of the role of corticothalamic pathways," *Cerebral cortex*, vol. 8, pp. 428-436, 1998.
- [92] E. L. White and S. M. Hersch, "Thalamocortical synapses of pyramidal cells which project from Sml to Msl cortex in the mouse," *Journal of Comparative Neurology*, vol. 198, pp. 167-181, 1981.
- [93] E. L. White and S. M. Hersch, "A quantitative study of thalamocortical and other synapses involving the apical dendrites of corticothalamic projection cells in mouse Sml cortex," *Journal of neurocytology*, vol. 11, pp. 137-157, 1982.
- [94] S. Hersch and E. White, "Quantification of synapses formed with apical dendrites of Golgi-impregnated pyramidal cells: variability in thalamocortical inputs, but consistency in

- the ratios of asymmetrical to symmetrical synapses," *Neuroscience*, vol. 6, pp. 1043-1051, 1981.
- [95] S. M. Hersch and E. L. White, "Thalamocortical synapses involving identified neurons in mouse primary somatosensory cortex: a terminal degeneration and golgi/EM study," *Journal of Comparative Neurology*, vol. 195, pp. 253-263, 1981.
- [96] D. C. West, *et al.*, "Layer 6 cortico-thalamic pyramidal cells preferentially innervate interneurons and generate facilitating EPSPs," *Cerebral cortex*, vol. 16, pp. 200-211, 2006.
- [97] I. Reichova and S. M. Sherman, "Somatosensory corticothalamic projections: distinguishing drivers from modulators," *Journal of neurophysiology*, vol. 92, pp. 2185-2197, 2004.
- [98] K. Tarczy-Hornoch, *et al.*, "Intracortical excitation of spiny neurons in layer 4 of cat striate cortex in vitro," *Cerebral cortex*, vol. 9, pp. 833-843, 1999.
- [99] J. F. Staiger, *et al.*, "Recurrent axon collaterals of corticothalamic projection neurons in rat primary somatosensory cortex contribute to excitatory and inhibitory feedback-loops," *Anatomy and embryology*, vol. 194, pp. 533-543, 1996.
- [100] A. Mercer, *et al.*, "Excitatory connections made by presynaptic cortico-cortical pyramidal cells in layer 6 of the neocortex," *Cerebral cortex*, vol. 15, pp. 1485-1496, 2005.
- [101] L. C. Katz, "Local circuitry of identified projection neurons in cat visual cortex brain slices," *The Journal of neuroscience*, vol. 7, pp. 1223-1249, 1987.
- [102] M. Hübener, *et al.*, "Morphological types of projection neurons in layer 5 of cat visual cortex," *Journal of Comparative Neurology*, vol. 301, pp. 655-674, 1990.
- [103] S. C. Van Horn and S. M. Sherman, "Differences in projection patterns between large and small corticothalamic terminals," *Journal of Comparative Neurology*, vol. 475, pp. 406-415, 2004.
- [104] A. Thomson and A. Bannister, "Postsynaptic pyramidal target selection by descending layer III pyramidal axons: dual intracellular recordings and biocytin filling in slices of rat neocortex," *Neuroscience*, vol. 84, pp. 669-683, 1998.
- [105] L. L. Porter and E. L. White, "Synaptic connections of callosal projection neurons in the vibrissal region of mouse primary motor cortex: an electron microscopic/horseradish peroxidase study," *Journal of Comparative Neurology*, vol. 248, pp. 573-587, 1986.
- [106] E. Elhanany and E. L. White, "Intrinsic circuitry: synapses involving the local axon collaterals of corticocortical projection neurons in the mouse primary somatosensory cortex," *Journal of Comparative Neurology*, vol. 291, pp. 43-54, 1990.
- [107] E. L. White and D. Czeiger, "Synapses made by axons of callosal projection neurons in mouse somatosensory cortex: emphasis on intrinsic connections," *Journal of Comparative Neurology*, vol. 303, pp. 233-244, 1991.
- [108] C. D. Gilbert and T. N. Wiesel, "Functional organization of the visual cortex," *Progress in brain research*, vol. 58, pp. 209-218, 1983.
- [109] A. M. Thomson, *et al.*, "Single axon IPSPs elicited in pyramidal cells by three classes of interneurons in slices of rat neocortex," *The Journal of physiology*, vol. 496, pp. 81-102, 1996.
- [110] N. Weiler, *et al.*, "Top-down laminar organization of the excitatory network in motor cortex," *Nature neuroscience*, vol. 11, pp. 360-366, 2008.

- 
- [111] G. M. G. Shepherd and K. Svoboda, "Laminar and columnar organization of ascending excitatory projections to layer 2/3 pyramidal neurons in rat barrel cortex," *The Journal of neuroscience*, vol. 25, p. 5670, 2005.
- [112] I. Bureau, *et al.*, "Interdigitated paralemniscal and lemniscal pathways in the mouse barrel cortex," *PLoS biology*, vol. 4, p. e382, 2006.
- [113] J. Lund, *et al.*, "Anatomical organization of the primary visual cortex (area 17) of the cat. A comparison with area 17 of the macaque monkey," *The Journal of comparative neurology*, vol. 184, pp. 599-618, 1979.
- [114] K. Martin and D. Whitteridge, "Form, function and intracortical projections of spiny neurones in the striate visual cortex of the cat," *The Journal of physiology*, vol. 353, pp. 463-504, 1984.
- [115] S. Murakami and Y. Okada, "Contributions of principal neocortical neurons to magnetoencephalography and electroencephalography signals," *The Journal of physiology*, vol. 575, pp. 925-936, 2006.
- [116] C. F. Stevens and Y. Wang, "Facilitation and depression at single central synapses," *Neuron*, vol. 14, pp. 795-802, 1995.
- [117] R. S. Zucker, "Short-term synaptic plasticity," *Annual review of neuroscience*, vol. 12, pp. 13-31, 1989.
- [118] R. S. Zucker and W. G. Regehr, "Short-term synaptic plasticity," *Annual review of physiology*, vol. 64, pp. 355-405, 2002.
- [119] D. Fioravante and W. G. Regehr, "Short-term forms of presynaptic plasticity," *Current Opinion in Neurobiology*, vol. 21, pp. 269-274, 2011.
- [120] P. Dayan and L. F. Abbott, *Theoretical neuroscience*: Cambridge, MA: MIT Press, 2001.
- [121] R. F. Thompson and W. A. Spencer, "Habituation: a model phenomenon for the study of neuronal substrates of behavior," *Psychological review*, vol. 73, p. 16, 1966.
- [122] H. Fruhstorfer, *et al.*, "Short-term habituation of the auditory evoked response in man," *Electroencephalography and clinical Neurophysiology*, vol. 28, pp. 153-161, 1970.
- [123] T. Rosburg, *et al.*, "Habituation of auditory evoked potentials in intracranial and extracranial recordings," *Psychophysiology*, vol. 43, pp. 137-144, 2006.
- [124] R. Näätänen and T. Picton, "The N1 wave of the human electric and magnetic response to sound: a review and an analysis of the component structure," *Psychophysiology*, vol. 24, pp. 375-425, 1987.
- [125] T. Rosburg, *et al.*, "Short-term habituation of auditory evoked potential and neuromagnetic field components in dependence of the interstimulus interval," *Experimental brain research*, vol. 205, pp. 559-570, 2010.
- [126] T. Rosburg, *et al.*, "The dipole location shift within the auditory evoked neuromagnetic field components N100m and mismatch negativity (MMNm)," *Clinical Neurophysiology*, vol. 115, pp. 906-913, 2004.
- [127] M. Sams, *et al.*, "The human auditory sensory memory trace persists about 10 sec: Neuromagnetic evidence," *Journal of Cognitive Neuroscience*, vol. 5, pp. 363-370, 1993.
- [128] F. M. Hanlon, *et al.*, "Distinct M50 and M100 auditory gating deficits in schizophrenia," *Psychophysiology*, vol. 42, pp. 417-427, 2005.
- [129] H. Soininen, *et al.*, "Habituation of auditory N100 correlates with amygdaloid volumes and

- frontal functions in age-associated memory impairment," *Physiology & behavior*, vol. 57, pp. 927-935, 1995.
- [130] W. Wang, *et al.*, "Intensity dependence of auditory evoked potentials is pronounced in migraine," *Neurology*, vol. 46, pp. 1404-1404, 1996.
- [131] I. P. Jääskeläinen, *et al.*, "Human posterior auditory cortex gates novel sounds to consciousness," *Proceedings of the National Academy of Sciences of the United States of America*, vol. 101, p. 6809, 2004.
- [132] P. J. C. May and H. Tiitinen, "Mismatch negativity (MMN), the deviance - elicited auditory deflection, explained," *Psychophysiology*, vol. 47, pp. 66-122, 2010.
- [133] V. Castellucci, *et al.*, "Neuronal mechanisms of habituation and dishabituation of the gill-withdrawal reflex in *Aplysia*," *Science*, vol. 167, p. 1745, 1970.
- [134] V. F. Castellucci and E. R. Kandel, "A quantal analysis of the synaptic depression underlying habituation of the gill-withdrawal reflex in *Aplysia*," *Proceedings of the National Academy of Sciences*, vol. 71, pp. 5004-5008, 1974.
- [135] A. Liley and K. North, "An electrical investigation of effects of repetitive stimulation on mammalian neuromuscular junction," *J Neurophysiol*, vol. 16, pp. 509-527, 1953.
- [136] W. Betz, "Depression of transmitter release at the neuromuscular junction of the frog," *The Journal of physiology*, vol. 206, p. 629, 1970.
- [137] L. G. Wu and W. J. Betz, "Kinetics of synaptic depression and vesicle recycling after tetanic stimulation of frog motor nerve terminals," *Biophysical journal*, vol. 74, pp. 3003-3009, 1998.
- [138] Y. Sara, *et al.*, "Fast vesicle recycling supports neurotransmission during sustained stimulation at hippocampal synapses," *The Journal of neuroscience*, vol. 22, pp. 1608-1617, 2002.
- [139] A. Todorovic, *et al.*, "Prior expectation mediates neural adaptation to repeated sounds in the auditory cortex: an MEG study," *The Journal of neuroscience*, vol. 31, pp. 9118-9123, 2011.
- [140] M. Bear, *et al.*, "Neuroscience Exploring the Brain.(2007)," ed: Lippincotts Williams & Wilkins.
- [141] H. Markram, *et al.*, "Interneurons of the neocortical inhibitory system," *Nature Reviews Neuroscience*, vol. 5, pp. 793-807, 2004.
- [142] E. D. De Robertis and H. S. Bennett, "Some features of the submicroscopic morphology of synapses in frog and earthworm," *The Journal of biophysical and biochemical cytology*, vol. 1, pp. 47-58, 1955.
- [143] I. Mintz, *et al.*, "Calcium control of transmitter release at a cerebellar synapse," *Neuron*, vol. 15, pp. 675-688, 1995.
- [144] W. A. Catterall and A. P. Few, "Calcium channel regulation and presynaptic plasticity," *Neuron*, vol. 59, pp. 882-901, 2008.
- [145] N. J. Maragakis and J. D. Rothstein, "Glutamate transporters: animal models to neurologic disease," *Neurobiology of disease*, vol. 15, pp. 461-473, 2004.
- [146] M. Tsodyks, *et al.*, "Neural networks with dynamic synapses," *Neural computation*, vol. 10, pp. 821-835, 1998.
- [147] M. V. Tsodyks and H. Markram, "The neural code between neocortical pyramidal neurons depends on neurotransmitter release probability," *Proceedings of the National Academy of Sciences*, vol. 94, p. 719, 1997.
- [148] J. H. Bollmann, *et al.*, "Calcium sensitivity of glutamate release in a calyx-type terminal,"

- Science*, vol. 289, pp. 953-957, 2000.
- [149] R. Schneggenburger and E. Neher, "Intracellular calcium dependence of transmitter release rates at a fast central synapse," *Nature*, vol. 406, pp. 889-893, 2000.
- [150] V. N. Murthy, *et al.*, "Heterogeneous release properties of visualized individual hippocampal synapses," *Neuron*, vol. 18, pp. 599-612, 1997.
- [151] X. Lou, *et al.*, "Allosteric modulation of the presynaptic  $\text{Ca}^{2+}$  sensor for vesicle fusion," *Nature*, vol. 435, pp. 497-501, 2005.
- [152] M. Wehr and A. M. Zador, "Synaptic mechanisms of forward suppression in rat auditory cortex," *Neuron*, vol. 47, pp. 437-445, 2005.
- [153] M. Galarreta and S. Hestrin, "Frequency-dependent synaptic depression and the balance of excitation and inhibition in the neocortex," *Nature neuroscience*, vol. 1, pp. 587-594, 1998.
- [154] H. Markram, *et al.*, "Differential signaling via the same axon of neocortical pyramidal neurons," *Proceedings of the National Academy of Sciences*, vol. 95, p. 5323, 1998.
- [155] P. P. Atluri and W. G. Regehr, "Determinants of the time course of facilitation at the granule cell to Purkinje cell synapse," *The Journal of neuroscience*, vol. 16, pp. 5661-5671, 1996.
- [156] M. Blatow, *et al.*, " $\text{Ca}^{2+}$  Buffer Saturation Underlies Paired Pulse Facilitation in Calbindin-D28k-Containing Terminals," *Neuron*, vol. 38, pp. 79-88, 2003.
- [157] B. Katz and R. Miledi, "The role of calcium in neuromuscular facilitation," *The Journal of physiology*, vol. 195, pp. 481-492, 1968.
- [158] K. J. Friston, *et al.*, "Dynamic causal modelling," *NeuroImage*, vol. 19, pp. 1273-1302, 2003.
- [159] D. W. Marquardt, "An algorithm for least-squares estimation of nonlinear parameters," *Journal of the Society for Industrial & Applied Mathematics*, vol. 11, pp. 431-441, 1963.
- [160] M. Lampton, "Damping-undamping strategies for the Levenberg-Marquardt nonlinear least-squares method," *Computers in Physics*, vol. 11, pp. 110-115, 1997.
- [161] F. Tadel, *et al.*, "Brainstorm: a user-friendly application for MEG/EEG analysis," *Computational Intelligence and Neuroscience*, vol. 2011, p. 8, 2011.
- [162] D. Weinstein, *et al.*, "Lead-field bases for electroencephalography source imaging," *Annals of biomedical engineering*, vol. 28, pp. 1059-1065, 2000.
- [163] R. Pascual-Marqui, "Standardized low-resolution brain electromagnetic tomography (sLORETA): technical details," *Methods Find Exp Clin Pharmacol*, vol. 24, pp. 5-12, 2002.
- [164] R. D. Pascual-Marqui, "Instantaneous and lagged measurements of linear and nonlinear dependence between groups of multivariate time series: frequency decomposition," *arXiv preprint arXiv:0711.1455*, 2007.
- [165] H. M. Huizenga, *et al.*, "Spatiotemporal EEG/MEG source analysis based on a parametric noise covariance model," *Biomedical Engineering, IEEE Transactions on*, vol. 49, pp. 533-539, 2002.
- [166] C. M. Bishop, *Pattern recognition and machine learning*: springer, 2006.
- [167] A. P. Dempster, *et al.*, "Maximum likelihood from incomplete data via the EM algorithm," *Journal of the Royal Statistical Society. Series B (Methodological)*, pp. 1-38, 1977.
- [168] J. L. W. V. Jensen, "Sur les fonctions convexes et les inégalités entre les valeurs moyennes," *Acta Mathematica*, vol. 30, pp. 175-193, 1906.
- [169] S. Kullback and R. A. Leibler, "On information and sufficiency," *The Annals of Mathematical*

- Statistics*, pp. 79-86, 1951.
- [170] R. E. Kass and A. E. Raftery, "Bayes factors," *Journal of the American Statistical Association*, vol. 90, pp. 773-795, 1995.
- [171] A. E. Raftery, "Bayesian model selection in social research," *Sociological methodology*, vol. 25, pp. 111-164, 1995.
- [172] R. L. Rogers, *et al.*, "Neuromagnetic evidence of a dynamic excitation pattern generating the N100 auditory response," *Electroencephalography and Clinical Neurophysiology/Evoked Potentials Section*, vol. 77, pp. 237-240, 1990.
- [173] G. Zouridakis, *et al.*, "Multiple bilaterally asymmetric cortical sources account for the auditory N1m component," *Brain topography*, vol. 10, pp. 183-189, 1998.
- [174] J. Ahveninen, *et al.*, "Task-modulated "what" and "where" pathways in human auditory cortex," *Proceedings of the National Academy of Sciences*, vol. 103, p. 14608, 2006.
- [175] N. Zacharias, *et al.*, "Stimulation - history effects on the M100 revealed by its differential dependence on the stimulus onset interval," *Psychophysiology*, vol. 49, pp. 909-919, 2012.
- [176] Z. Lu, *et al.*, "Behavioral lifetime of human auditory sensory memory predicted by physiological measures," *Science*, vol. 258, pp. 1668-1670, 1992.
- [177] T. Picton, *et al.*, "Intracerebral sources of human auditory-evoked potentials," *Audiology and Neurotology*, vol. 4, pp. 64-79, 1999.
- [178] M. Velasco, *et al.*, "Subcortical correlates of the somatic, auditory and visual vertex activities in man. I. Bipolar EEG responses and electrical stimulation," *Electroencephalography and clinical Neurophysiology*, vol. 61, pp. 519-529, 1985.
- [179] M. Velasco and F. Velasco, "Subcortical correlates of the somatic, auditory and visual vertex activities. II. Referential EEG responses," *Electroencephalography and clinical Neurophysiology*, vol. 63, pp. 62-67, 1986.
- [180] M. Hämäläinen, *et al.*, "Magnetoencephalography—theory, instrumentation, and applications to noninvasive studies of the working human brain," *Reviews of modern Physics*, vol. 65, p. 413, 1993.
- [181] N. J. Ingham and D. McAlpine, "Spike-frequency adaptation in the inferior colliculus," *Journal of neurophysiology*, vol. 91, pp. 632-645, 2004.
- [182] C. C. H. Petersen, "Short-term dynamics of synaptic transmission within the excitatory neuronal network of rat layer 4 barrel cortex," *Journal of neurophysiology*, vol. 87, pp. 2904-2914, 2002.
- [183] J. A. Varela, *et al.*, "A quantitative description of short-term plasticity at excitatory synapses in layer 2/3 of rat primary visual cortex," *The Journal of neuroscience*, vol. 17, pp. 7926-7940, 1997.
- [184] G. T. Finnerty, *et al.*, "Sensory experience modifies the short-term dynamics of neocortical synapses," *Nature*, vol. 400, pp. 367-371, 1999.
- [185] S. Taulu, *et al.*, "The signal space separation method," *Arxiv preprint physics/0401166*, 2004.
- [186] M. Hämäläinen, "MNE software User's Guide, Version 2.5," MGH/HMS/MIT Athinoula A. Martinos Center for Biomedical Imaging, Massachusetts, USA2006.
- [187] B. Fischl, "FreeSurfer," *NeuroImage*, vol. 62, pp. 774-781, 2012.
- [188] A. Gramfort, *et al.*, "OpenMEEG: opensource software for quasistatic bioelectromagnetics,"

- Biomedical engineering online*, vol. 9, p. 45, 2010.
- [189] C. C. Dickey, *et al.*, "Smaller left Heschl's gyrus volume in patients with schizotypal personality disorder," *American Journal of Psychiatry*, vol. 159, pp. 1521-1527, 2002.
- [190] S. Laxminarayan, *et al.*, "Modeling habituation in rat EEG-evoked responses via a neural mass model with feedback," *Biological Cybernetics*, pp. 1-27, 2012.
- [191] W. H. Organization, "Dementia fact sheet N. 362 2012," ed.
- [192] B. Duthey, "Background paper 6.11: Alzheimer disease and other dementias," *A Public Health Approach to Innovation*, pp. 1-74, 2013.
- [193] C. Ferri, *et al.*, "World Alzheimer Report 2009-Executive Summary," *Edited by: Prince M, Jackson J. London: Alzheimer's Disease International*, pp. 1-22, 2009.
- [194] J. L. Shaffer, *et al.*, "Predicting cognitive decline in subjects at risk for Alzheimer disease by using combined cerebrospinal fluid, MR imaging, and PET biomarkers," *Radiology*, vol. 266, pp. 583-591, 2013.
- [195] K. Honjo, *et al.*, "Alzheimer's disease, cerebrovascular disease, and the  $\beta$ -amyloid cascade," *The Canadian Journal of Neurological Sciences*, vol. 39, pp. 712-728, 2012.
- [196] M. P. Mattson, "Glutamate and neurotrophic factors in neuronal plasticity and disease," *Annals of the New York Academy of Sciences*, vol. 1144, pp. 97-112, 2008.
- [197] H. Braak and K. Del Tredici, "Where, when, and in what form does sporadic Alzheimer's disease begin?," *Current opinion in neurology*, vol. 25, pp. 708-714, 2012.
- [198] W.-P. Chen, *et al.*, "Effect of sample size for normal database on diagnostic performance of brain FDG PET for the detection of Alzheimer's disease using automated image analysis," *Nuclear medicine communications*, vol. 29, pp. 270-276, 2008.
- [199] C. Rowe, *et al.*, "Imaging  $\beta$ -amyloid burden in aging and dementia," *Neurology*, vol. 68, pp. 1718-1725, 2007.
- [200] W. E. Klunk, *et al.*, "Imaging brain amyloid in Alzheimer's disease with Pittsburgh Compound - B," *Annals of neurology*, vol. 55, pp. 306-319, 2004.
- [201] G. M. McKhann, *et al.*, "The diagnosis of dementia due to Alzheimer's disease: Recommendations from the National Institute on Aging-Alzheimer's Association workgroups on diagnostic guidelines for Alzheimer's disease," *Alzheimer's & Dementia*, vol. 7, pp. 263-269, 2011.
- [202] T. J. Revett, *et al.*, "Glutamate system, amyloid  $\beta$  peptides and tau protein: functional interrelationships and relevance to Alzheimer disease pathology," *Journal of psychiatry & neuroscience: JPN*, vol. 38, p. 6, 2013.
- [203] C. Reitz, *et al.*, "Epidemiology of Alzheimer disease," *Nature Reviews Neurology*, vol. 7, pp. 137-152, 2011.
- [204] A. C. Paula - Lima, *et al.*, "Deregulation of excitatory neurotransmission underlying synapse failure in Alzheimer's disease," *Journal of neurochemistry*, vol. 126, pp. 191-202, 2013.
- [205] W. Danysz and C. G. Parsons, "Alzheimer's disease,  $\beta$  - amyloid, glutamate, NMDA receptors and memantine - searching for the connections," *British journal of pharmacology*, vol. 167, pp. 324-352, 2012.
- [206] B. S. Meldrum, "Glutamate as a neurotransmitter in the brain: review of physiology and pathology," *The Journal of nutrition*, vol. 130, pp. 1007S-1015S, 2000.

- [207] S. R. Platt, "The role of glutamate in central nervous system health and disease—a review," *The Veterinary Journal*, vol. 173, pp. 278-286, 2007.
- [208] J. Brito-Moreira, *et al.*, "A $\beta$  oligomers induce glutamate release from hippocampal neurons," *Current Alzheimer Research*, vol. 8, pp. 552-562, 2011.
- [209] C. L. Russell, *et al.*, "Amyloid-beta acts as a regulator of neurotransmitter release disrupting the interaction between synaptophysin and VAMP2," *PloS one*, vol. 7, p. e43201, 2012.
- [210] A. Parpura-Gill, *et al.*, "The inhibitory effects of  $\beta$ -amyloid on glutamate and glucose uptakes by cultured astrocytes," *Brain Research*, vol. 754, pp. 65-71, 1997.
- [211] T. Harkany, *et al.*, "b-Amyloid neurotoxicity is mediated by a glutamate-triggered excitotoxic cascade in rat nucleus basalis," *European Journal of Neuroscience*, vol. 12, pp. 2735-2745, 2000.
- [212] H. L. Scott, *et al.*, "Aberrant expression of the glutamate transporter excitatory amino acid transporter 1 (EAAT1) in Alzheimer's disease," *The Journal of neuroscience: the official journal of the Society for Neuroscience*, vol. 22, pp. RC206-RC206, 2002.
- [213] C. Jacob, *et al.*, "Alterations in expression of glutamatergic transporters and receptors in sporadic Alzheimer's disease," *Journal of Alzheimer's Disease*, vol. 11, pp. 97-116, 2007.
- [214] L. P. Mark, *et al.*, "Pictorial review of glutamate excitotoxicity: fundamental concepts for neuroimaging," *American journal of neuroradiology*, vol. 22, pp. 1813-1824, 2001.
- [215] T. C. Foster, "Calcium homeostasis and modulation of synaptic plasticity in the aged brain," *Aging cell*, vol. 6, pp. 319-325, 2007.
- [216] S. T. Ferreira and W. L. Klein, "The A $\beta$  oligomer hypothesis for synapse failure and memory loss in Alzheimer's disease," *Neurobiology of learning and memory*, vol. 96, pp. 529-543, 2011.
- [217] M. P. Mattson, "Calcium and neurodegeneration," *Aging cell*, vol. 6, pp. 337-350, 2007.
- [218] T. Gillessen, *et al.*, "Excitatory amino acid neurotoxicity," in *Molecular and Cellular Biology of Neuroprotection in the CNS*, ed: Springer, 2002, pp. 3-40.
- [219] M. P. Mattson, "Excitotoxic and excitoprotective mechanisms," *Neuromolecular medicine*, vol. 3, pp. 65-94, 2003.
- [220] M. Shleper, *et al.*, "D-serine is the dominant endogenous coagonist for NMDA receptor neurotoxicity in organotypic hippocampal slices," *The Journal of neuroscience*, vol. 25, pp. 9413-9417, 2005.
- [221] M. Martina, *et al.*, "D - Serine differently modulates NMDA receptor function in rat CA1 hippocampal pyramidal cells and interneurons," *The Journal of physiology*, vol. 548, pp. 411-423, 2003.
- [222] C. W. Cotman and D. T. Monaghan, "Excitatory amino acid neurotransmission: NMDA receptors and Hebb-type synaptic plasticity," *Annual review of neuroscience*, vol. 11, pp. 61-80, 1988.
- [223] G. L. Collingridge and W. Singer, "Excitatory amino acid receptors and synaptic plasticity," *Trends in pharmacological sciences*, vol. 11, pp. 290-296, 1990.
- [224] D. A. Butterfield and C. B. Pocernich, "The glutamatergic system and Alzheimer's disease," *CNS drugs*, vol. 17, pp. 641-652, 2003.
- [225] K. Zito and V. Scheuss, "NMDA receptor function and physiological modulation," *Encyclopedia*



- of neuroscience*, vol. 6, pp. 1157-1164, 2009.
- [226] Y. Ugawa, *et al.*, "Somatosensory evoked potentials recovery (SEP-R) in myoclonic patients," *Electroencephalography and Clinical Neurophysiology/Evoked Potentials Section*, vol. 80, pp. 21-25, 1991.
- [227] M. C. Angulo, *et al.*, "Postsynaptic glutamate receptors and integrative properties of fast-spiking interneurons in the rat neocortex," *Journal of neurophysiology*, vol. 82, pp. 1295-1302, 1999.
- [228] R. F. Schmidt, *et al.*, *Physiologie des menschen: mit pathophysiologie*: Springer-Verlag, 2007.
- [229] A. Nakamura, *et al.*, "Somatosensory homunculus as drawn by MEG," *NeuroImage*, vol. 7, pp. 377-386, 1998.
- [230] J. Shlens, "A tutorial on principal component analysis," *arXiv preprint arXiv:1404.1100*, 2014.
- [231] K. R. Magnusson, *et al.*, "Selective vulnerabilities of N-methyl-D-aspartate (NMDA) receptors during brain aging," *Frontiers in aging neuroscience*, vol. 2, 2010.
- [232] Z. Yang, *et al.*, "Synaptic commitment: developmentally regulated reciprocal changes in hippocampal granule cell NMDA and AMPA receptors over the lifespan," *Journal of neurophysiology*, vol. 99, pp. 2760-2768, 2008.
- [233] P. Méndez and A. Bacci, "Assortment of GABAergic plasticity in the cortical interneuron melting pot," *Neural plasticity*, vol. 2011, 2011.
- [234] C. E. Flores and P. Méndez, "Shaping inhibition: activity dependent structural plasticity of GABAergic synapses," *Frontiers in Cellular Neuroscience*, vol. 8, p. 327, 2014.
- [235] T. Ohno-Shosaku, *et al.*, "Endogenous cannabinoids mediate retrograde signals from depolarized postsynaptic neurons to presynaptic terminals," *Neuron*, vol. 29, pp. 729-738, 2001.
- [236] M. Kano, *et al.*, "Endocannabinoid-mediated control of synaptic transmission," *Physiological reviews*, vol. 89, pp. 309-380, 2009.
- [237] V. Chevaleyre, *et al.*, "Endocannabinoid-mediated synaptic plasticity in the CNS," *Annu. Rev. Neurosci.*, vol. 29, pp. 37-76, 2006.
- [238] D. Piomelli, "The molecular logic of endocannabinoid signalling," *Nature Reviews Neuroscience*, vol. 4, pp. 873-884, 2003.
- [239] K. C.-K. Malina, *et al.*, "Imbalance between excitation and inhibition in the somatosensory cortex produces postadaptation facilitation," *The Journal of neuroscience*, vol. 33, pp. 8463-8471, 2013.
- [240] J. W. Newcomer, *et al.*, "NMDA receptor function, memory, and brain aging," *Dialogues in clinical neuroscience*, vol. 2, p. 219, 2000.
- [241] R. J. Moran, *et al.*, "The brain ages optimally to model its environment: evidence from sensory learning over the adult lifespan," *PLoS Computational Biology*, vol. 10, 2014.

## Appendix A

**Table A.1 Estimated source activities at the N100m peak of each stimulus in [100nAm]**

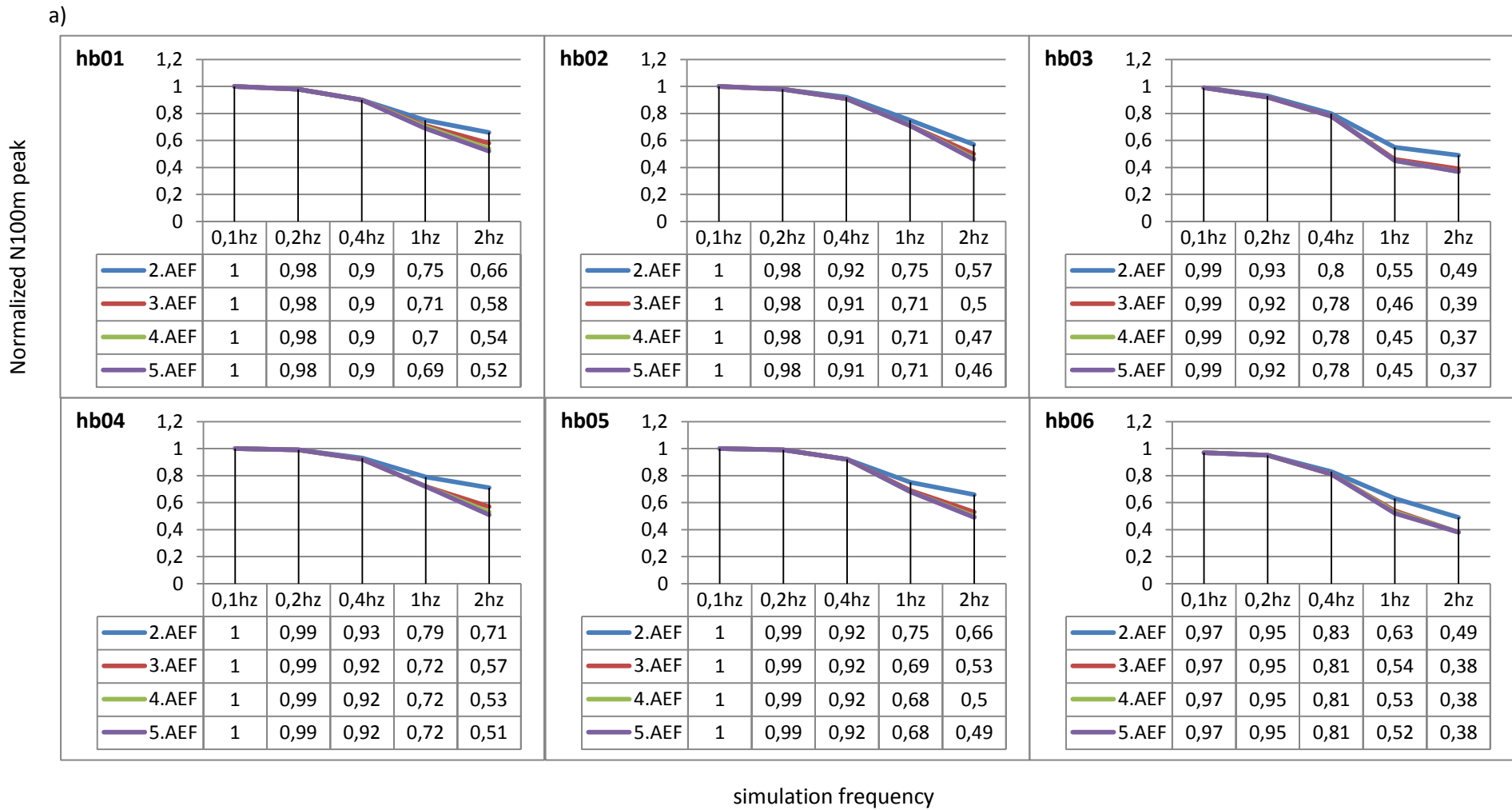
[100nAm]	1st	2nd	3rd	4th	5th	6th	7th	8th	9th	10th
<b>hb01</b>	11,85	8,242	6,546	6,136	6,247	5,438	5,287	4,669	4,912	5,386
<b>hb02</b>	8,454	4,304	4,375	4,516	3,838	4,056	3,494	3,101	3,13	1,933
<b>hb03</b>	11,88	5,76	5,353	3,889	4,309	4,391	3,339	3,255	3,096	3,836
<b>hb04</b>	9,98	6,938	5,697	5,454	4,741	4,563	3,551	4,134	3,503	3,068
<b>hb05</b>	8,695	5,115	4,848	3,932	4,121	2,799	4,177	3,681	2,509	3,568
<b>hb06</b>	6,958	3,187	3,193	2,408	2,142	1,809	1,961	1,836	1,741	1,232
<b>hb07</b>	14,33	4,392	3,732	3,963	3,233	3,493	2,679	3,464	2,324	2,76
<b>hb08</b>	9,817	5,56	2,525	2,963	3,419	0,9223	1,326	1,091	1,627	0
<b>hb09</b>	9,836	5,449	4,508	5,517	3,858	4,285	3,201	4,15	4,661	4,216
<b>hb10</b>	6,499	2,436	3,23	3,479	2,12	2,492	2,548	2,292	2,717	2,675
<b>hb11</b>	15,4	9,304	9,958	8,214	8,051	7	7,536	6,662	6,876	5,933
<b>hb12</b>	12,06	6,24	7,293	5,343	5,083	5,197	4,136	4,057	4,021	3,874
<b>hb13</b>	13,01	2,346	3,707	2,468	2,767	2,013	2,697	1,429	1,419	1,479

Table A.2 Goodness of fit comparison of LCCM and JRM

	goodness of fit		goodness of prediction		Log model evidence		Log Bayesian factor
	LCCM	JRM	LCCM	JRM	LCCM	JRM	LCCM-JRM
<b>hb01</b>	0,95	0,95	0,73	0,73	1166	1160	6
<b>hb02</b>	0,92	0,88	0,61	0,75	1156	1143	13
<b>hb03</b>	0,94	0,89	0,65	0,29	1190	1072	118
<b>hb04</b>	0,85	0,83	0,44	0,32	825	809	16
<b>hb05</b>	0,89	0,73	0,56	0,12	901	681	220
<b>hb06</b>	0,91	0,87	0,49	0,34*	1010	908	102
<b>hb07</b>	0,86	0,84	0,16	0,23*	1066	1051	15
<b>hb08</b>	0,87	0,85	0,04*	0,03*	907	905	2
<b>hb09</b>	0,91	0,87	0,59	0,35	1036	982	54
<b>hb10</b>	0,91	0,9	0,47	0,49	859	848	11
<b>hb11</b>	0,95	0,95	0,74	0,75	1061	970	91
<b>hb12</b>	0,75	0,72	0,42	0,43*	738	691	47
<b>hb13</b>	0,91	0,75	0,84	0,45	1151	790	361

*Note.* LCCM = local cortical circuit model, JRM = Jansen and Rit model.

The goodness of fit describes how good the model can be used to explain the observed data. The goodness of prediction describes how good the model can simulated/predicted the future data. The log Bayesian factor is calculated by that Log model evidence of LCCM minus Log model evidence of JRM, which described how much the observed data favor the LCCM over the JRM. A factor bigger than 3 means that strong evidence supported LCCM. By participant hb06, hb07, hb08 and hb12, the JRM failed to simulation the recovery process of 10s stimulus free time. The LCCM failed to simulation the recovery of hb08 as well.



Note. AEF = auditory evoked field.

b)

Normalized N100m peak

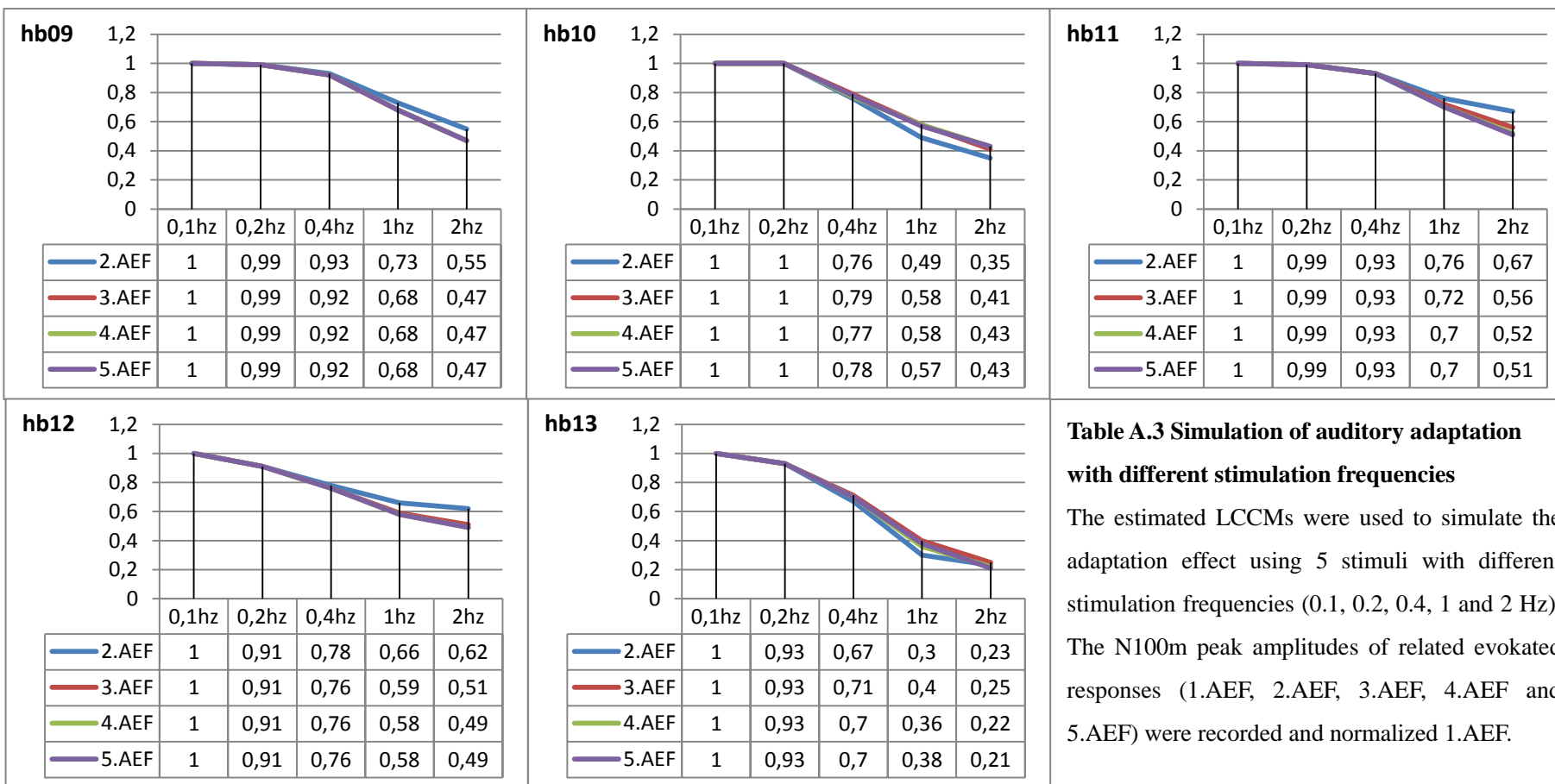


**Table A.3 Simulation of auditory adaptation with different stimulation frequencies**

The estimated LCCMs were used to simulate the adaptation effect using 5 stimuli with different stimulation frequencies (0.1, 0.2, 0.4, 1 and 2 Hz). The N100m peak amplitudes of related evoked responses (1.AEF, 2.AEF, 3.AEF, 4.AEF and 5.AEF) were recorded and normalized 1.AEF.

simulation frequency

Note. AEF = auditory evoked field.

Table A.4 Estimated synaptic connection strength (normalized of e-&gt;sp)

	sp->dp	sp->si	sp->di	dp->sp	dp->e	dp->di	dp->si	si->sp	si->dp	di->dp	di->sp	e->sp	e->dp
<b>hb01</b>	0,82	0,46	0,08	0	1,17	0,29	0	0,37	0,18	0,24	0,11	1	0,72
<b>hb02</b>	0,8	0,34	0,12	0	1,04	0,33	0,99	0,4	0	0,34	7,58	1	1,08
<b>hb03</b>	1,2	0,29	0	0	0,72	1,68	0	0,41	0	0,23	0,04	1	1,61
<b>hb04</b>	1,53	0,41	0	0	1,36	0,4	0	0,22	0	0,48	0,58	1	1,22
<b>hb05</b>	1,04	0,76	1,25	0	0,63	0,21	0,42	0,68	1,6	0,64	0	1	3,73
<b>hb06</b>	3,96	0,42	0,42	0	0,47	0,48	0,06	0,36	1,05	0,39	0	1	0
<b>hb09</b>	1,63	0,34	0	0	1,4	0,15	0	0,22	0,1	1,51	1,62	1	1,44
<b>hb10</b>	2,29	0,35	0,06	0,87	0,6	0,5	0	0,54	0	0,55	0,13	1	0
<b>hb11</b>	2,27	0,26	0,75	0,75	0,9	0,13	0	0,73	0	0,31	1,24	1	0,09
<b>hb12</b>	2,2	0,35	0	0	0,9	0,44	0	0,36	0	1,32	0	1	0,38
<b>hb13</b>	0,31	0,16	0	0	4,1	0,25	11,5	0,11	0,03	0,25	0	1	0,68

Note. sp = superficial pyramidal cells, dp = deep pyramidal cells, e = excitatory interneurons, si = superficial inhibitory interneurons, di = deep inhibitory interneurons.

**Table A.5 Adaptation-recovery dynamics for each excitatory synaptic connection**

<b>Cmin</b>	<b>e-&gt;sp</b>	<b>sp-&gt;dp</b>	<b>sp-&gt;si</b>	<b>sp-&gt;di</b>	<b>e-&gt;dp</b>	<b>dp-&gt;e</b>	<b>dp-&gt;di</b>	<b>dp-&gt;si</b>	<b>dp-&gt;sp</b>
<b>hb01</b>	0,3	0,05	0,25	0,15	0,15	0,6	0,6	-	-
<b>hb02</b>	0,15	0,98	0,98	0,98	0,45	0,2	0,15	0,05	-
<b>hb03</b>	0,1	0,8	0,75	-	0,35	0,25	0,25	-	-
<b>hb04</b>	0,2	0,8	0,6	-	0,3	0,15	0,2	-	-
<b>hb05</b>	0,1	0,93	0,95	0,93	0,3	0,1	0,2	0,3	-
<b>hb06</b>	0,2	0,5	0,35	0,6	-	0,35	0,25	0,4	-
<b>hb09</b>	0,15	0,8	0,85	-	0,7	0,3	0,5	-	-
<b>hb10</b>	0,65	0,94	0,9	0,85	-	0,7	0,4	-	0,75
<b>hb11</b>	0,55	0,8	0,9	0,6	0,2	0,9	0,85	-	0,93
<b>hb12</b>	0,5	0,05	0,1	-	0,35	0,55	0,65	-	-
<b>hb13</b>	0,1	0,93	0,96	-	0,83	0,988	0,988	0,988	-

<b><math>\Delta C</math></b>	<b>e-&gt;sp</b>	<b>sp-&gt;dp</b>	<b>sp-&gt;si</b>	<b>sp-&gt;di</b>	<b>e-&gt;dp</b>	<b>dp-&gt;e</b>	<b>dp-&gt;di</b>	<b>dp-&gt;si</b>	<b>dp-&gt;sp</b>
<b>hb07</b>	0,1	0,15	0,4	0,4	0,5	0,2	0,25	-	-
<b>hb08</b>	0,1	0,1	0,1	0,1	0,1	0,5	0,45	0,2	-
<b>hb11</b>	0,05	0,1	0,1	-	0,4	0,45	0,45	-	-
<b>hb12</b>	0,2	0,15	0,15	-	0,45	0,35	0,5	-	-
<b>hb13</b>	0,5	0,03	0,03	0,03	0,15	0,3	0,1	0,5	-
<b>hb14</b>	0,1	0,25	0,25	0,25	-	0,25	0,4	0,35	-
<b>hb18</b>	0,2	0,15	0,05	-	0,25	0,4	0,3	-	-
<b>hb19</b>	0,05	0,03	0,05	0,08	-	0,15	0,4	-	0,15
<b>hb20</b>	0,1	0,05	0,08	0,25	0,4	0,05	0,07	-	0,05
<b>hb21</b>	0,4	0,15	0,4	-	0,4	0,25	0,3	-	-
<b>hb22</b>	0,2	0,02	0,01	-	0,12	0,007	0,007	0,007	-

*Note.* sp = superficial pyramidal cells, dp = deep pyramidal cells, e = excitatory interneurons, si = superficial inhibitory interneurons, di = deep inhibitory interneurons.

For each estimated LCCM, the maximal adaptation level (= minimal synaptic efficacy) Cmin (converged after 4-6 stimuli) as well as the recovery amount inside 500ms  $\Delta C$  were listed.

## Appendix B

**Table B.1 Somatosensory activity (N20m) of the single and paired stimulations**

[fT/cm]	single(s1)	ISI30(s2)	ISI60(s2)	ISI90(s2)	ISI120(s2)	ISI150[ms](s2)
<b>AD1</b>	153,71	60,95	98,41	212,00	187,81	143,95
<b>AD2</b>	242,86	77,49	135,35	241,23	291,91	236,09
<b>AD3</b>	39,27	25,27	24,82	53,43	56,82	60,03
<b>AD4</b>	143,38	42,60	93,06	131,20	119,61	119,92
<b>AD5</b>	85,05	30,03	66,94	126,27	127,57	97,00
<b>AD6</b>	185,94	71,90	197,95	297,48	306,01	254,96
<b>MCI1</b>	153,54	52,09	138,06	169,86	216,64	182,74
<b>MCI2</b>	82,58	27,81	50,59	40,22	57,19	50,07
<b>MCI3</b>	126,80	35,59	74,76	139,32	199,87	133,04
<b>MCI4</b>	55,32	23,11	39,81	70,34	60,81	61,48
<b>MCI5</b>	89,78	63,04	76,59	95,90	100,70	109,22
<b>MCI6</b>	95,32	43,54	59,82	90,44	177,62	113,79
<b>H1</b>	82,13	57,93	65,31	71,29	79,92	104,43
<b>H2</b>	53,44	21,04	18,53	43,69	37,76	34,13
<b>H3</b>	132,76	68,49	106,35	150,01	146,37	141,64
<b>H4</b>	89,21	29,47	58,45	90,15	94,70	86,80
<b>H5</b>	105,12	44,82	88,31	125,84	127,97	96,29
<b>H6</b>	89,59	41,14	71,96	105,41	107,54	82,42
<b>H7</b>	156,70	83,88	128,00	166,39	168,20	179,87
<b>H8</b>	117,26	35,01	104,55	112,32	111,43	124,98
<b>H9</b>	117,45	43,25	70,67	110,11	133,37	97,15
<b>H10</b>	73,25	33,41	48,49	73,51	66,78	52,76
<b>H11</b>	113,33	49,65	115,66	160,78	138,15	118,86



<b>H12</b>	114,08	57,31	70,23	134,58	142,47	79,55
<b>H13</b>	125,45	56,18	95,45	92,37	100,31	93,27
<b>H14</b>	33,10	27,59	27,56	41,72	40,18	35,97
<b>H15</b>	82,84	23,69	60,07	72,93	85,06	87,36
<b>H16</b>	274,40	131,29	215,16	232,07	232,53	250,56
<b>H17</b>	73,65	33,06	64,65	76,11	70,81	49,32
<b>H18</b>	87,15	45,58	73,41	83,19	80,31	80,80
<b>Y1</b>	81,22	37,98	43,40	69,98	66,58	53,07
<b>Y2</b>	87,76	49,77	61,78	84,13	79,11	82,49
<b>Y3</b>	83,91	50,73	56,91	57,91	90,94	83,20
<b>Y4</b>	46,02	4,40	28,05	37,76	37,91	29,94
<b>Y5</b>	130,55	67,60	106,07	128,09	121,50	110,90
<b>Y6</b>	106,33	49,16	55,20	70,46	85,96	71,77
<b>Y7</b>	61,71	11,36	90,80	45,32	54,56	42,87
<b>Y8</b>	77,03	20,82	45,97	68,67	57,39	60,10
<b>Y9</b>	69,43	22,71	49,75	67,95	65,21	56,13
<b>Y10</b>	49,25	13,73	33,68	48,21	41,61	45,79

*Note.* AD = Alzheimer disease, MCI = mild cognitive impairment, H = healthy elderly, Y = young, ISI = inter stimuli interval. s1 = N20m of the first somatosensory evoked field (SEF), s2 = N20m of the second SEF

The somatosensory activity was modeled by the first PCA component of the pair of gradiometers with the largest amplitude at about 20ms. The N20m amplitudes were measured with P10m-N20m peak to peak value. For the paired stimulation, the second evoked N20m were listed in the Table.

**Table B.2 Average N20m amplitude of the somatosensory activity over single and paired stimulations**

Participant	s1-N20m mean activity [fT/cm]	Participant	s1-N20m mean activity [fT/cm]
AD1	132,3	H9	117,4
AD2	240,6	H10	73,6
AD3	29,8	H11	114,6
AD4	153,9	H12	91,9
AD5	79,8	H13	110,4
AD6	173,8	H14	34,3
MCI1	146,6	H15	84,1
MCI2	65,6	H16	252,8
MCI3	123,1	H17	68,2
MCI4	132,1	H18	93
MCI5	55,8	Y1	74,6
MCI6	94,8	Y2	92,8
H1	82,7	Y3	85,9
H2	48,7	Y4	60,9
H3	128,4	Y5	133,5
H4	84,3	Y6	103,1
H5	104	Y7	84,3
H6	77,7	Y8	81,9
H7	169,5	Y9	93,1
H8	108,6	Y10	71,1

*Note.* AD = Alzheimer disease, MCI = mild cognitive impairment, H = healthy elderly, Y = young

The somatosensory activity was modeled by the first PCA component of the pair of gradiometers with the largest amplitude at about 20ms. The mean s1-N20m was averaged over all s1-N20ms of single and paired stimulations with inter-stimulus-interval 30,60,90,120 and 150 ms.

**Table B.3 Goodness of fit of LCCM and JRM fitting somatosensory evoked field (single stimulus condition)**

GoF	LCCM	JRM	GoF	LCCM	JRM
AD1	0,98	0,61	H3	0,97	0,75
AD2	0,98	0,9	H4	0,97	0,87
AD3	0,99	0,7	H5	0,98	0,89
AD4	0,98	0,81	H6	0,71	0,75
AD5	0,98	0,63	H7	0,97	0,84
MCI1	0,98	0,8	H8	0,97	0,46
MCI2	0,85	0,58	H9	0,94	0,71
MCI3	0,98	0,45	H10	0,99	0,89
MCI4	0,99	0,93	H11	0,98	0,63
MCI5	0,95	0,51	H12	0,96	0,93
MCI6	0,98	0,69	H13	0,97	0,65
H1	0,96	0,82	H14	0,95	0,35
H2	0,96	-0,08	H15	0,97	0,51

*Note.* AD = Alzheimer disease, MCI = mild cognitive impairment, H = healthy elderly, GoF = goodness of fit, LCCM = local cortical circuit model, JRM = Jansen and Rit model.

**Table B.4 Goodness of fit of LCCM fitting somatosensory evoked field (single stimulus condition) with as well as without the implementation of the Levenberg-Maquardt algorithm**

GoF	with LM	without LM	GoF	with LM	without LM
AD1	0,98	0,29	H3	0,97	0,49
AD2	0,98	0,74	H4	0,97	0,89
AD3	0,99	0,59	H5	0,98	0,83
AD4	0,85	0,85	H6	0,71	0,55
AD5	0,98	0,48	H7	0,97	0,85
MCI1	0,98	0,68	H8	0,97	0,39
MCI2	0,85	0,67	H9	0,94	0,59
MCI3	0,98	0,59	H10	0,99	0,78
MCI4	0,95	0,73	H11	0,98	0,41
MCI5	0,95	0,51	H12	0,96	0,67
MCI6	0,98	0,65	H13	0,97	0,67
H1	0,96	0,48	H14	0,95	0,37
H2	-0,11	0,12	H15	0,07	0,04

*Note.* AD = Alzheimer disease, MCI = mild cognitive impairment, H = healthy elderly, GoF = goodness of fit, LM = Levenberg-Maquardt algorithm.

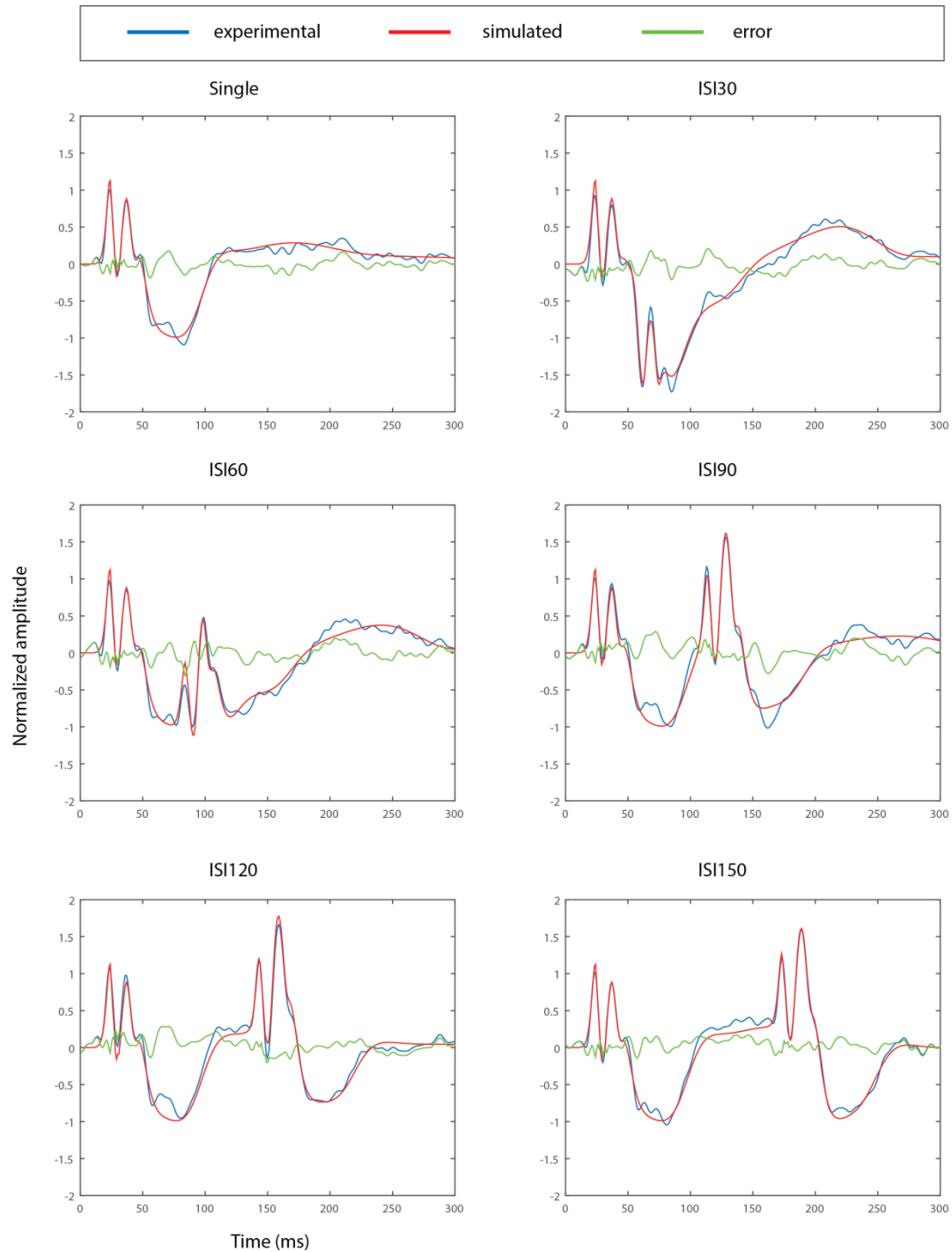
**Table B.5 Goodness of fit of LCCM fitting somatosensory evoked field (all conditions)**

<b>GoF</b>	<b>single</b>	<b>ISI30</b>	<b>ISI60</b>	<b>ISI90</b>	<b>ISI120</b>	<b>ISI150[ms]</b>
<b>AD1</b>	0,98	0,96	0,96	0,98	0,98	0,98
<b>AD2</b>	0,98	0,97	0,94	0,97	0,96	0,97
<b>AD3</b>	0,98	0,97	0,97	0,98	0,98	0,97
<b>AD4</b>	0,97	0,96	0,98	0,99	0,97	0,98
<b>AD5</b>	0,92	0,88	0,89	0,97	0,96	0,94
<b>AD6</b>	0,99	0,97	0,99	0,99	0,99	0,99
<b>MCI1</b>	0,98	0,96	0,97	0,97	0,97	0,97
<b>MCI2</b>	0,93	0,91	0,85	0,90	0,88	0,93
<b>MCI3</b>	0,94	0,92	0,90	0,95	0,94	0,94
<b>MCI4</b>	0,96	0,96	0,94	0,98	0,97	0,96
<b>MCI5</b>	0,89	0,90	0,89	0,92	0,90	0,90
<b>MCI6</b>	0,94	0,84	0,90	0,93	0,96	0,94
<b>H1</b>	0,90	0,94	0,94	0,94	0,94	0,94
<b>H2</b>	0,97	0,95	0,92	0,97	0,95	0,96
<b>H3</b>	0,97	0,93	0,96	0,96	0,97	0,97
<b>H4</b>	0,96	0,95	0,92	0,96	0,95	0,92
<b>H5</b>	0,96	0,94	0,94	0,92	0,93	0,93
<b>H6</b>	0,91	0,86	0,90	0,93	0,91	0,89
<b>H7</b>	0,94	0,93	0,93	0,89	0,91	0,91
<b>H8</b>	0,95	0,95	0,90	0,96	0,95	0,93
<b>H9</b>	0,91	0,76	0,91	0,93	0,90	0,82
<b>H10</b>	0,97	0,98	0,96	0,96	0,97	0,99
<b>H11</b>	0,96	0,92	0,93	0,97	0,97	0,97
<b>H12</b>	0,98	0,96	0,94	0,95	0,96	0,95
<b>H13</b>	0,96	0,96	0,95	0,96	0,95	0,96
<b>H14</b>	0,95	0,94	0,97	0,95	0,95	0,96

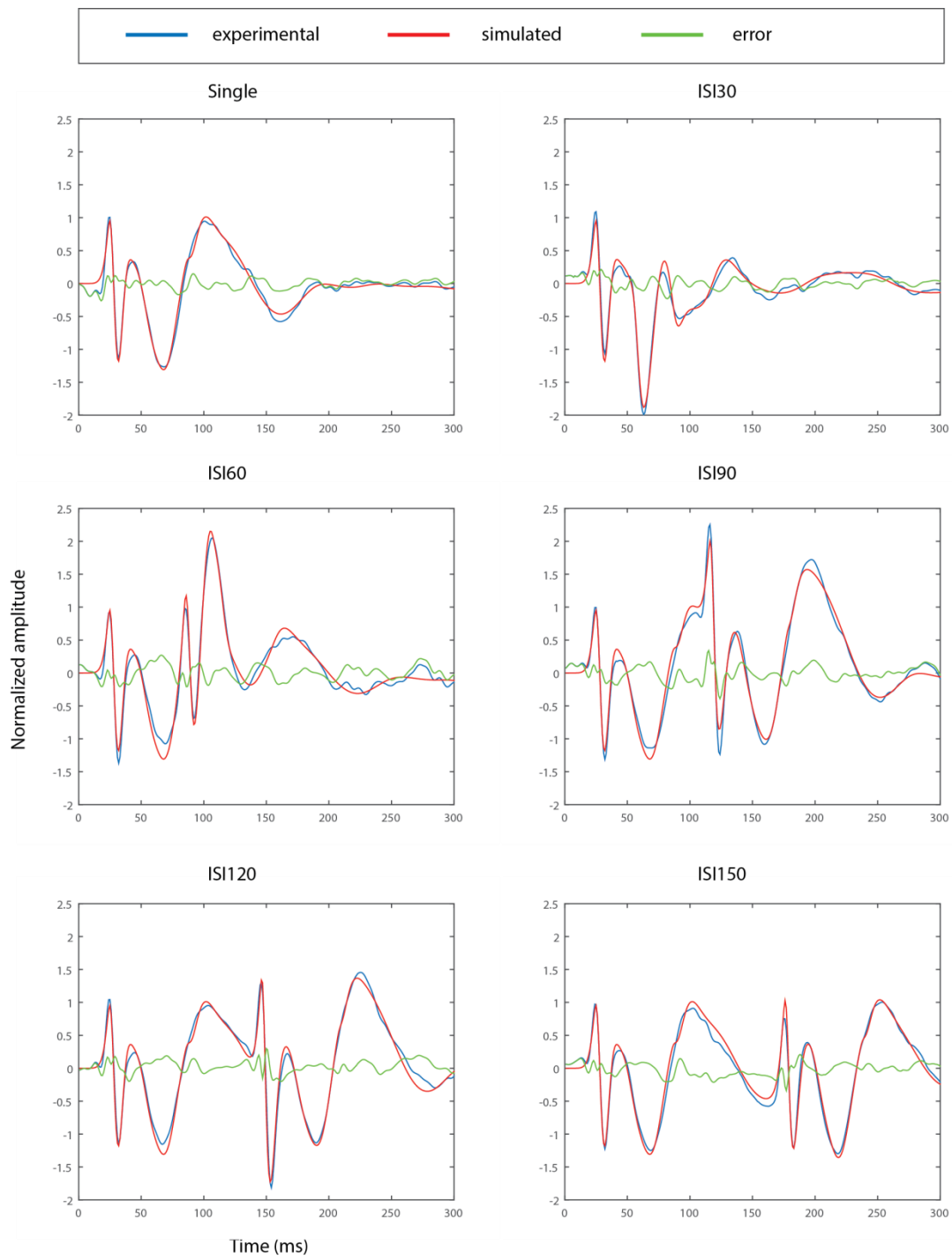
<b>H15</b>	0,97	0,97	0,96	0,97	0,98	0,97
<b>H16</b>	0,97	0,96	0,95	0,96	0,96	0,96
<b>H17</b>	0,94	0,83	0,93	0,95	0,94	0,84
<b>H18</b>	0,95	0,96	0,95	0,93	0,92	0,94
<b>Y1</b>	0,93	0,92	0,88	0,94	0,88	0,89
<b>Y2</b>	0,97	0,98	0,97	0,97	0,98	0,97
<b>Y3</b>	0,97	0,92	0,95	0,97	0,98	0,98
<b>Y4</b>	0,94	0,96	0,93	0,95	0,96	0,93
<b>Y5</b>	0,97	0,97	0,94	0,97	0,96	0,97
<b>Y6</b>	0,98	0,98	0,98	0,98	0,99	0,98
<b>Y7</b>	0,94	0,96	0,95	0,92	0,94	0,93
<b>Y8</b>	0,96	0,97	0,97	0,94	0,97	0,93
<b>Y9</b>	0,95	0,93	0,93	0,93	0,95	0,93
<b>Y10</b>	0,90	0,93	0,95	0,94	0,96	0,96

*Note.* AD = Alzheimer disease, MCI = mild cognitive impairment, H = healthy elderly, Y = young, GoF = goodness of fit, ISI = inter-stimulus-interval.

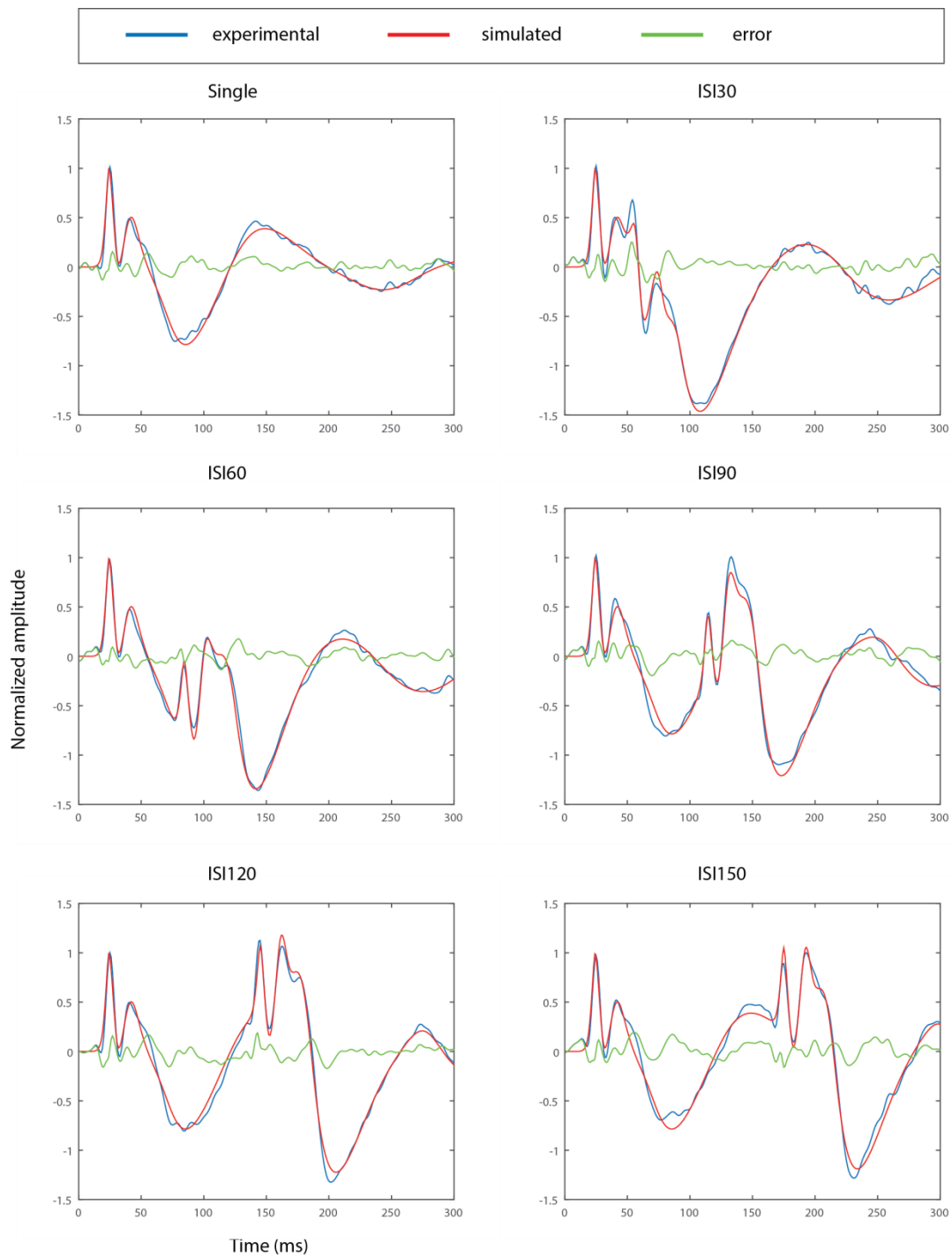
## Appendix C



Healthy elderly: H10



Patient: AD1



Young: Y6

**Figure C.1** Estimated brain activity (blue) and LCCM-modeled (red) time courses displayed together with the differences (green) between both.



## List of Figures

2.1 Two operators to simulate the neuron signal transmission in the neural mass model. ...	11
2.2 Observed value of impulse response of prepyriform cortex.....	12
2.3 The kernel function $h(t)$ .....	13
2.4 The kernel function $h(t)$ with two time constants. ....	14
2.5 The modified sigmoid function.....	15
2.6 Simulated normal distributions of 50,000 Neurons. ....	16
2.7 Simulated summarized firing rate of 50,000 Neurons in a Neural mass. ....	16
2.8 Jansen and Rit model for a single cortical column. ....	17
2.9 Input density functions.....	18
2.10 Output of Jansen and Rit model.....	19
2.11 The major interlaminar inhibitory projections. ....	25
2.12 Local circuit excitatory spiny cell targets of pyramidal and spiny stellate cells. ....	26
2.13 Local circuit excitatory spiny cell targets of inhibitory interneurons.....	27
2.14 Local cortical circuit model.....	29
2.15 Functional anatomy of an active zone.....	37
2.16 Illustration of probability density functions of normal distributed prior, likelihood as well as posterior. ....	45
2.17 Estimation of source location and activity via image approach. ....	46
2.18 The log normal distribution of the model parameter.....	61
2.19 Illustration of the exponential distribution. ....	62
2.20 Goodness of Fits of using as well as not using Levenberg-Maquardt algorithm in the E-step of the Bayesian inverse estimation. ....	67
2.21 The Goodness of fit of each iterative steps of using as well as not using levenberg-Maquardt algorithm. ....	68

---

3.1 Stimulation design of the experiment of auditory adaptation. ....	78
3.2 Anatomical view of the Heschl's gyrus as well as Planum temporale. ....	80
3.3 ROI of the N100m. ....	80
3.4 Adaptation of the source activities at N100m peak time. ....	81
3.5 Goodness of fits for the first five responses. ....	82
3.6 Individual fitting results. ....	83-84
3.7 Goodness of predictions for the last five responses. ....	85
3.8 Individual prediction results. ....	86-87
3.9 Simulation of a 10 stimuli - 10 second pause - 10 stimuli - circle. ....	88
3.10 Log Bayesian factors. ....	89
3.11 Simulation of auditory adaptation with different inter-stimuli-intervals. ....	90
3.12 Simulation of adaptation of paired stimuli with different stimulation frequencies. ....	91
3.13 The 5% quantile of a normal distribution. ....	93
3.14 Estimated laminar connection pattern of the N100m source generator. ....	94
3.15 The estimated prominent laminar signal pathways of the auditory N100m source generator. ....	98
3.16 Adaptation-recovery patterns of laminar synaptic connections. ....	99
3.17 Histogram of the synaptic connection types. ....	100
3.18 Estimated adaptation - recovery dynamics of the synaptic connections. ....	102
3.19 Histograms of synaptic adaptation - recovery dynamics. ....	103
3.20 Summarized computational findings for the N100m source generator in right Heschl's gyrus. ....	105
3.21 Pathological synaptic signal transmission in Alzheimer Disease. ....	113
3.22 Recovery function of Somatosensory evoked fields. ....	115
3.23 Stimulation design of the somatosensory adaptation. ....	117
3.24 The gradiometer pair were chosen according to having the largest amplitude at about 20ms. ....	118
3.25 The first PCA component of the somatosensory evoked fields. ....	120

---

3.26 Recovery function of Somatosensory evoked fields for patients, healthy elderly and young people. ....	121
3.27 Fitting somatosensory evoked field to single stimulus. ....	127
3.28 Box-plot of goodness of fit (GOF) of LCCM. ....	132
3.29 Significantly different model parameters between young, healthy elderly and patient group. ....	134
C.1 Estimated brain activity (blue) and LCCM-modeled (red) time courses displayed together with the differences (green) between both. ....	170-172

## List of Tables

2.1 Parameters of the Jasen and Rit mdoel (1995). .....	20
2.2 Excitatory and inhibitory inputs and targets from each cortical layer. ....	28
2.3 Interpretation of Bayesian factor. ....	58
2.4 Prior formulations of the synaptic connections in the LCCM. ....	63
3.1 Prior setup of the LCCM for the auditory adaptation experiment. ....	75-76
3.2 Prior setup of the JRM for the auditory adaptation experiment. ....	76-77
3.3 Adaptation in respect of the stimulation frequency. ....	91
3.4 Estimated “uncertain” connections. Non-zero connections are marked with “X”. ....	92
3.5 Estimated most prominent connections in auditory N100m source generator. ....	94-97
3.6 Adaptation-recovery pattern of laminar synaptic connections. ....	100
3.7 The median values of the connection efficiency after adaptation as well as the median values of the amount of recovery inside 500ms. ....	101
3.8 Prior setup for LCCM in somatosensory adaptation experiment. ....	123-124
3.9 Prior setup for JRM in somatosensory adaptation experiment. ....	125
3.10 Fitting of somatosensory cortex activity (single as well as paired conditions) using suppressed as well as constant inhibitory connections. ....	130
3.11 GoFs of LCCM using constant inhibitory synaptic connections. ....	131
3.12 Log model evidence of models using suppressed and constant inhibitory connections. .....	132
A.1 Estimated source activities at the N100m peak of each stimulus in [100nAm]. ....	158
A.2 Goodness of fit comparison of LCCM and JRM. ....	159
A.3 Simulation of auditory adaptation with different stimulation frequencies. ....	160-161
A.4 Estimated synaptic connection strength (normalized of e->sp). ....	162
A.5 Adaptation-recovery dynamics for each excitatory synaptic connection. ....	163

---

B.1 Somatosensory activity (N20m) of the single and paired stimulations. ....	164-165
B.2 Average N20m amplitude of the somatosensory activity over single and paired stimulations. ....	166
B.3 Goodness of fit of LCCM and JRM fitting somatosensory evoked field (single stimulus condition).....	167
B.4 Goodness of fit of LCCM fitting somatosensory evoked field (single stimulus condition) with as well as without the implementation of the Levenberg-Maquardt algorithm. ....	167
B.5 Goodness of fit of LCCM fitting somatosensory evoked field (all conditions). ....	168-169

## List of Equations

Equations in Chapter 2:		Equation 24	41
Equation 1	12	Equation 25	42
Equation 2	13	Equation 26	43
Equation 3	13		
Equation 4	13	Equations for parameter estimation	
Equation 5	14	Equation 27	47
Equation 6	14	Equation 28	47
Equation 7	17	Equation 29	47
Equation 8	18	Equation 30	48
Equation 9	18	Equation 31	48
Equation 10	19	Equation 32	48
Equation 11	19	Equation 33	49
Equation 12	19	Equation 34	49
Equation 13	31	Equation 35	49
Equation 14	31	Equation 36	49
Equation 15	31	Equation 37	49
Equation 16	31 -32	Equation 38	49
Equation 17	32	Equation 39	49
Equation 18	32	Equation 40	49
Equation 19	38	Equation 41	51
Equation 20	38	Equation 42	51
Equation 21	39	Equation 43	51
Equation 22	39	Equation 44	51
Equation 23	40	Equation 45	51

---

Equation 46	51	Equation 65	57
Equation 47	52	Equation 66	57
Equation 48	52	Equation 67	57
Equation 49	52	Equation 68	58
Equation 50	52	Equation 69	58
Equation 51	53	Equation 70	58
Equation 52	53	Equation 71	59
Equation 53	53	Equation 72	59
Equation 54	53	Equation 73	59
Equation 55	54	Equation 74	60
Equation 56	54	Equation 75	61
Equation 57	54	Equation 76	62
Equation 58	54	Equation 77	63
Equation 59	54	Equation 78	64
Equation 60	54	Equation 79	64
Equation 61	55		
Equation 62	56	Equations in Chapter 3	
Equation 63	57	Equation 80	88
Equation 64	57	Equation 81	93

# Erklärung

Ich versichere, dass ich die vorliegende Arbeit ohne unzulässige Hilfe Dritter und ohne Benutzung anderer als der angegebenen Hilfsmittel angefertigt habe. Die aus anderen Quellen direkt oder indirekt übernommenen Daten und Konzepte sind unter Angabe der Quelle gekennzeichnet.

Bei der Auswahl und Auswertung folgenden Materials haben mir die nachstehend aufgeführten Personen in der jeweils beschriebenen Weise unentgeltlich geholfen:

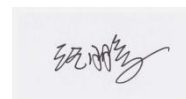
1. PD Dr. habil. Thomas Knösche: Interpretation der Analysen
2. Dr.rer.nat. Burkhard Masse: Analysen der MEG
3. Dr. Akinori Nakamura: Durchführung, Interpretation und Analysen der MEG des SEF-Experiments

Weitere Personen waren an der inhaltlich-materiellen Erstellung der vorliegenden Arbeit nicht beteiligt. Insbesondere habe ich hierfür nicht die entgeltliche Hilfe von Vermittlungs- bzw. Beratungsdiensten ( Promotionsberater oder anderer Personen ) in Anspruch genommen. Niemand hat von mir unmittelbar oder mittelbar geldwerte Leistungen für Arbeiten erhalten, die im Zusammenhang mit dem Inhalte der vorgelegten Dissertation stehen.

Die Arbeit wurde bisher weder im In- noch im Ausland in gleicher oder ähnlicher Form einer Prüfungsbehörde vorgelegt.

Ich bin darauf hingewiesen worden, dass die Unrichtigkeit der vorstehenden Erklärung als Täuschungsversuch angesehen wird und den erfolglosen Abbruch des Promotionsverfahrens zu Folge hat.

Leipzig, 09. October 2015



Peng Wang